

(12)

AD-A185 782

**AD-TR-87-08
VOLUME I**



**THIRTEENTH BIENNIAL
GUIDANCE TEST
SYMPOSIUM**

**DTIC
ELECTE**
NOV 10 1987

S

D

**6, 7, & 8 OCTOBER 1987
HOLLOMAN AFB, NEW MEXICO
88330-5000**

Publication of this report does not constitute approval or disapproval of the ideas or findings. It is published in the interest of scientific and technical information exchange.

Approved for public release; distribution is unlimited.

The Public Affairs Office has reviewed this report, and it is releasable to the National Technical Information Service where it will be available to the general public, including foreign nationals.

87 10 27 061

UNCLASSIFIED

SECURITY CLASSIFICATION OF THIS PAGE

ADA185782

REPORT DOCUMENTATION PAGE

1a. REPORT SECURITY CLASSIFICATION UNCLASSIFIED			1b. RESTRICTIVE MARKINGS NONE		
2a. SECURITY CLASSIFICATION AUTHORITY N/A			3. DISTRIBUTION/AVAILABILITY OF REPORT APPROVED FOR PUBLIC RELEASE: DISTRIBUTION UNLIMITED		
2b. DECLASSIFICATION/DOWNGRADING SCHEDULE N/A					
4. PERFORMING ORGANIZATION REPORT NUMBER(S) N/A			5. MONITORING ORGANIZATION REPORT NUMBER(S) AD-TR-87-08 (VOLUME I)		
6a. NAME OF PERFORMING ORGANIZATION 6585th TEST GROUP		6b. OFFICE SYMBOL (If applicable) 6585TG/PRX	7a. NAME OF MONITORING ORGANIZATION 3246th TEST WING		
6c. ADDRESS (City, State and ZIP Code) HOLLOMAN AFB NM 88330-5000			7b. ADDRESS (City, State and ZIP Code) EGLIN AFB FL 32542-5000		
8a. NAME OF FUNDING/SPONSORING ORGANIZATION 6585th TEST GROUP (AFSC)		8b. OFFICE SYMBOL (If applicable) 6585TG/GD	9. PROCUREMENT INSTRUMENT IDENTIFICATION NUMBER N/A		
8c. ADDRESS (City, State and ZIP Code) HOLLOMAN AFB NM 88330-5000			10. SOURCE OF FUNDING NOS.		
			PROGRAM ELEMENT NO.	PROJECT NO.	TASK NO.
			65708F		JON9993NGTS
11. TITLE (Include Security Classification) THIRTEENTH BIENNIAL GUIDANCE TEST SYMPOSIUM PROCEEDINGS (VOL I)					
12. PERSONAL AUTHOR(S) Authors' names are indicated on individual papers					
13a. TYPE OF REPORT SYMPOSIUM PAPERS		13b. TIME COVERED FROM 87-10-06 TO 87-10-08		14. DATE OF REPORT (Yr., Mo., Day) 1987 OCTOBER 15	
15. PAGE COUNT					
16. SUPPLEMENTARY NOTATION					
17. COSATI CODES			18. SUBJECT TERMS (Continue on reverse if necessary and identify by block number)		
FIELD	GROUP	SUB. GR.			
19. ABSTRACT (Continue on reverse if necessary and identify by block number)					
<p>These proceedings contain papers presented at the Thirteenth Biennial Guidance Test Symposium. This symposium, hosted by the Central Inertial Guidance Test Facility, Holloman Air Force Base, New Mexico, on 6-8 October 1987, was directed toward the exchange of information, stimulation of new ideas, and discussion of current techniques associated with the test and evaluation of inertial guidance and navigation systems and components.</p> <p>The papers presented included such topics as new test and calibration techniques for accelerometers and ring laser gyros, advances in flight reference systems, new test equipment, and new software developments.</p>					
20. DISTRIBUTION/AVAILABILITY OF ABSTRACT UNCLASSIFIED/UNLIMITED <input type="checkbox"/> SAME AS RPT. <input checked="" type="checkbox"/> DTIC USERS <input type="checkbox"/>			21. ABSTRACT SECURITY CLASSIFICATION UNCLASSIFIED		
22a. NAME OF RESPONSIBLE INDIVIDUAL GRADY S. NICHOLSON, Symposium Manager			22b. TELEPHONE NUMBER (Include Area Code) (505) 479-1228		22c. OFFICE SYMBOL 6585TG/PRX

FOREWORD


The Thirteenth Biennial Guidance Test Symposium was held at Holloman Air Force Base, New Mexico, on 6-8 October 1987. This symposium was hosted by the Central Inertial Guidance Test Facility (CIGTF). The purpose of this meeting was to bring together approximately 300 people from industry, educational institutions, foreign governments, the Department of Defense, and other Government agencies. The goal was to provide a forum for the exchange of technical information and the stimulation of new ideas related to current techniques associated with the development and evaluation of inertial guidance and navigation systems.

Many excellent papers were received for presentation at this meeting, but due to the time allotted to this symposium, only a portion of those papers submitted could be included in the Program.

The Paper Selection Committee included Mr. Philip Eubanks, Air Logistics Command; Mr. Earl Feder, U.S. Army Avionics RD Activity; Col L. R. Sugerman (USAF, RET), Physical Science Laboratory; Capt Peter Vaccaro, Aeronautical Systems Division; Mr. Ronald L. Ringo, Air Force Wright Aeronautical Laboratories; Lt Col Marty Marler, Ballistic Missile Office; Mr. John McHale, Naval Air Systems Command; Col Keith G. Gilbert, Air Force Weapons Laboratory; Dr. Harold Pastrick, Science Applications International.

In addition to those mentioned above and the contributing authors, a large number of people contributed to the success of this symposium. I wish to express my appreciation to each for their efforts. Special thanks go to our Symposium Manager, Mr. Grady S. Nicholson, and his assistant, Mrs. Dora Walker.

Publication of this report does not constitute approval or disapproval of the ideas or findings. It is published in the interest of scientific and technical information exchange.


WILLIAM C. KERCHNER, Lt Col, USAF
Director, Guidance Test Division

Accession For	
NTIS CRA&I	<input checked="checked" type="checkbox"/>
DTIC TAB	<input type="checkbox"/>
Unannounced	<input type="checkbox"/>
Justification	
By	
Distribution/	
Availability Codes	
Dist	Avail and/or Spec
A-1	



ABSTRACT

These proceedings contain papers presented at the Thirteenth Biennial Guidance Test Symposium. This symposium, hosted by the Central Inertial Guidance Test Facility, is directed toward the exchange of information, stimulation of new ideas, and discussion of current techniques associated with the development and evaluation of inertial guidance and navigation systems. The papers presented included such topics as new test and calibration techniques for accelerometers and ring laser gyros, advances in flight reference systems, new test equipment, and new software developments. This volume contains the unclassified papers which have no distribution limitation.

AD-TR-87-08

VOLUME I

PROCEEDINGS OF THE THIRTEENTH BIENNIAL
GUIDANCE TEST SYMPOSIUM

CONDUCTED AT

HOLLOMAN AIR FORCE BASE, NEW MEXICO

Hosted By

6585TH TEST GROUP
CENTRAL INERTIAL GUIDANCE TEST FACILITY

6-8 OCTOBER 1987

TABLE OF CONTENTS

SO1A	"Calibration of a Ring Laser Gyro Inertial Navigation System," John W. Diesel, Litton Aero Products, Moorpark CA	SO1A
SO1B	"Simultaneous Estimation and Detection of Bias Shifts for Inertial Navigation Systems," Richard V. Spencer, General Electric Company, 100 Plastics Avenue, Pittsfield MA; Kevin Clements, Worcester Polytechnic Institute Electrical Engineering Department, 100 Institute Road, Worcester MA	SO1B
SO1C	"Covariance Analysis and Post-Processing of Gravity Compensation Effects for Aided Multi-State Navigation Systems," Paul Zavattero, Northrop Electronics Division, 2301 W. 120th Street, P.O. Box 5032, Hawthorne CA	SO1C
SO1D	"Commonality in the Design and Production of the H-423 (F') and H-770 (F-15) RLG Inertial Navigation Systems," David Anderson, Ed Wheeler, Michael Hadfield, Honeywell Inc., Military Avionics Division, Clearwater FL	SO1D
SO2A	"Reference Position Vector," Nancy McClanahan, 6585th Test Group, Central Inertial Guidance Test Facility, Holloman AFB NM	SO2A
SO2B	"Robotics Applications in the Testing of Inertial Sensors," Joy Y. Greig, Central Inertial Guidance Test Facility, 6585th Test Group, Holloman AFB NM; Zdzislaw H. Lewantowicz, Air Force Institute of Technology, Wright-Patterson AFB OH	SO2B
SO2C	"The Optimum Solution of Instrument Quantization Effects," Thomas Reed, Charles Stark Draper Laboratory, Inc., Cambridge MA	SO2C
SO3A	"Evaluation of a Miniature Horizontal Pendulum Tilt Transducer," H. D. Valliant and L. J. Burris, LaCoste and Romberg Gravity Meters, Inc., 6606 N. Lamar, Austin TX; J. Levine, Joint Institute for Laboratory Astrophysics, National Bureau of Standards and University of Colorado, Boulder CO	SO3A
SO3B	"An Improved Data Reduction Procedure for Accelerometer Centrifuge Data," George H. Neugebauer, 28850 Pebble Beach Dr., Sun City CA	SO3B

TABLE OF CONTENTS (Continued)

S03C	"Control Test and Validation for a Large Diameter High Stability Centrifuge," S. Willis, M. Harshman, B. Popovich, M. Guardiani, R. Strane, J. Profeta, Contraves Goerz Corporation, 610 Epsilon Dr., Pittsburg PA	S03C
S04A	"The Global Positioning System as an Aid to the Testing of Inertial Navigation Units," C. P. Bruner, A. Matthews, R. E. Morgan, Litton Guidance & Control Systems, 5500 Canoga Avenue, Woodland Hills CA	S04A
S04B	"A Cause of Divergence in the Kalman Gain Equation," James B. Gose, Physical Science Laboratory, P.O. Box 30002-NMSU, Las Cruces NM	S04B
S04C	"Rate and Dynamic Tests on the Canadian Strapdown Gyroscope (CSG-2)," M. Vinnins, L. D. Gallop, F. Paquet, Defence Research Establishment Ottawa, Department of National Defence, Ottawa, Canada	S04C
S04D	"The German Honeywell Ring Laser Gyro (Status Report on Development and Test Results)," Dr. B. Bolzmann, Honeywell Regelsysteme GmbH, Unternehmensbereich Sondertechnik, Honeywellstr, D-6457 Maintal 1	S04D
Due to time constraints, the following papers were not presented at the symposium.		
S04D1	"Application of Knowledge Based Systems to the Maintenance of Inertial System Electronics," Kenneth B. Cohen, Directorate of Inertial Engineering, Aerospace Guidance and Metrology Center, Newark Air Force Station, OH	S04D1
S04D2	"Convective Heat Transfer and its Effect on Inertial Measurement Units," John J. Meehan, Rockwell International, Autonetics Strategic Systems Division, Electronics Operations, 3370 Miraloma Avenue, P.O. Box 4192, Anaheim CA	S04D2

"Calibration of a Ring Laser Gyro Inertial Navigation System," John W. Diesel, Litton Aero Products, Moorpark CA (S01A)

"Simultaneous Estimation and Detection of Bias Shifts for Inertial Navigation Systems," Richard V. Spencer, General Electric Company, 100 Plastics Avenue, Pittsfield MA; Kevin Clements, Worcester Polytechnic Institute Electrical Engineering Department, 100 Institute Road, Worcester MA (S01B)

"Covariance Analysis and Post-Processing of Gravity Compensation Effects for Aided Multi-State Navigation Systems," Paul Zavattero, Northrop Electronics Division, 2301 W. 120th Street, P.O. Box 5032, Hawthorne CA (S01C)

"Commonality in the Design and Production of the H-423 (F³) and H-770 (F-15) RLG Inertial Navigation Systems," David Anderson, Ed Wheeler, Michael Hadfield, Honeywell Inc., Military Avionics Division, Clearwater FL (S01D)

THIRTEENTH BIENNIAL GUIDANCE TEST SYMPOSIUM

CALIBRATION OF A RING LASER GYRO
INERTIAL NAVIGATION SYSTEM

AUTHOR: JOHN W. DIESEL

LITTON AERO PRODUCTS
MOORPARK, CALIFORNIA

ABSTRACT

An INS using strapdown RLG's has considerably different calibration requirements from those of an INS using a gimballed platform or an AHRS using strapdown gyros. In particular, the RLG scale factor errors and misalignment errors must be calibrated to a few parts per million, and a few microradians, respectively. This paper explains how these requirements are met to achieve one nautical mile per hour navigation accuracies. The procedure is used on all of Litton's commercial RLG systems including the LTN90, LTN90-100, and LTN92. It is also applicable to military RLG systems.

Litton uses an indirect method of calibration which is relatively independent of table accuracy. It requires only an inexpensive fixture to rotate the system instead of a rate table. The system is rotated through various angles to fixed positions at which the apparent direction and magnitude of gravity is measured. The calibration coefficients are determined by observing differences in these measurements.

The rotation sequence is optimized so that a complete set of calibration coefficients is determined explicitly at each temperature in a minimum time. This makes it unnecessary to calibrate in a temperature controlled room. Instead, the system is cooled overnight to 0°C. The system is then calibrated at room temperature but in a closed box so that the uncontrolled system temperature rises from 0°C to +60°C while the calibration measurements are being made. By rapidly repeating the rotation sequence, many complete sets of coefficients are obtained over this temperature range. The polynomial model for each coefficient versus temperature is then obtained by curve fitting.

Also, as each set of coefficients is obtained, it is added to the software compensation used during the next sequence. In this way, only a small correction is added at each step after the initial sequence. This "closed loop" method insures maximum accuracy, since the calibration errors converge to zero. Also, the equations become very linear so that higher order effects need not be considered.

Because of the RLG dither suspension system, there are additional g-sensitive misalignments of the gyros which must be accurately compensated in the operational software for some applications. This paper also explains the procedure for determining these parameters. Although the procedure is very complicated and time consuming, it need be performed only once since corresponding parameters have essentially the same values for all systems of the same design.

1. INTRODUCTION

Because of the rotational dynamics of the environment, strapdown systems require much greater accuracy in calibration of instrument parameters than a gimballed platform of the same navigation accuracy. In particular, for a one nautical mile per hour navigator, gyro and accelerometer misalignments must typically be calibrated to 5 arc seconds (Reference 1), and gyro scale factors must be calibrated to the order of 10 parts per million. In certain special applications, accuracies of 1 arc second and 2 parts per million are desirable. Gyro and accelerometer bias errors must also be calibrated more accurately than corresponding errors for a gimballed platform to achieve the same performance.

Fortunately, ring laser gyro (RLG) parameters are sufficiently stable that such calibration accuracies are achievable. Calibration techniques have been developed (References 1,2,3,4,5) which do not require expensive fixtures. However, these techniques require up to one hour (Reference 1) to determine all the parameters at a single temperature, and generally require calibration in a temperature controlled room. To avoid higher order effects in the measurements, some prior knowledge of the variation of the coefficients with temperature is sometimes required. It is desirable to use a procedure which does not have these restrictions, and requires the least expensive fixture which is still automatic. In this way, calibration and maintenance of the system in the field at remote facilities is possible, without sending the entire unit back to the factory.

This paper presents a calibration technique that is optimal in the sense that a minimum time is required to calibrate all the parameters at a single temperature. The technique is so fast that it can be used while the temperature is changing. By rapidly repeating the sequence all the parameters can be calibrated over the full range of temperatures in only a few hours. By using the solutions for each sequence in the next sequence, only small changes are required at each step, so that higher order effects are avoided. This affords maximum accuracy despite large fixture errors, so that fixture costs are minimized.

This paper does not discuss details of the instruments being calibrated, some of which are restricted or proprietary. Instead, the calibration procedure itself is explained. Sections 3 and 4 present the mathematical details of how the procedure actually works. Those readers not interested in such details can skip from Section 2 which describes the basic approach to Section 5 which describes the implementation of the approach. Conclusions are presented in Section 6.

2. CALIBRATION APPROACH

The key to accurate calibration with a relatively inaccurate test fixture is to use the strapdown instruments themselves to measure changes in fixture angular position (orientation). The fixture is used only to rotate the strapdown system from one fixed position to another, where the positions themselves need only be specified to an accuracy of a degree or so, one sigma. The change in angular position is accurately measured both by measuring the angular changes with the gyros and also by measuring the direction of gravity at both fixed positions using the accelerometers.

If the instruments were perfect, the change in position measured by the gyros and the change in position measured by the accelerometers would be the same. However, because of instrument errors, the measurements differ. This difference is a function of the calibration errors in the strapdown system. Since the calibration errors are small, this function is approximately linear. The calibration errors will be referred to as calibration "coefficients" since their values, as estimated by the calibration procedure, are used to provide software compensation in the operational system.

The calibration procedure thus consists of a sequence of angular position changes (rotations), each separated by pairs of orientations at fixed positions. Each difference between position change measured by the gyros and position change measured by the accelerometers is observed and is expressible mathematically as a linear equation in the unknown calibration coefficients. It is shown in a later section how a particular sequence of rotations is selected to yield a sufficient number of such equations to determine all the calibration coefficients.

To determine these relationships mathematically, the angular position of the system is described by direction cosines which are the components or "projections" of reference coordinate unit vectors along body coordinate unit vectors shown in Figure 1. The terminology used in Figure 1 and in the remainder of this paper is given in Table 1. The initial values of the direction cosines are determined by an alignment mechanization described in Section 4. The changes in these direction cosines, caused by rotations, are determined by a mechanization which, in effect, integrates the differential equations for the components along body axes of the reference unit vectors. This mechanization is described in the next section.

- $\vec{u}_X, \vec{u}_Y, \vec{u}_Z$ = Unit vectors along reference coordinate axes
 $\vec{u}_{BX}, \vec{u}_{BY}, \vec{u}_{BZ}$ = Unit vectors along body coordinate axes

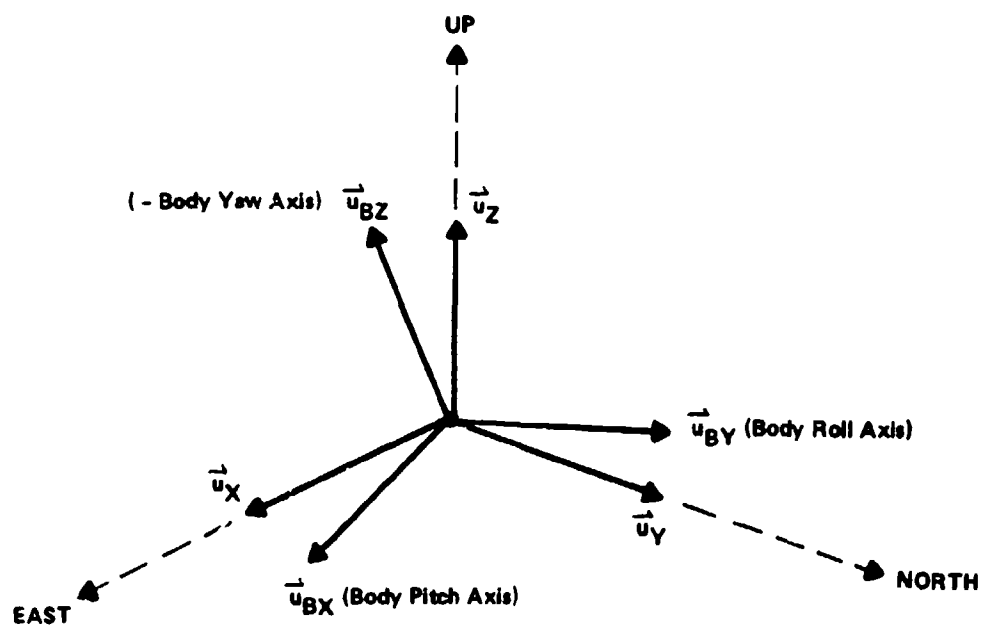


Figure 1. Definition of Coordinate Systems

Table 1. Definition of Symbols

A_X, A_Y, A_Z	Accelerometer outputs resolved along reference axes, ft/sec ²
A_X^B, A_Y^B, A_Z^B	Accelerometer outputs resolved along body axes, ft/sec ²
A_{1X}, A_{1Y}, A_{1Z}	Compensated accelerometer instrument outputs, ft/sec ²
a_X, a_Y, a_Z	Accelerometer bias errors, ft/sec ²
a_{XX}, a_{YY}, a_{ZZ}	Accelerometer scale factor errors, (ft/sec ²)/(ft/sec ²)
a_{XY}, a_{XZ}	X accelerometer misalignment toward Y, Z, respectively, radians
a_{YZ}, a_{YX}	Y accelerometer misalignment toward Z, X, respectively, radians
a_{ZX}, a_{ZY}	Z accelerometer misalignment toward X, Y, respectively, radians
\dot{a}_k^j	Observed change in horizontal acceleration along X, for set j, rotation k, ft/sec ²
B (superscript)	Components of vector resolved along body axes
(No superscript)	Components of vector resolved along reference axes
$\beta_X, \beta_Y, \beta_Z$	Gyro bias errors, radians/sec
$\beta_{XX}, \beta_{YY}, \beta_{ZZ}$	Gyro scale factor errors, (rad/sec)/(rad/sec)
β_{XY}, β_{XZ}	X gyro misalignment toward Y, Z, respectively, radians
β_{YZ}, β_{YX}	Y gyro misalignment toward Z, X, respectively, radians
β_{ZX}, β_{ZY}	Z gyro misalignment toward X, Y, respectively, radians
β_{ij0}	i gyro misalignment toward j axis under zero specific force, radians
β_{ij-k}	i gyro misalignment toward j axis due to specific force along k axis, radians/g
\dot{b}_k^j	Observed change in horizontal acceleration along Y, for set j, rotation k, ft/sec ²
C_B^R	Direction cosine matrix of reference axes with respect to body axes, dimensionless
C_{ij}	Direction cosine of i reference axis along j body axis, dimensionless
δ (prefix)	Differential error in prefixed variable
Δ (prefix)	Change in prefixed variable during rotation or coning period
e_V	Error in estimated velocity, ft/sec
g	Magnitude of gravity vector, ft/sec ²
K_1, K_2, K_3	Time variable gains in estimation filter 1/sec, 1/sec ² , 1/sec ³
$\omega_X, \omega_Y, \omega_Z$	Components of angular rate of body axes relative to reference axes, rad/sec
$\omega_{1X}, \omega_{1Y}, \omega_{1Z}$	Compensated gyro outputs, rad/sec
$\Omega_X, \Omega_Y, \Omega_Z$	Earth rate components, rad/sec
ϕ_X, ϕ_Y, ϕ_Z	Misalignments of reference axes about X, Y, Z axes, radians
t	Variable time, sec
T	Period of rotation or coning, sec
V_X, V_Y, V_Z	Velocity components, ft/sec
X, Y, Z	Reference axes
x_B, y_B, z_B	Body axes
$\dot{}$ (superscript)	First derivative of variable with respect to t, sec ⁻¹
$\ddot{}$ (superscript)	Second derivative of variable with respect to t, sec ⁻²

3. MECHANIZATION EQUATIONS AND ERROR MODELS FOR CALIBRATION MEASUREMENTS

This section will explain:

- (1) The mechanization for observing the difference between the position change measured by the gyros and the position change measured by the accelerometers, and
- (2) The error model by which these differences are related to the calibration coefficients.

The position change measured by the gyros is determined by a mechanization for integrating the differential equations for the direction cosines. This mechanization is illustrated schematically in the upper half of Figure 2, which is a visual representation of the actual equations shown in Table 2. The inputs to the differential equations are the scaled and compensated outputs of the gyros corrected for earth rate. Since both the gyros and accelerometers are strapdown, their outputs are in body coordinates. The earth rate corrections must also be converted from reference to body coordinates, as indicated at (a) in Figure 2. After subtracting these components at (b), the corrected angular rates in body coordinates are fed into the differential equations for the direction cosines which are computed and integrated at (c). As indicated, these are really the differential equations for components of reference coordinate unit vectors along body coordinates.

As stated, this is an "equivalent" mechanization. The actual mechanization solves differential equations for "quaternions" from which the direction cosines are computed directly. Since the same function of determining orientation is required in the strapdown navigation system, the algorithms used in calibration are borrowed from the navigation system mechanization. The only difference is that craft rates are not computed here, since Schuler tuning is not required.

The lower half of Figure 2 or Table 2 shows how the positions before and after the rotation are measured by the accelerometer, and how the difference in position is compared with that measured by the gyros. The positions are measured simply by measuring the direction of gravity as indicated by the horizontal components of the accelerometer outputs at (e). The azimuth orientation cannot be obtained in this way, but it is not needed. The comparison with gyro position change is obtained at (d) by resolving accelerometer outputs through the direction cosines computed by the gyros before observing horizontal components. This acceleration measurement mechanization is also borrowed from the navigation system mechanization, except that Coriolis corrections are not computed and the accelerations are not integrated into velocity.

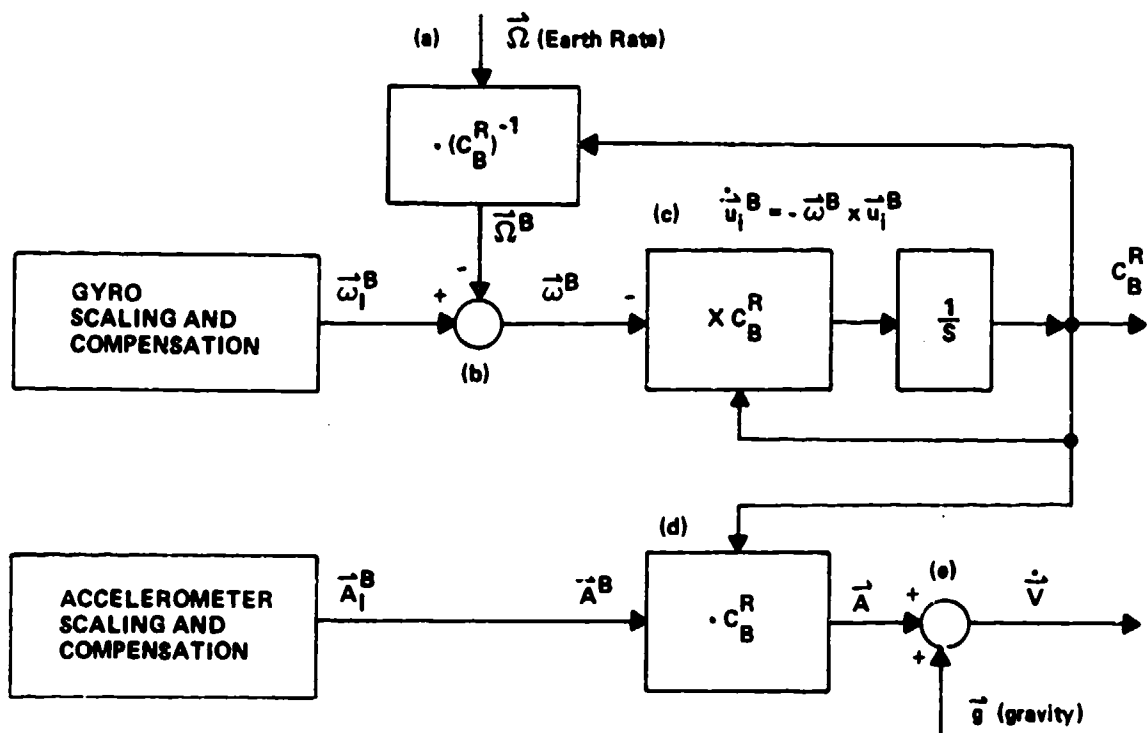


Figure 2. Diagram of Equivalent Mechanization for Measuring Horizontal and Vertical Accelerations

Table 2. Equivalent Mechanization Equations for Measuring Horizontal and Vertical Accelerations

(a) <u>RESOLVE EARTH RATE TO BODY AXES:</u>	(b) <u>CORRECT ANGULAR RATES FOR EARTH RATE:</u>
$\Omega_X^B = C_{XX}\Omega_X + C_{VX}\Omega_Y + C_{ZX}\Omega_Z$	$\omega_X^B = \omega_{IX}^B - \Omega_X^B$
$\Omega_Y^B = C_{XY}\Omega_X + C_{VY}\Omega_Y + C_{ZY}\Omega_Z$	$\omega_Y^B = \omega_{IY}^B - \Omega_Y^B$
$\Omega_Z^B = C_{XZ}\Omega_X + C_{VZ}\Omega_Y + C_{ZZ}\Omega_Z$	$\omega_Z^B = \omega_{IZ}^B - \Omega_Z^B$
(c) <u>INTEGRATE DIRECTION COSINES FROM ANGULAR RATES:</u>	
$\dot{C}_{XX} = C_{XY}\omega_Z^B - C_{XZ}\omega_Y^B$; $\dot{C}_{VX} = C_{VY}\omega_Z^B - C_{VZ}\omega_Y^B$; $\dot{C}_{ZX} = C_{ZY}\omega_Z^B - C_{ZZ}\omega_Y^B$	
$\dot{C}_{XY} = C_{XZ}\omega_X^B - C_{XX}\omega_Z^B$; $\dot{C}_{YY} = C_{YZ}\omega_X^B - C_{YX}\omega_Z^B$; $\dot{C}_{ZY} = C_{ZZ}\omega_X^B - C_{ZX}\omega_Z^B$	
$\dot{C}_{XZ} = C_{XX}\omega_Y^B - C_{XY}\omega_X^B$; $\dot{C}_{YZ} = C_{YX}\omega_Y^B - C_{VY}\omega_X^B$; $\dot{C}_{ZZ} = C_{ZX}\omega_Y^B - C_{ZY}\omega_X^B$	
(d) <u>RESOLVE ACCELEROMETER OUTPUTS:</u>	(e) <u>CORRECT ACCELERATIONS FOR GRAVITY:</u>
$A_X = C_{XX}A_X^B + C_{XY}A_Y^B + C_{XZ}A_Z^B$	$\delta \dot{V}_X = A_X$
$A_Y = C_{YX}A_X^B + C_{VY}A_Y^B + C_{YZ}A_Z^B$	$\delta \dot{V}_Y = A_Y$
$A_Z = C_{ZX}A_X^B + C_{ZY}A_Y^B + C_{ZZ}A_Z^B$	$\delta \dot{V}_Z = A_Z - g$

The error model for this mechanization is illustrated in Figure 3, which is a visual representation of the equations in Table 3. As is typical in inertial system error analysis, the error model diagram is in many ways similar to the mechanization diagrams, except that the mechanization variables are replaced by differential error variables. The alpha and beta calibration coefficients of Figure 3 correspond to the accelerometer and gyro scaling and compensation of Figure 2. These coefficients have either single or double subscripts. The single subscript X, Y, or Z indicates a bias error along the axis of the subscript. The double subscript denotes a scale factor error if the subscripts are both the same or a misalignment if the subscripts differ. The meaning of the subscripts is clear from the definitions at (1) and (4) of Table 3.

The nine direction cosines of Figure 2 are not replaced by corresponding error variables. Instead, they are replaced by the three components of vector "phi" in the upper right hand corner of Figure 3. These three components represent the misalignment of the reference axes, and therefore summarizes the errors in the direction cosines. Their rates of change are the errors in angular rates about body axes resolved into errors in angular rates about reference axes. In addition, the rates of change include the cross product between the misalignment angle and earth rate. This accounts for resolving earth rate through misaligned axes. A similar cross product is added to the acceleration error to account for resolving gravity through misaligned axes.

The observed difference in gyro and accelerometer measurement of the rotation angle is obtained as the change in horizontal acceleration from the lower right half of Figure 2, as measured at the fixed positions before and after the rotation. Since the true acceleration is zero at these fixed positions, this change is the same as the change in the horizontal acceleration error at the lower right half of Figure 3. The error model of Figure 3 will be used in the next section to express this change in terms of the calibration coefficients for the specific rotations of the calibration procedure.

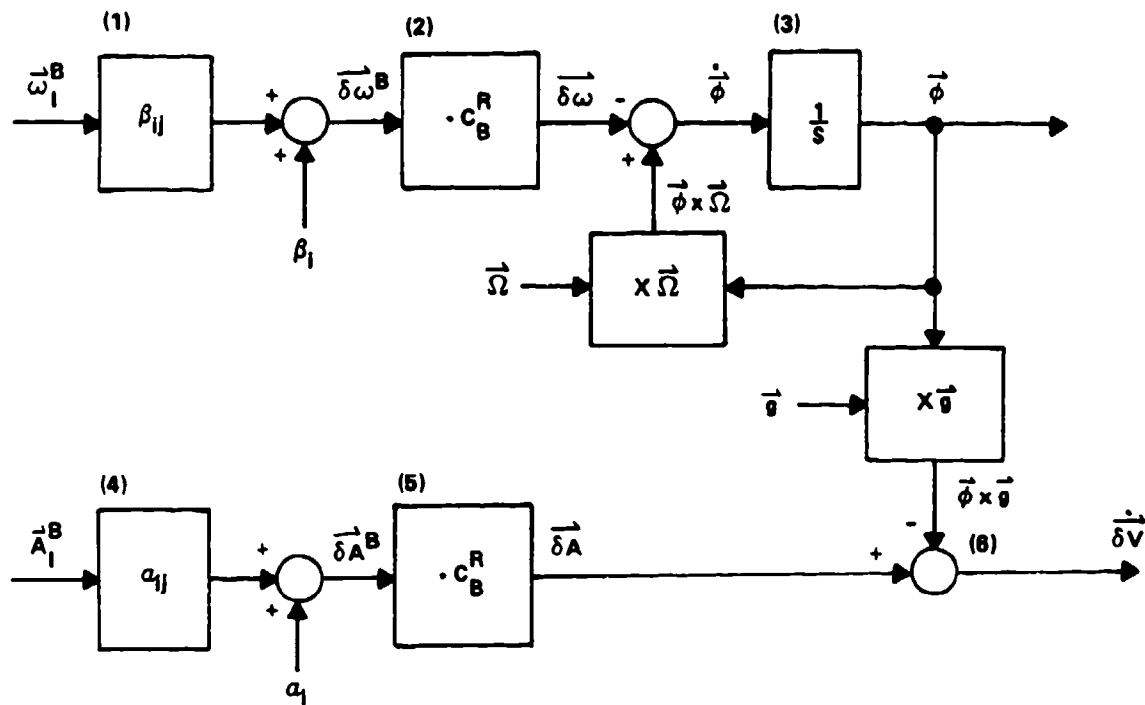


Figure 3. Diagram of Error Model for Horizontal and Vertical Acceleration Measurement

Table 3. Error Model for Horizontal and Vertical Acceleration Measurements

(1) GYRO BIAS, SCALE FACTOR AND MISALIGNMENT ERRORS:

$$\delta \omega_X^B = \beta_X + \beta_{XX} \omega_{1X}^B + \beta_{XY} \omega_{1Y}^B + \beta_{XZ} \omega_{1Z}^B$$

$$\delta \omega_Y^B = \beta_Y + \beta_{YX} \omega_{1X}^B + \beta_{YY} \omega_{1Y}^B + \beta_{YZ} \omega_{1Z}^B$$

$$\delta \omega_Z^B = \beta_Z + \beta_{ZX} \omega_{1X}^B + \beta_{ZY} \omega_{1Y}^B + \beta_{ZZ} \omega_{1Z}^B$$

(2) RESOLVE TO REFERENCE AXES:

$$\delta \omega_X = C_{XX} \delta \omega_X^B + C_{XY} \delta \omega_Y^B + C_{XZ} \delta \omega_Z^B$$

$$\delta \omega_Y = C_{YX} \delta \omega_X^B + C_{YY} \delta \omega_Y^B + C_{YZ} \delta \omega_Z^B$$

$$\delta \omega_Z = C_{ZX} \delta \omega_X^B + C_{ZY} \delta \omega_Y^B + C_{ZZ} \delta \omega_Z^B$$

(3) INTEGRATE REFERENCE AXIS MISALIGNMENTS:

$$\dot{\phi}_X = -\delta \omega_X - \Omega_Y \phi_Z + \Omega_Z \phi_Y$$

$$\dot{\phi}_Y = -\delta \omega_Y - \Omega_Z \phi_X + \Omega_X \phi_Z$$

$$\dot{\phi}_Z = -\delta \omega_Z - \Omega_X \phi_Y + \Omega_Y \phi_X$$

(4) ACCELERATION BIAS, SCALE FACTOR AND MISALIGNMENT ERRORS:

$$\delta A_X^B = a_X + a_{XX} A_{1X}^B + a_{XY} A_{1Y}^B + a_{XZ} A_{1Z}^B$$

$$\delta A_Y^B = a_Y + a_{YX} A_{1X}^B + a_{YY} A_{1Y}^B + a_{YZ} A_{1Z}^B$$

$$\delta A_Z^B = a_Z + a_{ZX} A_{1X}^B + a_{ZY} A_{1Y}^B + a_{ZZ} A_{1Z}^B$$

(5) RESOLVE TO REFERENCE AXES:

$$\delta A_X = C_{XX} \delta A_X^B + C_{XY} \delta A_Y^B + C_{XZ} \delta A_Z^B$$

$$\delta A_Y = C_{YX} \delta A_X^B + C_{YY} \delta A_Y^B + C_{YZ} \delta A_Z^B$$

$$\delta A_Z = C_{ZX} \delta A_X^B + C_{ZY} \delta A_Y^B + C_{ZZ} \delta A_Z^B$$

(6) ERRORS IN HORIZONTAL AND VERTICAL ACCELERATION:

$$\delta \dot{V}_X = \delta A_X - g \phi_Y$$

$$\delta \dot{V}_Y = \delta A_Y + g \phi_X$$

$$\delta \dot{V}_Z = \delta A_Z$$

4. ROTATION SEQUENCE, OBSERVATION EQUATIONS, AND SOLUTIONS

The observation equations for determining the calibration coefficients are obtained from a particular sequence of rotations, shown in Figure 4. The observations are obtained by measuring the indicated horizontal accelerations, using the mechanization of Figure 2, at the fixed positions at the beginning and end of each rotation.

As shown, there are three sets of three rotations each, making a total of nine. Considering Set 1 first, the starting position has the body axes approximately aligned with the reference axes of Figure 1, which is X east, Y north, and Z up. The first rotation is 180 degrees about the roll axis, which is north, ending with the body X and Z axis west, and down, respectively. A second 180 degree rotation about the roll axis ends with body axes at their original starting position. A third and final 180 degree rotation about the vertical ends with body X and Y axes west, and south, respectively. The second and third sets of rotations are the same as the first, except that the starting positions of the body axes are different, as indicated.

The 180 degree rotations can be implemented in as little as 10 seconds each, and the measurement at each position can be made in as little as 5 seconds, using the filter of Figure 5 to be explained shortly. Although in actual operation these times are at least doubled to reduce design tolerances, the entire sequence requires only a few minutes. This sequence generates all the calibration coefficients except gyro bias errors. For comparison, to generate these coefficients with other calibration procedures which would require realigning the system between each rotation would take about an hour (Reference 1). The three gyro bias errors can also be determined by repeating only rotation No. 3 from Set 1, with an observation period of about three minutes at each of the two fixed positions. This will also be explained shortly in connection with Figure 5.

As stated, the observations are the differences in measured horizontal acceleration at beginning and end of each rotation, using the mechanization of Figure 2. These observations are indicated by a and b in Table 4, which correspond to the X and Y channels, respectively. Since true acceleration is zero, the horizontal accelerations are replaced by horizontal acceleration errors, in order to express them in terms of the alpha and beta calibration coefficients. These relationships are presented in Table 4, and are derived in Appendix A using the error model of Figure 3 or Table 3. It will be seen that each observation is a linear combination of both alpha and beta coefficients. This is because each observation represents the difference between the change in position as measured by the accelerometers and the gyros, respectively.

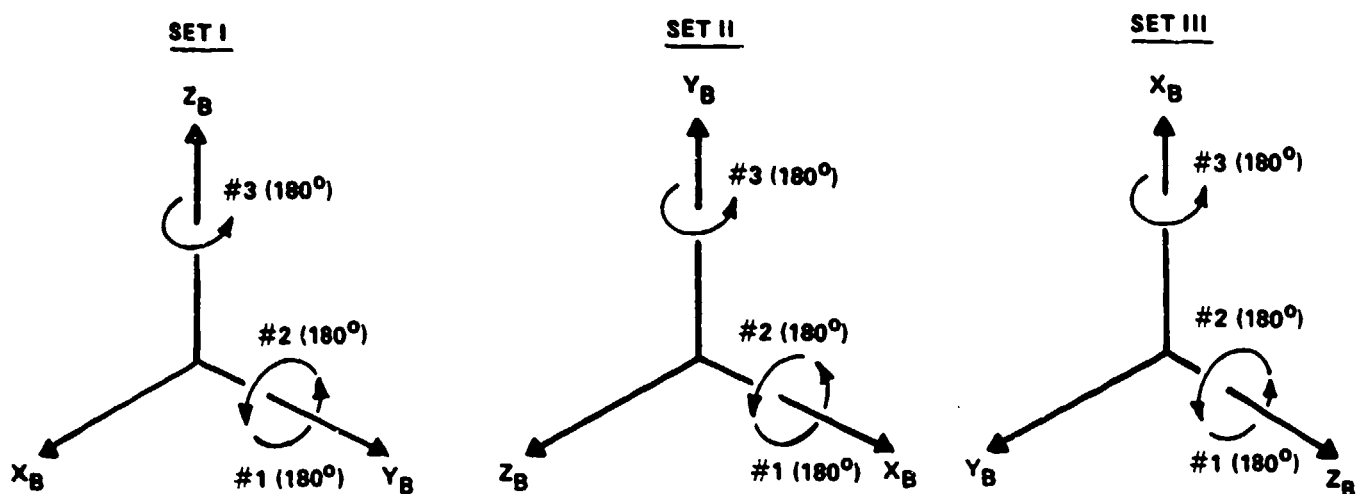


Figure 4. Starting Positions and Rotations for Measurements

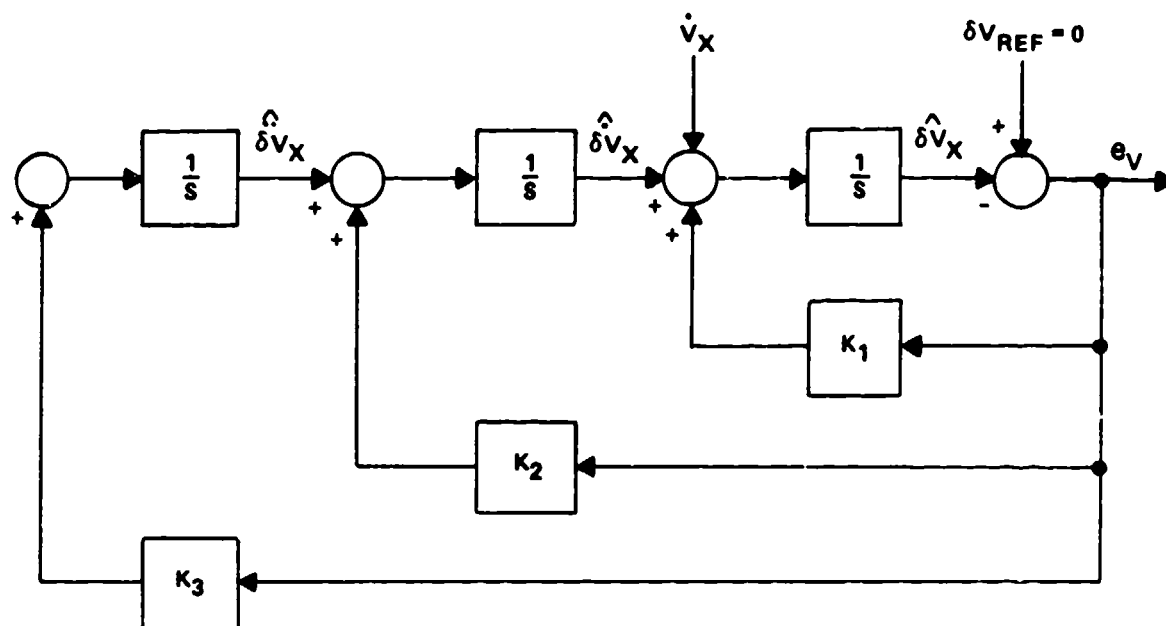


Figure 5. Filter for Estimating Horizontal Accelerations and Horizontal Acceleration Rates

The observation equations of Table 4 are solved explicitly for the calibration coefficients to obtain the solutions in Table 5. As shown, these are obtained by setting three accelerometer misalignments to zero. This is equivalent to defining the reference axes in such a way that the XY plane is defined by the X and Y accelerometers, and so that the X reference axis coincides with the X accelerometer axis.

The accelerometer scale factor errors are not shown in Tables 4 and 5. They are obtained directly from the measured vertical accelerations at the beginning and end of rotations 1 and 2. The Z, Y, and X scale factor errors are obtained from the vertical acceleration measurements of the three sets, respectively, after subtracting the accelerometer bias errors computed in Table 5.

Because of instrument noise, the horizontal acceleration measurements must actually be made using filters. Since the X and Y channel filters are identical, only the X channel filter is shown in Figure 5. The input is the horizontal acceleration from the mechanization of Figure 2. There are three estimated states, as shown. These are optimal estimates in the sense that the gains K are time variable stored gains based on Kalman filter simulations. This same filter is used on the vertical channel to obtain the measurements of accelerometer scale factor error.

In addition to using this filter to generate observations for the accelerometer scale factors and the calibration coefficients in Table 5, it is used to estimate gyro bias errors and reference axis misalignments. This is done using measurements from the special Set 1 Rotation 3 test. The estimated X and Y acceleration rate is used to determine Y and X gyro biases, respectively, as well as reference axis azimuth misalignment. The observation equations and solutions are shown in Table 6, which is derived in Appendix A.

Also shown in Table 6 is the observation and solution for Z gyro bias error. This is determined by a filter like that in Figure 5, but with heading angle as input rather than acceleration. The third state estimated is then heading rate instead of acceleration rate. Since the system is at a fixed position, heading rate is approximately equal to Z-gyro bias error, as shown in Appendix A.

Finally, Table 6 shows that the estimated horizontal accelerations are used to compute reference axis misalignments about X and Y. These estimates are used, together with estimated azimuth misalignment, to reset the direction cosines. This is the reference axis alignment mechanization referred to earlier.

Table 4. Observation Equations for CAL Coefficients

Notation for SET I; ROTN. k; $a_k^I = \delta \dot{V}_X(T) - \delta \dot{V}_X(0)$; $b_k^I = \delta \dot{V}_Y(T) - \delta \dot{V}_Y(0)$

	SET I	SET II	SET III
ROTN. #1	$a_1^I = -2a_X + (\beta_{YY}\pi) \cdot g$ $b_1^I = -2(a_{YZ} + \beta_{ZY}) \cdot g$	$a_1^{II} = -2a_Z + (\beta_{XX}\pi) \cdot g$ $b_1^{II} = -2(a_{XY} + \beta_{YX}) \cdot g$	$a_1^{III} = -2a_Y + (\beta_{ZZ}\pi) \cdot g$ $b_1^{III} = -2(a_{ZX} + \beta_{XZ}) \cdot g$
ROTN. #2	$a_2^I = +2a_X + (\beta_{YY}\pi) \cdot g$ $b_2^I = +2(a_{YZ} + \beta_{ZY}) \cdot g$	$a_2^{II} = +2a_Z + (\beta_{XX}\pi) \cdot g$ $b_2^{II} = +2(a_{XY} + \beta_{YX}) \cdot g$	$a_2^{III} = +2a_Y + (\beta_{ZZ}\pi) \cdot g$ $b_2^{III} = +2(a_{ZX} + \beta_{XZ}) \cdot g$
ROTN. #3	$a_3^I = -2a_X + 2(-a_{XZ} + \beta_{XZ}) \cdot g$ $b_3^I = -2a_Y + 2(-a_{YZ} + \beta_{YZ}) \cdot g$	$a_3^{II} = -2a_Z + 2(-a_{ZY} + \beta_{ZY}) \cdot g$ $b_3^{II} = -2a_X + 2(-a_{XY} + \beta_{XY}) \cdot g$	$a_3^{III} = -2a_Y + 2(-a_{YX} + \beta_{YX}) \cdot g$ $b_3^{III} = -2a_Z + 2(-a_{ZX} + \beta_{ZX}) \cdot g$

Table 5. Solution of Observation Equations

GYRO SCALE FACTORS	$\beta_{YY} = \frac{a_2^I + a_1^I}{2\pi g}$	$\beta_{XX} = \frac{a_2^{II} + a_1^{II}}{2\pi g}$	$\beta_{ZZ} = \frac{a_2^{III} + a_1^{III}}{2\pi g}$
ACCEL. BIASES	$a_X = \frac{a_2^I - a_1^I}{4}$	$a_Z = \frac{a_2^{II} - a_1^{II}}{4}$	$a_Y = \frac{a_2^{III} - a_1^{III}}{4}$
REFERENCE AXIS DEFINITION	$a_{XZ} = 0$	$a_{YZ} = 0$	$a_{XY} = 0$
GYRO AND ACCEL. MISALIGNMENTS	$\beta_{XZ} = \frac{a_3^I + 2a_X}{2g}$	$\beta_{XY} = \frac{b_3^{II} + 2a_X}{2g}$	$a_{ZX} = -\frac{b_1^{III}}{2g} - \beta_{XZ}$
	$\beta_{YZ} = \frac{b_3^I + 2a_Y}{2g}$	$\beta_{YX} = -\frac{b_1^{II}}{2g}$	$\beta_{ZX} = \frac{b_3^{III} + 2a_Z}{2g} + a_{ZX}$
	$\beta_{ZY} = -\frac{b_1^I}{2g}$	$a_{ZY} = -\frac{a_3^{II} + 2a_Z}{2g} + \beta_{ZY}$	$a_{YX} = -\frac{a_3^{III} + 2a_Y}{2g} + \beta_{YX}$

Table 6. Gyro Bias Errors and Reference Axis Misalignment

OBSERVATION EQUATIONS FOR SPECIAL SET I ROTATION 3:

$$\begin{aligned}
 \delta \ddot{V}_X(0) &\approx -g(-\beta_Y + \Omega_X \phi_Z) & ; & \quad \delta \ddot{V}_X(T) \approx -g(+\beta_Y + \Omega_X \phi_Z) \\
 \delta \ddot{V}_Y(0) &\approx +g(-\beta_X - \Omega_Y \phi_Z) & ; & \quad \delta \ddot{V}_Y(T) \approx +g(+\beta_X - \Omega_Y \phi_Z) \\
 \delta \dot{V}_X(0) &\approx \delta A_X(0) - g\phi_Y & ; & \quad \delta \dot{V}_X(T) \approx -\delta A_X(0) - g\phi_Y \\
 \delta \dot{V}_Y(0) &\approx \delta A_X(0) + g\phi_X & ; & \quad \delta \dot{V}_Y(T) \approx -\delta A_X(0) + g\phi_X \\
 \dot{\phi}_Z(0) &\approx -\beta_Z & ; & \quad \dot{\phi}_Z(T) \approx -\beta_Z
 \end{aligned}$$

SOLUTION OF OBSERVATION EQUATIONS:

$$\begin{aligned}
 \beta_X &= \frac{\delta \ddot{V}_Y(T) - \delta \ddot{V}_Y(0)}{2g} & ; & \quad \beta_Y = \frac{\delta \ddot{V}_X(T) - \delta \ddot{V}_X(0)}{-2g} & ; & \quad \beta_Z = \frac{\dot{\phi}_Z(T) + \dot{\phi}_Z(0)}{-2} \\
 \phi_X &= \frac{\delta \dot{V}_Y(T) + \delta \dot{V}_Y(0)}{2g} & ; & \quad \phi_Y = \frac{\delta \dot{V}_X(T) + \delta \dot{V}_X(0)}{-2g} & ; & \quad \phi_Z = \frac{\delta \ddot{V}_Y(T) + \delta \ddot{V}_Y(0)}{-2g\Omega_Y}
 \end{aligned}$$

5. IMPLEMENTATION

The previous sections have described a sequence of rotations and measurements which are sufficient to determine each of the calibration coefficients. However, this assumes that each coefficient has only a single value. Although this is approximately true at a particular temperature, the system may be operated at different temperatures, and at temperatures which are slowly changing with time. Since many coefficients change significantly over the operating temperature range, a procedure is required to determine these values. The operational system must then provide for measuring the temperature so that the correct calibration coefficients can be calculated at each temperature and used for compensation in the software.

The particular sequence of rotations and measurements described in Section 4 was selected to provide a complete set of solutions explicitly in a minimum time. This is important since it becomes unnecessary to calibrate at many constant temperatures in a temperature controlled room. Instead, the system is previously cooled to a temperature of approximately 0°C . The system temperature is then allowed to increase from 0 to 60°C over a period of several hours by enclosing it in an insulating box while the calibration sequence is repeated rapidly on an inexpensive fixture at room temperature. Figure 6 shows a typical fixture together with insulating box as used for this purpose at remote facilities.

As each complete set of coefficients is determined, it is incorporated in the software compensation for the next set of measurements. In this way only a small correction is necessary at each step. However, the solution for each coefficient and the temperature at which it was computed is stored for a recursive least squares curve fit over the entire temperature range. The recursive least-square fit and control of the fixture are accomplished in a computer board in the system. A separate computer is therefore not required. Examples of coefficient measurements and the least-squares polynomial approximation are shown in Figures 7, 8, and 9. These figures also show the error in the fit, which is the curve near the horizontal axis and which is scaled on the right-hand margin of the figure.

The errors in the fit are caused primarily by noise. For gyro bias error measurement, the error is approximately the gyro white noise coefficient divided by square root of the observation time. This yields less than 0.02 degree per hour error for measurement times of 100 seconds. For all the coefficients except gyro bias error, the noise causes errors in measuring horizontal acceleration. The two principal sources are accelerometer noise at the two fixed positions, and random walk change in reference axis misalignment. The latter is caused by gyro white noise in angular rate during the period of rotation between the two fixed positions. Both noise levels are sufficiently small that they

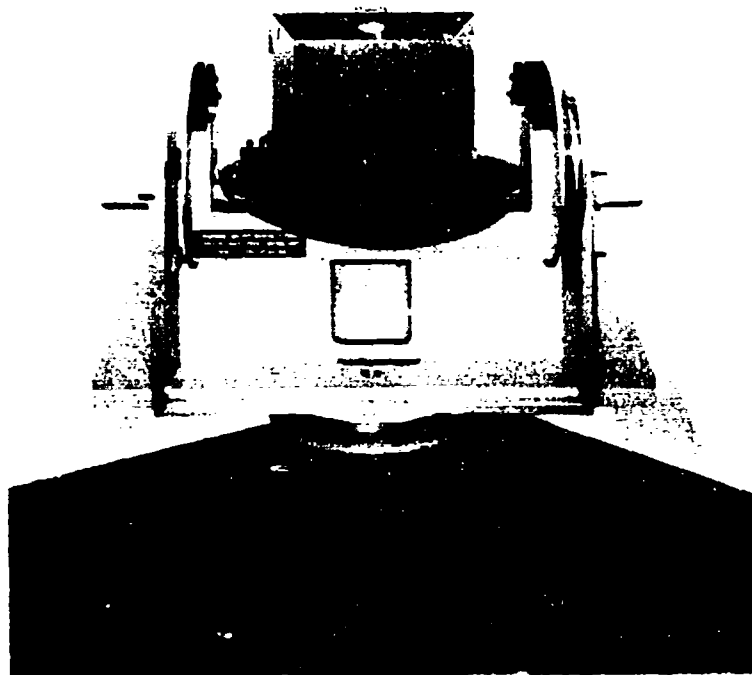


Figure 6. Type of Calibration Fixture used at Remote Facilities

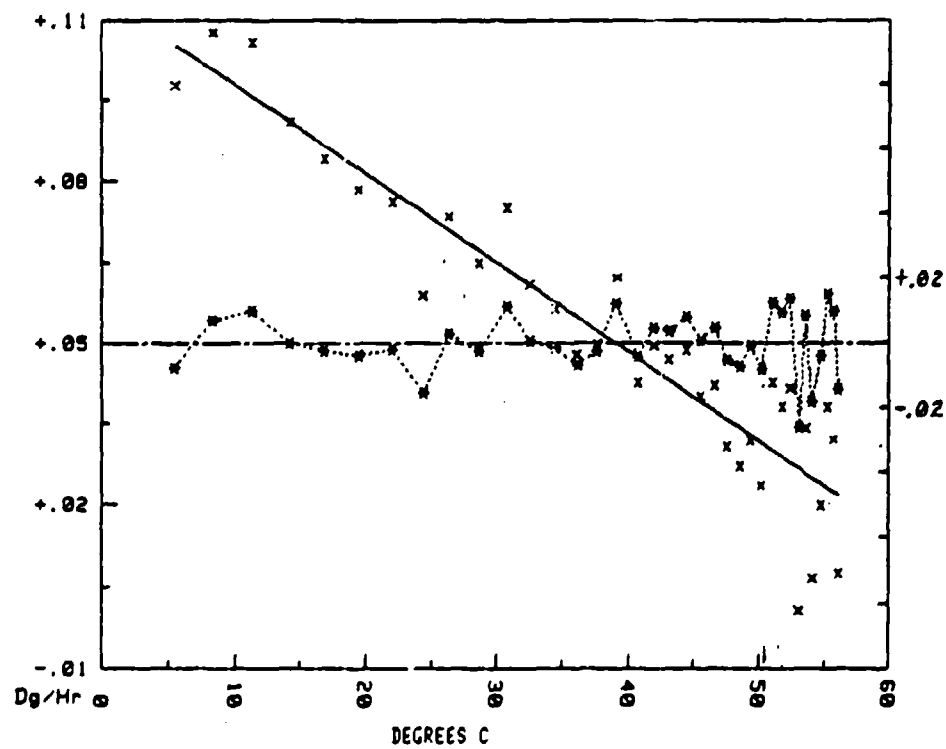


Figure 7. Least-Squares Fit to Gyro Bias Error

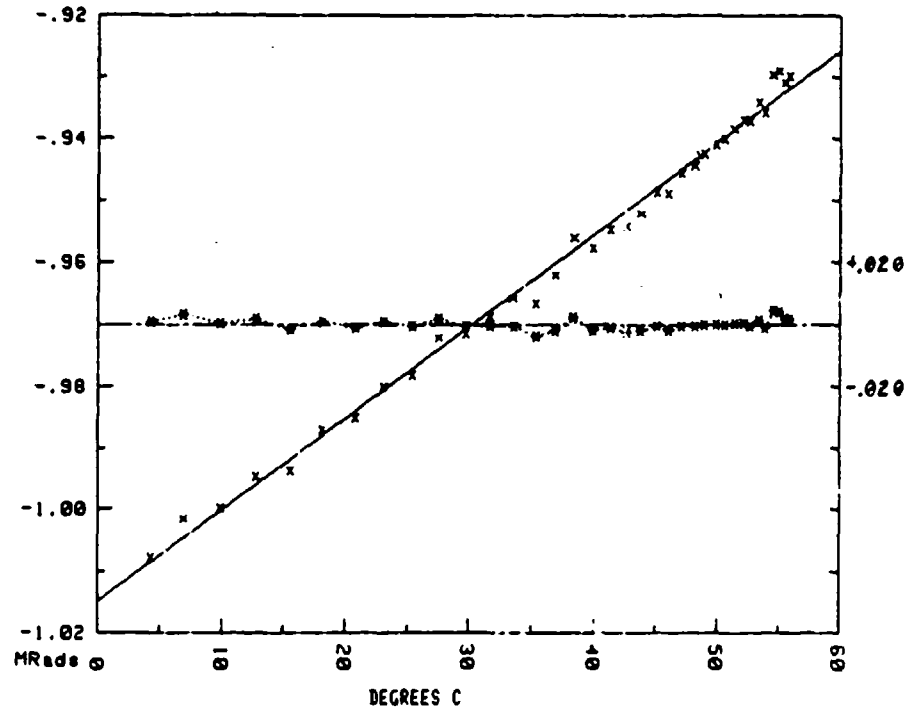


Figure 8. Least-Squares Fit to Gyro Misalignment Error

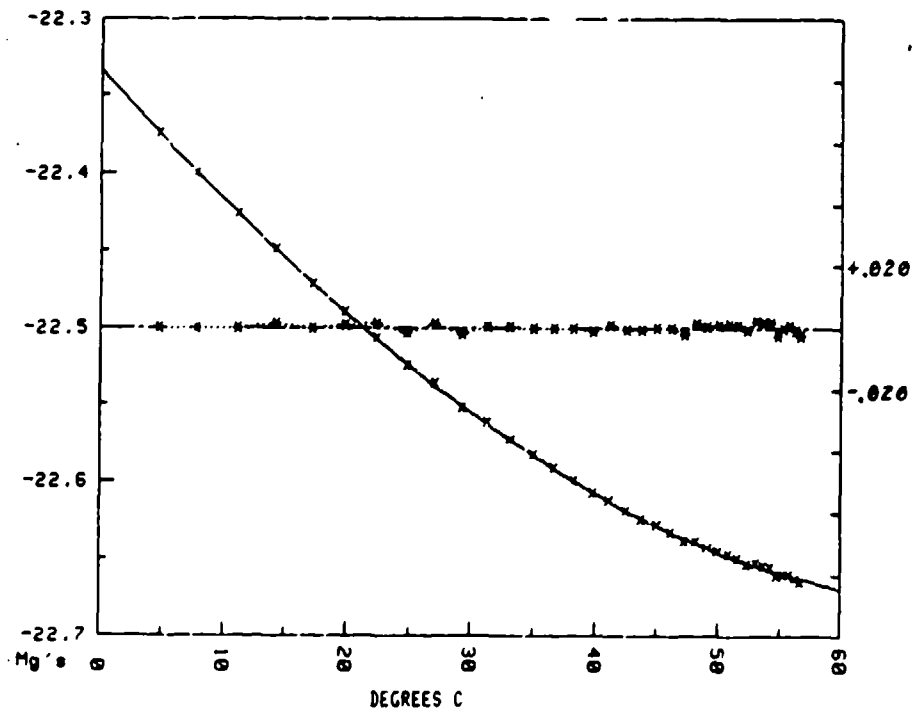


Figure 9. Least-Squares Fit to Accelerometer Bias Error

cause errors of less than 10 parts per million assuming a rotation time of 20 seconds and a measurement time of 5 seconds at each position. Because of the least squares fitting to the measurement, the error in the coefficient is reduced to less than 5 parts per million.

In a commercial aircraft, the system performance in nautical miles per hour is determined primarily by gyro bias error. The accuracy of the gyro bias calibration procedure over temperature is illustrated in Figure 10. After calibrating the system, the system was aligned in a temperature controlled chamber at the temperature shown. In the navigation mode following alignment the system was rotated 180 degrees in heading and the position errors were plotted. This is a worst case maneuver for navigation performance. As shown, the error was well below one nautical mile per hour.

The required misalignment calibration accuracy in a commercial aircraft is only about 5 arc seconds, one sigma (Reference 1). However, in some military applications like ASW where long orbit maneuvers are performed, greater accuracy is required. To achieve such accuracy, g-sensitive misalignments of the gyros must be compensated in the operational software. Calibration of the coefficients for this compensation is discussed in Appendix 8. The procedure is time consuming and requires an accurate three axis rate table as shown in Figure 11. Since the coefficients are approximately the same for all systems of the same design, the procedure need be performed only once at the factory, rather than being repeated for individual systems. The pre-determined g-sensitive calibration coefficients are then used to correct g-sensitive misalignments during the normal calibration of individual systems.

An example of the resulting navigation performance during a Scorsby test is shown in Figure 12. The temperature was varied from 10°C to approximately 35°C during the test. The north gyro bias correction estimated during alignment was approximately 0.008 deg/hour. Although this would have been automatically corrected at the beginning of the nav mode, the correction was deliberately inhibited. This was to compensate for the fact that east gyro bias error did not propagate since nav heading and align heading were the same. The resulting east position error was about 0.5 nautical miles/hour as expected. The north position error was due to misalignments. This error and east position error not caused by gyro bias error were each less than 1/4 nautical miles/hour, corresponding to an angular rate error of 0.004 degrees/hour. Since coning rates during Scorsby were measured as 1000 degrees/hour, this indicates misalignments of 4 parts per million, or less than an arc second.

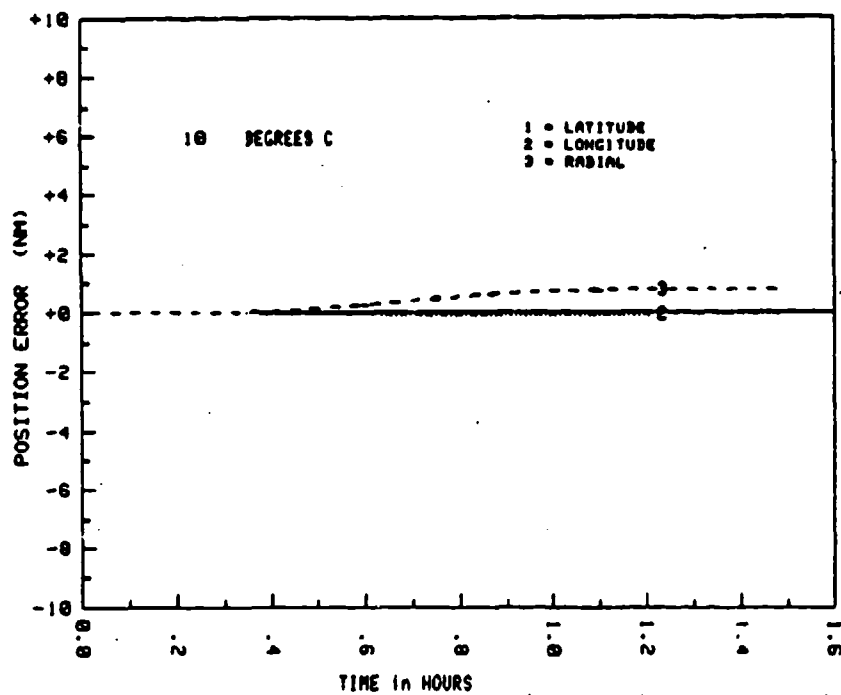


Figure 10. Navigation Performance at Low Temperature Following 180 Degree Turn

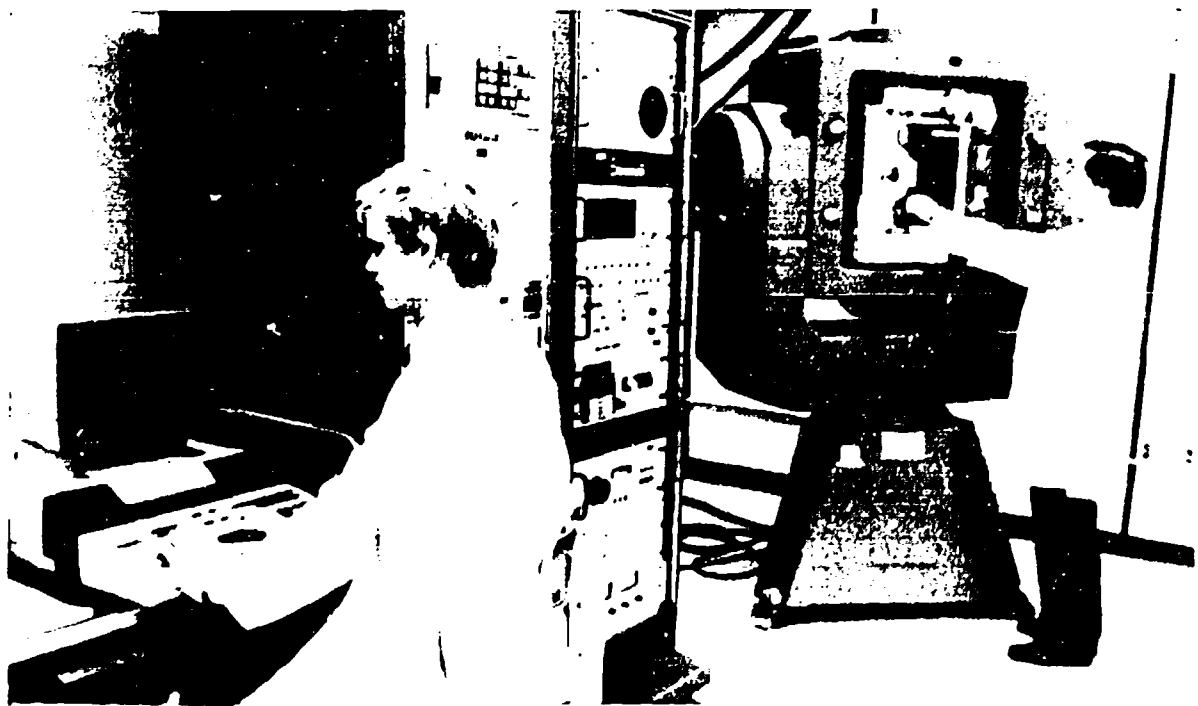


Figure 11. Accurate Three Axis Rate Table used for Coning Tests at Factory

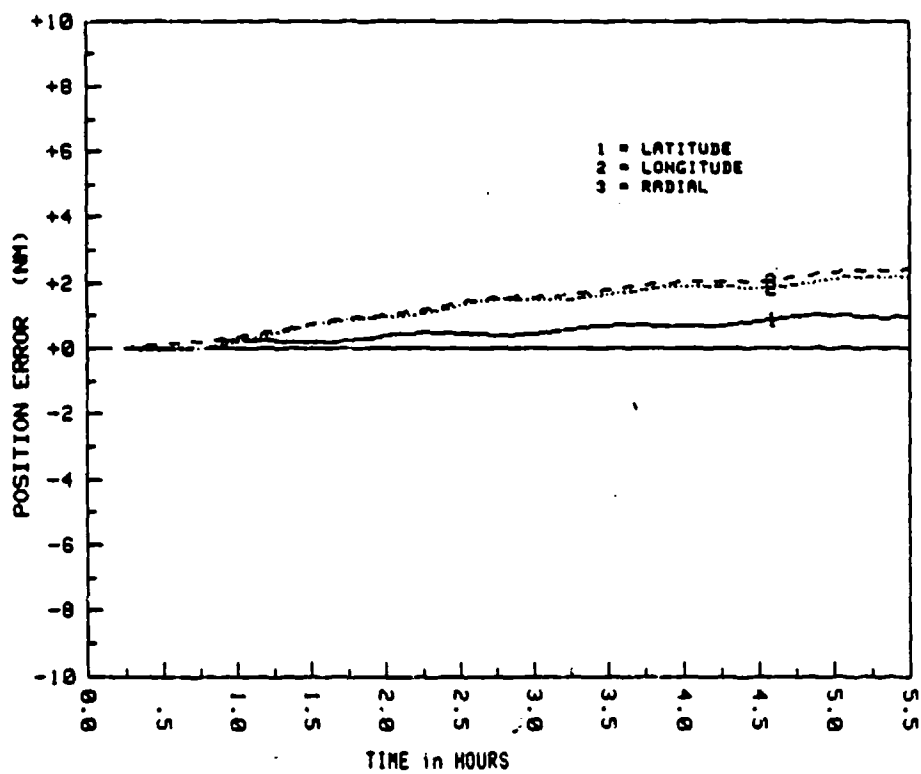


Figure 12. Navigation Performance During Scorsby Test

6. CONCLUSIONS

A calibration procedure has been described which yields a complete set of coefficients in a minimum time. The advantages of the procedure are:

- (1) It permits systems to be calibrated and maintained at remote facilities using only an inexpensive fixture and no external computer.
- (2) It generates all the calibration coefficients to a maximum accuracy over the full temperature range in only a few hours, with no prior information about the coefficients.
- (3) It calibrates the coefficients for the system as a whole as it is used in actual operation, and does not rely on stored data for individual instruments.
- (4) It is fully automatic, and requires no human intervention during the calibration period.

REFERENCES

1. Calibration Procedures for Laser Gyro Strapdown Inertial Navigation Systems, P.G. Savage, Proceedings of the 9th Annual Electro-Optics/Laser Conference and Exhibition, Anaheim, California, October, 1977.
2. Slab Calibration for Strapdown Systems, A.A. Morgan, Eighth Biennial Guidance Test Symposium, Central Inertial Guidance Test Facility, Holloman AFB, New Mexico.
3. A Calibration Technique for a Laser Gyro Strapdown Inertial Navigation System, A. Brown, R. Ebner, J. Mark, Symposium Gyro Technology, Stuttgart, Germany, 1983.
4. Calibration Technique for Laser Gyro Strapdown Inertial Navigation Systems, L. Camberlein, F. Mazzanti, Symposium Gyro Technology, Stuttgart, Germany, 1985.
5. Fast Orthogonal Calibration of a Ring Laser Strapdown System, J. Mark, D. Tazartes, T. Hilly, Symposium Gyro Technology, Stuttgart, Germany, September, 1986.
6. Applied Optimal Estimation, Technical Staff, The Analytic Sciences Corporation, A. Gelb Editor, 1974.

APPENDIX A DERIVATION OF OBSERVATION EQUATIONS

The observation equations result from applying the error model of Table 3 to the positions and rotations of Figure 4. Only the observation equations for Set I will be derived, since the corresponding equations for Sets II and III are obtained by simply permuting X, Y, Z subscripts in Table 4.

The observations a and b in Table 4 are changes in horizontal acceleration at the positions before and after the rotation, indicated by 0 and T. From the error model in Table 3, these are expressed at (6) in terms of X, Y components of accelerometer error, and X, Y components of reference axis misalignments. The changes in misalignment result from gyro errors and are evaluated in Table A1 for the rotations of Set I. The changes in components of accelerometer error are evaluated in Table A2, for the rotations of Set I.

The changes in reference axis misalignment angle are obtained by integrating the angular rates at (3) in Table 3 from 0 to T. Gyro bias errors and errors in resolving earth rate along misaligned axes are each of the order 0.01 arc seconds/second, and will contribute only a fraction of an arc second change during the interval 0 to T between fixed positions. Therefore, only errors due to scale factor errors and misalignment errors are considered in the integrals at the top of Table A1.

The direction cosines and angular rates along body axes are first evaluated for rotations 1, 2, and 3 as shown. The variable of integration is then changed to roll angle for rotations 1 and 2, and to heading angle for rotation 3. The integrals are then easily expressed in terms of the scale factor and misalignment calibration coefficients as shown.

At the top half of Table A2, the changes in horizontal acceleration are expressed using the equations in (4), (5) of the error model in Table 3. The positions in Figure 4 are used to evaluate the direction cosine as shown. The changes for rotations 1, 2, and 3 are then easily expressed in terms of the accelerometer bias and misalignment calibration coefficients as shown.

Using the notation at the top of Table 4, and substituting the horizontal error expressions at (6) in Table 3 as evaluated in Tables A1 and A2 results in the observation equations for Set I in Table 4. The equations for Sets II and III are then obtained by permuting subscripts as indicated by the starting positions of Figure 4.

Table A1. Change in Reference Axis Misalignment

3x1		3x3		3x3		3x1	1x1
-----	--	-----	--	-----	--	-----	-----

$$\begin{bmatrix} \Delta\phi_X \\ \Delta\phi_Y \\ \Delta\phi_Z \end{bmatrix} = - \int_0^T \begin{bmatrix} C_B^R(t) \end{bmatrix} \begin{bmatrix} \beta_{XX} & \beta_{XY} & \beta_{XZ} \\ \beta_{YX} & \beta_{YY} & \beta_{YZ} \\ \beta_{ZX} & \beta_{ZY} & \beta_{ZZ} \end{bmatrix} \begin{bmatrix} \omega_{1X}^B \\ \omega_{1Y}^B \\ \omega_{1Z}^B \end{bmatrix} dt$$

FOR ROTATION #1, ROTATION #2:

$$C_B^R(t) = \begin{bmatrix} \cos \phi(t) & 0 & -\sin \phi(t) \\ 0 & 1 & 0 \\ \sin \phi(t) & 0 & \cos \phi(t) \end{bmatrix} ; \begin{bmatrix} \omega_{1X}^B \\ \omega_{1Y}^B \\ \omega_{1Z}^B \end{bmatrix} dt = \begin{bmatrix} 0 \\ d\phi \\ 0 \end{bmatrix}$$

FOR ROTATION #3:

$$C_B^R(t) = \begin{bmatrix} \cos \psi(t) & -\sin \psi(t) & 0 \\ \sin \psi(t) & \cos \psi(t) & 0 \\ 0 & 0 & 1 \end{bmatrix} ; \begin{bmatrix} \omega_{1X}^B \\ \omega_{1Y}^B \\ \omega_{1Z}^B \end{bmatrix} dt = \begin{bmatrix} 0 \\ 0 \\ d\psi \end{bmatrix}$$

ROTATION #1:

3x1		3x1		3x1		3x1	3x1
-----	--	-----	--	-----	--	-----	-----

$$\begin{bmatrix} \Delta\phi_X \\ \Delta\phi_Y \\ \Delta\phi_Z \end{bmatrix} = - \int_0^\pi \begin{bmatrix} (\beta_{XY} \cos \phi + \beta_{ZY} \sin \phi) d\phi \\ (\beta_{YY}) d\phi \\ (-\beta_{XY} \sin \phi + \beta_{ZY} \cos \phi) d\phi \end{bmatrix} = \begin{bmatrix} -2\beta_{ZY} \\ -\pi\beta_{YY} \\ +2\beta_{XY} \end{bmatrix}$$

ROTATION #2:

$$\begin{bmatrix} \Delta\phi_X \\ \Delta\phi_Y \\ \Delta\phi_Z \end{bmatrix} = - \int_\pi^{2\pi} \begin{bmatrix} (\beta_{XY} \cos \phi + \beta_{ZY} \sin \phi) d\phi \\ (\beta_{YY}) d\phi \\ (-\beta_{XY} \sin \phi + \beta_{ZY} \cos \phi) d\phi \end{bmatrix} = \begin{bmatrix} +2\beta_{ZY} \\ -\pi\beta_{YY} \\ -2\beta_{XY} \end{bmatrix}$$

ROTATION #3:

$$\begin{bmatrix} \Delta\phi_X \\ \Delta\phi_Y \\ \Delta\phi_Z \end{bmatrix} = - \int_0^{-\pi} \begin{bmatrix} (\beta_{XZ} \cos \psi - \beta_{YZ} \sin \psi) d\psi \\ (\beta_{XZ} \sin \psi + \beta_{YZ} \cos \psi) d\psi \\ (\beta_{ZZ}) d\psi \end{bmatrix} = \begin{bmatrix} +2\beta_{YZ} \\ -2\beta_{XZ} \\ -\pi\beta_{ZZ} \end{bmatrix}$$

Table A2. Change in Horizontal and Vertical Accelerometer Error

$$\begin{aligned}
 & \begin{matrix} 3 \times 1 \\ \Delta \delta A_X \\ \Delta \delta A_Y \\ \Delta \delta A_Z \end{matrix} = \begin{matrix} 3 \times 3 \\ C_B^R(T) \end{matrix} \left\{ \begin{matrix} 3 \times 3 \\ \begin{bmatrix} a_{XX} & a_{XY} & a_{XZ} \\ a_{YX} & a_{YY} & a_{YZ} \\ a_{ZX} & a_{ZY} & a_{ZZ} \end{bmatrix} \end{matrix} \cdot \begin{matrix} 3 \times 1 \\ \begin{bmatrix} A_X(T) \\ A_Y(T) \\ A_Z(T) \end{bmatrix} \end{matrix} + \begin{matrix} 3 \times 1 \\ \begin{bmatrix} a_X \\ a_Y \\ a_Z \end{bmatrix} \end{matrix} \right\} \\
 & - \begin{matrix} 3 \times 3 \\ C_B^R(0) \end{matrix} \left\{ \begin{matrix} 3 \times 3 \\ \begin{bmatrix} a_{XX} & a_{XY} & a_{XZ} \\ a_{YX} & a_{YY} & a_{YZ} \\ a_{ZX} & a_{ZY} & a_{ZZ} \end{bmatrix} \end{matrix} \cdot \begin{matrix} 3 \times 1 \\ \begin{bmatrix} A_X(0) \\ A_Y(0) \\ A_Z(0) \end{bmatrix} \end{matrix} + \begin{matrix} 3 \times 1 \\ \begin{bmatrix} a_X \\ a_Y \\ a_Z \end{bmatrix} \end{matrix} \right\}
 \end{aligned}$$

ROTATION #1:

$$C_B^R(0) = \begin{bmatrix} 1 & 0 & 0 \\ 0 & 1 & 0 \\ 0 & 0 & 1 \end{bmatrix} ; \begin{matrix} A_X(0) \\ A_Y(0) \\ A_Z(0) \end{matrix} = \begin{matrix} 0 \\ 0 \\ 0 \end{matrix} ; C_B^R(T) = \begin{bmatrix} -1 & 0 & 0 \\ 0 & 1 & 0 \\ 0 & 0 & -1 \end{bmatrix} ; \begin{matrix} A_X(T) \\ A_Y(T) \\ A_Z(T) \end{matrix} = \begin{matrix} 0 \\ 0 \\ -g \end{matrix}$$

$$\begin{aligned}
 \Delta \delta A_X &= \begin{bmatrix} (+a_{XZ} \theta) & (+a_{XZ} \theta) & -2a_X & -2a_X \\ (+a_{YZ} \theta) & -(-a_{YZ} \theta) & 0 & -2a_{YZ} \theta \\ (+a_{ZZ} \theta) & (+a_{ZZ} \theta) & -2a_Z & -2a_Z \end{bmatrix} \\
 \Delta \delta A_Y &= \begin{bmatrix} (+a_{XZ} \theta) & (+a_{XZ} \theta) & -2a_X & -2a_X \\ (+a_{YZ} \theta) & -(-a_{YZ} \theta) & 0 & -2a_{YZ} \theta \\ (+a_{ZZ} \theta) & (+a_{ZZ} \theta) & -2a_Z & -2a_Z \end{bmatrix} \\
 \Delta \delta A_Z &= \begin{bmatrix} (+a_{XZ} \theta) & (+a_{XZ} \theta) & -2a_X & -2a_X \\ (+a_{YZ} \theta) & -(-a_{YZ} \theta) & 0 & -2a_{YZ} \theta \\ (+a_{ZZ} \theta) & (+a_{ZZ} \theta) & -2a_Z & -2a_Z \end{bmatrix}
 \end{aligned}$$

ROTATION #2:

$$C_B^R(0) = \begin{bmatrix} -1 & 0 & 0 \\ 0 & 1 & 0 \\ 0 & 0 & -1 \end{bmatrix} ; \begin{matrix} A_X(0) \\ A_Y(0) \\ A_Z(0) \end{matrix} = \begin{matrix} 0 \\ 0 \\ -g \end{matrix} ; C_B^R(T) = \begin{bmatrix} 1 & 0 & 0 \\ 0 & 1 & 0 \\ 0 & 0 & 1 \end{bmatrix} ; \begin{matrix} A_X(T) \\ A_Y(T) \\ A_Z(T) \end{matrix} = \begin{matrix} 0 \\ 0 \\ +g \end{matrix}$$

$$\begin{aligned}
 \Delta \delta A_X &= \begin{bmatrix} (+a_{XZ} \theta) & (+a_{XZ} \theta) & 2a_X & +2a_X \\ (+a_{YZ} \theta) & -(-a_{YZ} \theta) & 0 & +2a_{YZ} \theta \\ (+a_{ZZ} \theta) & (+a_{ZZ} \theta) & 2a_Z & +2a_Z \end{bmatrix} \\
 \Delta \delta A_Y &= \begin{bmatrix} (+a_{XZ} \theta) & (+a_{XZ} \theta) & 2a_X & +2a_X \\ (+a_{YZ} \theta) & -(-a_{YZ} \theta) & 0 & +2a_{YZ} \theta \\ (+a_{ZZ} \theta) & (+a_{ZZ} \theta) & 2a_Z & +2a_Z \end{bmatrix} \\
 \Delta \delta A_Z &= \begin{bmatrix} (+a_{XZ} \theta) & (+a_{XZ} \theta) & 2a_X & +2a_X \\ (+a_{YZ} \theta) & -(-a_{YZ} \theta) & 0 & +2a_{YZ} \theta \\ (+a_{ZZ} \theta) & (+a_{ZZ} \theta) & 2a_Z & +2a_Z \end{bmatrix}
 \end{aligned}$$

ROTATION #3:

$$C_B^R(0) = \begin{bmatrix} 1 & 0 & 0 \\ 0 & 1 & 0 \\ 0 & 0 & 1 \end{bmatrix} ; \begin{matrix} A_X(0) \\ A_Y(0) \\ A_Z(0) \end{matrix} = \begin{matrix} 0 \\ 0 \\ +g \end{matrix} ; C_B^R(T) = \begin{bmatrix} -1 & 0 & 0 \\ 0 & -1 & 0 \\ 0 & 0 & 1 \end{bmatrix} ; \begin{matrix} A_X(T) \\ A_Y(T) \\ A_Z(T) \end{matrix} = \begin{matrix} 0 \\ 0 \\ +g \end{matrix}$$

$$\begin{aligned}
 \Delta \delta A_X &= \begin{bmatrix} (-a_{XZ} \theta) & (+a_{XZ} \theta) & -2a_X & -2a_X - 2a_{XZ} \theta \\ (-a_{YZ} \theta) & -(+a_{YZ} \theta) & -2a_Y & -2a_Y - 2a_{YZ} \theta \\ (+a_{ZZ} \theta) & (+a_{ZZ} \theta) & 0 & 0 \end{bmatrix} \\
 \Delta \delta A_Y &= \begin{bmatrix} (-a_{XZ} \theta) & (+a_{XZ} \theta) & -2a_X & -2a_X - 2a_{XZ} \theta \\ (-a_{YZ} \theta) & -(+a_{YZ} \theta) & -2a_Y & -2a_Y - 2a_{YZ} \theta \\ (+a_{ZZ} \theta) & (+a_{ZZ} \theta) & 0 & 0 \end{bmatrix} \\
 \Delta \delta A_Z &= \begin{bmatrix} (-a_{XZ} \theta) & (+a_{XZ} \theta) & -2a_X & -2a_X - 2a_{XZ} \theta \\ (-a_{YZ} \theta) & -(+a_{YZ} \theta) & -2a_Y & -2a_Y - 2a_{YZ} \theta \\ (+a_{ZZ} \theta) & (+a_{ZZ} \theta) & 0 & 0 \end{bmatrix}
 \end{aligned}$$

The observations for gyro bias errors and reference axis misalignments in Table 6 are also made at the positions before and after the rotation, indicated by 0 and T. At the top of Table A3 the rate of change of horizontal acceleration error is obtained by differentiating the horizontal acceleration errors shown at the right. The rate of change of horizontal accelerometer error is then set to zero. For this approximation to be valid when the temperatures are changing, accelerometer scaling and compensation must include compensation for variations with temperature. As for the other approximations in Table A3, this assumption is valid because the solutions for the calibration coefficients are used in the scaling and compensation for repeated iterations of the entire sequence. Similarly, the estimated reference axis misalignments are used to correct the direction cosines for the next iteration. In this way, all the errors tend to converge toward zero.

Next, the rates of change of reference axis misalignments are evaluated from Table 3, and the product of earth rate and misalignments about X, Y is set to zero. This approximation is valid because the reference axes, represented by direction cosines, have been previously aligned so that level axis tilts are no more than a few arc seconds. Therefore, the products are small compared to 0.01 degrees per hour.

The third set of approximations in Table A3 is obtained by setting products of scale factor and misalignment errors by earth rate to zero. This is valid because the errors in scale factor and misalignment are only a few parts per million after the first few iterations.

The observations of Table 6 at 0 and T are evaluated from the error model in Table 3, using the approximations of Table A3, and also the direction cosines in Table A3. An additional approximation implicit in Table 6 is that the level axis misalignments are the same at 0 and T. Actually, these misalignments change due to gyro misalignment errors, as indicated in Table A1, Rotation 3. However, these errors are only a few microradians after the first few iterations.

Table A3. Approximations Used In Special Set I,
Rotation 3 Observations

APPROXIMATIONS AT 0 AND T:

$$\delta \ddot{V}_X = \delta \dot{A}_X - g \dot{\phi}_Y \approx -g \dot{\phi}_Y ; \quad \delta \dot{V}_X = \delta A_X - g \phi_Y$$

$$\delta \ddot{V}_Y = \delta \dot{A}_Y + g \dot{\phi}_X \approx +g \dot{\phi}_X ; \quad \delta \dot{V}_Y = \delta A_Y + g \phi_X$$

$$\dot{\phi}_X = -\delta \omega_X - \Omega_Y \phi_Z + \Omega_Z \phi_Y \approx -\delta \omega_X - \Omega_Y \phi_Z$$

$$\dot{\phi}_Y = -\delta \omega_Y - \Omega_Z \phi_X + \Omega_X \phi_Z \approx -\delta \omega_Y + \Omega_X \phi_Z$$

$$\dot{\phi}_Z = -\delta \omega_Z - \Omega_X \phi_Y + \Omega_Y \phi_X \approx -\delta \omega_Z$$

$$\delta \omega_X^B = \beta_X + \beta_{XX} \Omega_X^B + \beta_{XY} \Omega_Y^B + \beta_{XZ} \Omega_Z^B \approx \beta_X$$

$$\delta \omega_Y^B = \beta_Y + \beta_{YX} \Omega_X^B + \beta_{YY} \Omega_Y^B + \beta_{YZ} \Omega_Z^B \approx \beta_Y$$

$$\delta \omega_Z^B = \beta_Z + \beta_{ZX} \Omega_X^B + \beta_{ZY} \Omega_Y^B + \beta_{ZZ} \Omega_Z^B \approx \beta_Z$$

FOR SET I, ROTATION #3:

$$C_B^R(0) = \begin{bmatrix} 1 & 0 & 0 \\ 0 & 1 & 0 \\ 0 & 0 & 1 \end{bmatrix} ; \quad C_B^R(T) = \begin{bmatrix} -1 & 0 & 0 \\ 0 & -1 & 0 \\ 0 & 0 & 1 \end{bmatrix}$$

$$\delta \omega_X(T) = -\delta \omega_X(0) = -\beta_X$$

$$\delta \omega_Y(T) = -\delta \omega_Y(0) = -\beta_Y$$

$$\delta \omega_Z(T) = +\delta \omega_Z(0) = +\beta_Z$$

$$\delta A_X(T) = -\delta A_X(0)$$

$$\delta A_Y(T) = -\delta A_Y(0)$$

APPENDIX B MEASUREMENT OF LASER GYRO ANISOELASTIC MISALIGNMENTS

Because of the dither suspension, the laser gyro exhibits errors due to the specific forces acting on the instrument. To achieve calibration accuracies of an arc second or better, it is necessary to compensate for these errors in the operational software. This appendix explains the mathematical model for the errors and a procedure for calibrating them so that they can be compensated for in software.

Due to specific force, the gyro will rotate about its axis as well as bend. Both types of flexure may be real or may be equivalent errors in the readout of dither angle. The mathematical model of Table B1 can be used to represent both types of errors as variable misalignments of the gyros. A rotation error is represented by rotating the reference axes, which are arbitrary, to move with the gyro. This causes an equivalent misalignment of the other gyros in the opposite direction. Since the model of Table B1 contains equivalent bending in directions other than that of the specific force, the misalignments are referred to as "anisoelastic".

The anisoelastic misalignments will cause steady angular rate errors, similar to gyro drift, when repetitious maneuvers such as extended "orbit" maneuvers or Scorsby motions occur. The triple subscript beta coefficients of Table B1 must therefore be determined in order that these equations, together with specific force measurements, can be used to compensate the gyro outputs in the operational software.

The coefficients are determined by a sequence of coning tests illustrated in Figure B1. It is seen that there are three sets of tests with one of the three body axes in both up and down positions on each. In each position the system undergoes coning motion separately about each axis. Thus, there are three coning tests in the up position and three coning tests in the down position for each set, making a total of eighteen coning tests. In each test, the coning rate is measured as the angular rate about the body axis of the coning. Also, the reference axis misalignment rates are measured by observing the total angular change about each of the three axes during the interval of the test. This is done by observing the direction cosines, computed from the mechanization in Figure 2 or Table 2 of the main text.

The observation equations, which relate the observed misalignment rates to the anisoelastic coefficients, are derived in Table B2. The observed rates are related to the misalignment angles by the error model of Table 3 in the main text. The gyro bias errors and scale factor errors are first calibrated to 0.01 degrees per hour, and 2 parts per million, respectively. They are then negligible compared to the effects of misalignments at the nominal coning

Table B1. Error Model for Gyro Anisoelastic Misalignments

$$\begin{aligned}
 \beta_{XY}(t) &= \beta_{XY0} + \beta_{XY-X} \frac{A_X^B(t)}{g} + \beta_{XY-Y} \frac{A_Y^B(t)}{g} + \beta_{XY-Z} \frac{A_Z^B(t)}{g} \\
 \beta_{XZ}(t) &= \beta_{XZ0} + \beta_{XZ-X} \frac{A_X^B(t)}{g} + \beta_{XZ-Y} \frac{A_Y^B(t)}{g} + \beta_{XZ-Z} \frac{A_Z^B(t)}{g} \\
 \beta_{YZ}(t) &= \beta_{YZ0} + \beta_{YZ-X} \frac{A_X^B(t)}{g} + \beta_{YZ-Y} \frac{A_Y^B(t)}{g} + \beta_{YZ-Z} \frac{A_Z^B(t)}{g} \\
 \beta_{YX}(t) &= \beta_{YX0} + \beta_{YX-X} \frac{A_X^B(t)}{g} + \beta_{YX-Y} \frac{A_Y^B(t)}{g} + \beta_{YX-Z} \frac{A_Z^B(t)}{g} \\
 \beta_{ZX}(t) &= \beta_{ZX0} + \beta_{ZX-X} \frac{A_X^B(t)}{g} + \beta_{ZX-Y} \frac{A_Y^B(t)}{g} + \beta_{ZX-Z} \frac{A_Z^B(t)}{g} \\
 \beta_{ZY}(t) &= \beta_{ZY0} + \beta_{ZY-X} \frac{A_X^B(t)}{g} + \beta_{ZY-Y} \frac{A_Y^B(t)}{g} + \beta_{ZY-Z} \frac{A_Z^B(t)}{g}
 \end{aligned}$$

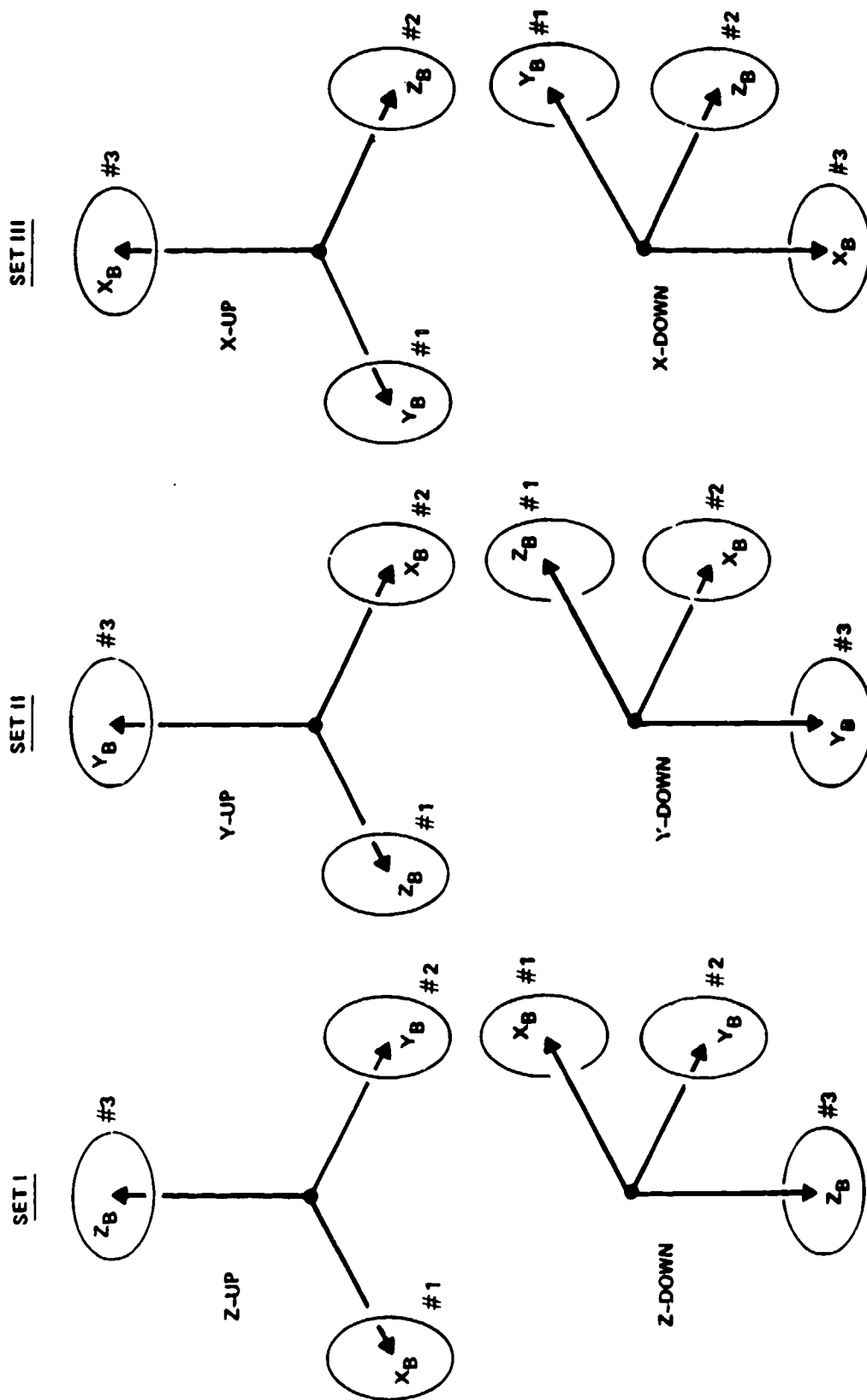


Figure B1. Coning Tests used to Determine Anisotropic Coefficients

rate of 10,000 deg/hr, so that only the misalignments are shown in the error model at the top of Table B2.

The misalignments are determined by expressing specific forces in terms of the direction cosine matrix for substitution into the equations of Table B1. This is done for X-coning, Z-up, and Z-coning, Z-up in Table B2. The resulting observation equations are shown in each case as the approximate average angular rates, normalized by the coning rate. In evaluating these average rates, small angles were assumed and higher order terms set to zero. Also, many terms are products of sines and cosines which average to zero. To reduce the number of observation equations, the corresponding observation with Z-down is subtracted from each, since the fixed misalignments will cancel from the difference, while the anisoelastic misalignments will reverse sign and become additive.

The final observation equations, obtained by subtracting Z-down averages from Z-up averages, and dividing by two, are represented by the coefficients in Table B3, Set I, No. 1 and No. 3, corresponding to X-coning and Z-coning, respectively. Equations No. 2, Y coning for Set I, are obtained by exchanging subscripts X and Y, since the results are symmetrical. The equations for Set II and Set III are obtained from Set I by simply permuting X, Y, and Z subscripts, as shown.

The solution of the observation equations in Table B3 is obtained by least-squares fit, since there are 27 equations in 18 unknowns. To reduce the dimension of the matrices it is observed that the equations and unknowns can be partitioned into four smaller groups, as shown in Table B4. The first three groups consist of seven identical equations in four unknowns each. These are solved in Table B5. The fourth group of equations are not linearly independent. However, they can be solved, as shown in Table B5, by assuming that these unknown coefficients are due to rotations only, which reduces the number of unknowns in the group from six to three. This assumption is equivalent to assuming that the gyros do not bend in a direction perpendicular to the applied specific force, which is reasonable.

Table B2. Reference Axis Misalignment Rates Due To Anisoelastic Misalignments During Coning

DEFINITIONS:		θ - CONE HALF ANGLE (RAD)
		ω - CONING FREQUENCY (RAD/SEC)
		$\omega_C = \omega\theta^2/2$ (CONING RATE)
		$C = \cos \omega t$
		$S = \sin \omega t$
MISALIGNMENT RATES WITH NO GYRO BIAS OR SCALE FACTOR ERRORS:		
$\begin{bmatrix} \delta\omega_X \\ \delta\omega_Y \\ \delta\omega_Z \end{bmatrix} = \begin{bmatrix} C_B^R(t) \end{bmatrix} \cdot \begin{bmatrix} 0 & \beta_{XY}(t) & \beta_{XZ}(t) \\ \beta_{YX}(t) & 0 & \beta_{YZ}(t) \\ \beta_{ZX}(t) & \beta_{ZY}(t) & 0 \end{bmatrix} \begin{bmatrix} \omega_X^B(t) \\ \omega_Y^B(t) \\ \omega_Z^B(t) \end{bmatrix}$		
WHERE TABLE B1 DEFINES $\beta_{ij}(t)$ FROM:		$\begin{bmatrix} A_X^B(t) \\ A_Y^B(t) \\ A_Z^B(t) \end{bmatrix} = \begin{bmatrix} C_B^R(t) \end{bmatrix}^{-1} \begin{bmatrix} 0 \\ 0 \\ 1 \end{bmatrix}$
FOR X-CONING, Z-UP:		
$\begin{aligned} \omega_X^B(t) &= \frac{\omega\theta^2}{2} \\ \omega_Y^B(t) &= \omega\theta C \\ \omega_Z^B(t) &= -\omega\theta S \end{aligned} ; \quad C_B^R = \begin{bmatrix} 1 & -\theta C & \theta S \\ \theta C & 1 & 0 \\ -\theta S & 0 & 1 \end{bmatrix} ; \quad \begin{bmatrix} A_X^B(t) \\ A_Y^B(t) \\ A_Z^B(t) \end{bmatrix} = \begin{bmatrix} -\theta S \\ 0 \\ 1 \end{bmatrix} \cdot \theta$		
APPROXIMATE AVERAGE ANGULAR RATES (NORMALIZED BY ω_C):		
$\begin{aligned} \overline{\delta\omega_X}/\omega_C &= \beta_{XZ-X} \\ \overline{\delta\omega_Y}/\omega_C &= (\beta_{XY0} + \beta_{YX0}) + \beta_{XY-Z} + \beta_{YX-Z} + \beta_{YZ-X} \\ \overline{\delta\omega_Z}/\omega_C &= (\beta_{XZ0} + \beta_{ZX0}) + \beta_{XZ-Z} + \beta_{ZX-Z} \end{aligned}$		
FOR Z-CONING, Z-UP:		
$\begin{aligned} \omega_X^B(t) &= \omega\theta C \\ \omega_Y^B(t) &= -\omega\theta S \\ \omega_Z^B(t) &= \frac{\omega\theta^2}{2} \end{aligned} ; \quad C_B^R = \begin{bmatrix} 1 & 0 & \theta C \\ 0 & 1 & -\theta S \\ -\theta C & \theta S & 1 \end{bmatrix} ; \quad \begin{bmatrix} A_X^B(t) \\ A_Y^B(t) \\ A_Z^B(t) \end{bmatrix} = \begin{bmatrix} -\theta C \\ +\theta S \\ 1 \end{bmatrix} \cdot \theta$		
APPROXIMATE AVERAGE ANGULAR RATES (NORMALIZED BY ω_C):		
$\begin{aligned} \overline{\delta\omega_X}/\omega_C &= (\beta_{ZX0} + \beta_{XZ0}) + \beta_{ZX-Z} + \beta_{XZ-Z} - \beta_{XY-Y} \\ \overline{\delta\omega_Y}/\omega_C &= (\beta_{ZY0} + \beta_{YZ0}) + \beta_{ZY-Z} + \beta_{YZ-Z} - \beta_{YX-X} \\ \overline{\delta\omega_Z}/\omega_C &= -\beta_{ZY-Y} - \beta_{ZX-X} \end{aligned}$		

Table B3. Observation Matrix for Determining Anisoelastic Coefficients from Coning Tests

		x_1	$\beta_{zy,y}$	$\beta_{zx,x}$	$\beta_{xz,z}$	$\beta_{xy,y}$	$\beta_{yx,x}$	$\beta_{yz,z}$	$\beta_{xy,y}$	$\beta_{yz,z}$	$\beta_{xz,x}$	$\beta_{zx,z}$	$\beta_{yx,y}$	$\beta_{xy,x}$	$\beta_{zy,y}$	$\beta_{zx,x}$	$\beta_{yz,z}$	z	
SET I	#1			+1									+1					$\Delta\omega_{z_1}^I/\omega_c$	
													+1					$\Delta\omega_{y_1}^I/\omega_c$	
														+1		+1		$\Delta\omega_{x_1}^I/\omega_c$	
	#2					+1		+1							+1			$\Delta\omega_{z_2}^I/\omega_c$	
															+1		+1		$\Delta\omega_{y_2}^I/\omega_c$
										+1								+1	$\Delta\omega_{x_2}^I/\omega_c$
	#3	-1	-1															.	
				+1	-1						+1								.
						-1	+1	+1											.
SET II	#1				+1								+1						
															+1		+1	+1	
									+1										
	#2	+1	-1			-1	-1				+1								
				-1	+1										+1				
	#3	+1																	
										+1									
															+1		+1	+1	
SET III	#1			-1	-1														
						+1	-1	+1											
		-1	+1							+1									
	#2					+1		+1										.	
															+1			.	
																+1	+1	+1	.
	#3		+1								+1							$\Delta\omega_{z_3}^{III}/\omega_c$	
															+1	+1		+1	$\Delta\omega_{y_3}^{III}/\omega_c$
											+1								$\Delta\omega_{x_3}^{III}/\omega_c$

Table B4. Partitioning of Observation Equations and Unknowns

DEFINITION: $\Delta\omega_i = \frac{\omega_i(\text{UP}) - \omega_i(\text{DOWN})}{2}$							
GROUP 1			GROUP 2	GROUP 3	GROUP 4		
UNKNOWN COEFFICIENTS	x_1	β_{XY-Y}	β_{YZ-Z}	β_{ZX-X}	x_1	$\beta_{ZY-X} = -\beta_{YZ-X}$	
	x_2	β_{XZ-Z}	β_{YX-X}	β_{ZY-Y}	x_2	$\beta_{XZ-Y} = -\beta_{ZX-Y}$	
	x_3	β_{YX-Y}	β_{ZY-Z}	β_{XZ-X}	x_3	$\beta_{YX-Z} = -\beta_{XY-Z}$	
	x_4	β_{ZX-Z}	β_{XY-X}	β_{YZ-Y}			
OBSERVATION	z_1	$\Delta\omega_{Z_1}^{II}/\omega_C$	$\Delta\omega_{Z_2}^I/\omega_C$	$\Delta\omega_{Z_3}^{III}/\omega_C$	z_1	$\Delta\omega_{Y_1}^{II}/\omega_C$	
	z_2	$\Delta\omega_{Z_1}^I/\omega_C$	$\Delta\omega_{Z_2}^{III}/\omega_C$	$\Delta\omega_{Z_3}^{II}/\omega_C$	z_2	$\Delta\omega_{X_2}^I/\omega_C$	
	z_3	$\Delta\omega_{Y_2}^{III}/\omega_C$	$\Delta\omega_{Y_3}^{II}/\omega_C$	$\Delta\omega_{X_1}^I/\omega_C$	z_3	$\Delta\omega_{Y_3}^{III}/\omega_C$	
	z_4	$\Delta\omega_{X_3}^{III}/\omega_C$	$\Delta\omega_{X_1}^{II}/\omega_C$	$\Delta\omega_{Y_2}^I/\omega_C$	z_4	$\Delta\omega_{Y_1}^I/\omega_C$	
	z_5	$\Delta\omega_{Z_1}^{III}/\omega_C$	$\Delta\omega_{Z_2}^{II}/\omega_C$	$\Delta\omega_{Z_3}^I/\omega_C$	z_5	$\Delta\omega_{X_2}^{III}/\omega_C$	
	z_6	$\Delta\omega_{X_2}^{II}/\omega_C$	$\Delta\omega_{Y_3}^I/\omega_C$	$\Delta\omega_{X_1}^{III}/\omega_C$	z_6	$\Delta\omega_{X_3}^{II}/\omega_C$	
	z_7	$\Delta\omega_{X_3}^I/\omega_C$	$\Delta\omega_{Y_1}^{III}/\omega_C$	$\Delta\omega_{Y_2}^{II}/\omega_C$			

Table B5. Least-Squares Solution of Partitioned Observation Equations

<u>OBSERVATION EQUATIONS:</u>		<u>LEAST-SQUARES SOLUTION:</u>	
$M \times N$	$N \times 1$	$M \times 1$	$N \times 1$
$[A]$	$X = Z$	$M > N$	$X = [C]^{-1} B$
		$N \times N$	$N \times M$
		$[C] = [A^T] [A]$	$B = [A^T] Z$
<u>GROUPS 1, 2, 3</u>		<u>GROUPS 1, 2, 3</u>	
<u>OBSERVATION MATRIX:</u>		<u>SOLUTION:</u>	
7×4	4×4	4×4	4×4
$[A] = \begin{bmatrix} +1 & +1 & +1 & +1 \\ +1 & +1 & +1 & +1 \\ -1 & -1 & +1 & +1 \\ -1 & +1 & +1 & +1 \end{bmatrix}$	$[C] = \begin{bmatrix} 4 & -1 & 2 & -1 \\ -1 & 4 & -1 & 2 \\ 2 & -1 & 3 & 0 \\ -1 & 2 & 0 & 3 \end{bmatrix}$	$[C]^{-1} = \frac{1}{48}$	$\begin{bmatrix} 21 & -3 & -15 & 9 \\ -3 & 21 & 9 & -15 \\ -15 & 9 & 29 & -11 \\ 9 & -15 & -11 & 29 \end{bmatrix}$
	$\det [C] = 48$		$B = \begin{bmatrix} Z_1 - Z_5 + Z_6 - Z_7 \\ Z_2 - Z_5 - Z_6 + Z_7 \\ Z_1 + Z_3 + Z_6 \\ Z_2 + Z_5 + Z_7 \end{bmatrix}$
<u>GROUP 4 SOLUTION:</u>			
$X_1 = \frac{Z_1 - Z_4}{2}$	$X_2 = \frac{Z_2 - Z_5}{2}$	$X_3 = \frac{Z_3 - Z_6}{2}$	

SIMULTANEOUS ESTIMATION AND DETECTION OF BIAS SHIFTS FOR INERTIAL NAVIGATION SYSTEMS

Richard V. Spencer
General Electric Company
100 Plastics Avenue
Pittsfield, Massachusetts 01201

Kevin Clements
Worcester Polytechnic Institute
Electrical Engineering Department
100 Institute Road
Worcester, Massachusetts 01609

SO1B

SIMULTANEOUS ESTIMATION AND DETECTION OF BIAS SHIFTS FOR INERTIAL NAVIGATION SYSTEMS

Richard V. Spencer
General Electric Company
100 Plastics Avenue
Pittsfield, Massachusetts 01201

Kevin Clements
Worcester Polytechnic Institute
Electrical Engineering Department
100 Institute Road
Worcester, Massachusetts 01609

Abstract

The problem of detecting and estimating the magnitude of shifts in otherwise constant parameters is considered. An algorithm is presented in which multiple shifts can be detected and estimated within the framework of a multiply-partitioned estimation algorithm, thus alleviating the computational burden of a bank of Kalman filters. The performance of the algorithm is demonstrated by simulation of a rocket sled test of an inertial guidance system.

Introduction

Error models for inertial instruments normally model the error states as either biases or, in some instances, as low order Markov processes. Experimental data indicate that certain errors normally modeled as biases may be subject to jumps or shifts of random amplitude occurring at random points in time.

In this paper, an algorithm for simultaneously detecting bias shifts and estimating the shift amplitudes is presented. The algorithm is based on the calculation of the probabilities of hypotheses with respect to bias shift occurrence. When a postulated hypothesis probability becomes large enough, then the hypothesis is accepted and a bias shift is detected.

In the past, a major deterrent to implementing hypothesis conditioned shift detection has been the computational requirements induced by the need for a bank of estimators, one for each hypothesis. Recently, however, it has been shown that under certain circumstances the computational burden can be greatly reduced by employing the techniques of decoupled bias and state estimation.¹⁻⁴ If the models and/or shifts to be distinguished are discriminated only by bias or shifting bias parameters, then the bank of estimators can be implemented as a single estimator for all common states which feeds a bank of low order bias estimators representing only the changeable aspect associated with each hypothesis.

A common situation, however, involves multiple bias shifts. Friedland⁶⁻⁷ introduced a nonlinear estimation algorithm in which calculated estimation covariances are increased every time a shift (failure) is detected. Here the ideas of Caglayan⁵ and Friedland are employed to allow both model selection and detection/estimation of multiple bias shifts within the framework of a multiply-partitioned estimation algorithm of expandable dimension which can be restructured as necessary.

The methods described herein were motivated by a need to detect and estimate possible shifts in the error parameters of inertial instruments before, during, and after being subjected to the environment of a rocket sled test. The utility of the algorithms is demonstrated by simulation of known shifts in such an environment.

Problem Statement

High resolution data is often used to calibrate and/or assess the overall performance of inertial navigation systems. Typically the guidance system model includes a large number of slowly varying error parameters taken as constants over the duration of the test. The combination of high resolution data, high expectations of test utility, and many modeled bias errors can lead to substantial computational, numerical, and mismodeling problems in the state estimation process, including the necessity to detect small variations in the system model. Variations can include unmodeled Markov processes and sudden, environmentally or otherwise induced shifts in modeled biases. The problem then is to construct an estimation/detection algorithm which is numerically stable, computationally efficient, and capable of discriminating small deviations in the system model.

A system model can be constructed which consists of dynamic (\dot{x}), bias (\dot{b}), and shift (\dot{e}) portions of the state vector. For the analysis of guidance/track data from a rocket sled test, \dot{x} , consists of 3 dimensions of position, velocity, and attitude deviations as well as any modeled Markov processes associated with the inertial components or track survey. \dot{b} consists of accelerometer bias errors, scale factor errors, etc., as well as gyro bias, mass-unbalance, anisoelectric, etc. drift errors. Because the inertial component errors are not perfectly stable and may shift due to environmental or other factors, \dot{e} consists of postulated shifts in selected elements of \dot{b} .

Solution

A collection of possible system models is considered. Each model corresponds to a particular bias shift hypothesis.

Each of the system models corresponds to a bias shift at some time, t_i , for the k^{th} bias state. Then the bias shift detection problem is equivalent to determining which of the possible system models is the correct one given the measurement data. In order to identify the correct system model, it will be necessary to construct a Kalman filter corresponding to each model in order to create a measurement residual sequence for each model.

Normally the computational requirements of such a bank of Kalman filters would be excessively burdensome. Here, however, an efficient extension of the bias-dynamic decoupled estimation algorithm of Friedland¹ is employed. The estimation algorithm, which is illustrated in Figure 1, extends Friedland's ideas to allow many "bias" partitions in the estimator. This also makes possible the addition of additional bias states to an existing estimator. That feature then allows a bank of estimators to be constructed by adding several parallel connected low order bias estimators in a series connection with the primary estimator. Then when a shift is detected the primary estimator can easily be reconfigured by removing the appropriate parallel filter and reconnecting it at the end of the series filter. The series/parallel filter architecture is illustrated in Figure 2.

Friedland¹ considered a system composed partially of dynamic states, \tilde{x} , and partially of constant parameters, \tilde{b} . He partitioned the state vector between the two classes, such that

$$\underline{y}(i+1) = \begin{bmatrix} \tilde{x} \\ \tilde{b} \end{bmatrix}_{i+1} = \begin{bmatrix} \theta_x(i) & \theta_{xb}(i) \\ 0 & I \end{bmatrix} \begin{bmatrix} \tilde{x} \\ \tilde{b} \end{bmatrix}_i + \begin{bmatrix} I \\ 0 \end{bmatrix} \underline{\xi}(i) \quad (1)$$

with estimation covariance,

$$P(i) = E \{ (y(i) - \hat{y}(i)) \hat{y}(i) - \hat{y}(i))^T \} \\ = \begin{bmatrix} P_x(i) + V_{xb}(i) M_b(i) V_{xb}^T(i) & V_{xb}(i) M_b(i) \\ M_b(i) V_{xb}^T(i) & M_b(i) \end{bmatrix} \quad (2)$$

where

$$\underline{\xi}(i) \text{ is a process noise vector with } E \{ \underline{\xi}(i) \underline{\xi}^T(j) \} \\ = Q(i) \delta_{ij}.$$

The observations are of the form

$$\underline{y}(i) = [H(i) \ C_b(i)] \begin{bmatrix} \tilde{x} \\ \tilde{b} \end{bmatrix}_i + \underline{n}(i), \quad (3)$$

where $\underline{n}(i)$ is a measurement noise vector with

$$E \{ \underline{n}(i) \underline{n}^T(j) \} = R(i) \delta_{ij}$$

$\underline{\xi}(i)$ and $\underline{n}(j)$ are assumed independent for all i and j .

The resulting recursive filter is of the form:

$$\hat{v}_{xb}^-(i+1) = \theta_x(i) \hat{v}_{xb}^-(i) + \theta_{xb}(i) \quad (4)$$

$$S_b(i+1) = H^{(i+1)} \hat{v}_{xb}^-(i+1) + C_b(i) \quad (5)$$

$$P_x^-(i+1) = \theta_x(i) P_x^-(i) \theta_x^T(i) + Q(i) \quad (6)$$

$$K_x(i+1) = P_x^-(i+1) H^T(i+1) (H(i+1) P_x^-(i+1) H^T(i+1) \\ + R(i+1))^{-1} \quad (7)$$

$$\hat{\tilde{x}}(i+1) = \theta_x(i) \hat{\tilde{x}}(i) + K_x(i+1) (y(i+1) \\ - H(i+1) \theta_x(i) \hat{\tilde{x}}(i)) \quad (8)$$

$$P_x^-(i+1) = P_x^-(i+1) - K_x(i+1) H^{(i+1)} P_x^-(i+1) \quad (9)$$

$$\hat{v}_{xb}(i+1) = \hat{v}_{xb}^-(i+1) - K_x(i+1) S_b(i+1) \quad (10)$$

$$M_b(i+1) = M_b(i) - M_b(i) S_b^T(i+1) [H(i+1) P_x^-(i+1) H^T(i+1) \\ + R(i+1) + S_b(i+1) M_b(i) S_b^T(i+1)]^{-1} \\ * S_b(i+1) M_b(i) \quad (11)$$

$$K_b(i+1) = M_b(i+1) [V_{xb}^T(i+1) H^T(i+1) \\ + C_b^T(i+1)] R^{-1}(i+1) \quad (12)$$

$$\hat{\tilde{b}}(i+1) = \hat{\tilde{b}}(i) + K_b(i+1) [y(i+1) - H(i+1) \theta_x(i) \hat{\tilde{x}}(i) \\ - S_b(i+1) \hat{\tilde{b}}(i)] \quad (13)$$

$$\hat{\tilde{x}}(i+1) = \hat{\tilde{x}}(i+1) + v_{xb}(i+1) \hat{\tilde{b}}(i+1) \quad (14)$$

Duffy⁴ noted that Equations (11) and (12) could be replaced by

$$K_b(i+1) = M_b(i) S_b^T(i+1) [H(i+1) P_x^-(i+1) H^T(i+1) \\ + R(i+1) + S_b(i+1) M_b(i) S_b^T(i+1)]^{-1} \quad (15)$$

$$M_b(i+1) = M_b(i) - K_b(i+1) S_b(i+1) M_b(i) \quad (16)$$

thus saving one inversion, three matrix multiplies and a matrix add. In either case, the equations for \tilde{x} amount to a Kalman filter that ignores \tilde{b} , while the equations for \tilde{b} amount to a Kalman filter that ignores \tilde{x} but has a measurement sensitivity matrix, $S_b = H V_{xb} + C_b$, a measurement noise covariance, $H P_x H^T + R$, and a pseudo-measurement, $\underline{y} - K \theta_x \tilde{x}$. The interpretation of decoupled estimation as two filters, one of which estimates a constant vector observed in white noise, was also noted by Mendel and Washburn⁹ and by Friedland. Such an interpretation leads to several algorithmic possibilities, including an information filter¹⁰⁻¹² approach to the bias estimation, and U-D factorization within the original decoupled estimation framework. It also leads to the realization that additional bias estimators can be cascaded indefinitely in series with the original dynamic and bias estimators, thus resulting in the algorithm depicted in Figure 1.

The estimation detection algorithm structure is depicted in Figure 3. It consists of the Kalman filter, F_0 , whose model includes the dynamic states, \tilde{x} , the bias states \tilde{b} and those bias shift states previously detected. The residual and residual variance computed by F_0 form the input to a parallel set of one-state bias filters F_1, F_2, \dots, F_f . The one-state bias filters correspond to bias shifts at times $t_1, t_{1-1}, \dots, t_{f-1}$. The residuals and residual variances computed by the one-state bias filters as well as those of F_0 are used to compute

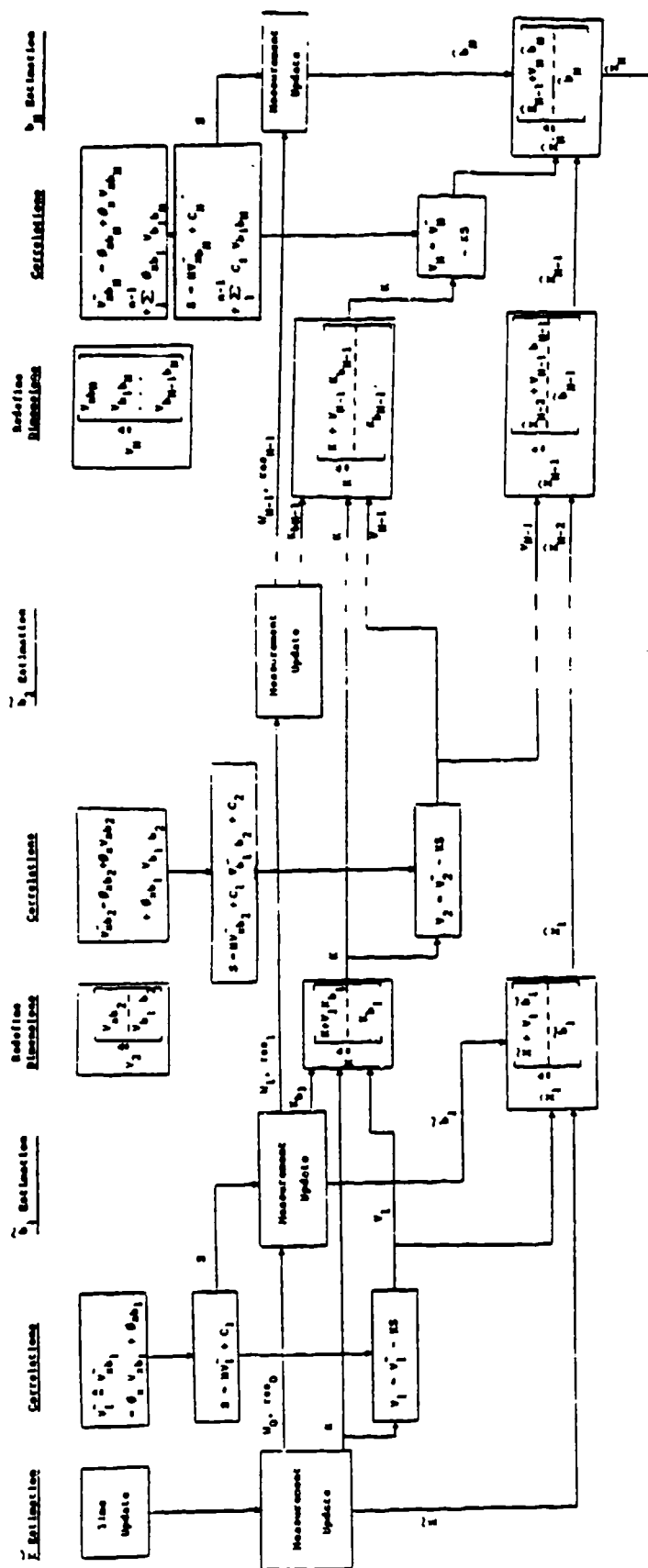


Figure 1: Multipartitioned Estimation Algorithm

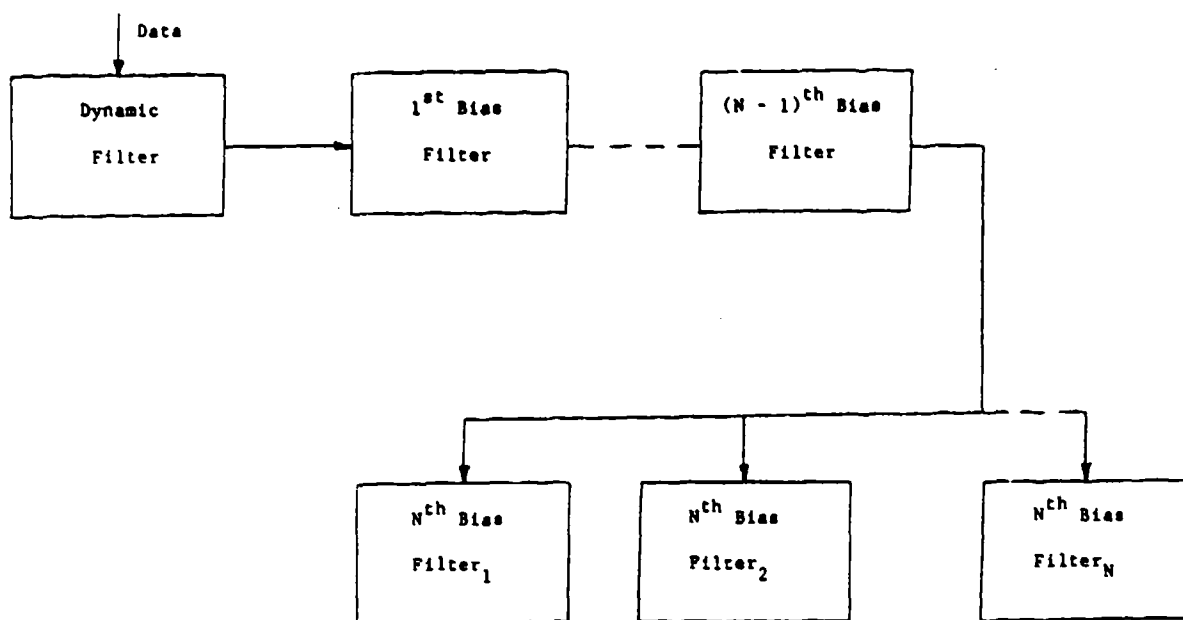


Figure 2: Series/Parallel Filter Architecture

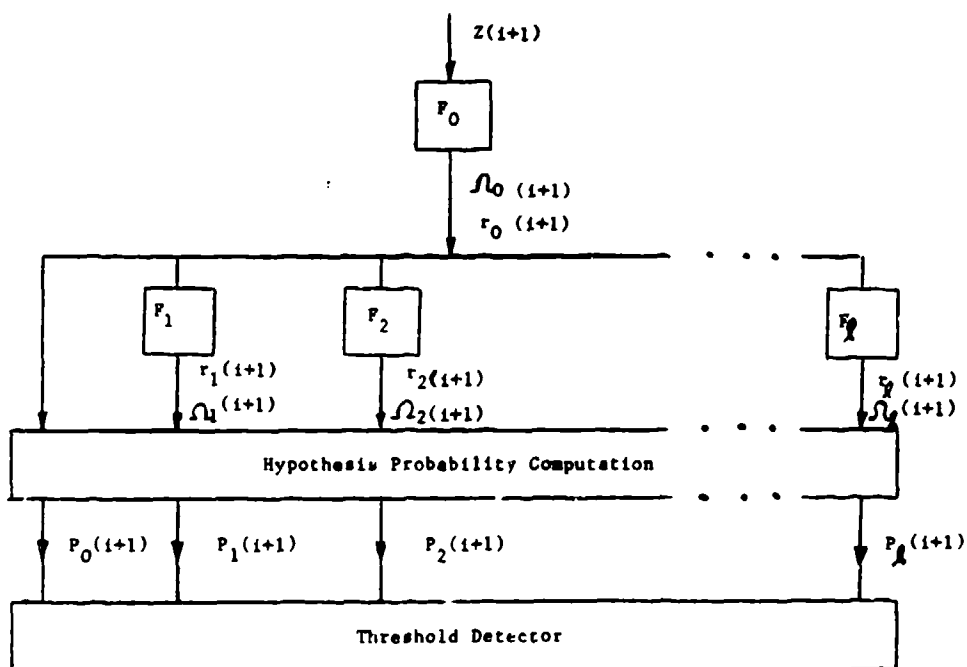


Figure 3

Estimation/Detection Algorithm

$P_0(i+1)$, the probability of no bias shift in the time window from t_i to t_{i-k+1} , and $P_k(i+1)$ $\{1 \leq k \leq J\}$ the probability that a bias shift occurred at t_{i-k+1} . The bias shift events are modeled as mutually exclusive and hence their probabilities must sum to one.

$$\sum_{k=0}^J P_k(i+1) = 1. \quad (17)$$

The bias shift probabilities can be calculated recursively using Bayes' rule. This recursive computation is written as

$$P_k(i+1) = \frac{f[Z(i+1) | M_k, Z(i)] P_k(i)}{\sum_{k=0}^J f[Z(i+1) | M_k, Z(i)] P_k(i)} \quad (18)$$

$f[Z(i+1) | M_k, Z(i)]$ is the probability density function of $Z(i+1)$ given a jump at time t_{i-k} and prior measurement data $\{Z(1) \dots Z(i)\}$. If gaussian statistics and scalar measurements are assumed, then equation 18 reduces to

$$P_k(i+1) = B_k(i+1) P_k(i) / \gamma(i+1) \quad (19)$$

where

$$B_k(i+1) = \left[\Omega_k(i+1) \right]^{-1/2} \exp \left\{ -\frac{1}{2} \left[\gamma_k(i+1) / \Omega_k(i+1) \right] \right\} \quad (20)$$

and

$$\gamma(i+1) = \sum_{k=0}^J B_k(i+1) P_k(i) \quad (21)$$

The test for bias shift detection is done using $P_0(i+1)$, thus we are testing whether a bias shift occurred at time t_{i-k+1} using measurement data up to time t_{i+1} . If $P_0(i+1)$ is greater than some pre-specified threshold value, then the hypothesis that a bias shift occurred at t_{i-k+1} is accepted and the one-state bias filter, F_0 , is included in P_0 . If $P_0(i+1)$ is less than the threshold then F_0 is discarded and the time window for testing bias shifts is moved forward when the succeeding measurement is processed. It should be noted that if F_0 is discarded rather than retained in P_0 it is not necessary to reinitialize F_1 thru F_{J-1} when the next measurement is processed since they will correspond to F_2 thru F_J at the next measurement time. Only when a bias shift is detected is it required to reinitialize the entire parallel bank of filters.

Simulation Results

In order to test the applicability of the above estimation/detection algorithms, a simulation of a typical rocket sled test of an inertial guidance system was conducted. The test consisted of approximately 3 minutes of operation in a 1-g field, followed by sled ignition and approximately 50 seconds of motion, finally followed by approximately 4 minutes of operation in 1-g after stopping. The modeled system consisted of 3 accelerometers

each with bias and scale factor errors, and 3 gyros each with bias, mass unbalance, compliance, and random (Markov) drift rate errors. In addition dynamic position, velocity, and attitude errors were modeled.

Three distinct cases were considered, data from a normal system, data from a system in which the accelerometer scale factor on one axis (primarily along the sled track) shifted while the sled was in motion, and data from a system in which the gyro bias drift rate on one axis (cross track) shifted while the sled was in motion. The down track position Kalman filter residuals for the latter two cases are shown in Figures 4 and 5. The estimator is able to somewhat follow the scale factor (SFEX) shift, but does poorly in the estimation of the shifted gyro drift (BDY).

Two situations are considered for bias shift detection performance. First a situation is considered where the data analyst has correctly guessed which parameter may have shifted. The bias shift detector (BSD) is then incorporated in order to identify the magnitude and timing of the actual shift.

First the case of a shifted scale factor (SFEX) is considered. Figure 6 shows that the estimator/detector algorithm is able to follow the shift considerably better than the estimator alone, resulting in whitened residuals as shown in Figure 7. A time sequence of the shift probabilities as calculated by the BSD is shown in Figures 8 through 14. The time spacing is 0.5 seconds and the BSD consists of 30 one-state estimators; so the detection window is 15 seconds wide. The time of the actual scale factor shift is 210. The indicated time is that associated with the shift probability which is about to be tested against the threshold of 0.5. Thus at $t(D) = 200$, the data in the window reflects only 5 seconds of the shift effect and the BSD has not yet begun to respond. At $t(D) = 210$, the BSD would ideally detect the shift, and indeed the probability of no shift is virtually zero, but no one cell has yet been identified. Finally at $t(D) = 216$, the leftmost shift probability exceeds the threshold and finally, 6 seconds late, a detection is made. Then in the next time increment the shift probabilities realign themselves, reflecting no more shifts.

Next the case of a shifted gyro drift (BDY) is considered. Here the estimation/detection performance is less impressive. Three shifts were identified, 7.5, 27., and 93. seconds after the actual shift, thus reflecting the lesser degree of observability of gyro drift. The total drift estimate, however, is better (28% error at end vs. 62% without the detection algorithm), and the residuals are considerably reduced as can be seen by comparing Figure 15 with Figure 5.

Finally, three cases were considered in which the data analyst incorrectly guessed at the shift situation. The detection algorithm performed very well (no detections) in two of the cases and gave strong indications that it was not satisfied in the third. First, a BSD looking for SFEX shifts was applied to data in which no parameter shifts at all were reflected. No false detections were made, as indicated by the time history of the BSD probability of no shift (P_0) shown in Figure 16. In fact, during sled motion when the scale factor observability increases, the probability of no shift also in-

creases. Next, a BSD looking for SFEK shifts was applied to data in which a BDY shift was reflected. Again no false detections were made. The probability of no shift is shown in Figure 17. Finally, a BSD looking for BDY shifts was applied to data in which a SFEK shift was reflected. The BSD made four false detections, but three of those were in succession (at $t_D = 231.$, 231.5 , and $232.$) and as indicated in Figure 18, the residuals indicate that the detection algorithm is still not satisfied. Thus, a strong indication is given that the data analyst is barking up the wrong tree.

References

1. B. Friedland, "Treatment of Bias in Recursive Filtering", IEEE Transactions on Automatic Control, Vol. AC-14, No. 6, August, 1969, pp. 359-367
2. J. L. Lin and A. P. Sage, "Algorithms for Discrete Sequential Maximum Likelihood Bias Estimation and Associated Error Analysis", IEEE Transactions on Systems, Man, and Cybernetics, Vol. SMC-1, No. 4, October, 1971, pp. 314-324
3. S. S. Godbole, "Comparison of Friedland's and Lin-Sage's Bias Estimation Algorithms", IEEE Transactions on Automatic Control, Vol. AC-19, No. 2, April, 1974, pp. 143-145
4. T. Duffy, "Decoupled Estimation Techniques Applied to Trajectory Reconstruction", AIAA/AAS Astrodynamics Conference, San Diego, California, August, 1976, Paper No. 76-820
5. A. K. Caglayan, "Simultaneous Failure Detection and Estimation in Linear Systems", Proceedings of the 1980 IEEE Conference on Decision and Control, Albuquerque, New Mexico, December, 1980, pp. 1038-1041
6. B. Friedland, "Maximum Likelihood Estimation of a Process with Random Transitions (Failures)", IEEE Transactions on Automatic Control, Vol. AC-24, No. 6, December, 1979, pp. 932-937
7. B. Friedland, "Multidimensional Maximum Likelihood Failure Detection and Estimation", IEEE Transactions on Automatic Control, Vol. AC-26, No. 2, April, 1981, pp. 567-570
8. J. M. Mendel and H. D. Washburn, "Multistage Estimation of Bias States", Proceedings of the 1976 IEEE Conference on Decision and Control, Clearwater Beach, Florida, December, 1976, pp. 629-630
9. B. Friedland, "Notes on Separate - Bias Estimation", IEEE Transactions on Automatic Control, Vol. AP-23, No. 4, August, 1978, pp. 735-738
10. B. Friedland, "On the Calibration Problem", IEEE transactions on Automatic Control, Vol. AC-22, No. 6, December, 1977, pp. 899-905
11. G. J. Bierman, "The Treatment of Bias in the Square-Root Information Filter/Smother", Proceedings of the 1973 IEEE Conference on Decision and Control, San Diego, California, December, 1973, pp. 632-639
12. P. G. Kaminski, A. E. Bryson and S. F. Schmidt, "Discrete Square Root Filtering: A Survey of Current Techniques", IEEE Transactions on Automatic Control, Vol. AC-16, No. 6, December, 1971, pp. 727-735

FIGURE 4 - ESTIMATION RESIDUALS
(SFEX SHIFTED AT T=210.)

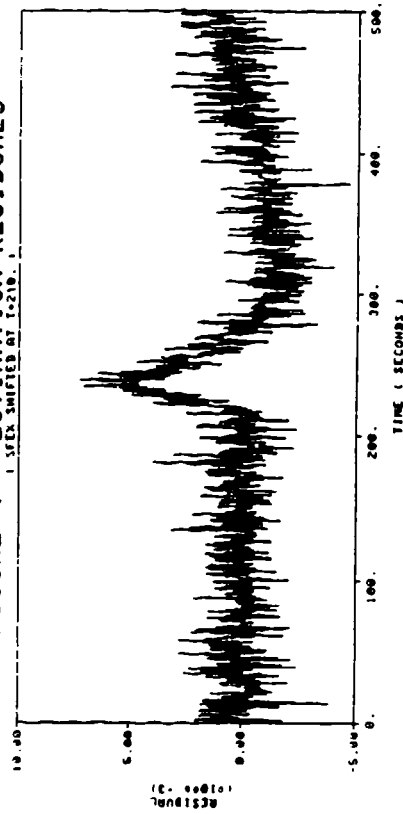


FIGURE 5 - ESTIMATION RESIDUALS
(SFEX SHIFTED AT T=210.)

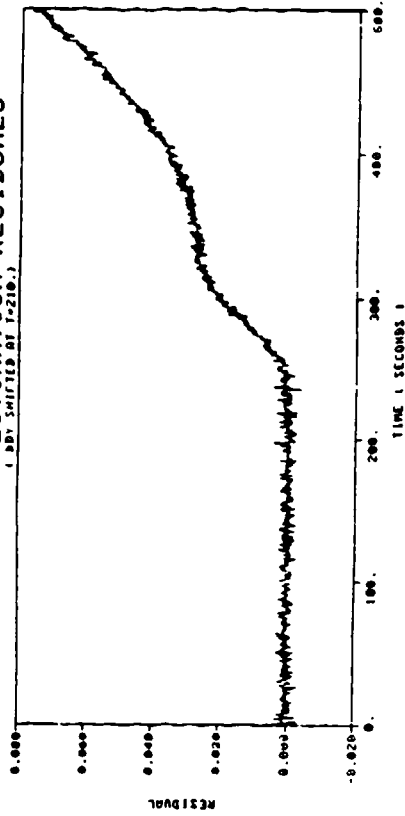


FIGURE 6 SFEX ESTIMATES (SFEX+SHIFT)
(SFEX SHIFTED AT T=210.)

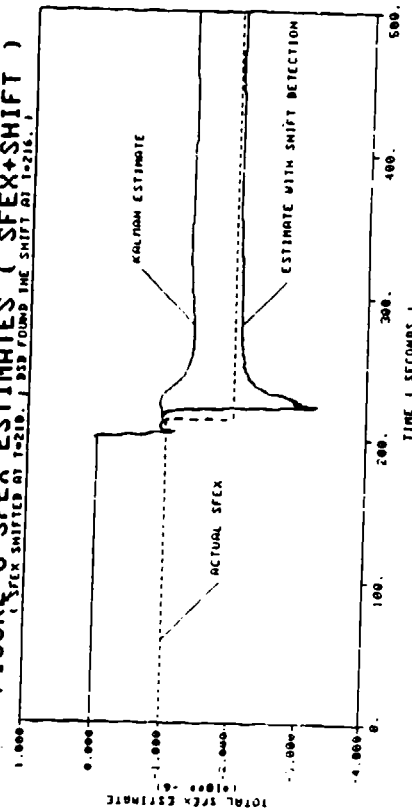


FIGURE 7 - ESTIMATION/DETECTION RESIDUALS
(DETECTION IN CORRECTLY ASSUMED SHIFTS IN SFEX)

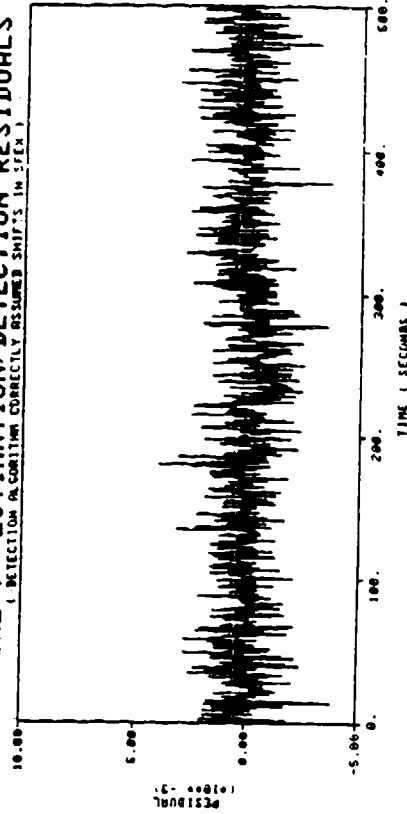


Figure 8. BIAS SHIFT PROBABILITIES

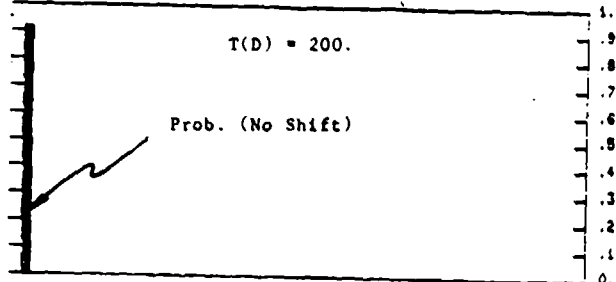


Figure 9. BIAS SHIFT PROBABILITIES

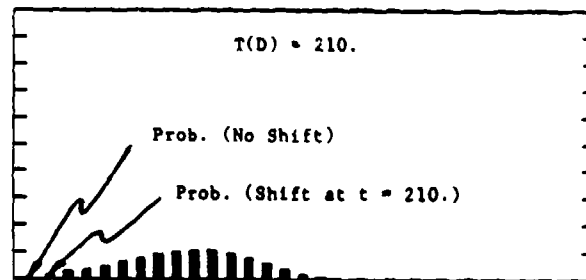


Figure 10. BIAS SHIFT PROBABILITIES

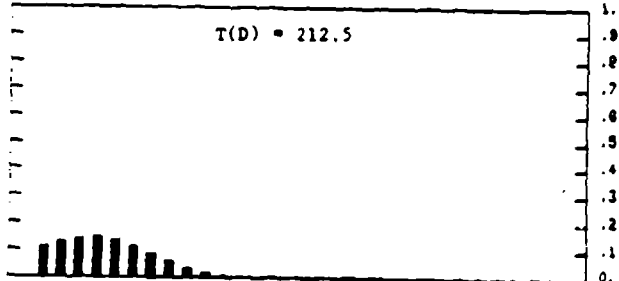


Figure 11. BIAS SHIFT PROBABILITIES

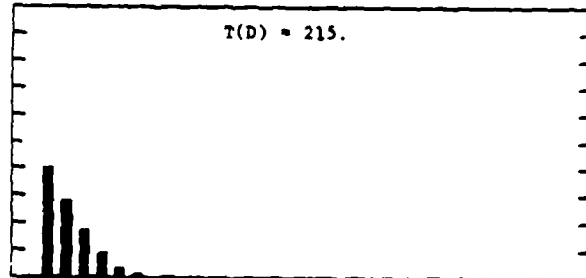


Figure 12. BIAS SHIFT PROBABILITIES

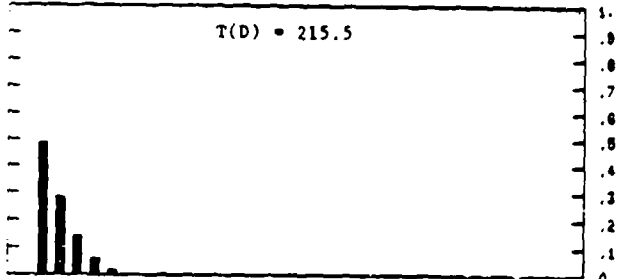


Figure 13. BIAS SHIFT PROBABILITIES

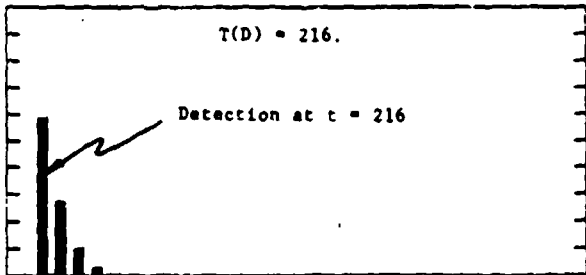


Figure 14. BIAS SHIFT PROBABILITIES

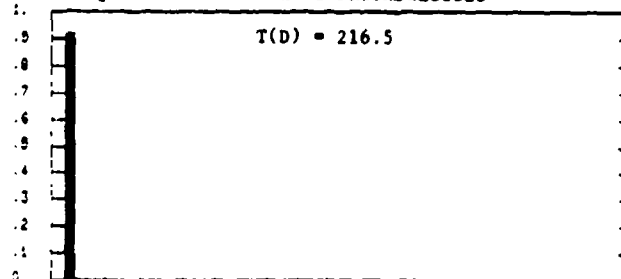


FIGURE 15 ESTIMATION/DETECTION RESIDUALS
(DETECTION ALGORITHM CORRECTLY ASSUMED SHIFTS IN SPKX)

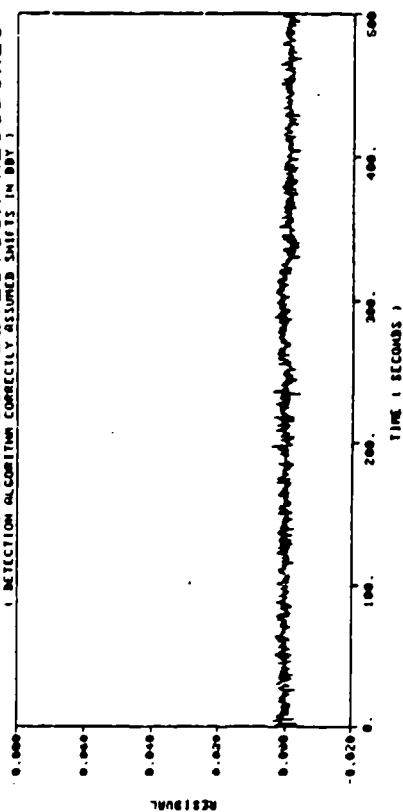


FIGURE 16 - PROBABILITY OF NO SHIFT
(ACTUAL DATA CONTAINED NO SHIFTS, 1 BSD ASSUMED SHIFTS IN SPKX)

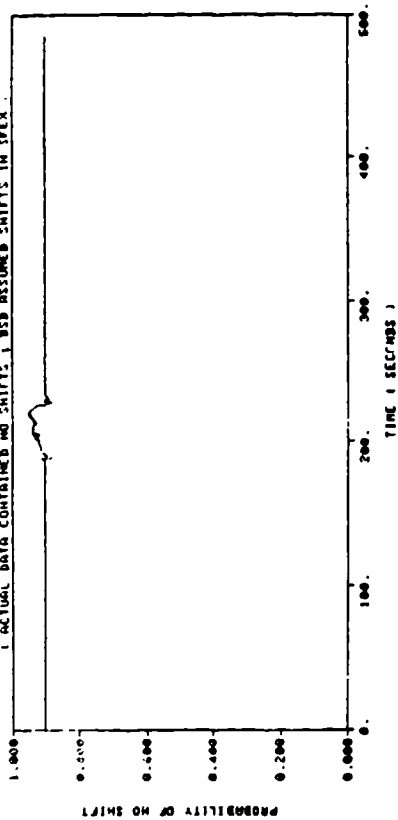


FIGURE 17 - PROBABILITY OF NO SHIFT
(1 BSD SHIFTED AT T=210, 1 BSD ASSUMED SHIFTS IN SPKX)

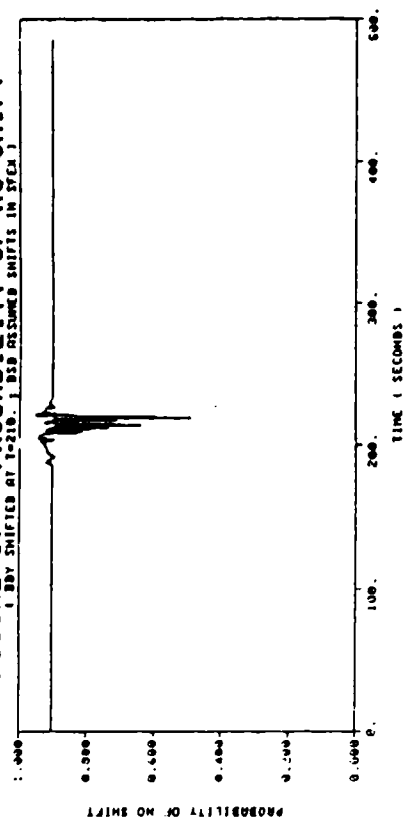
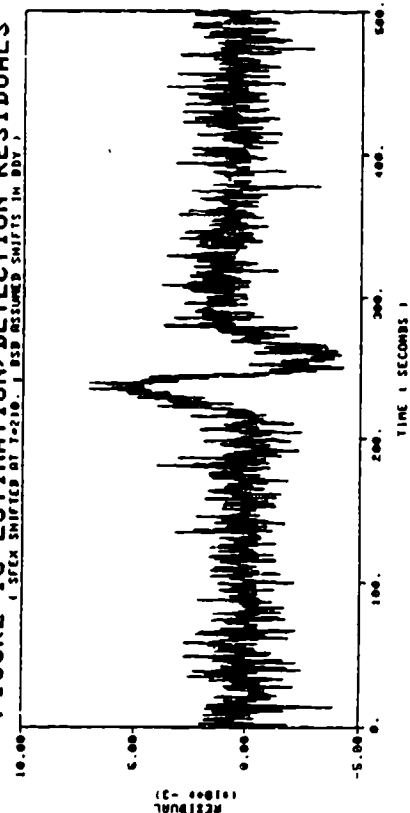


FIGURE 18 ESTIMATION/DETECTION RESIDUALS
(SPKX SHIFTED AT T=210, 1 BSD ASSUMED SHIFTS IN DDY)



**Covariance Analysis and Post-Processing of Gravity
Compensation Effects for Aided Multi-State
Navigation Systems**

Paper No. 87-13

Thirteenth Biennial Guidance Test Symposium

Holloman Air Force Base

October 7 1987

**Paul Zavattero
NORTHROP ELECTRONICS DIVISION
2301 W. 120th Street
P.O. Box 5032
Hawthorne, CA 90251-5032**

ABSTRACT

High-accuracy navigation systems frequently employ a multi-state on-board Kalman filter for processing external updates. Gravity compensation errors may be significant error contributors for such systems, even when an on-board state-space gravity model is employed in conjunction with an accurate stored map of gravity data. It is not known how to model gravity compensation errors faithfully in the state-space format suitable for on-board implementation when the vehicle changes its direction of travel or altitude, or when the gravity compensation technique utilized relies on stored grids of gravity map values derived from a finite gravity data base. These factors have tended to complicate the covariance analysis of the contribution of gravity errors and their mismodelling to system performance. This paper presents a method for propagating navigation system error covariances under the following circumstances: (1) A multi-state filter is implemented on board, (2) Gravity errors are modeled as filter states, (3) Instrument errors are mismodelled by the on-board filter, and (4) External updates are processed by the implemented filter. The vehicle maneuver time history is taken to be arbitrary, and the actual cross-correlations between gravity errors at points along the vehicle trajectory are assumed given by an arbitrary spatially correlated model which need not be stationary or isotropic. The analysis approach can be mechanized as an add-on to an existing linear covariance analysis program. The analysis also provides a means for computing the cross-correlation between measured gravity quantities and the vehicle state, for use in optimal estimation schemes in a post-processing environment.

The covariance calculation presented in this paper provides the same result as the Edwards nested integrals mechanization.¹ However, a different mechanization is used which results in a significant reduction in computer storage burden. The original Edwards approach requires the storage of the state transition matrix for each discrete time interval simulated. The approach given here requires the storage of a three-column matrix with the same number of rows as the state transition matrix for each simulated discrete time interval. In addition, the issues of instrument mismodelling and filter gravity model implementations are handled explicitly in this paper.

The covariance propagation method derived here is similar to the standard dual-state formulation used for mismodelling sensitivity analyses, except that the actual gravity errors are regarded as drivers to the system errors and are not included in the state. Use of the recursive discrete error state propagation formulation enables system errors to be represented as a linear combination of the gravity errors at the discrete vehicle locations, along with uncorrelated IMU instrument noise drivers and external measurement errors. The weights defining the current error state as a linear combination of the gravity errors at the previous vehicle locations are maintained and updated at each time step. These weights can also be used to compute the cross-correlation of the system errors with measured gravity quantities for use in post-processing.

A simulation example is presented using an 37-state navigation filter for simulation of a mobile strategic missile application in which velocity updates are processed by the on-board Kalman filter. A first-order Markov gravity

model is implemented in the filter, while actual gravity errors are correlated according to the spatially defined Sperry Three-Dimensional Algebraic Gravity model. An additional example is given showing the utilization of the covariance analysis approach in post-processing observables to estimate gravity errors encountered by the vehicle. Sensitivity of navigation errors during open-loop missile flight to gravity error frequency content is presented for a ballistic missile simulation example.

1.0 Introduction

This note defines an algorithm for computation of mean square navigation errors, and their cross-correlations, when gravity compensation errors are spatially correlated and not readily represented as the outputs of a linear system driven by white noise. The covariance propagation algorithm defined here gives the type of result provided by the Edwards nested integral approach which used numerical integration of a matrix Riccati equation. The computations defined here are arranged using the discrete approximation to the continuous error dynamics. The mechanization given here also provides a means for calculating the cross-correlations between the navigation state and observables such as gravity measurements, position reference derived measurements of navigation errors, or observations of velocity errors. This paper presents an approach to using these cross-correlations for least-squares estimation of navigation errors and gravity errors in a post-processing environment.

The basis of the mechanization is that the discrete approximation expresses the navigation errors due to gravity errors as a linear combination of the gravity errors at each of the points of the vehicle's discrete position time history. By linearity the covariance of the navigation errors due to gravity is a linear combination of the cross-correlations of the gravity errors at the discrete vehicle locations.

The covariance propagation equations given here use the assumption that an implemented suboptimal Kalman filter processes external measurements to compute corrections to indicated position, velocity, and platform misalignments, and to update estimates of IMU error parameters and gravity errors. The filter's corrections are applied to the navigator at each iteration, with the exception of the estimate of the error in gravity compensation. Rather than passing the suboptimal filter gravity estimate to the navigator for use in integrating the vehicle equations of motion, an equivalent formulation is used: The filter's estimate of gravity error is maintained in its state vector and is propagated at each step into position and velocity corrections. These corrections are applied.

The computational storage burden for the mechanization presented here depends on the number l of gravity states modelled by the on-board filter, the number m of INS states modelled by the on-board filter, and the number of states driving the actual navigation errors which are left unmodelled by the filter. Storage required also depends on whether control is applied from the filter in correcting the navigation-indicated quantities. If control is applied from all the filter states except for the gravity states, then for each non-zero time increment simulated, an $(l+m) \times 3$ matrix must be stored. The k^{th} such stored matrix defines the contribution of gravity errors at time t_k

to the current state. When the state is propagated over a time interval, or when an external update is incorporated, all the stored $(l+m) \times 3$ matrices must be recalled from memory, updated in accordance with the modifications made to the current state, and restored for later use. The stored weighting matrices are used for the calculation of the cross-correlation of the current gravity with the current navigation state which is required to propagate the navigation error covariance. Because they define the current state as a superposition of the previous gravity errors, the weighting matrices can be used to calculate cross-correlations between the state and other quantities such as gravity measurements in an area in which a navigation test is conducted. All quantities involved in the covariance propagation method presented here are derived from variables ordinarily computed by standard navigation error analysis programs.

Section 2.0 presents the analysis groundrules and a derivation of the covariance analysis algorithm. In Section 3.0, a post-processing technique is presented using a batch processing least-squares approach to estimating navigation quantities and gravity errors. This approach is based on standard least-squares estimation using the inversion of normal matrices, but uses observables whose cross-correlations are computed using the method presented in Section 2.0. In Section 4.0, three simulation examples are presented to illustrate how the covariance propagation and post-processing schemes can be applied to simulation analysis of practical navigation problems. The topics presented in Section 4.0, using hypothetical, simplified instrument and gravity models, are: (1) Performance of a simple first-order Markov gravity model in bounding gravity-induced errors in land navigation, (2) Use of IMU-derived observables to determine gravity errors in post-processing land navigation data, and (3) Effect of frequency content of gravity errors on in-flight, open-loop navigation performance.

2.0 Navigation Error Covariance Propagation with Arbitrarily Correlated Gravity Errors

This section defines equations for discrete propagation of the covariance matrix of navigation errors induced by INS instrument errors and spatially correlated gravity errors and controlled by application of external updates incorporated using an implemented suboptimal filter.

The approach follows the standard dual-state formalism used to handle filter mismodelling analysis except that the dual-state vector is driven by spatially correlated gravity errors as well as the white noise INS error drivers. Gravity errors may be represented as states in the suboptimal filter but actual gravity errors are regarded as drivers for the actual navigation errors.

Among the assumptions used in the analysis are:

1. The iteration time step is short enough so that, given the state dynamics, gravity errors can be assumed constant over the discrete time interval.

2. An external measurement is processed instantaneously by the suboptimal filter at each time step. Use of a zero measurement matrix extends the applicability of the analysis to the case where external measurements are processed only occasionally.

3. Control from filter states, except for gravity estimates, is applied instantaneously via a reset. After the suboptimal filter state update, actual navigation errors are adjusted by the suboptimal filter's state estimates. Use of a zero control distribution matrix makes the equations given here usable for the case where control is applied less frequently.

The dual state propagated consists of the concatenation of the filter state, immediately after application of control, with the actual navigation system error state immediately after application of control.

The navigation configuration analyzed here is indicated schematically in Figure 2-1, and can be summarized as follows.⁶ Between external measurements, navigation indicated position and velocity are updated by integrating the sum of sensed specific force output by the IMU and computed gravity values. The Kalman filter estimates the errors in the IMU parameter estimates used to correct the raw IMU outputs, the errors in navigation indicated position and velocity, attitude, and the errors in the computed gravity values. At specified intervals, the Kalman filter's estimates are applied to the indicated navigation values in the form of instantaneous corrections or resets of position, velocity, attitude, and IMU parameter values. For convenience it is assumed that the Kalman filter's estimate of the errors in the computed gravity values that are integrated by the navigator are not passed to the navigator for use in its integration procedure. Instead the gravity error estimate is propagated into equivalent corrections in position and velocity.

The Kalman filter's state vector x is defined as follows:

$$\hat{x} = [\hat{\delta p}_e \ \hat{\delta v}_c \ \hat{\psi}_c \ \hat{\delta w}_m \ \hat{\delta a}_m \ \hat{\delta M}_m \ \hat{g}]^T$$

$\hat{\delta p}_e$ = estimated error in navigation-indicated E-frame position vector

$\hat{\delta v}_c$ = estimated error in navigation-indicated earth-relative velocity vector, coordinatized in the C-frame

$\hat{\psi}_c$ = platform misalignment

$\hat{\delta w}_m$ = estimated error in the modelled gyro parameters used to convert IMU outputs

$\hat{\delta a}_m$ = estimated error in the modelled accelerometer parameters used to correct IMU outputs

\hat{g} = estimate of the error in the three components of anomalous gravity integrated by the navigator, with additional filter-assumed driving states

$\hat{\delta M}_m$ = filter's estimates of correlated errors in external reference navigation aids.

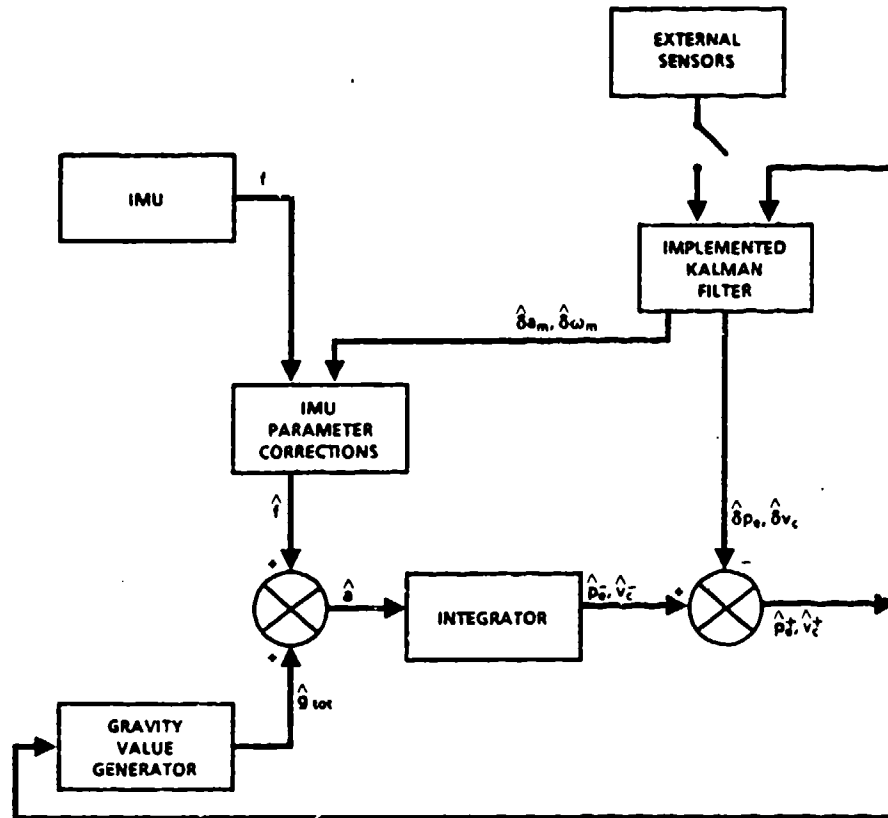


Figure 2-1 Schematic Navigation Flow Example

- | | | | |
|---|--|--------------------------------------|---|
| \hat{a} | = sensed acceleration | \hat{p}_e, \hat{v}_c | = position, velocity obtained by integration of \hat{a} and \hat{g}_{tot} |
| f | = sensed specific force | $\hat{\delta p}_e, \hat{\delta v}_c$ | = Kalman filter estimates of errors in position, velocity |
| \hat{g}_{tot} | = computed gravity value | | |
| $\hat{\delta \omega}_m, \hat{\delta a}_m$ | = Kalman filter estimate of errors in parameters used to correct raw IMU outputs | | |

The state vector \bar{x} whose covariance is to be propagated and which includes the actual navigation errors, is defined to be the concatenation of the filter state estimates with actual errors, with the exception of gravity errors. Actual gravity errors are not regarded as part of the error state, but as drivers to it. The components of the dual state are

$$\bar{x} = [\hat{x} \quad \delta p_e \quad \delta v_c \quad \psi_c \quad \delta w_m \quad \delta a_m \quad \delta M_m \quad \delta w_u \quad \delta a_u \quad \delta M_u]^T$$

Here \hat{x} is the vector of filter state estimates.

The components δp_e , δv_c and ψ_c are the actual errors in the corresponding terms estimated by the filter.

The components δw_m and δa_m are the errors in the IMU compensation terms modelled by the filter.

The states δw_u and δa_u are unmodelled gyro and accelerometer error terms. The term \hat{g} included in the filter state \hat{x} is the gravity estimate of the Kalman filter. Consequently propagation of the covariance of the state \bar{x} yields the covariance of the Kalman filter's estimate of gravity errors. The corresponding block of the Kalman filter's covariance matrix, which is used by the implemented filter in computing its gains, gives the filter's statistics for the errors in its estimate \hat{g} .

The measurement errors δM_m and δM_u are respectively the errors in external references modelled and unmodelled by the filter.

At every iteration, the corrections contained in the filter's states, excluding the filter gravity states \hat{g} , are applied to the navigator, so that after control is applied, the values for those Kalman filter states are all equal to 0. The gravity estimate \hat{g} is never applied, only updated. This gives rise to a position and velocity correction to be applied at every step, whether or not an external measurement is available.

In this section a derivation is given for a simple expression for the propagation of the extended error state \bar{x}_k (just after application of control at time t_k) to its value at t_{k+1} in the form:

$$\bar{x}_{k+1} = \Phi_k^{k+1} \bar{x}_k + \bar{\Gamma}_k g_k + \bar{G}_k u_k + \bar{G}'_k v_k \quad (1)$$

where

g_k = error in computed gravity value added to sensed specific force by the navigator in solving vehicle equation of motion between external updates (anomalous gravity deviation from analytical model plus map interpolation)

u_k = INS error white noise drivers

v_k = uncorrelated external measurement errors.

The dependance of the matrices Φ_k^{k+1} , $\bar{\Gamma}_k$, \bar{G}_k , and \bar{G}'_k on the plant dynamics and the implemented filter gains is derived in this section. This state propagation equation is used to develop the covariance propagation.

Covariance Propagation

Use of the discrete state propagation in Equation (1) gives rise to a discrete covariance propagation equation. Because the driving gravity error g_k is correlated with the current state \bar{x}_k , a new term is involved in the covariance propagation. The covariance propagation method is presented below. At the conclusion of this section, the derivation of the state propagation of Equation (1) is given.

The following recursive equation is derived for the covariance $E\{\bar{x}_{k+1}\bar{x}_{k+1}^T\}$:

$$\begin{aligned} P_{k+1} &= E\{\bar{x}_{k+1}\bar{x}_{k+1}^T\} \\ &= \phi_k^{k+1} E\{\bar{x}_k\bar{x}_k^T\} (\phi_k^{k+1})^T + \bar{G}_k E\{u_k u_k^T\} \bar{G}_k^T + \bar{G}_k' E\{v_k v_k^T\} (\bar{G}_k')^T \\ &\quad + \bar{\Gamma}_k E\{g_k g_k^T\} \bar{\Gamma}_k^T + \phi_k^{k+1} R_k \bar{\Gamma}_k^T + \bar{\Gamma}_k R_k^T (\phi_k^{k+1})^T \end{aligned} \quad (2)$$

$$\text{where } R_k = \phi_0^k E\{\bar{x}_0 g_k^T\} + \sum_{j=0}^{k-1} [\phi_{k-j}^k \bar{\Gamma}_{k-j-1}] E\{g_{k-j-1} g_k^T\}, \text{ if } k \geq 1 \quad (3)$$

The derivation of this expression can be presented as follows.

The assumption on the statistics of the driving terms are:

1. $E\{u_k u_k^T\} = 0$ if $k \neq 1$. INS error source drivers are white.
2. $E\{v_k v_k^T\} = 0$ if $k \neq 1$. External measurement errors are white.
3. $E\{u_k v_k^T\} = 0$ External measurement errors are uncorrelated with INS error state drivers.
4. $E\{u_k g_k^T\} = 0$, $E\{v_k g_k^T\} = 0$. INS error state white noise drivers and white external measurement errors are uncorrelated with gravity compensation errors.
5. $E\{\bar{x}_k u_k^T\} = 0$, $E\{\bar{x}_k v_k^T\} = 0$. INS error drives and external measurements are uncorrelated with the current state.

The assumption made on the correlation of the gravity errors is that they are correlated according to a defined model:

$$E\{g_k g_l^T\} = f(k, l).$$

Typically the correlations of g_k and g_l depend on the vehicle's positions \bar{R}_k and \bar{R}_l at the times t_k and t_l :

$$E\{g_k g_l^T\} = f(\bar{R}_k, \bar{R}_l).$$

This is the case if the gravity value generator of Figure 2-1 (which generates gravity values to be integrated by the navigator to solve the vehicle equations of motion between updates) computes gravity according to an ellipsoidal model or by interpolating a stored map of gravity disturbance values.

The complication in propagating the covariance of the state x_{k+1} from its covariance at time t_k is that a state space propagation equation for gravity of the form

$$g_{k+1} = \phi_g g_k + \Gamma_g w_{gk}, \quad w_{gk} = \text{white noise sequence}$$

may not be available. For example, if the vehicle crosses its path, $g_{k+m} = g_k$, then a white noise sequence would be required to satisfy the requirement that

$$E\{g_{k+m} g_k^T\} = E\{g_k g_k^T\}$$

Unless the vehicle travels in a straight line it is not known how to arrange the required driving noises for the standard state space propagation which proceeds by augmenting the state x_k to include g_k , and treats the w_{gk} as drivers for the augmented state. As a result, in propagating the covariance of the state \bar{x}_{k+1} from its value at time t_k , it will be seen that the correlation

$$E\{\bar{x}_k g_k^T\}$$

must be computed.

The error state covariance is defined as

$$P_k = E\{\bar{x}_k \bar{x}_k^T\}$$

To obtain P_{k+1} from its predecessor P_k , Equation (1) for the propagation of the state \bar{x}_{k+1} from its predecessor is used as follows:

$$P_{k+1} = E\{[\phi_k^{k+1} \bar{x}_k + \bar{\Gamma}_k g_k + \bar{G}_k u_k + \bar{G}'_k v_k][\bar{x}_k^T (\phi_k^{k+1})^T + g_k^T \bar{\Gamma}_k^T + u_k^T \bar{G}_k^T + v_k^T (\bar{G}'_k)^T]\}$$

which gives Equation (2)

$$P_{k+1} = \phi_k^{k+1} P_k (\phi_k^{k+1})^T + \bar{G}_k E\{u_k u_k^T\} \bar{G}_k^T + \bar{G}'_k E\{v_k v_k^T\} (\bar{G}'_k)^T + \bar{\Gamma}_k E\{g_k g_k^T\} \bar{\Gamma}_k^T \\ + \phi_k^{k+1} E\{\bar{x}_k g_k^T\} \bar{\Gamma}_k^T + \bar{\Gamma}_k E\{g_k \bar{x}_k^T\} (\phi_k^{k+1})^T$$

In order to make this equation for covariance propagation practical to implement, the calculation of the cross-correlation of the current state \bar{x}_k with the current gravity error g_k must be handled in an efficient manner. One such approach will now be given.

The last two terms in the right-hand side of Eq. (2) are mutual transposes. A convenient expression for computing $E\{\bar{x}_k g_k^T\}$ is obtained from fact that \bar{x}_k is a superposition of the driving errors u_0, u_1, \dots, u_{k-1} and the gravity errors g_0, g_1, \dots, g_{k-1} . However, only the gravity errors g_0, g_1, \dots, g_{k-1} are correlated with the current gravity value g_k . An auxiliary state for the purpose of deriving the cross-correlation of \bar{x}_k with g_k can be defined recursively by the transition matrix ϕ_k^{k+1} and superposition integral Γ_k used in propagating the state \bar{x}_k :

$$y_0 = \bar{x}_0$$

$$y_{k+1} = \phi_k^{k+1} y_k + \bar{\Gamma}_k g_k,$$

Then it is apparent that this state y_k is correlated in the same way with g_k as the actual state \bar{x}_k :

$$E\{y_k g_k^T\} = E\{\bar{x}_k g_k^T\}.$$

The state y_k can be expanded as a superposition of the gravity values of g_0, g_1, \dots, g_{k-1} , for example:

$$\begin{aligned} y_k &= \phi_{k-1}^k y_{k-1} + \bar{\Gamma}_{k-1} g_{k-1} \\ &= \phi_{k-1}^k (\phi_{k-2}^{k-1} y_{k-2} + \bar{\Gamma}_{k-2} g_{k-2}) + \bar{\Gamma}_{k-1} g_{k-1} \\ &= \phi_{k-1}^k \phi_{k-2}^{k-1} y_{k-2} + \phi_{k-1}^k \bar{\Gamma}_{k-2} g_{k-2} + \bar{\Gamma}_{k-1} g_{k-1} \\ &= \phi_{k-1}^k \phi_{k-2}^{k-1} \phi_{k-3}^{k-2} y_{k-3} + \phi_{k-1}^k \phi_{k-2}^{k-1} \bar{\Gamma}_{k-3} g_{k-3} + \phi_{k-1}^k \bar{\Gamma}_{k-2} g_{k-2} + \bar{\Gamma}_{k-1} g_{k-1} \end{aligned}$$

By defining the products of matrices involved as

$$\phi_{k-l}^k = \phi_{k-1}^k \phi_{k-2}^{k-1} \dots \phi_{k-l}^{k-l+1}, \text{ and letting } \phi_k^k = I,$$

it is apparent that

$$y_k = \phi_0^k y_0 + (\phi_1^k \bar{\Gamma}_0) g_0 + (\phi_2^k \bar{\Gamma}_1) g_1 + (\phi_3^k \bar{\Gamma}_2) g_2 + \dots + (\phi_k^k \bar{\Gamma}_{k-1}) g_{k-1}$$

This defines the state y_k as a superposition of the earlier gravity errors g_0, g_1, \dots, g_{k-1} and the initial state y_0 .

It follows that the correlation of y_k with g_k is also a superposition:

$$E\{y_k g_k^T\} = \phi_0^k E\{y_0 g_k^T\} + (\phi_1^k \bar{\Gamma}_0) E\{g_0 g_k^T\} + (\phi_2^k \bar{\Gamma}_1) E\{g_1 g_k^T\} + \dots + (\phi_k^k \bar{\Gamma}_{k-1}) E\{g_{k-1} g_k^T\}$$

Since $y_0 = \bar{x}_0$, and $E\{\bar{x}_k g_k^T\} = E\{y_k g_k^T\}$, it follows that the desired correlation in Eq. (3) is given by

$$E\{\bar{x}_k g_k^T\} = \phi_0^k E\{\bar{x}_0 g_k^T\} + \sum_{j=0}^{k-1} (\phi_{j+1}^k \bar{\Gamma}_j) E\{g_j g_k^T\}$$

In the implementation presented here, this representation of the correlation $E\{\bar{x}_k g_k^T\}$ is used in updating the covariance P_k as given in Eq. (2).

The correlation of the initial error state \bar{x}_0 with later values of gravity g_k , $E\{\bar{x}_0 g_k^T\}$, must be computed separately using assumptions on how the initial error state was obtained at the initial site.

In the mechanization presented here, the matrices $\phi_{j+1}^k \bar{\Gamma}_j$ are stored and updated. Certain entries of these matrices are always zero. The unmodelled INS gyro errors δw_u and accelerometer errors δa_u , contained in the extended error state, and the unmodelled external update errors δM_u , are not driven by gravity errors, and since control is never applied to them from the Kalman filter, no mixing of gravity errors is obtained by that means.

The observation used in the mechanization defined here is that the collection of weights required for propagating the covariance P_{k+1} from P_k can be obtained by updating the weights that were required to obtain P_k from P_{k-1} . This is seen as follows. The matrices needed from computing $E\{\bar{x}_k g_k^T\}$ using Eq. (3), for use in obtaining P_{k+1} from P_k as in Eq. (2), are seen to be:

$$\phi_1^k \bar{\Gamma}_0, \phi_2^k \bar{\Gamma}_1, \dots, \phi_{k-1}^k \bar{\Gamma}_{k-2}, \phi_k^k \bar{\Gamma}_{k-1}$$

The matrices that had to be used in obtaining P_k from P_{k-1} were

$$\phi_1^{k-1} \bar{\Gamma}_0, \phi_2^{k-1} \bar{\Gamma}_1, \dots, \phi_{k-2}^{k-1} \bar{\Gamma}_{k-3}, \phi_{k-1}^{k-1} \bar{\Gamma}_{k-2}$$

Now by definition,

$$\phi_j^k = \phi_{k-1}^k \phi_j^{k-1}$$

Consequently, a typical matrix $\phi_{j+1}^k \bar{\Gamma}_j$ needed for obtaining P_{k+1} from P_k can be obtained as follows:

$$\phi_{j+1}^k \bar{\Gamma}_j = (\phi_{k-1}^k \phi_{j+1}^{k-1}) \bar{\Gamma}_j = \phi_{k-1}^k (\phi_{j+1}^{k-1} \bar{\Gamma}_j)$$

However, the matrix $\phi_{j+1}^{k-1} \bar{\Gamma}_j$ was required for obtaining P_k from its own predecessor P_{k-1} .

When the matrices $\phi_{j+1}^{k-1} \bar{\Gamma}_j$ are stored from the last pass in obtaining P_k , they can be updated by multiplying by ϕ_k^k .

In the mechanization of Eq. (2), obtaining P_{k+1} requires the product $\phi_k^{k+1} E\{\bar{x}_k g_k^T\} \bar{\Gamma}_k^T$. It has been found convenient to compute $E\{(\phi_k^{k+1} \bar{x}_k) g_k^T\}$ followed by post-multiplication of the result by $\bar{\Gamma}_k^T$. As given in Eq. (3), the correlation of \bar{x}_k with g_k is given by

$$E\{\bar{x}_k g_k^T\} = [\phi_0^k] E\{\bar{x}_0 g_k^T\} + \sum_{j=0}^{k-1} [\phi_{j+1}^k \bar{\Gamma}_j] E\{g_j g_k^T\} \quad (4)$$

Consequently

$$E\{(\phi_k^{k+1} \bar{x}_k) g_k^T\} = (\phi_k^{k+1} [\phi_0^k]) E\{\bar{x}_0 g_k^T\} + \sum_{j=0}^{k-1} (\phi_k^{k+1} [\phi_{j+1}^k \bar{\Gamma}_j]) E\{g_j g_k^T\} \quad (5)$$

The matrices in square brackets in Eqs. (4) and (5) are used to obtain P_k from P_{k-1} , and can be stored.

For the iteration that generates P_{k+1} , these matrices are recovered from memory and premultiplied by the current transition matrix ϕ_k^{k+1} , and restored:

$$\begin{aligned} \phi_0^{k+1} &= \phi_k^{k+1} [\phi_0^k] \\ \phi_{j+1}^{k+1} \bar{\Gamma}_j &= \phi_k^{k+1} [\phi_{j+1}^k \bar{\Gamma}_j] \end{aligned} \quad (6)$$

If the current time interval $[t_k, t_{k+1}]$ is non-zero, then $\bar{\Gamma}_k \neq 0$, and must be stored for later obtaining P_{k+2} from P_{k+1} . If $t_{k+1} = t_k$, then $\bar{\Gamma}_k$ does not need to be stored for later updating and processing.

The update procedure indicated in Eq. (6) is performed for every iteration. If the current time increment is non-zero, the correlations $E\{g_j g_k^T\}$ are computed, pre-multiplied by the updated entries $\phi_{j+1}^{k+1} \bar{\Gamma}_j$, and summed. The result is post-multiplied by $\bar{\Gamma}_k^T$.

In order to implement the mechanization of Eqs. (2) and (3), the correlations of gravity compensation errors $E\{g_k g_k^T\}$ must be computed by a subroutine. The correlation of the initial state \bar{x}_0 with the current gravity error g_k is also required, $E\{\bar{x}_0 g_k^T\}$.

State Propagation

The discussion above has presented the covariance propagation method from the state propagation given in Eq. (1). The derivation of Eq. (1) will now be given.¹⁴

The computation of the filter state \hat{x} and the actual error state x can be described as follows. Over a non-zero time interval $[t_k, t_{k+1}]$, the filter state is propagated and, if a measurement is available at t_{k+1} , updated. Over the same time interval, the actual errors are propagated and the effects of gravity compensation errors and IMU error sources over the time interval are incorporated. At time t_{k+1} , the filter estimates are applied to the navigation indicated quantities, and the errors in the filter's estimates are combined with the plant state x . This process is defined by Equations (7) - (12) below.

The Kalman filter state is propagated over the time interval $[t_k, t_{k+1}]$ by its computed state transition matrix.

$$\hat{x}_{k+1} = \phi_k^f \hat{x}_k \quad (7)$$

For convenience, define the state x to be actual errors, not including gravity errors:

$$x = [\delta p_e \quad \delta v_c \quad \psi \quad \delta w_m \quad \delta a_m \quad \delta M_m \quad \delta w_u \quad \delta a_u \quad \delta M_u]^T$$

Over the time interval $[t_k, t_{k+1}]$ the actual errors are driven by the white noise IMU driving errors u_k and gravity errors g_k :

$$x_{k+1}^- = \phi_k x_k + F_k g_k + G_k u_k \quad (8)$$

The 3×1 gravity error vector g_k consists of the actual errors in the anomalous gravity compensation value integrated by the navigator. Between updates, only position and velocity errors are affected by the gravity compensation errors.

INS driving noises do not affect filter estimates of gravity between updates.

The external measurement recorded at time t_{k+1} is assumed to be a linear combination of actual systems errors and measurement errors:

$$z_k = H_k x_{k+1}^- + v_k, \quad H_k = \text{actual measurement matrix} \quad (9)$$

When an external measurement z_k is available, the Kalman filter assumes that z_k is a linear combination of the states that it models, according to an assumed measurement matrix H_k^f . The Kalman filter computes a gain vector K_k which it uses to update its estimate instantaneously:

$$\hat{x}_{k+1}^+ = \hat{x}_{k+1}^- + K_k (z_k - H_k^f \hat{x}_{k+1}^-) = (I - K_k H_k^f) \hat{x}_{k+1}^- + K_k z_k \quad (10)$$

Next, control is applied to the propagated state x_{k+1}^- :

$$x_{k+1} = x_{k+1}^- - C_k \hat{x}_{k+1}^+ \quad (11)$$

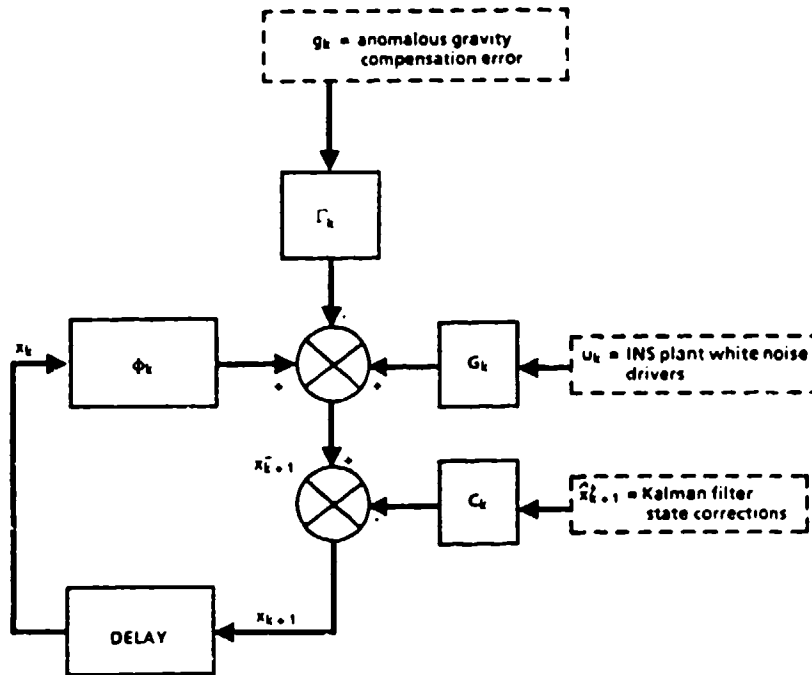


Figure 2-3 Schematic Flow Diagram for Extended Error State Propagation

$$\bar{x}_{k+1}^- = \phi_k \bar{x}_k + \Gamma_k g_k + G_k u_k : \text{ between updates}$$

$$\bar{x}_{k+1} = \bar{x}_{k+1}^- - C_k \hat{x}_{k+1}^+ : \text{ application of control from Kalman state estimate}$$

These facts enable the development of a simple propagation equation for the extended error state \bar{x}_k in the following form:

$$\bar{x}_{k+1}^- = \phi_k^{k+1} \bar{x}_k + \bar{\Gamma}_k g_k + \bar{G}_k u_k + \bar{G}_k' v_k$$

The dependence of the matrices ϕ_k^{k+1} , $\bar{\Gamma}_k$, \bar{G}_k and \bar{G}_k' on the previously defined quantities ϕ_k , ϕ_k^f , H_k , H_k^f , Γ_k , G_k , K_k , C_k and C_k^f can be shown using the familiar dual state formalism used for filter sensitivity analyses.

The propagation across an external update and reset is obtained in one expression that condenses the following steps:

A. Propagation across a time interval between updates:

$$\bar{x}_{k+1}^- = \begin{bmatrix} \hat{x}_{k+1}^- \\ x_{k+1}^- \end{bmatrix} = \begin{bmatrix} \phi_k^f & 0 \\ 0 & \phi_k \end{bmatrix} \begin{bmatrix} \hat{x}_k \\ x_k \end{bmatrix} + \begin{bmatrix} 0 \\ G_k \end{bmatrix} u_k + \begin{bmatrix} 0 \\ -\Gamma_k \end{bmatrix} g_k$$

B. Measurement formation:

$$z_k = H_k x_{k+1}^- + v_k$$

C. The filter has an assumed measurement matrix H_k^f and generates a gain K_k to incorporate the update instantaneously:

$$\bar{x}_{k+1}^+ = \begin{bmatrix} \hat{x}_{k+1}^- \\ x_{k+1}^- \end{bmatrix} + \begin{bmatrix} K_k \\ 0 \end{bmatrix} \begin{bmatrix} -H_k^f \\ H_k \end{bmatrix} \begin{bmatrix} \hat{x}_{k+1}^- \\ x_{k+1}^- \end{bmatrix} + \begin{bmatrix} K_k \\ 0 \end{bmatrix} v_k$$

D. Finally control is applied instantaneously to generate \bar{x}_{k+1} :

$$\bar{x}_{k+1} = \begin{bmatrix} \hat{x}_{k+1}^+ \\ x_{k+1}^+ \end{bmatrix} = \bar{x}_{k+1}^+ - \begin{bmatrix} C_k^f & 0 \\ C_k & 0 \end{bmatrix} \begin{bmatrix} \hat{x}_{k+1}^+ \\ x_{k+1}^+ \end{bmatrix}$$

Rewriting step C gives

$$\bar{x}_{k+1}^+ = \begin{bmatrix} I - K_k H_k^f & K_k H_k \\ 0 & I \end{bmatrix} \begin{bmatrix} \hat{x}_{k+1}^- \\ x_{k+1}^- \end{bmatrix} + \begin{bmatrix} K_k \\ 0 \end{bmatrix} v_k$$

Rewriting step D similarly, and combining it with step C and step A gives

$$\begin{aligned} \bar{x}_{k+1} &= \begin{bmatrix} I - C_k^f & 0 \\ -C_k & I \end{bmatrix} \begin{bmatrix} \hat{x}_{k+1}^+ \\ x_{k+1}^+ \end{bmatrix} \\ &= \begin{bmatrix} (I - C_k^f)(I - K_k H_k^f) & (I - C_k^f)K_k H_k \\ -C_k(I - K_k H_k^f) & -C_k K_k H_k + I \end{bmatrix} \begin{bmatrix} \hat{x}_{k+1}^- \\ x_{k+1}^- \end{bmatrix} + \begin{bmatrix} (I - C_k^f)K_k \\ -C_k K_k \end{bmatrix} v_k \\ &= \begin{bmatrix} U_{11} & U_{12} \\ U_{21} & U_{22} \end{bmatrix} \begin{bmatrix} \hat{x}_{k+1}^- \\ x_{k+1}^- \end{bmatrix} + \begin{bmatrix} v_k \\ w_k \end{bmatrix} v_k \\ &= \begin{bmatrix} U_{11} \phi_k^f & U_{12} \phi_k \\ U_{21} \phi_k^f & U_{22} \phi_k \end{bmatrix} \begin{bmatrix} \hat{x}_k \\ x_k \end{bmatrix} + \begin{bmatrix} U_{12} G_k \\ U_{22} G_k \end{bmatrix} u_k + \begin{bmatrix} U_{12} \Gamma_k \\ U_{22} \Gamma_k \end{bmatrix} g_k + \begin{bmatrix} v_k \\ w_k \end{bmatrix} v_k \end{aligned}$$

where

$$U_{11} = (I - C_k^f)(I - K_k H_k^f)$$

$$U_{12} = (I - C_k^f)K_k H_k$$

$$U_{21} = -C_k(I - K_k H_k^f)$$

$$U_{22} = -C_k K_k H_k + I$$

$$V_k = (I - C_k^f) K_k$$

$$W_k = -C_k K_k$$

This is the required form for Equation (1),

$$\bar{x}_{k+1} = \phi_k^{k+1} \bar{x}_k + \bar{\Gamma}_k g_k + \bar{G}_k u_k + \bar{G}_k' v_k$$

with

$$\phi_k^{k+1} = \begin{bmatrix} U_{11} \phi_k^f & U_{12} \phi_k \\ U_{21} \phi_k^f & U_{22} \phi_k \end{bmatrix}$$

$$\bar{\Gamma}_k = \begin{bmatrix} U_{12} \Gamma_k \\ U_{22} \Gamma_k \end{bmatrix}, \quad \bar{G}_k = \begin{bmatrix} U_{12} G_k \\ U_{22} G_k \end{bmatrix}, \quad \bar{G}_k' = \begin{bmatrix} (I - C_k^f) K_k \\ -C_k K_k \end{bmatrix}$$

Numerical computation of the terms involved in Eq. (15) is facilitated by the simple form of C_k , and the common expression $C_k K_k H_k$. If no external measurement is processed, K_k , H_k , and H_k are all 0, and this reduces the computational burden.

Implementation Considerations

Practical implementation of the covariance propagation mechanization requires a computation of gravity correlations $E\{g_k g_l^T\}$ and computation of the correlation of the current gravity error g_k with the initial state \bar{x}_0 .

There are two ways to handle the calculation of the correlations $E\{g_k g_l^T\}$. g_k is the error in the anomalous gravity value which is added to the specific force sensed by the IMU, and then integrated to solve the vehicle equations of motion between updates. g_k drives the vehicle Shuler loops. The suboptimal filter forms an estimate \hat{g}_k of this error, and uses it to generate position and velocity corrections. Two ways are available to prepare a gravity value for integration by the navigator, with a corresponding model in the Kalman filter. One is to use the ellipsoid model representation of the earth's gravity field using a central force term and a second-order spherical harmonic (J_2) correction term. In this case the error g_k is the difference between actual gravity and this approximation. The implemented filter's statistical model for gravity is then defined accordingly with state space parameters (standard deviations and dynamics) chosen to represent this error. Incorporation of gravity map data is then handled by the Kalman filter, and map data is not integrated directly by the navigator. Instead, map values are interpolated to the current vehicle position, and processed by the filter as a linear combination of its state g_k . Map interpolation error is modelled as a

measurement error. A related approach is to have gravity map values interpolated by the gravity value generator within the navigation system, with the result added to the corrected IMU measurements of specific force. In this case the gravity error g_k is the residual interpolation error. The Kalman filter must be provided with a state space model for this interpolation error. While the two approaches are closely related, differences in performance can result depending on how well the filter's state space model represents the error g_k , and different modelling sensitivities may result.

The remaining requirement for covariance propagation using Eqs. (2) and (3) is the calculation of the correlation $E\{\bar{x}_0 g_k^T\}$ of the initial state \bar{x}_0 with the current gravity error g_k . The correlation of gravity compensation errors with initial calibration errors is in general non-zero. This is because calibration errors at the initial site depend on the errors in the gravity survey errors. If the later gravity compensation errors g_k are correlated with the gravity survey errors at the site then these values will have some correlation with the initial calibration errors, and the calculation of $E\{\bar{x}_0 g_k^T\}$ must be handled accordingly. The initial calibration errors depend on the errors in the initial site survey estimate. If the gravity compensation error g_k is an error in interpolated map values, and the map interpolation error is correlated with initial site survey error, then a correlation of g_k with initial alignment would in principle have to be computed. Map interpolation errors should be relatively high frequency, with short correlation distances, so that as the vehicle becomes more distant from the initial site, this correlation is attenuated.

Correlation of the initial position errors and platform errors with gravity errors involves two groups of errors at the initial site. The first set of errors consists of the position errors at the initial site. The second group consists of the initial platform misalignments and IMU error parameters. The second group of errors depends on the quality of the initial calibration performed at the initial site. The correlations of these initial errors must be represented in computing the remaining components of $E\{\bar{x}_0 g_k^T\}$. Two questions of interest are:

1. How are calibration and alignment errors at the initial site a linear combination of errors in initial site gravity survey values?
2. How are gravity survey values at the initial calibration and alignment site correlated with gravity compensation errors applied to the navigator during later navigation?

Using the mechanization for covariance propagation defined here, however, it is possible to first estimate the rough magnitude of the contribution that this initial correlation makes to later navigation errors, since by Eqs. (2) and (3) it contributes to P_{k+1} as follows:

$$\phi_0^{k+1} E\{\bar{x}_0 g_k^T\} \bar{r}_k^T + (\phi_0^{k+1} E\{\bar{x}_0 g_k^T\} \bar{r}_k^T)^T$$

Hence a bound on the magnitude of the effect can be obtained by analysis of ϕ_0^{k+1} and $\bar{\Gamma}_k^T$ and a range of assumptions on the size on the initial correlation $E\{\bar{x}_0 \bar{x}_k^T\}$.

3.0 Post-Processing Estimation of Gravity Errors

This section presents an application of the covariance propagation approach given in Section 2.0 to the problem of estimating, in a post-processing environment, the gravity errors encountered by a test vehicle. The observables assumed available for post-processing are measurements of the error in the INS-indicated earth-relative velocity. In a land navigation scenario, velocity errors are observable when the vehicle stops. Observation of errors in indicated position may be available when the vehicle passes a surveyed checkpoint. These observables can be handled in a similar manner.

The approach taken here to post-processing of velocity data to estimate gravity errors uses least-squares estimation.²⁰ Least-squares estimation requires two sets of cross-correlations. First, the correlations between the observables and the quantity to be estimated must be computed. A mechanization of Eq. (3) enables the calculation of the cross-correlations of velocity errors at any time with a gravity quantity of interest. Second, the cross-correlations between velocity errors at the times when velocity is observed is required. These can be obtained from an application of the discrete state propagation given in Eq. (1). This second set of correlations defines the normal matrix which must be inverted for the least-squares estimation procedure. The reason that a completely recursive estimation scheme for gravity errors is not readily apparent in this case is that for the problem considered here, gravity errors are a major driver to the observables available, and they are not in general easily represented in a convenient recursive state space form. In this section, the general least-squares estimation approach is briefly sketched. Then the computations of the required cross-correlations are detailed using the quantities developed in Section 2.0.

Least-Squares Estimation Approach

Given a vector \bar{z} of m measurements, an estimate \hat{x} is to be formed of a scalar x as a linear combination of the components of \bar{z} :

$$\hat{x} = K\bar{z}$$

where

$$K = 1 \times m \text{ gain vector.}$$

In addition to the measurements themselves, the following cross-correlations are assumed known:

$$R_{zz} = E\{\bar{z}\bar{z}^T\}$$

and

$$R_{xz} = E\{x\bar{z}^T\}$$

In least-squares estimation the gain K is sought which minimizes the expected square estimate error:

$$\sigma_e^2 = E\{(\hat{x} - x)^2\}$$

According to the orthogonality principle, the gain vector K which minimizes the RMS estimate error is the one for which the resulting estimate error $\hat{x} - x$ is orthogonal to the data:

$$E\{(\hat{x} - x)\bar{z}^T\} = 0$$

The orthogonality requirement defines a linear equation to which K is the unique solution:

$$\begin{aligned} 0 &= E\{(\hat{x} - x)\bar{z}^T\} = E\{(K\bar{z} - x)\bar{z}^T\} \\ &= KE\{\bar{z}\bar{z}^T\} - E\{x\bar{z}^T\} \\ &= KR_{zz} - R_{xz} \end{aligned}$$

If the square matrix R_{zz} is non-singular, the optimal gain K is

$$K = R_{xz} R_{zz}^{-1}$$

It can be shown that the resultant mean-square error in the optimal estimate is

$$\sigma_e^2 = \sigma_x^2 - R_{xz} R_{xx}^{-1} R_{xz}^T$$

where $\sigma_x^2 = E\{x^2\}$

Thus, knowledge of the cross-correlations given above enables a calculation of the statistics of the estimate error.

This general framework can be applied to post-processing estimation of gravity quantities from IMU-derived observables. For the case of interest here, the measurement vector \bar{z} consists of a set of observations of errors in INS-indicated velocity.

$$\bar{z} = [\bar{\delta}v_{\alpha_1} \quad \bar{\delta}v_{\alpha_2} \quad \dots \quad \bar{\delta}v_{\alpha_m}]^T$$

where the velocity error $\bar{\delta}v_{\alpha_j}$ is observed at the discrete time t_{α_j} . $\bar{\delta}v_{\alpha_j}$ consists of three components of the error state \bar{x}_{α_j} defined in Section 2.0:

$$\bar{\delta}v_{\alpha_j} = H_v \bar{x}_{\alpha_j} + \bar{v}_{\alpha_j}$$

where

H_v = projection matrix

\bar{v}_{α_j} = observation error (assumed white)

In a land navigation application, the observation error for velocity involves spurious vibration effects which must be removed by averaging or some related procedure. The quantity to be estimated from this vector of measurements \bar{z} is a gravity quantity γ , such as gravity anomaly or deflection at a point of interest. Ordinarily γ would be a gravity component at a point that the vehicle has traversed.

Cross-Correlations between Estimated and Observable Quantities

The cross-correlation $R_{\gamma\bar{z}}$ between γ and the measurement vector \bar{z} requires calculating the cross-correlations between and the velocity errors δv_r at time t_r

$$E\{\gamma \delta v_r^T\}, r = \alpha_1, \alpha_2, \dots, \alpha_m$$

Since δv_r is a set of components of the error state \bar{x}_r at time t_r ,

$$\delta v_r = H_v \bar{x}_r + \bar{v}_r$$

it follows that

$$E\{\gamma \delta v_r^T\} = E\{\gamma \bar{x}_r^T\} H_v^T,$$

assuming that the observation errors \bar{v}_r are uncorrelated with the gravity quantity γ . From Eq. (1), \bar{x}_r is a superposition of gravity errors at times t_0, t_1, \dots, t_{r-1} :

$$\bar{x}_r = \sum_{j=0}^{r-1} [\phi_{j+1}^r \Gamma_j] g_j + \phi_0^r \bar{x}_0 + (\text{instrument white noise drivers})$$

Assuming that γ is uncorrelated with INS instrument noise drivers and external measurement errors, the cross-correlation of γ with the state \bar{x}_r can be written

$$E\{\gamma \bar{x}_r^T\} = \sum_{j=0}^{r-1} E\{\gamma g_j^T\} [\phi_{j+1}^r \Gamma_j]^T + E\{\gamma \bar{x}_0^T\} (\phi_0^r)^T$$

Thus, if the cross-correlations $E\{\gamma g_j^T\}$ between γ and the gravity compensation errors driving the error state \bar{x} are known, the cross-correlation between γ and the observable δv_r can be found by superposition:

$$E\{\gamma \delta v_r^T\} = \sum_{j=0}^{r-1} E\{\gamma g_j^T\} \Gamma_j^T (\phi_{j+1}^r)^T H_v^T + E\{\gamma \bar{x}_0^T\} (\phi_0^r)^T H_v^T \quad (13)$$

This enables calculation of $E\{\gamma \bar{z}^T\}$ as a concatenation of 1×3 matrices obtained by repeated application of Eq (13) for $r = \alpha_1, \alpha_2, \dots, \alpha_m$. One particular case of interest is when the quantity to be estimated is a component of the gravity compensation error g_i at time t_i .

Correlations of Velocity Observables

The calculation of the autocorrelation R_{zz} of the measurement vector \bar{z} in this case requires the calculation of m^2 cross-correlations of the form

$$E\{\bar{\delta v}_r \bar{\delta v}_s^T\} \quad \text{where } r, s = \alpha_i, \alpha_j$$

These correlations can be formed as follows. If

$$r = s,$$

then $E\{\bar{\delta v}_r \bar{\delta v}_r^T\}$ can be obtained from the covariance matrix P_r of the error state \bar{x}_r at time t_r . Since

$$\bar{\delta v}_r = H_v \bar{x}_r + \bar{V}_r,$$

it follows that

$$\begin{aligned} E\{\bar{\delta v}_r \bar{\delta v}_r^T\} &= H_v E\{\bar{x}_r \bar{x}_r^T\} H_v^T + E\{\bar{V}_r \bar{V}_r^T\} \\ &= H_v P_r H_v^T + E\{\bar{V}_r \bar{V}_r^T\} \end{aligned}$$

The computation of the cross-correlation $E\{\bar{\delta v}_r \bar{\delta v}_s^T\}$, for $s > r$, can be found by recursively maintaining and updating the correlation of $\bar{\delta v}_r$ with the error state \bar{x}_k . Computing the cross-correlation $E\{\bar{\delta v}_r \bar{x}_s^T\}$ yields the required correlation $E\{\bar{\delta v}_r \bar{\delta v}_s^T\}$ because

$$\begin{aligned} E\{\bar{\delta v}_r \bar{\delta v}_s^T\} &= E\{\bar{\delta v}_r (H_v \bar{x}_s + \bar{V}_s)^T\} \\ &= E\{\bar{\delta v}_r \bar{x}_s^T\} H_v^T \end{aligned} \quad (14)$$

The correlation $E\{\bar{\delta v}_r \bar{x}_s^T\}$ is gotten from a recursive procedure. To start the recursion, note that

$$\begin{aligned} E\{\bar{\delta v}_r \bar{x}_r^T\} &= E\{(H_v \bar{x}_r + \bar{V}_r) \bar{x}_r^T\} \\ &= H_v E\{\bar{x}_r \bar{x}_r^T\} = H_v P_r \end{aligned} \quad (15)$$

Given $E\{\bar{\delta v}_r \bar{x}_k^T\}$, the cross-correlation of $\bar{\delta v}_r$ with the state \bar{x}_{k+1} can be obtained as follows. From Eq. (1),

$$\bar{x}_{k+1} = \phi_k^{k+1} \bar{x}_k + \Gamma_k g_k + \bar{G}_k u_k + \bar{G}'_k v_k$$

it follows that

$$E\{\bar{\delta}v_r \bar{x}_{k+1}^T\} = E\{\bar{\delta}v_r \bar{x}_k^T\}(\phi_k^{k+1})^T + E\{\bar{\delta}v_r g_k^T\}r_k^T \quad (16)$$

since the noise drivers u_k and v_k form a white sequence. The second term in Eq. (16), $E\{\bar{\delta}v_r g_k^T\}$, can be computed using Eq. (13). The first term in Eq. (16) is obtained from the correlations $E\{\bar{\delta}v_r \bar{x}_k^T\}$. Equation (14) provides the required cross-correlation $E\{\bar{\delta}v_r \bar{\delta}v_s^T\}$.

Post-Processing Approach Summary

1. For the times t_{α_i} for which velocity errors δv_{α_i} are observed, compute the cross-correlations $E\{\gamma \delta v_{\alpha_i}^T\}$ using Eq. (13) for the gravity quantity γ of interest.
2. Concatenate the results of Step 1 to form the cross-correlation $R_{\gamma z}$.
3. Compute the correlations between observed velocity errors $\bar{\delta}v_{\alpha_i}$ and $\bar{\delta}v_{\alpha_j}$ using Eqs. (13), (14) and (16).
4. Assemble the 3x3 correlations matrices obtained in Step 3 to form the square correlation matrix R_{zz} .
5. Compute the optimal gain K from the inverse of R_{zz} ,

$$K = R_{\gamma z} R_{zz}^{-1},$$

and form the estimate:

$$\hat{\gamma} = K \bar{z}$$

6. Compute the expected square estimate error:

$$\begin{aligned} E\{(\hat{\gamma} - \gamma)^2\} &= E\{\gamma^2\} - R_{\gamma z} R_{zz}^{-1} R_{\gamma z}^T \\ &= E\{\gamma^2\} - K R_{\gamma z}^T \end{aligned} \quad (17)$$

The approach given above can be extended to enable inclusion of gravity survey data and position checkpoints.

Implementation Considerations

The main limitation on the general approach indicated here is that incorporation of more measurements requires the inversion of a larger normal matrix R_{zz} .

If the observables contain white noise observation errors, singularity of R_{zz} need not pose a significant problem. Selection of appropriate measurements for processing, including elimination of redundant measurements, can reduce the processing burden.

A simulation example for this estimation approach is given in Section 4.0. In the scenario considered there, it is assumed that at three locations, seven observations of velocity errors are made at 1-minute intervals. Each velocity vector observed has three components, so the square normal matrix R_{zz} involved has $3 \times 7 \times 3 = 63$ rows. In addition, it was assumed that the three components of gravity were surveyed at the initial vehicle location. For this case, matrix inversion using Cholesky¹⁹ decomposition of R_{zz} gave adequate numerical performance. Post-processing larger amounts of data can be based on the singular value techniques given in Reference (19).

4.0 Simulation Examples

The purpose of this section is to indicate how the methods described in Sections 2.0 and 3.0 can be applied to three problem areas: (1) Analysis of the effect of in-flight gravity errors on open-loop ICBM navigation performance; (2) Improvement of performance, in a land navigation application, by enhancement of an on-board filter's model for gravity map errors; and (3) Estimation of gravity errors in a land navigation test by post-processing of IMU-derived velocity observables.

The results given in this section are based on simplified instrument and environmental models under idealized scenarios. Intrinsically new numerical results are not presented here; however, results reported elsewhere in earlier work and obtained by other means are generally confirmed. Because of the hypothetical nature of the simulation results presented here, the conclusions offered at the end of this section are essentially qualitative and have been discussed elsewhere in the literature. As stated above, the purpose of the presentation of results in this paper is the illustration of the applicability of the numerical approaches derived earlier in this paper to problem areas which can be and have been addressed by other techniques in the literature. Therefore, numerical results have been obtained in normalized form suitable for illustration of the qualitative issues.

The three simulation examples are presented in the subsections below. Each example is introduced with a brief (and incomplete) survey of pertinent results presented by other authors, for the purpose of indicating how the simulation results given here confirm earlier work. The surveys of related work given below show that the simulation analyses do not demonstrate new information pertaining to gravity modelling for high accuracy navigation. The results given here do, however, indicate that the covariance analysis and post-processing algorithms presented above are potentially applicable to areas of analysis which have been thoroughly studied in earlier work.

Example 4.1 Effect of In-flight Gravity Errors

This subsection presents an application of the covariance propagation algorithm developed in Section 2.0 for the most straightforward case, in which no external updates are processed. The simulated case considered is that of an ideal IMU lofted on an ICBM trajectory through an anomalous gravity field; the topic considered in qualitative terms is the response of impact error to gravity error frequency content during open-loop navigation performed during powered flight.

The effect of gravity error modelling on CEP has been considered for a number of strategic applications by several authors. The effect of gravity errors on airborne navigation system performance has been analyzed by Bernstein and Hess⁴, Harriman and Harrison⁵, Lowrey, Pinson and Oak²², Chatfield²¹, Edwards¹, and Heller³, among others. The first two of these papers present the navigation errors induced for vehicles travelling at constant altitude and at constant velocity, using frequency domain analysis of statistical gravity models for errors at the earth's surface extrapolated to the required altitude. The paper by Harriman and Harrison demonstrated that for long-term unaided flight, the frequency content of the gravity errors near the Schuler frequency for the given vehicle speed was critical for performance. The paper by Chatfield used Monte-Carlo emulation of the Tscherning-Rapp degree variance model⁷ to predict the effects of gravity map accuracy on performance over a complex vehicle trajectory. Lowrey, Pinson, and Oak analyzed performance for an airborne application using state-space models for gravity compensation errors. They found that the frequency content of the gravity compensation errors, represented by varied correlation distance parameters in the state space model used, played a noticeable role on the effect of the gravity errors on system performance. In the paper by Edwards, aircraft and cruise missile performance was evaluated using the Edwards nested integrals technique on which the covariance analysis approach given in this paper is based. Performance predictions yielded by state space models were compared to those resulting from the Tscherning-Rapp model for vehicles with a complex trajectory.

Gravity modelling issues for strategic missile applications were reviewed by Heller³. In that paper, several different types of gravity models were presented and compared, including the Attenuated White Noise (AWN) model derived by Heller and Jordan⁸, the Sperry Three-Dimensional Algebraic Gravity (STAG) model presented by Jordan, Moonan and Weiss¹⁰, and the Tscherning-Rapp model⁷. In the paper by Heller, the normalized relative contribution of in-flight gravity errors to ballistic missile impact CEP were given for the Jordan third-order Markov gravity model⁹, the AWN model, and the STAG model. Normalized results were also presented on the effect of gravity mismodelling during navigation by a missile carrier prior to ballistic missile launch.

Numerical parameters for the AWN model were presented by Heller and Jordan from a data base of gravity survey data and satellite-derived data⁸. The gravity model used in this section for analysis of in-flight errors uses the STAG model form with normalized parameters chosen to generally agree with those given by Heller and Jordan. The parameters for the STAG model used in this paper will now be compared to those of the Heller-Jordan model. The AWN model is an analytical, spatially-defined correlation model. The AWN model for the expected value of the product of anomalous potential T at a point (X,Y,Z) with anomalous potential at (U,V,W) is, in the flat-earth approximation,

$$E\{T(X,Y,Z)T(U,V,W)\} = \frac{4D^2 \sigma_T^2 (2D+z_1+z_2)}{[u^2+v^2+(2D+z_1+z_2)^2]^{3/2}}$$

where

$$u = U-X, v = V-Y, z_1 = [X^2+Y^2+Z^2]^{1/2} - D, z_2 = [U^2+V^2+W^2]^{1/2} - D$$

D = distance parameter

σ_T^2 = anomalous potential variance

The parameters σ_T and D can be controlled to enable a fit to an empirical gravity autocorrelation function. Correlations of gravity components are gotten by differentiation of the potential covariance function, since the gravity components are obtained from the gradient of potential. A set of parameters for this model was given in the Heller-Jordan paper, shown in Table 4-1 below.

Model Component	RMS Disturbance Potential (mgal-km)	Normalized RMS Disturbance Potential	Distance Parameter D (km)
1	40100	.98	2189
2	6070	.15	1055
3	5420	.13	376
4	2300	.06	76
5	72.1	.002	10
RSS	41000	1.00	--

Table 4-1 AWN Gravity Model Parameters
(from Heller-Jordan³, 1979)

The STAG model form¹⁰ for the anomalous potential autocorrelation function is

$$E\{T(X,Y,Z)T(U,V,W)\} = \frac{\sigma_T^2}{[(1+(z_1+z_2)/D)^2 + (u^2+v^2)/D^2]^{1/2}}$$

where

u = U-X, v = V-Y, z_1, z_2 = altitude, u,v = horizontal shift distances

D = distance parameter, σ_T^2 = anomalous potential variance

A set of normalized variances was formed for a four-component STAG model following the normalized Heller-Jordan parameters in Table 4-1. Distance parameters were chosen to generally resemble those of the AWN model, except that the very low-frequency component in the AWN model is not included, since it does not model well in the flat-earth approximation. The parameters adopted for the STAG model in this paper are shown in Table 4-2.

Model Component	Normalized Anomaly RMS		Distance Parameter D (km)	
	Heller-Jordan AWN	STAG	Heller-Jordan AWN	STAG
1 (very low frequency)	.47	--	2189	--
2 (low frequency)	.11	.15	1055	500
3 (mid frequency)	.37	.37	376	180
4 (mid frequency)	.77	.87	76	35
5 (high frequency)	.18	.25	10	5
RSS	1.0	1.0	--	--

Table 4-2 Normalized Heller-Jordan AWN Model Parameters and Normalized STAG Model Parameters

The normalized STAG model parameters shown in Table 4-2 were used for a qualitative evaluation of the effect of the frequency content of gravity errors during in-flight navigation on ballistic missile performance. For the simulation, gravity errors were assumed correlated according to the STAG model parameters given in Table 4-2. The state propagation given in Equation (1) consisted of position and velocity errors driven by gravity errors only, and covariance propagation was implemented using Eq. (2). The correlations for the gravity compensation errors were mechanized in an east-north-up frame. Because the four components of the STAG model are assumed to be statistically independent, the contributions of each component can be evaluated separately. Table 4-3 shows the contribution to gravity-induced CEP when the vehicle is lofted on a ballistic trajectory. CEP is normalized because the original gravity field itself is normalized.

Table 4-3 confirms the significance of the frequency content of gravity errors on airborne navigation performance. A traditional frequency-domain analysis for the ballistic case is complicated by the fact that the significant altitude changes over the vehicle trajectory cause the driving gravity errors to be quite nonstationary over the flight. The small effect of the very highest-frequency component could have been expected, since upward continuation of high-frequency disturbances results in rapid attenuation. In general, the effect of gravity modelling assumptions on prediction of ballistic missile performance reported in Reference (3) is seen in the results presented here as well.

STAG Model Component	Normalized Anomaly RMS	Correlation Distance (km)	Contribution to Gravity-Induced CEP
1	.15	500	.31
2	.37	180	.92
3	.87	35	.24
4	.25	5	.04
RSS	1.0	--	1.00

Table 4-3 Effect of Gravity Error Frequency Content During Powered Flight on Gravity-Induced CEP

Example 4.2 Estimation of Gravity Errors by Post-Processing

This section presents an application of the gravity error estimation approached given in Section 3.0. A simulated land navigation scenario is considered in which velocity updates are processed by an inertial navigator which starts at a known initial site, navigates while travelling on land, and stops intermittently. At the stopping points, navigation-indicated earth-relative velocity is recorded. When the vehicle is stopped, actual earth-relative velocity is zero, and any nonzero navigation-indicated relative velocity value is an error signal which is a linear combination of INS errors, gravity compensation errors during travel, and observation errors induced by vehicle vibration. Hence the observed velocity errors are statistically correlated with the errors in gravity compensation used in navigating during

vehicle motion. Section 3.0 gives a means for forming least-squares estimates of the gravity compensation errors from the observed velocity errors, using the computed cross-correlations of the observables and the gravity errors at a point of interest along the vehicle ground track or elsewhere. Least-squares theory also provides a value for the RMS errors in an estimate of this kind. In this section, simulation results on the RMS performance of the gravity estimation approach developed earlier are presented.

In the idealized hypothetical scenario considered in this simulation example, the normalized four-component STAG model given in Example 4.1 is taken to represent the gravity compensation error away from the initial calibration and alignment site. The topic considered here in qualitative terms is the dependence of the quality of the gravity estimates on the distance between stopping points where velocity observations are available. The effect of the distance between stopping points has been analyzed by Huddle¹³ and others¹⁵. The applicability of inertial navigation system data to estimation of gravity errors has also been presented in the paper by Rose and Nash¹². High accuracy is obtainable for land navigation from velocity and position checkpoint data. These papers, among others, have indicated that gravity deflections and anomaly can be estimated accurately even by medium-accuracy inertial navigators if vehicle stops are frequent enough. In general terms, earlier approaches have assumed that gravity errors may be modelled as state-space processes to which optimal smoothing techniques can be applied, or else the navigator is regarded as a measuring device for observing directly the change in deflection of the vertical from the initial surveyed site. For the least-squares approach pursued in this paper, it is not necessary to assume that the gravity errors can be represented as state-space processes. An arbitrary spatially correlated model for the gravity errors can be assumed. While no new results are presented in this section, the qualitative significance of the distance between stopping points is confirmed.

The gravity model used here is the normalized model shown in Table 4-2. Table 4-5 shows the inertial measurement unit model used. This model follows the 48-state model form presented by Widnall and Grundy⁶, with additional random constant states to represent trends in accelerometer errors and gyro mass unbalance errors. These additional states were included to demonstrate that a multi-state IMU model can be utilized in the estimation approach given in Section 3.0. The important IMU contributors to gravity estimation errors in land navigation have been identified by Huddle¹³. In land navigation, the g -environment is benign, so that g^2 effects are much less significant than in the acceleration environment of ballistic missile flight. The nonlinearities were included in the model not because they are significant error contributors, but to show that a large number of IMU states can be taken into account in post-processing if necessary.

The vehicle scenario considered here begins with an initial calibration and alignment performed at a surveyed site. The vehicle then travels due east for thirty minutes to a stopping point. At the stopping point, velocity updates are processed by an on-board Kalman filter whose function is to bound navigation errors during the test, particularly altitude. Two more repetitions of the thirty minute travel period with seven minute stops are conducted. The on-board Kalman filter uses only a simple first-order Markov

Gravity Model	Parameters	Normalized CEP
AWN	See Table 4-2	.92
Third-Order Markov	$\sigma_{g1} = 47 \text{ mgal}, D_1 = 27.8 \text{ km.}$ $\sigma_{g2} = 20 \text{ mgal}, D_2 = 371 \text{ km.}$	1.0

Table 4-4 Effect of Gravity Models in Ballistic Missile CEP
(from Heller³, 1981)

State Variables	Number of Components
Position, Velocity, Attitude	9
Accelerometer bias and scale factor	6
Accelerometer and gyro input axis misalignment	9
Gyro scale factor and mass unbalance errors	15
Gyro bias	3
Accelerometer scale factor, gyro mass unbalance trends	12
Accelerometer and gyro bias trends	6
Accelerometer and gyro g errors	24

Table 4-5 INS Error States for Simulated Estimation
of Normalized Gravity Field

model for gravity errors, with normalized gravity component variances equal to those of the STAG model, and a correlation distance of thirty nautical miles for each of the three gravity components. The three sets of velocity observables at the three stopping points are utilized to estimate gravity compensation errors at points along the vehicle track using the approach in Section 3.0. The parameter varied here is the vehicle speed. The two values considered for vehicle speed are 12 kts. and 60 kts., so that vehicle stopping points are separated by 6 nmi. or 30 nmi. In principle, vehicle speed variation is not identical to change in stopping point separation, because the different vehicle speeds will change the shape of the spectrum of the gravity errors seen by the vehicle as it travels through the spatially correlated field. Hence, results identical to those presented here would not be expected if the vehicle obtained 6 nmi. or 30 nmi. stopping point separation by travelling at some other speed for a different duration than thirty minutes.

Predicted RMS errors were computed using Eq. (17) for the scenario described above. Table 4-6 shows the results obtained for this normalized hypothetical case. Gravity errors were estimated at 2-nmi. intervals along the vehicle track. Estimate accuracies are compared for gravity estimates formed from observations 30 nmi. apart and from observations of velocity at stopping points separated by 6 nmi. Generally, the characteristic shape for smoothed gravity errors presented by Huddle is seen in Table 4-6, with the largest errors in gravity estimates seen about halfway between the stopping points. Considerable estimation improvement results from processing velocity data from stopping points which are closely spaced. The results presented in Table 4-6 can be taken to be a worst case for gravity estimation accuracy, since the only reference data other than velocity is the initial site data. In addition, no path retracing or path crossovers occur for the stright-track scenario considered here, so that in this case gravity cannot be separated from IMU errors using the fact that the gravity errors are repeatable.

The simulation results given here are based on the assumption that the STAG gravity model used by the post-processing estimator is correct. As with any least-squares estimation procedure, use of statistical models which do not match actual data will result in degradation in the performance of the estimator. Significant terrain variations in the test area have the potential to degrade least-squares estimation of gravity quantities unless they are accounted for properly, as shown by Forsberg and Tscherning²³ from gravity data in the White Sands area. Since terrain variations introduce gravity errors which are, to a significant extent, deterministic if the test area topography is known, it may in principle be useful in applications to remove the effect of terrain-induced gravity errors prior to least-squares processing.

The method presented here for least-squares estimation of gravity errors can be regarded as a type of least-squares collocation estimation of gravity errors, as discussed by Moritz¹⁸. A means of computing the cross-correlations between IMU-derived observables and gravity quantities has been presented in Section 3.0. These cross-correlations are required for processing IMU-derived observables using collocation.

Distance Along Track from Start (nmi)	RMS Post-Processing Estimate Errors (% of Normalized 4-Component STAG Field)			
	Gravity Component			
	South		Vertical	
	6 nmi between stops	30 nmi between stops	6 nmi between stops	30 nmi between stops
2	4.1	6.7	2.1	6.7
4	3.9	11.0	3.2	8.9
6	3.2	13.2	2.4	9.3
8	3.2	14.1	2.6	10.2
10	3.2	13.7	2.6	12.0
12	3.2	12.3	2.4	13.7
14	3.5	10.8	2.1	15.0
16	3.7	9.8	2.1	15.7
18	3.7	9.3	2.4	15.7

Table 4-6 Gravity Estimation Performance in Post-Processing Normalized Four-Component STAG Gravity Field

Example 4.3 Performance of an On-board Gravity Model for Land Navigation

In this section, the performance of an on-board gravity model is considered for a land-navigation application. The two purposes of this simulation section are as follows. First, it is shown that the covariance propagation method presented in Section 2.0 is computationally feasible for the analysis of the performance of complex multi-state systems. Second, an application is given of the optimal estimation approach defined in Section 3.0. The method defined there is used for a preliminary evaluation of how much performance improvement could be obtained by on-board filter implementation of a more sophisticated gravity model than the one used for the simulation example. In the simplified simulation example discussed in this section, a straightforward three-state first-order Markov gravity model is assumed for the implemented filter. An idealized one-parameter STAG model, spatially correlated in east-north-up coordinates, is taken to define the correlations of the actual gravity errors which the filter attempts to model. The IMU model in Table 4-5 is utilized as shown in Example 4-2 above.

In the scenario considered here, an INS is calibrated at an initial starting point, then travels due east at 60 kts. After 30 minutes of travel, the vehicle stops and the implemented filter incorporates observations of velocity available from the fact that the actual earth-relative velocity is zero. Two additional 30-minute dashes are then performed with velocity updating at stopping points. For this hypothetical simulation case, the on-

board filter gravity model consists of a simple first-order Markov model for the along-track, cross-track and vertical gravity errors. Actual gravity errors for this simulation are assumed correlated according to a one-parameter STAG model, spatially correlated in east-north-up coordinates. The variances of the filter's along-track, cross-track, and vertical errors match those of the STAG model. This is made possible by the benign straight-track, constant-altitude vehicle scenario under which the spatial correlations of the STAG model exactly define along-track, cross-track and vertical components for state-space representation by the filter. If a curved path rather than a straight track had been assumed, an additional source of mismodelling would have been involved. Despite these considerations, the mismodelling between the filter's representation of the gravity errors and their actual correlations is quite severe in this example. The first-order Markov spectral densities do not resemble those of the STAG model. In addition, the STAG model for the actual gravity errors maintains a significant cross-correlation between along-track and vertical gravity errors, which is not represented by the on-board filter.

The topic considered in this example is the extent to which performance of the on-board filter can be improved by means of a more faithful representation, in the filter, of the statistics of the actual gravity errors. This topic is addressed using the optimal least-squares estimation approach given in Section 3.0. RMS errors predicted for the optimal estimates of INS-indicated position using the velocity data at the stopping points were computed from Eq. (17). This computation required generation of the inverse of the matrix of cross-correlations of the velocity observables, and the computation of the cross-correlation between the velocity observables and errors in the INS-indicated position. Then, the RMS errors in the on-board filter's estimates of position were computed using the covariance propagation approach defined in Section 2.0

The effects of gravity mismodelling on high-accuracy land navigation performance have been addressed in the paper by Hubbs, Pinson and Smith¹⁶. The paper by Kriegsman and Mahar¹⁷ also addresses gravity modelling issues for high accuracy land navigation. These papers present covariance analysis results on CEP and navigation errors for a high-accuracy land mobile ICBM application. They use significantly more sophisticated state-space models for gravity disturbances than the one used in this paper. These papers showed that for high-accuracy inertial navigators, gravity errors can be significant contributors to CEP and launch point errors. The paper by Hubbs, Pinson and Smith addressed the effect of mismodelling between the on-board filter gravity model implementation and the actual gravity errors. From an analysis of complex spatially correlated gravity disturbance models, they derived a state-space model which reflected a significant cross-correlation between the along-track and vertical gravity disturbance errors. They showed that if such a cross-correlation was present in the actual gravity errors, then a significant accuracy benefit can be gained by representing the cross-correlation in the on-board filter's state-space model. In their paper, accuracy improvement was seen in navigated position and indicated platform attitude, and also in impact CEP.

Table 4-7 presents a comparison of errors in position after three 30-minute travel segments of a land navigator following the scenario described above. RMS errors in the on-board filter's estimates are compared with RMS errors in an optimal estimate of position, from the same set of velocity observations at stopping points that is used by the on-board filter. The qualitative conclusion supported by Table 4-7 is that the first-order Markov implementation is far from optimal. Significant improvement in all channels is seen to result from an accurate representation of the actual gravity errors in the estimation process. However, the complexity of the state-space filter implemented gravity model that would be required to more closely approach the optimal performance has to be determined by other means. Accurate straight-track state space models for the STAG model have already been presented¹⁰ and could be reviewed. However, no state-space model suitable for on-board implementation is known which can accurately represent gravity correlations when the vehicle follows a curved path, changes altitude, or retraces or crosses over its path. Under those circumstances, the departure from optimality of on-board filter estimates can still be considered using the optimal estimation of Section 3.0, since the complexity of vehicle path does not enter into the optimal estimation approach given there. This is because the gravity correlations required for optimal estimation are computed from a position-dependent spatially correlated model, not a state space representation.

Estimation Method	Normalized RMS Errors in Position (ND)		
	Latitude	Longitude	Altitude
On-board Kalman Filter ¹	1.0	1.0	1.0
Optimal Estimate from Post-Processing ²	.4	.4	.3
1: Gravity errors modelled as first-order Markov by on-board filter 2: Gravity errors modelled optimally using one-component STAG Model			

Table 4-7 Performance of On-board Filter Estimates of Position at Third Stop vs. Optimal Estimate RMS Error

5.0 Conclusions

A numerical method for the covariance analysis of the effect of spatially correlated gravity errors on multi-state inertial navigation system performance has been presented. This method allows for unconstrained vehicle trajectories and arbitrary spatially correlated gravity models, and propagates covariances when an on-board Kalman filter with a state-space gravity model is used to process external updates and to reset the navigation state. A method for post-processing estimation of gravity errors encountered by a test vehicle has been defined. The range of applicability of the two methods was indicated in three idealized simulation examples considering topics addressed by earlier papers referenced here. The conclusion is that the general numerical approaches presented in this paper are usable for analysis of the effects of gravity errors on system performance.

References

1. R.M. Edwards, "Gravity Model Performance in Inertial Navigation", J. Guidance, Vol. 5 No. 1, Jan. -Feb. 1982
2. P.M. DeRusso, R.J. Roy, and G.M. Close, "State Variables for Engineers", John Wiley and Sons, 1965
3. W.G. Heller, "Gravitational Field Uncertainty Modeling in Aided Inertial Systems", AIAA Guidance and Control Conference, August 1981, Paper No. 81-1767-CP
4. U. Bernstein and R.I. Hess, "The Effects of Vertical Deflections on Aircraft Inertial Systems", AIAA J., Vol 14 No. 10, Oct. 1976
5. D.W. Harrison and J.C. Harrison, "A Statistical Analysis of Gravity-Induced Errors in Airborne Inertial Navigation", AIAA Guidance and Control Conference, August 1984
6. W.S. Widnall and P.A. Grundy, "Inertial Navigation System Error Models", Intermetrics, Inc., Cambridge, MA., TR-03-73, May 1973
7. C.C. Tscherning and R.H. Rapp, "Closed Covariance Expressions for Gravity Anomalies, Geoid Undulations, and Deflections of the Vertical Implied by Anomaly Degree Variance Models", Report No. 208, Dept. of Geod. Sci., Ohio State University, Columbus, Ohio May 1974
8. W.G. Heller and S.K. Jordan, "Attenuated White Noise Statistical Gravity Model", J. Geophys. Res., Vol.84 No. B9, August 10, 1979
9. S.K. Jordan, "Self-Consistent Statistical Models of the Gravity Anomaly, Vertical Deflections, and Undulation of the Geoid", J. Geophys. Res., Vol. 77, No. 20, July 1972
10. S.K. Jordan, P.J. Moonan, and J.D. Weiss, "State Space Models for Gravity Disturbance Gradients", IEEE Trans. Aero. and Elec. Sys., Vol. AES-17, No. 5, Sept. 1981
11. R.A. Nash, Jr., "The Estimation and Control of Terrestrial Inertial Navigation System Errors due to Vertical Deflections", IEEE Trans. Automat. Contr., Vol. AC-13, No. 4 Aug. 1968
12. R.C. Rose and R.A. Nash, Jr., "Direct Recovery of Deflections of the Vertical Using an Inertial Navigator", IEEE Proc. Geosci. Electron., Vol. GE-10, No. 2, April 1972
13. J.R. Huddle, "Theory and Performance for Position and Gravity Survey with an Inertial System", J. Guid. and Control, Vol. 1, No. 3 May-June 1978
14. A. Gelb, "Applied Optimal Estimation", M.I.T. Press, Cambridge, MA. 1974

15. "Proceedings of the 1st International Symposium on Inertial Technology for Surveying and Geodesy", The Canadian Institute of Surveying, Ottawa, Canada, October 12-14, 1977
16. R.A. Hubbs, J.C. Pinson, and J.M. Smith, "Residual Gravity Modelling for High Accuracy Land Navigation", AIAA Guidance and Control Conference, August 1986
17. B.A. Kriegsmann and K.B. Mahar, "J&G Effects in Mobile Inertial Navigation Systems", AIAA Guidance and Control Conference, August 1985
18. H. Moritz, "Least-Squares Estimation in Physical Geodesy", Rept. 130, Dept. of Geod. Sci., Ohio State University, Columbus, Ohio 1970
19. C.L. Lawson and R.J. Hanson, "Solving Least-Squares Problems", Prentice-Hall, Inc., Englewood Hills, N.J., 1974
20. A. Papoulis, "Probability, Random Variables, and Stochastic Processes", McGraw-Hill Book Company, New York, 1965
21. A.B. Chatfield, Jr., "Initial Estimates of the Gravity Model Contributions to Strategic Missile Errors", ASD-TR-78-30, August 1978
22. J.A. Lowrey, III, J.C. Pinson, D.G. Dethlefsen, and G.Y. Oak, "Gravity Modeling Study for Airborne Applications", AFWAL-TR-81-1139, July 1981
23. R. Forsberg and C. Tscherning, "The Use of Height Data in Gravity Field Approximation by Collocation", J. Geophys. Res., Vol. 86, No. B9, September 1981
24. D.O. Benson, Jr., "Scanning, Tracking and Mapping State Variable Estimation Algorithms", IEEE Trans. Aerosp. and Elec. Sys., Vol. AES-21, No. 4, July 1985

COMMONALITY IN THE DESIGN AND PRODUCTION
OF THE H-423 (F³) AND H-770 (F-15)
RLG INERTIAL NAVIGATION SYSTEMS

David Anderson, Program Manager
Ed Wheeler, Technical Director
Michael Hadfield, Senior Project Staff Engineer

Presented at the
Thirteenth Guidance Test Symposium

Holloman Air Force Base, New Mexico

October 6-8, 1987

HONEYWELL INC.
Military Avionics Division
Clearwater, FL
34624-7290

SOLD

ABSTRACT

Honeywell is currently under contract with the USAF to produce standard medium accuracy (F^3) Inertial Navigation Systems (H-423/HG1069D) for use on C-130 SCNS, F-4 NWDS, F-111 AMP, HH-53J, C-17, and OV-1E applications; is under contract with McDonnell Aircraft Company to design and certify an Inertial Navigation System (H-770) for the F-15 A through E models; and is also under contract with the USAF and MCAIR to produce this system for use on the F-15 A through E. This paper addresses the design commonality achieved between these two systems to minimize nonrecurring design costs and recurring procurement costs. The production and flight test status of both programs is also discussed.

1. INTRODUCTION

Honeywell is currently performing on several closely related contracts to provide the U.S. Air Force with its MIL-LINS (Military Laser Inertial Navigation System) products. These contracts include:

1. An Air Force (SNU 84-1) multi-year production contract for its F³ (Form, Fit, Function) medium-accuracy standard INUs, for initial use on: C-130 SCNS transport/cargo aircraft, F-4 NWDS fighter aircraft, F-111 AMP fighter aircraft, HH-53J helicopters, C-17 STOL transport/cargo aircraft, and OV-1E observation aircraft.
2. A McDonnell Aircraft Company (MCAIR) PS68-870204 Full Scale Development (FSD) contract to design, build, test, certify, and produce the first 50 inertial navigator units (INUs) for the Air Force F-15E aircraft.
3. An Air Force FNU 85-1 multi-year production contract to produce the first 120, and a share of the remaining INUs to be used in all Air Force F-15 A through E model aircraft.

The high degree of commonality among these three programs, and the two Honeywell INUs (F³/H-423 and F-15/H-770) that result from them, has offered significant challenges to Honeywell and benefits to the Air Force and MCAIR. This paper addresses the design commonality features and constraints involved in these efforts, and also reports on the degree of commonality achieved, as well as the INU production/performance benefits from this integrated design approach. Figures 1 and 2 show the F³/H-423 and F-15/H-770 INU exterior views, respectively.

2. BACKGROUND

Following an initial entry into the commercial aircraft market with its strapdown ring laser gyro (RLG) inertial reference system (IRS) beginning in 1978, Honeywell has expanded its role as a supplier of medium-accuracy inertial navigation systems (INSS), with increasing emphasis on military applications. Military specifications for position, velocity, attitude accuracy, fast reaction time, stringent environment requirements, 1750A computers, high order software languages, and high reliability demand a systematic, thorough approach to the design of these products in order that all specified requirements can be met. In addition, development programs of this nature have become increasingly expensive, prompting INS suppliers to design for multiple-user applications. A proliferation of earlier, unique INSS within the user community has resulted in high logistics costs, which are also no longer tolerable. Therefore, commonality has become a desirable requirement for both suppliers and users.



Figure 1. F³/H-423 INU with Top Cover Removed

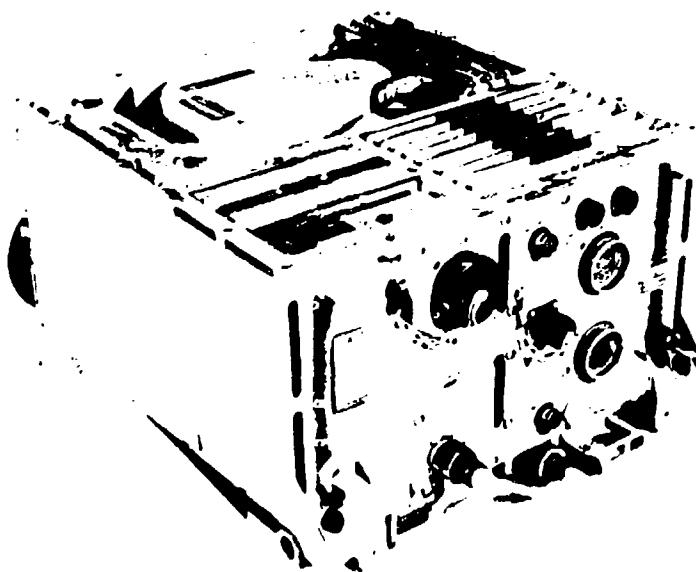


Figure 2. F-15/H-770 INU with Top Cover Removed

To meet this challenge, Honeywell launched a design and development program in 1983 with the goal of developing a number of common system "building blocks" encompassing both hardware and software functions and features. In this approach, development resources are expended only once for a specific, common building block, but several products can evolve from the basic design. Honeywell has used this design technique in the development of its MIL-LINS product family. From this common production line, Honeywell now delivers not only the USAF F³ (H-423) and F-15 (H-770) INUs, but also the U.S. Army Modular Azimuth Positioning Systems (MAPS), and the Swedish JAS 39 Gripen inertial systems.

Key milestones that have been met by Honeywell's F³ and F-15 development programs are:

- o 1983 -- ENAC 77-1 to SNU 84-1 redesign kickoff
- o 1984 -- MCAIR contract award for full-scale development of an H-770 RLG INS/INU for F-15 A through E aircraft
- o 1985 -- CIGTF Type I test completion for Standard F³/H-423 INU
- o 1985 -- USAF contract award for production of F³/F-15 INUs
- o 1986 -- First USAF flight test of an SNU 84-1-compliant INU
- o 1986 -- First flight of an RLG INU designed for F-15 aircraft
- o 1986 -- First FNU 85-1-compliant H-770 RLG INU delivery to CIGTF
- o 1986 -- First F³/H-423 RLG INU delivery to USAF
- o 1987 -- First SNU 84-1 production H-423 INU delivery to USAF.

3. BASIC INU FUNCTIONAL CONSIDERATIONS

Four functional elements exist in the design of a typical navigation unit, as illustrated in Figure 3 -- a simplified INU functional block diagram. They are (numbers coded to the diagram):

1. Inertial measurement function (gyros, accelerometers, supporting electronics, and mechanical structure)
2. Data processing function (for high-speed inertial sensor data/compensations, as well as lower-speed -- but more memory intensive -- navigation and input/output computations)
3. Signal data bus/analog and discrete interfaces with other vehicle avionics
4. Electrical power inputs and physical system interfaces/-characteristics.

Inertial measurement, and portions of the data processing function, can be invisible to an individual system user, and so offer excellent opportunities for commonality as long as they support the full range of performance requirements. However, the signal data, electrical power, and physical interfaces/-

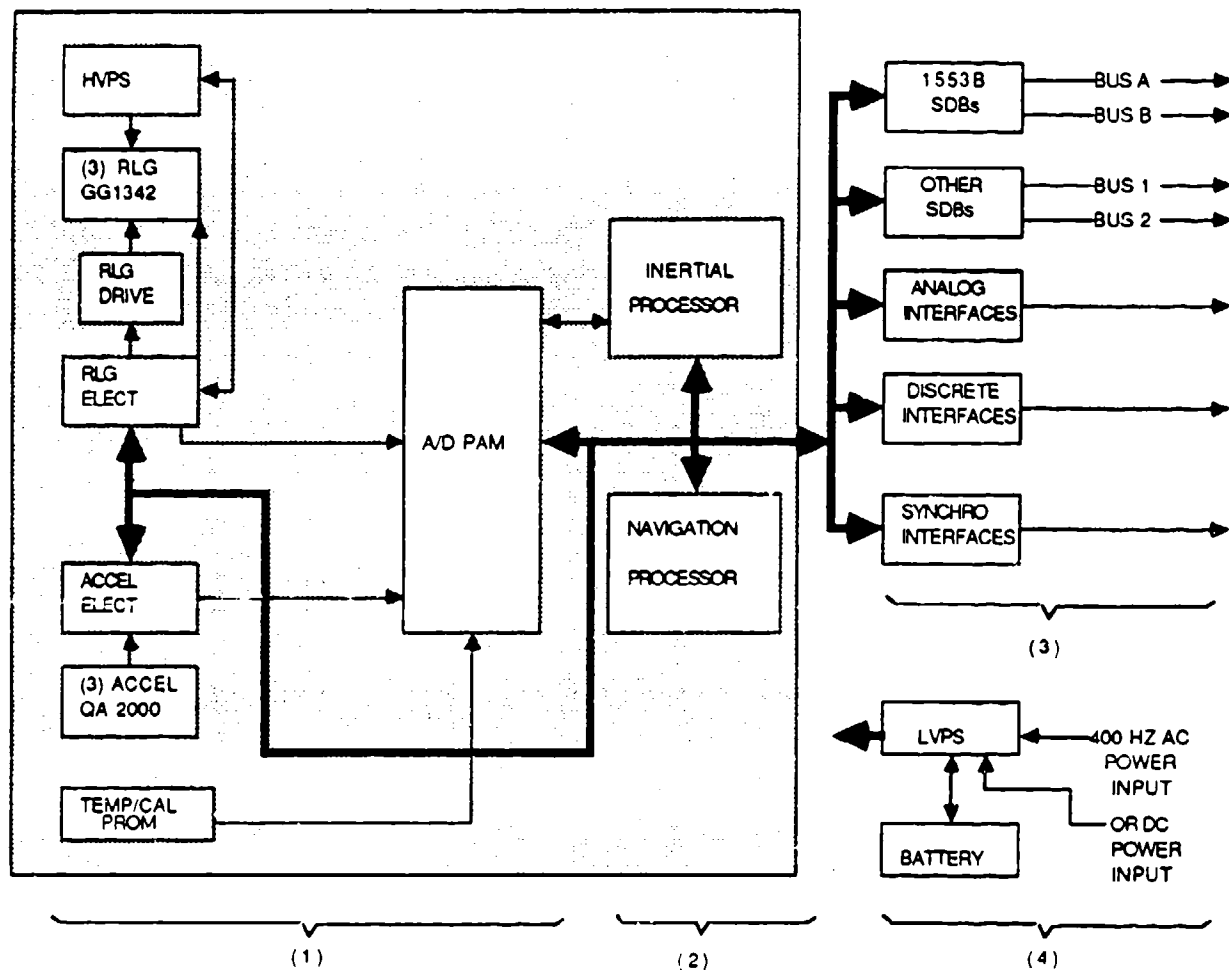


Figure 3. Simplified INU Functional Block Diagram

characteristics can be user- or application-specific, and hence present more problems in achieving commonality.

4. F³ AND F-15 INU REQUIREMENTS COMPARISONS

Before detailed H-423/H-770 INU design was begun, a significant effort was expended to generate a requirements matrix that encompassed both Standard (F³) and F-15 programs. The bases for these requirements originally were the SNU 84-1 and MCAIR PS 68-870204 specification documents, respectively. The MCAIR document was later incorporated into an Air Force specification, FNU 85-1, for USAF control of all F-15 INS requirements. A summary of this requirements comparison for performance, physical, and interface characteristics is provided in Table 1.

Table 1. F³/F-15 Requirements Comparison (1 of 2)
(Full Performance Levels Only)

Performance Characteristics		SNU 84-1 (F ³)	FNU 85-1 (F-15)
o Positioning Accuracy (@ one hour)			
GC Align			
240 seconds	NA	0.8 nmi/hr CEP	0.8 nmi/hr CEP
480 seconds			0.8 nmi/hr CEP
Stored Heading			
30 seconds	NA	NA	1.0 nmi/hr CEP
90 seconds		0.8 nmi/hr CEP	NA
o Velocity Accuracy			
GC Align			
240 seconds	NA		2.5 ft/sec rms
480 seconds		2.5 ft/sec rms	2.5 ft/sec rms
Stored Heading			
30 seconds	NA		2.66 ft/sec rms
90 seconds		5.0 ft/sec rms	NA
o Level Attitude Accuracy			
GC Align			
240 seconds	NA		0.033 deg rms (D)
480 seconds	NA		0.066 deg rms (S)
Stored Heading			
30 seconds	0.05 deg rms (D)		0.033 deg rms (D)
	0.067 deg rms (S)		0.066 deg rms (S)
90 seconds			
	NA		0.033 deg rms (D)
	NA		0.066 deg rms (S)
	0.1 deg rms (D)		NA
	0.1 deg rms (A)		NA
o Heading Accuracy			
CG Align			
240 seconds	NA		0.05 deg rms (D)
480 seconds	NA		0.5 deg rms (Mag)
	0.1 deg rms (D)		0.05 deg rms (D)
	0.2 deg rms (Mag)		0.5 deg rms (Mag)

Table 1. F³/F-15 Requirements Comparison (2 of 2)

Other Characteristics		SNU 84-1 (F ³)	FNU 85-1 (F-15)
o Reliability (MTBF-hrs)		4600 (AIT)	2250 (AUF)
o Maintainability (MTTR)		0.5 hr	1.25 hr
- Organizational Level			
Physical and Interface Characteristics:		RT/BC	RT Only (F-15E Aircraft)
1553-1 SDB		RT	NA
1553-2 SDB		Read on CMD, 0-5V TTL Output	NA
Boresight		NA	RT Only (F-15 A-D Aircraft)
H009 SDB		NA	RT/BC (F-15 A-D Aircraft)
NCI I/F		NA	Xmit Only
Radar Data Bus			
Analog Signals:			
Synchros			
Roll			
Pitch			
Mag Hdg			
Discretes			
D/A			
INU Form Factor (Size-inches)		Two Channel (Z Leg Gnd)	Two Channel (Bal)
INU Weight		Two Channel (Z Leg Gnd)	Two Channel (Bal)
INU Power*		One Channel (Z Leg Gnd)	NA
		13 Input/8 Output	15 Input/10 Output
		NA	(3) 10V Bipolar
		18.1L, 7.6H, 7.5W (3/4 ATR)	15.4L, 8.8H, 13.6W
		48 lbs (INU only)	(Same as ASN-109)
			62.5 lbs (w/Battery)
ac		1 Phase, 115V, 400 Hz, 28C VA	3 Phase, 115V, 400 Hz,
dc		28V, 240W, Max	180 VA
			Internal Battery

*No heater power or warm-up required

Abbreviations:

3AL -- Balanced (Active Z Leg)
 BC -- Back-up Bus Controller
 D -- Digital Output
 GND -- Ground

RT -- Remote Terminal
 S -- Synchro Output
 VA -- Volt Amperes

5. COMMONALITY DESIGN AND PRODUCTION CONSIDERATIONS

System Architecture. In establishing its system design concepts for F³ and F-15, Honeywell partitioned a typical INU into the four functional elements of inertial measurement, data processing, signal input/output (I/O), and power/physical features. The data processing function included all required executive, sensor data compensation and preprocessing, navigation, guidance, steering, and BIT functions; and a unique input/output element designed for each application. This approach allowed a large portion of hardware and software for each INU to be identically designed, fabricated, and tested, because inertial measurement and many of the computing elements were common to a great extent, and invisible to the external user. The I/O element and specialized system software tailored the outputs of these common elements to meet each user's needs. This mechanization approach was consistent with the functional diagram shown in Figure 3.

Common Assembly/Subassembly/Software Module Definition. Based on the functional partitioning described above and the requirements specified in Table 1, design decisions were made to define the common hardware and software functions and/or modules. The common module design goals for F³/H-423 and F-15/H-770 are provided in Table 2.

Design Groundrules. To further focus the design activity and address recurring cost issues, a number of design groundrules were established and controlled by a "Commonality Design Control Board," ensuring adherence to both commonality and specific program goals. These groundrules addressed those items most likely to increase system material, build, test, and support costs, rather than the detail specifics of the electrical and mechanical designs. A top-level summary of the groundrules and objectives of each element are:

- o Maximum utilization of common parts

- Reduces nonrecurring costs for source control drawings, and specification control drawings; as well as recurring costs for receiving inspection, component testing, etc.
- Allows material price reduction due to increased procurement quantities
- Reduces test equipment capital costs by minimizing types of parts to be tested

- o Maximum use of common mechanical designs/materials

- Reduces hardware proliferation (connectors, mounting hardware, potting/coating materials, wire/insulation, etc.)
- Minimizes number of material and process specifications
- Reduces variety of production tooling, layouts, procedures
- Reduces hardware inventory costs for assembly hardware

Table 2. F³/F-15 Commonality Design Goals

- o Ring Laser Gyroscopes and accelerometers with identical error budgets and designs
- o Inertial Sensor Support Electronics -- identical designs
 - Gyro electronics
 - Accelerometer electronics
- o Inertial Sensor Assemblies -- identical designs
 - Sensor mounting base
 - Inertial sensors (3 Honeywell GG1342 RLGs and 3 Sundstrand QA2000 accelerometers)
 - High voltage power supply
 - Temperature sensing/calibration memory
- o Dual computers -- identical designs for F³/F-15 IPs as well as F³/F-15 NPs
 - One high speed 1750A compliant processor with 32K EPROM and 16K RAM dedicated to front end, high speed inertial sensor data processing and compensations
 - One generalized 1750A compliant processor with expanded memory for navigation, guidance, I/O, and other user specific functions
- o Common Electronics -- similar designs, except A/D-BIT which are identical
 - Analog-digital conversion/built-in test functions
 - 1553B multiplex data bus
 - Analog synchro and discrete inputs/outputs
- o Low Voltage Power Supplies -- similar designs
 - Some common subassemblies
- o Software
 - Inertial processing -- identical
 - Alignment processing -- similar
 - Navigation processing -- similar
 - Attitude processing -- similar
 - BIT processing -- similar
 - Input/Output processing - similar

items (screws, washers, etc.) by limiting different types, sizes, metal grades, etc.

- o Maximum use of common software elements

- Minimizes nonrecurring software design costs
- Reduces verification costs
- Reduces documentation scope and costs
- Improves maintainability/configuration control

- o Common production test procedures

- Allows use of common test equipment
- Reduces test software generation
- Reduces support requirements due to common procedures (Product Assurance, Reliability, CAE, TE Repair and Maintenance, etc.)
- Reduces personnel training costs

- o Electrical designs for user-defined I/O and power supplies will be as similar as possible

- Provides common parts advantages
- Reduces Design Engineering support required for I/O and power supply designs
- Reduces test equipment requirements.

6. SUBASSEMBLY AND MODULE COMMONALITY ACHIEVEMENTS

Despite the differences between the INUs required for F³ and F-15, Honeywell has succeeded in its efforts to generate common INU "building blocks" that can be applied to both programs. Requirements differences between the systems have been accommodated without compromising the basic premises on which the commonality effort was established.

This section provides a description of the commonality shared between Honeywell's H-423 and H-770 systems (reference to Figure 3 will be helpful in understanding the subassembly functions). Unless otherwise noted, all subassemblies are form, fit, and functionally compatible. Those indicated as identical have the same part numbers.

- o Inertial sensors (identical): Based on a composite error budget defined for F³ and F-15 aircraft mission requirements, Honeywell chose a common set of inertial components for both applications. The inertial component set includes three Honeywell GG1342 RLGs and three Sundstrand QA2000 Accelerometers. These sensors have a long history of excellent performance in similar applications, meet all required performance criteria, have proven reliability, and are sufficiently compact to be packaged in a sensor triad that can be used in several different INU chassis configurations. Both types of

sensors require external support electronics, which are also common to F³ and F-15.

- o Inertial sensor assembly (identical at ISA level): Externally induced, high-speed motion -- both linear and rotational -- can give rise to significant system level errors in strapdown systems. Many of these error sources can be minimized through conservative mechanical design of the sensor mounting base, sensor assembly isolation system, and INU chassis. Due to the many different user environmental specifications and their impacts on system mechanical design, Honeywell designed a common sensor assembly base for all programs. Each user program then defines its own isolation system, the isolation system's natural frequency, and a mounting technique for ISA/INU chassis attachment. This approach permits high-volume procurement and build of ISA subassemblies (e.g., the mounting base, wiring harnesses, and some attachment hardware), yet allows user flexibility and prevents excessive nonrecurring sensor base design activity. A fully loaded ISA contains three RLGs, three accelerometers, a high voltage power supply (HVPS), a temperature sensing/calibration programmable read-only memory (Temp/Cal PROM), and associated harnesses.
- o Inertial sensor support electronics (identical): To provide the required secondary voltages and signal processing circuitry necessary to condition gyro and accelerometer outputs for use by other system electronics, four shop replaceable units (SRUs) were defined as part of the common baseline. These subassemblies include the gyro electronics, gyro drive electronics, HVPS, and the accelerometer electronics.
 - Gyro electronics (identical): The gyro electronics SRU contains all signal conditioning circuits necessary to convert RLG outputs to pulses, which can be counted by an accumulating device located on a separate SRU -- the analog-to-digital converter pulse accumulator module (A/D PAM).
 - Gyro drive electronics (identical): Several circuits used to condition and operate RLGs require relatively high voltages. These can couple into sensitive signal conditioning circuits and reduce noise immunity. To minimize this possibility, all circuits requiring voltages higher than +/-15 Vdc are partitioned on separate circuit boards.
 - HVPS (identical): Ignition and maintenance of the gas discharge required for RLG operation requires voltages in excess of 3500 Vdc. Due to the inherent packaging problems associated with these voltage levels, the need to minimize transmission of these supply voltages within the system, and obvious commonality implications, the HVPS was designed as a common element, and is mounted on the ISA. The HVPS provides both starting and running voltages to all three RLGs, controls and monitors discharge current in each

sensor independently, and provides certain lower voltages and signals for use by the gyro electronics assembly.

- Accelerometer electronics (identical): The Sundstrand QA2000 accelerometer operates by nulling an internal seismic proof mass pendulum with a restoring force/torquer coil current proportional to the input G-level. This torquing current is brought out of the accelerometer and converted to a voltage on the accelerometer electronics assembly. This voltage serves as the input to a digitizing circuit. The Accel Elex card operates as a three-channel, high-precision, voltage-to-frequency converter, generating pulses whose quantity over a fixed time interval represent average acceleration during that interval.
- o Inertial processor (IP) (identical): This 1750A-compliant processing element based on the Fairchild F9450 microprocessor, is equipped with 32K words of EPROM memory, 16K words of random access memory (RAM) (expandable to 48K), a direct memory access (DMA) controller for interprocessor communications, and I/O for input processing of inertial data. The IP is a high-speed preprocessor for the navigation processor (NP), inputting and operating on inertial data at a 1200 Hz rate. The IP is programmed in 1750A assembly language.
- o Navigation Processor (identical): This 1750A-compliant computer is also based on the F9450 microprocessor, but was designed for more general uses. The NP is equipped with 32K words of EPROM memory, 48K words of RAM memory, and extensive I/O capability, including provisions for various wait states to permit interface devices operating with different response times. The NP also has a four-channel DMA interface that is currently used for IP/NP and test set communications. The NP is programmed in Jovial higher order language.
- o Support electronics (identical): To reduce operating overhead for the system computers, additional electronics are included in the INU. These SRUs do preprocessing of various data, and store it for future use by the system computers. This permits the processing elements to access the data at a time best suited for its use. The two support electronics assemblies are the A/D PAM and the Temp/Cal PROM.
- A/D PAM (identical): The A/D PAM contains all analog input circuitry. It incorporates an input multiplexer to provide analog input channels, and a RAM buffer to hold all conversions for the respective processor. Additionally, this SRU contains pulse accumulation functions, implemented as LSICs, that accumulate digitized inertial data and store it for future processor access. The A/D PAM also provides a number of system clock signals, and has input and output discrete interfaces for internal INU control and built-in test functions.

-- Temp/Cal PROM (identical): This SRU incorporates electronics that condition signals from temperature sensors within each inertial component for use by the A/D PAM. In addition, the board includes an EEPROM that can be loaded with sensor and system calibration constants. The Temp/Cal PROM is mounted on the ISA, allowing each ISA to contain its own calibration data, and providing interchangeability between systems. The calibration memory is also used to store mission-critical performance data for future use (waypoints, steerpoints, BIT history, miscellaneous parameters, etc.).

- o LVPS (similar): Due to differences in input power specified for the INU in F³ and F-15 applications, the two supplies are not interchangeable. Despite their minor electrical and physical differences, however, the two supplies are very similar in overall electrical design, and share a number of common elements. Each supply incorporates a transformer/rectifier section, an EMI filter input section, a boost regulator section, and a dc/dc converter section, plus additional control and BIT circuits.
- o IP software (identical): A compilation of all user performance requirements and environmental exposures was used to define expected strapdown error sources, magnitudes, compensation techniques, high refresh rate outputs, and output filtering requirements. Based on these requirements, one version of IP software was developed to incorporate high-speed dynamic sensor compensation, high-speed attitude and velocity generation, and a precision attitude reference. Additionally, this software package incorporates a communications function for passing data to/from the NP, and has embedded BIT functions.

This software package also contains a "down-load" feature that permits excess memory on the IP board to be used for NP program storage. This function executes at system power-up, and can increase NP non-volatile program storage by approximately 6000 words.

- o NP software (similar): Due to differences between H-423 and H-770 aircraft interfaces, message structures, and mission requirements (INU aiding, in-flight alignment, interrupted align, etc.), system NP software was generated independently. Despite this unique tailoring of the NP software for the two programs, a number of functions remain common, including power up, power down, sensor thermal compensation, IP/NP download, and baro-altitude loop algorithms.

7. F³/H-423 (SNU 84-1 COMPLIANT) INU TECHNICAL DESCRIPTION

The H-423 Navigation Set consists of two line replaceable units (LRUs):

- o HG1069D INU
- o WG1021C Mount.

The HG1069D INU conforms to the form, fit, and function requirements of SNU 84-1, and has been dubbed an F³ INU. It is designed to operate with a control display unit (CDU) over a MIL-STD-1553B data bus network. The interface and software will accommodate either a general avionics or a dedicated CDU mechanization. The INU is a self-contained unit that interfaces with the mount and the aircraft electrical and cooling provisions. Figure 4 illustrates the general INU configuration, and the locations of plug-in SRUs.

The front of the INU chassis contains the locking handle, an alignment receptacle, a MIL-C-38999 Series 1 test connector (J1) and cap, the INU elapsed-time indicator, and two fault-ball BIT indicators. At the rear of the INU chassis, two MIL-C-83733 connectors are provided in accordance with SNU 84-1. These connectors mate with the aircraft avionics harness connectors, which are mounted on the rear vertical surface of the INU mount for the system input/output interface. Two support pin receptacles are located at either side, on the lower rear of the INU chassis. These mate with the rear alignment pins on the INU mount.

Cooling air enters a plenum area in the mount and passes into the INU through two ports on the unit's bottom surface. The cooling air is passed through two sealed heat exchangers in the side walls of the chassis, and exits at the rear of the chassis on either side.

As shown in Figure 4, the HG1069D INU consists of the following major subassemblies:

- o Inertial sensor assembly
- o Ten multilayer plug-in circuit card assemblies (CCAs)
- o Low voltage power supply (LVPS)
- o The chassis
- o Master interconnect board (MIB) and cabling subassembly
- o Top cover
- o Bottom cover.

The ISA is located in the forward compartment of the INU chassis with access provided by removing the top cover. Alignment pins ensure accurate and repeatable positioning within the chassis. This feature permits removal and replacement of the ISA without recalibration, because all alignment critical factors are pre-calibrated to the alignment pins, with the associated parameters stored in the ISA EEPROM.

The electronic circuit card bay is located in the rear compartment of the chassis, accessed by removing the top cover. Eight CCAs are located in this section, and plug into the MIB. Two additional CCAs are located in the bottom compartment of the chassis, with access provided by removing the bottom cover.

The LVPS module and power input section is located at the rear

H-423 INU

0185-125

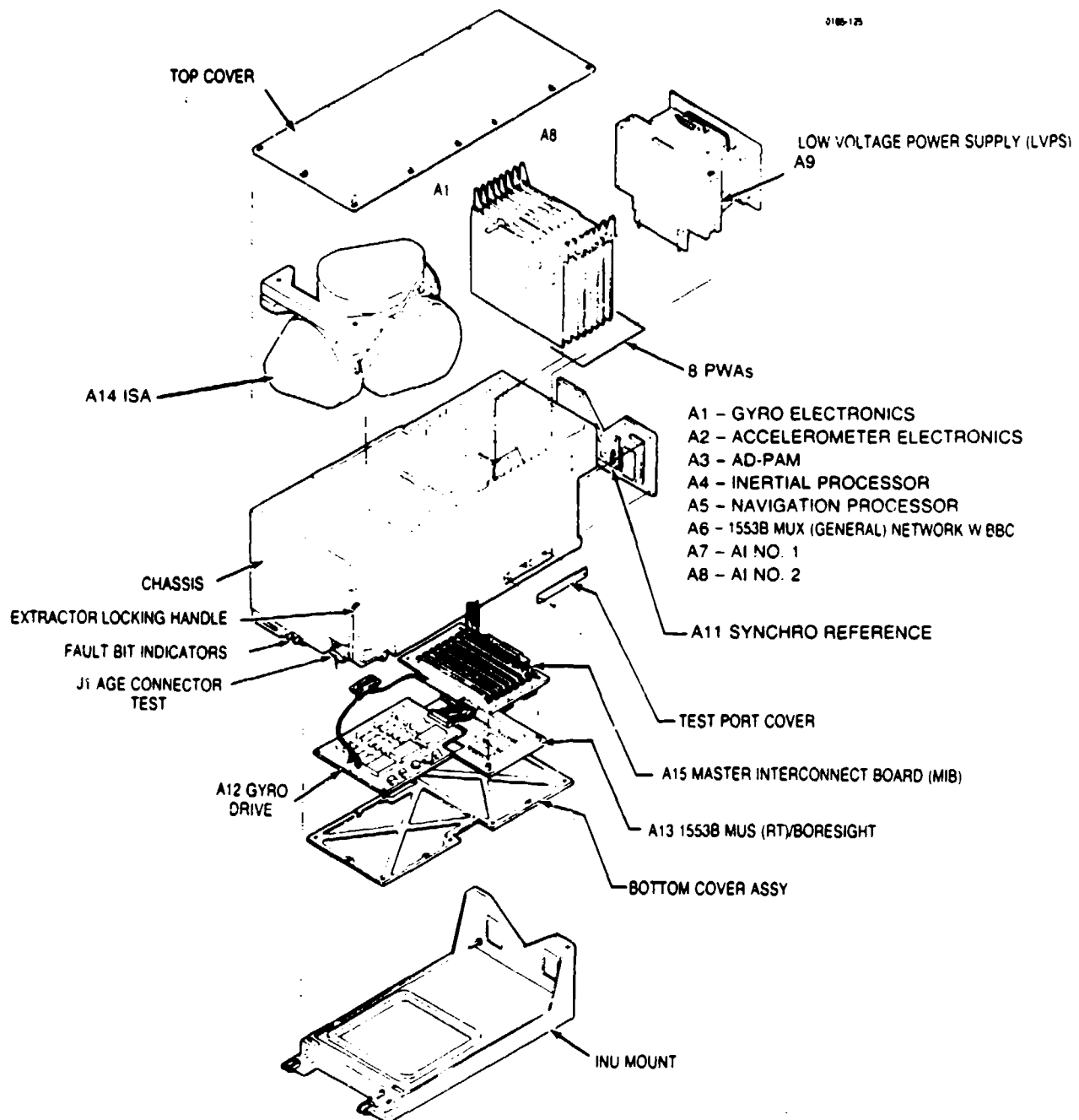


Figure 4. Honeywell F³/H-423 INU -- Exploded View

of the chassis. The LVPS is a plug-in module that engages the MIB. Access is provided by removing the top cover. Additional structural support is provided by four side-mounted bolts. The LVPS module provides EMI shielding from the CCA card bay. The power input section isolates the LVPS and CCAs from the aircraft input power sources with transformers and filters.

Figure 5 is a general diagram showing primary H-423 interfaces.

The primary interface for the HG1069D INU with other avionics systems is over one of the two MIL-STD-1553B dual-multiplexed data bus networks. A CDU in the avionics is the entry point for such data as mode selection and initial position. The CDU also displays navigation, steering, and performance parameters from the INU. The 1553 bus interfaces are normally controlled by an aircraft central computer (or master bus controller). The INU acts as a remote terminal (RT) on both the primary and backup buses. If required by aircraft configuration or master bus controller failure, the INU will perform the task of backup bus controller for direct data transfer between the INU and other avionics subsystems on Network 1. Network 2 1553B MUX bus channels operate only in the RT mode.

The H-423 INU provides analog and discrete interface signals for aircraft cockpit instrumentation and displays. Buffered synchro outputs of roll, pitch, and heading, as well as validity signals, are provided for attitude display indicators and autopilot usage. Analog outputs of computed course deviation, relative bearing, magnetic heading, and range to destination are output to the aircraft horizontal situation indicators.

8. H-770 (FNU 85-1 COMPLIANT) INU TECHNICAL DESCRIPTION

Honeywell's H-770 RLG INU was designed for compliance to the MCAIR PS68-870204 and USAF FNU 85-1 Specifications. These documents specify complete INU interchangeability for five different models (A through E) of the F-15 aircraft.

The H-770 is a self-contained INU equipped with a 28 Vdc battery for protection against aircraft ac power outages. Mechanically, it interfaces directly with the INU mount, where it is attached with two mounting bolts, receiving cooling air from a plenum assembly that is part of the mount. The H-770 (also known as the AN/ASN-147) conforms to the same general form factor as the predecessor ASN-109, and has been shown to be compatible with all existing F-15 A through D models using existing mounts and cabling. All electrical connectors are mounted on the front panel of the INU. All F-15 INUs use 3-phase, 115 Vac input power, which is conditioned by the INUs LVPS. In addition, the INU front panel incorporates an elapsed-time indicator and mechanically resettable fault indicators -- one each for the INU and battery.

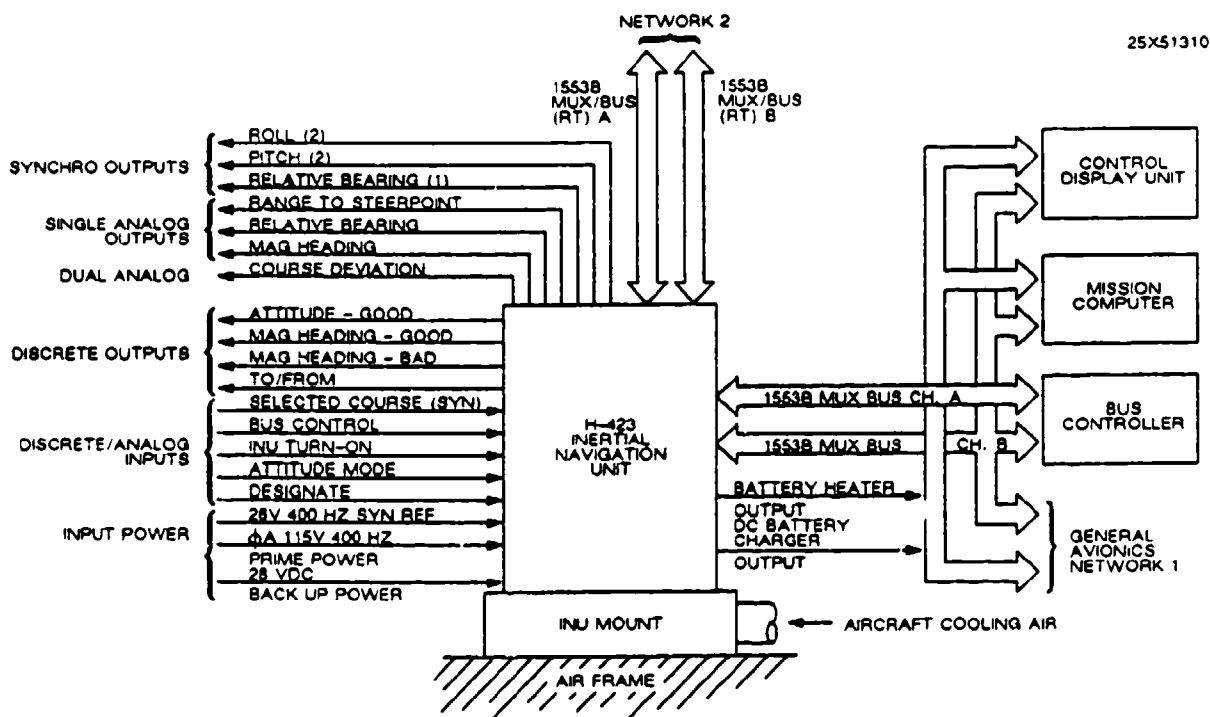


Figure 5. Primary F³/H-423 Interfaces

The exploded view in Figure 6 shows the cast aluminum chassis, and the relative locations of the plug-in subassemblies, the battery assembly, and connectors. The H-770 chassis layout differs from that of the H-423 INU in response to FNU 85-1 requirements for mount, cooling air, and connector interfaces. Chassis SRU location differences necessitated a two-section MIB to which the CCAs, LVPS, and ISA connect via plug-in interfaces. The external connectors used on the H-770 are of a different configuration than those used on the SNU 84-1 (H-423) system, and are located on the front panel, as specified in FNU 85-1.

As shown in Figure 6, the chassis contains the following plug-in SRUs:

- o Inertial sensor assembly
- o Nine circuit card assemblies
- o Three low voltage power supply assemblies
- o Battery pack assembly.

Commonality of SRUs used in the H-770 INU with those in the H-423 INU includes:

- o (A1) gyro electronics
- o (A2) accelerometer electronics
- o (A3) navigation processor

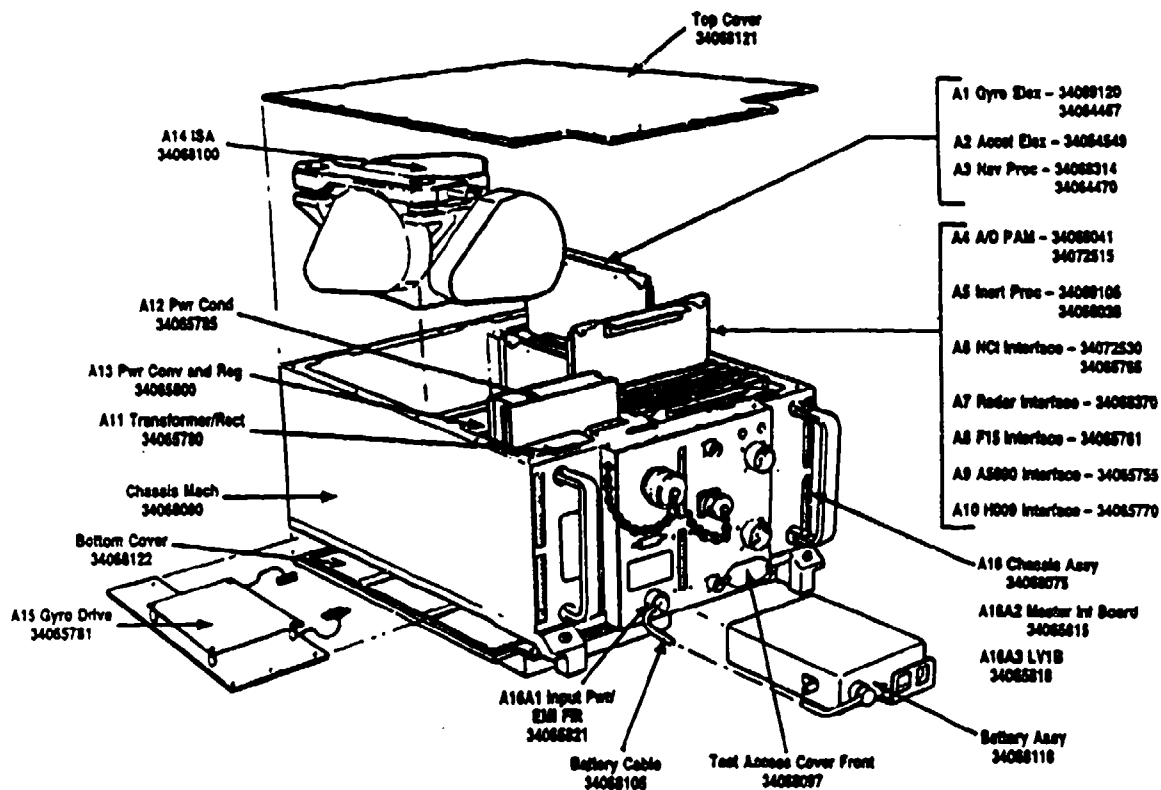


Figure 6. F-15/H-770 INU -- Exploded View

- o (A4) A/D PAM
- o (A5) inertial processor
- o (A14) ISA.

Replacing the two 1553B MUX CCAs used for the SNU 84-1 (H-423) are four bus interface CCAs:

- o (A6) NCI Bus Assembly
- o (A7) Radar Bus Assembly
- o (A9) 1553B MUX Assembly
- o (A10) H009 Bus Assembly.

The unique F-15 analog/discrete interface specified in FNU 85-1 has been configured through modification of the H-423 system/-analog interface card No. 1. The F-15 version is designated as (A8) F-15 interface.

The H-770 LVPS is a repartitioning of the H-423 LVPS and transformer rectifier, with an enhanced battery charger circuit. Three plug-in SRUs are used for the LVPS in the H-770:

- o (A11) transformer rectifier
- o (A12) power conditioner
- o (A13) power converter.

Some of the LVPS subassemblies are common to the H-423 and the F-15.

When installed on F-15 A through D models, the H-770 INU operates with three data buses and a variety of discretes used for communication and aircraft subsystem control. These interfaces are shown in Figure 7, as are those for F-15E installation. The A through D model interfaces are:

- o Central Computer (CC) communication -- accomplished over the H009 bus, a predecessor to MIL-STD-1553B. This 1.0 MHz serial data bus is implemented using dual redundant buses that include differential, transformer-coupled clock and data lines. Data is transmitted and received synchronously, based on the transmitted 1.0 MHz clock, and is refreshed at rates of up to 200 Hz, depending on requirements.
- o A second, transmit-only-upon command H009-type bus provided for direct interface with the Hughes APG 63 radar set. The radar bus differs slightly from H009 operation by using a "data initiate" discrete to signal beginning and end of data transmit periods. This bus is refreshed at a 200 Hz rate to allow sufficient bandwidth for radar motion compensation.
- o A third interface, for the navigation control indicator (NCI) -- a back-up bus that allows INU/NCI communication when the CC is not functioning. For normal operation, the CC and NCI communicate on the H009 bus, and the INU is only a listener. During CC NO-GO modes, the INU can become the NCI bus controller and the key pilot interface for INU moding, data entry, and control. This interface can also provide a number of miscellaneous parameters that can be inspected by the pilot and/or maintenance personnel for assessment of INU performance or checkout of indicated failures. The NCI back-up bus is updated at a 5.0 Hz rate by INU software.
- o Analog (synchro and discrete) interfaces for A-D models, including: redundant roll and pitch synchro channels for use by aircraft indicators; a set of low-power attitude synchro outputs for use by the flight control system; a number of validity discretes for disabling use of INU data during periods when data is not available or when an INU failure has occurred; and several other control discretes that indicate NCI status (GO vs. NO-GO), nose gear status (up vs. down), and fault indicator output discretes for visual indication on master caution/warning panels and avionics status panels.

The H-770 INU has a slightly different set of interfaces when installed in an F-15E aircraft. Due in large part to the implementation of the MIL-STD-1553B bus (with the INU operating as an RT only), INU/avionics interfaces on the F-15E Dual Role Fighter are streamlined significantly. In this application of the H-770, the H009 and NCI buses are not connected, and remain dormant. All CC communication is done via the 1553B bus, and

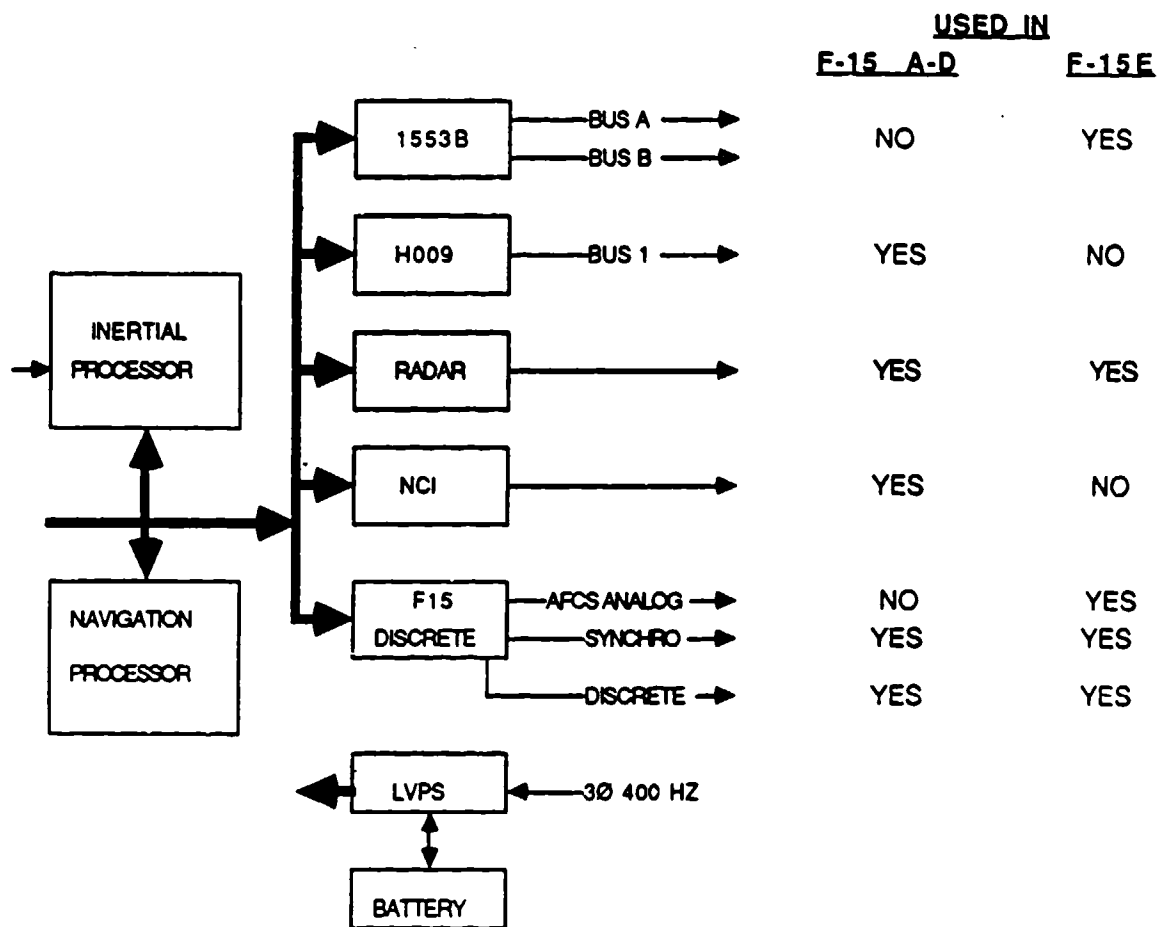


Figure 7. F-15/H-770 INU Interfaces

all pilot interface is accomplished using multi-purpose digital displays (MPDP) which interface with the CC. In the event of CC failure, the MPDP acts as bus controller. (The 1553B front-panel interface connector is capped when the INU is installed on A through D model aircraft.)

Interface to the new Hughes APG 70 radar set in the F-15E is accomplished via the previously described INU transmit-only radar bus. It differs from A through D model operation, however, in that the radar controls the "data initiate" signal to allow transmission of 26 data words, as opposed to only six data words for the APG 63. Radar data is processed by the CC before being transmitted to the INU via the 1553B multiplexed data bus at a 200 Hz rate.

In addition to the synchro and discrete interfaces discussed for A through D operation, three digital/analog output channels are provided for input to the newly designed automatic flight control system (AFCS) to be installed on E-model aircraft. These outputs -- roll, pitch, and vertical velocity -- will be used as

redundant backup inputs for AFCS operating modes, including terrain following.

9. F³/H-423 AND F-15/H-770 INU PRODUCTION STATUS

The F³/H-423 INU completed CIGTF Type I certification testing at Holloman Air Force Base in June, 1985, and entered full scale production with an initial contract award in August, 1985. First interim production INU delivery was accomplished in August, 1986, and the first SNU 84-1 fully compliant production unit in 1987. More than 20 production-model H-423 INUs had been delivered as of June, 1987, against a total of over 200 that are on contract. By the end of 1987, the Honeywell production line will be delivering 25 units per month (H-423, H-770, and MAPS configurations).

As mentioned earlier, the F-15/H-770 INU began full scale engineering development in 1984. Technically, the first production award decision was made in August, 1985, along with the one for the F³/H-423. However, specific production lot procurements did not begin until December, 1986, when MCAIR ordered the initial quantity of 50 units for F-15E. Several months later -- in February, 1987 -- the USAF exercised its first H-770 production lot buy with an order for 120 INUs to be installed in F-15 A through D model aircraft.

Additional production lot buys for F³ and F-15 INUs are expected from the U.S. Air Force. Production options exist over a five year period for over 4000 F³ INUs and 920 F-15 INUs, to be purchased competitively from the two suppliers -- Honeywell Inc., and Litton Systems, Inc.

10. INU PERFORMANCE TEST RESULTS

F³/H-423 INU. The basic F³/H-423 INU has been tested extensively over the past four years in a wide variety of high-performance and transport/cargo-type aircraft. The most extensive test series was conducted at CIGTF in its Type I Certification testing, which completed in June, 1985. Test results were reported, in a preliminary form, by Honeywell at the Twelfth Guidance Test Symposium, October, 1985, in a paper entitled "Certification Testing of the Honeywell H-423 as a Medium Accuracy F³ RLG INS," by David Anderson, Program Manager at Honeywell. The official Air Force test results were later documented in CIGTF Report AD-TR-85-80, "Honeywell H-423 F³ Verification Testing," dated November, 1985.

The Air Force test results showed the H-423 to be performing better than specification, with an overall position error rate of 0.45 nmi/hr, CEP, vs. the specified 0.8 nmi/hr, CEP. Summary results for the C-130/C-141 transport (high and low level), UH-1 helicopter, and F-4D fighter aircraft are shown in Table 3.

In current production testing, H-423 INUs are required to

Table 3. H-423 "F3" CIGTF Certification
Test Results Summary

Test	Nav Runs	Test Dates	Position (nmi/hr) CEP (0-60 min)	Velocity ft/sec (rms)	
				North	East
Laboratory	58	6/83-9/83	0.62	1.22	0.85
Transport (C-130/141)	33	6/84-12/84	0.43	1.26	1.35
Fighter (F-4D)	15	3/85-5/85	0.26	1.89	1.21
Helicopter (UH-1)	10	12/84-2/85	0.68	1.56	1.58
Qualification	15	5/85-9/85	0.56	1.15	1.66
CET	30	12/84-4/85	0.61	1.43	1.33
Spec			(0.80)	(2.50)	(2.50)

complete 10 production verification test (PVT) cycles prior to ATP. This is one of the keys to reliable field operation after delivery. The PVT cycle is a vibration and thermal stress screen to weed-out near-term failures, thus improving subsequent reliability. PVT thermal testing requires that the INU be stabilized at -40°C in an off mode. When the INU is then commanded into the align mode, the thermal environment is ramped up to $+71^{\circ}\text{C}$. After the align is complete, the INU remains in the navigation mode while the INU stabilizes to $+71^{\circ}\text{C}$. The INU is then power cycled and the process is repeated with a negative thermal ramp. Ten of these PVT cycles are required on each production INU, with a composite navigation performance of CEP @ 1 hour ≤ 1.0 nmi/hr. Results of this testing, plus ATP results, are summarized in Table 4.

The H423 INU is currently being used in three flight test programs at the 4950th Test Wing at Wright-Patterson Air Force Base. At the time of this printing, flight test data was available from only one of these programs. Table 5 summarizes the results of the first flight tests of a SNU 84-1 production INU. Because the flight test was not over an instrumented range, only terminal position data is available. The composite terminal CEP was 0.38 nmi/hr for 11 flights with a mean flight duration of 3.5 hr.

Flight testing is anticipated to begin on the C-130-SCNS, F-4 NWDS, HH-53J, and OV-1E applications by the end of 1987.

F-15/H-770 INU. In-house performance data for the H-770 system is listed in Table 6, which provides data gathered by Honeywell during verification and acceptance testing of full-scale development INUs. INU performance over all specified environments is excellent.

Figures 8 and 9 provide summaries of flight test performance gathered by MCAIR during its development test program. As can be seen from the test data, the H-770 INU is performing superbly in several different aircraft, using all hardware interfaces, and under widely differing conditions.

Table 7 provides Honeywell's estimates of INU performance during flight testing in an F-15B, and laboratory testing ($+25^{\circ}\text{C}$) at CIGTF. This data was gathered as part of the TYPE I verification required by the USAF for newly developed INUs. Once again, Honeywell's F-15 INU is delivering half-spec performance in a stringent test series.

Performance Footnote -- As this paper was being completed, some excellent, and very significant, new data was obtained on the F-15/H-770. This involves the accuracy, noise, and jitter characteristics, which are very important to stabilization and motion compensation of radars and electro-optical sensors, as well as inputs to flight control systems. These results will be the subject of another paper in the near future.

Table 4. F³ INU Performance Summary

ATP - [Composite GC(0° & 90°) + SH(90°)]
PVT - [10 Cycles (-40°C to +71°C to -40°C)]

INU S/N	North	Velocity (0-120 min) (ft/sec rms) East	Down	Position --- CEP (0-60 min) (mmi/hr)	
				ATP	PVT
Integration STD-0001 to 0006 (composite)	0.81	0.54	0.024	0.30	N/A
Interim Production STD-0007 to 0009 (composite)	0.71	0.58	0.022	0.32	0.78
Rev 3 Production					
May STD-0010 to 0016 (composite)	0.69	0.64	0.043	0.37	0.63
June STD-0017 to 0026 (composite)	0.56	0.56	0.045	0.30	0.66
Overall Composite	0.61	0.59	0.044	0.33	0.65
(Spec)	(2.50)	(2.50)	(2.00)	(0.80)	(1.00)

Table 5. KC135 Flight Test Results (4950th)
(SNU 84-1 INU S/N 213)

Flight #	Date	Nav Time (Hrs)	Terminal		Comment
			Error (nm)	RPER (nmi/hr)	
1	10/23/86	3.5	2.0	0.57	Shakedown Flight Init Pos Error?
2	11/03	5.6	5.9	1.05	
3	11/10	1.6	0.3	0.19	
4	11/13	1.4	0.2	0.14	Ground Aborts Side Slip Maneuvers 10 Day Cold Soak (<0°C) High Flight Dynamics
5	11/19	4.3	0.2	0.05	
6	11/24	4.3	0.9	0.21	
7	12/03	5.0	3.5	0.70	
8	12/04	4.1	0.8	0.20	
9	12/12	4.5	0.1	0.02	
10	12/15	2.6	1.4	0.54	
11	12/15	1.6	0.1	0.06	

Composite Terminal CEP = 0.38 nmi/hr

Table 6. F-15/H-770 INU Performance Summary
Honeywell Testing

ATP - [Composite GC(0 to 180, 90 to 180) + SH(45 to 225)]
MSPRAT - [10 Cycles (-54 to + 71 deg C)]

INU S/N.	Velocity-ATP (0-120 min) (ft/sec-rms)		Position --- CEP (0-60 min) (mm/hr)	
	North	East	ATP	MSPRAT
0001	1.19	0.64	0.42	---
0002	1.44	0.59	0.50	---
0003	0.94	0.41	0.30	---
0004	1.33	0.64	0.56	---
0006	1.01	1.27	0.39	---
0008	1.63	0.67	0.58	---
0009	0.65	1.17	0.51	0.40
0010	1.56	0.53	0.75	---
0011	1.33	0.73	0.68	---
0013	0.53	0.50	0.47	0.41
0014	0.67	0.76	0.32	0.39
Composite (n=11)	1.17	0.76	0.52	---
Spec	(2.5)	(2.5)	(0.80)	(1.0)

TERMINAL POSITION ERROR RATE-UNAIDED

GC FLTS (11/86-6/87)-0.8NM/HR CEP SPEC.

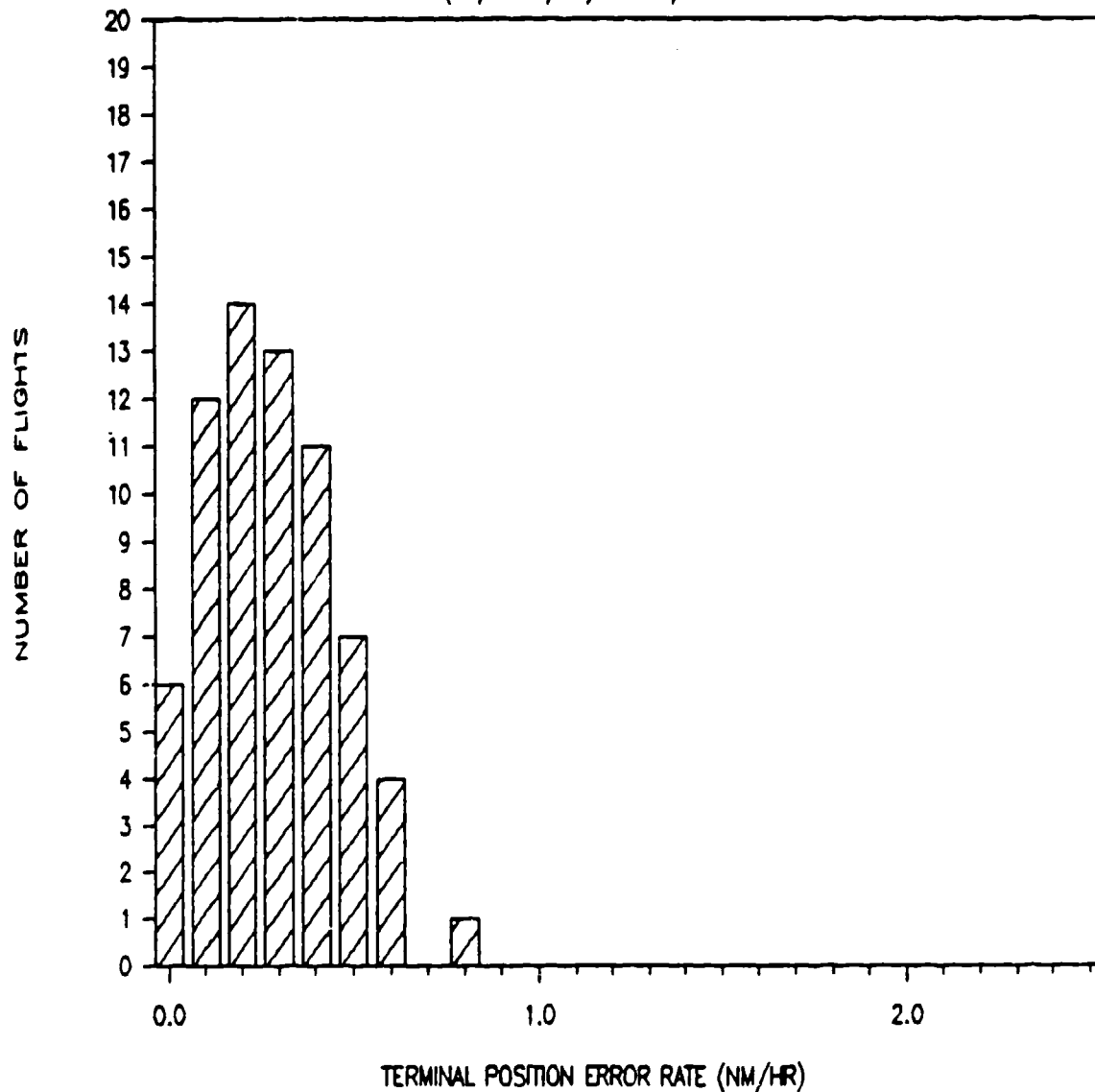


Figure 8. F-15/H-770 MCAIR Flight Test Data

BULLSEYE PLOT-UNAIDED

GC FLTS (11/85-6/87)-0.8NM/HR CEP SPEC.

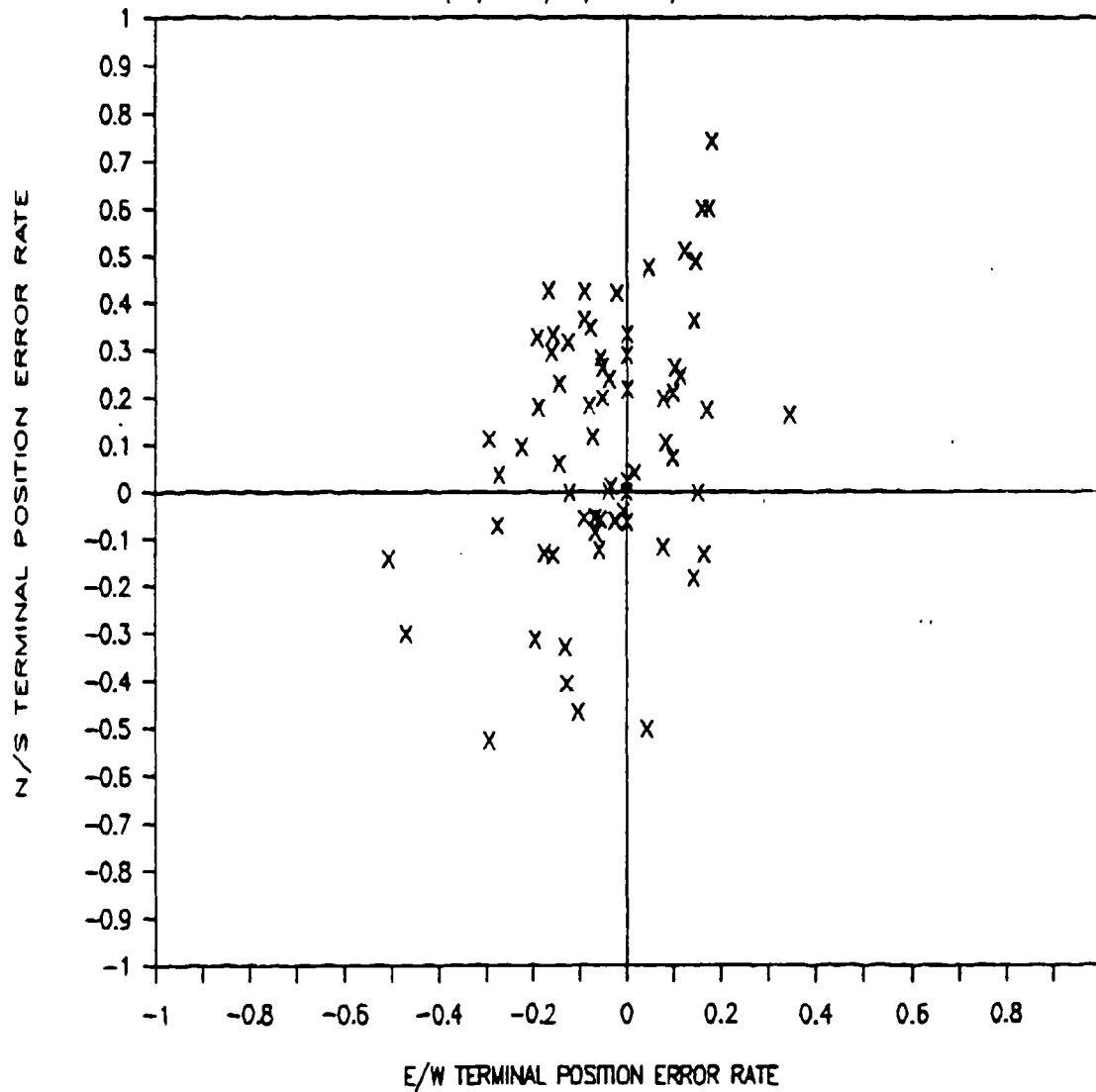


Figure 9. F-15/H-770 MCAIR Flight Test Data

Table 7. H-770 F-15 Performance Summary
 USAF CIGTF Data Summary
 (Honeywell Estimates)

Test Type	Velocity (0-120 min) (ft/sec-rms)		Position-CEP (0-60 min) (mi/hr)
	North	East	
o Gyro Compass Align	1.41	0.50	0.55
o Stored Heading Align	0.76	0.26	0.33
o 10 hr Static Nav	0.40	0.74	0.06
o 20 Position	1.29	0.66	0.41
o S-Turn	0.97	1.11	0.23
o Elec Pwr	0.77	0.39	0.25
o Fighter Flight Test	1.44	1.41	0.46
Composite (42 Runs)	1.07	0.82	0.38
Spec	(2.5)	(2.5)	(0.8)

"Reference Position Vector," Nancy McClanahan, 6585th Test Group, Central Inertial Guidance Test Facility, Holloman Air Force Base NM

(S02A)

"Robotics Applications in the Testing of Inertial Sensors," Joy Y. Greig, Central Inertial Guidance Test Facility, 6585th Test Group, Holloman AFB NM; Zdzislaw H. Lewantowicz, Air Force Institute of Technology, Wright-Patterson AFB OH

(S02B)

"The Optimum Solution of Instrument Quantization Effects," Thomas Reed, Charles Stark Draper Laboratory, Inc., Cambridge MA

(S02C)

REFERENCE POSITION VECTOR

BY

NANCY McCLANAHAN

6585TH TEST GROUP

CENTRAL INERTIAL GUIDANCE TEST FACILITY

HOLLOMAN AIR FORCE BASE, NEW MEXICO

THIS PAGE WAS LEFT BLANK INTENTIONALLY.

REFERENCE POSITION VECTOR

TABLE OF CONTENT

1.0	Introduction.....	1
2.0	Space-Time Data Collection.....	1
3.0	Survey.....	2
3.1	Survey References.....	2
3.2	Geodesy.....	5
4.0	Survey Transformation.....	8
4.1	Interpolation.....	8
4.2	Geodetic/Astronomic Transformation.....	11
4.3	Transformation of Distances.....	13
4.3.1	Finding the Location of Benchmarks and IC's.....	15
4.3.2	Finding the Relationship of BM's and IC's to West Rail..	19
4.3.3	Finding the Location of the West Rail.....	19
4.4	Gravity.....	21
5.0	LVDT Data Collection.....	22
6.0	LVDT Transformation.....	22
7.0	Time Correlation.....	23
8.0	Gravitational and Coriolis Acceleration Compensation.....	24
8.1	Gravity.....	24
8.2	Coriolis Acceleration.....	24
9.0	Conclusion.....	25

List of Figures

Figure	Title	Page
1	Space-time System	3
2	Track Survey References	4
3	Geoid-Ellipsoid Relationships	6
4	The Ellipsoid	7
5	LCEF Coordinate Frame	9
6	Crosstrack Survey Measurements12
7	Angle Locations for Geodetic to Astronomic Transformations14
8	Earth Centered Coordinate System16
9	Earth Centered Components - Ellipsoid17
10	Elevation Survey Measurements18
11	Crosstrack Rotations20

List of Tables

Table	Description	Page
1	Survey Measurements10

REFERENCE POSITION VECTOR

One of the functions of the high speed test track is to evaluate inertial guidance system (inertial test article) accuracy by comparing the location of the test article as determined by the test article itself with the true position of the test article as determined by an independent reference. With the advent of more accurate guidance systems, the independent reference must also be improved. The reference is created by surveying the track, collecting data during the test and then performing calculations to provide a usable position reference. The computations should use as few assumptions and approximations as possible. The method currently being used to calculate the independent reference is outlined here.

In the past, the track was surveyed independently of the surrounding area. Because the track was modeled to be on its own imaginary sphere which did not coincide with the ellipsoid or the geoid, some survey measurements could not be taken into account correctly. The method described here uses fewer approximations than the previously used method described by R. E. Holdeman in "The Use of the Holloman Track Reference System in the Quantitative Testing of Inertial Guidance Systems," and the Appendix to Section VI by Pat Schwind.

1.0 INTRODUCTION

The independent reference mentioned above is called a reference position vector. The creation of the reference position vector may be broken into major sections: space-time data collection; surveying; survey transformation; linear variable displacement transducer (LVDT) data collection; LVDT transformation; data correlation; and gravity and coriolis compensation.

2.0 SPACE-TIME DATA COLLECTION

The Holloman Test Track is a 50,788 foot long set of 2 rails, nominally 7 feet apart, mounted on a cement girder. The guidance system is carried down the track in a test vehicle (sled). In order to create the reference position vector, position vs. time of the sled must be determined.

Interrupter blades mark locations along the track which are associated with the time the sled passed them by means of a space-time head attached to the sled. Interrupters are steel blades 2 inches wide attached to the girder on the east side of the east rail for the first 35,200 feet of track and on the west side of the west rail from 35,000 feet to the end of the track at nominal intervals of 3.25 feet for the first 461 feet and 4.33 feet thereafter. The interrupter locations are called interrupter stations or track stations. A specific interrupter station is referenced by its nominal downtrack distance from the south reference point, Station 00 (STA00). For example, the first interrupter is station 1.66 and is 1.66 feet downtrack from STA00.

The space-time head transmits a light beam across a small gap. As the test vehicle moves down the track, the interrupters break the light beam which causes a voltage variation that is recorded on magnetic tape. (See Figure 1.) Analysis of the tape yields the time the space-time head passed each interrupter and the nominal distance downtrack of the interrupter, i.e., the interrupter station number. (See reference 2 for more details on the space-time data collection system and the physical track layout.)

The test article output and the reference must be compared to find system performance. The article being tested senses motion, relative to a start point, in three directions. Generally, the data output from the test article is velocity vs. time in three directions, which can be integrated to distance vs. time. The space-time data consists of station numbers vs. time (one dimension) and is not accurate enough to compare directly with test article data. The location of the track at interrupter stations with respect to a reference point must be accurately known in three dimensions to create a suitable reference.

3.0 SURVEY

Surveying is done to determine the location of the west rail at interrupter stations relative to STA00 in three dimensions. When comparing the test article output to the reference, both the system output and the reference must be in the same coordinate frame. The coordinate frame most commonly used is the launch centered, earth fixed frame (LCEF). This frame has the launch point as the origin, the astronomic vertical as one axis, and the astronomic tangent plane (plane perpendicular to the astronomic vertical at the earth's surface) containing the other two axes. There is more information about the LCEF coordinate frame in later sections.

3.1 Survey References.

A system of reference points is used in surveying the track location rather than surveying at each interrupter because 1) the interrupters can be knocked out by sleds and the heavy equipment that is used near the rails, 2) time and money prohibit surveying the over 8000 interrupters along the full track length, and 3) the reference points are physically easier to survey due to their shape and location. The surveying reference points are more widely spaced than interrupters.

The surveying reference points are interrupter control stations (IC's), benchmarks, the west rail, and interrupters. The IC's are benchmarks which are superior first order survey points located about 2600 feet apart, approximately 9 inches west of the west track rail centerline. Benchmarks (in addition to the IC benchmarks) are about 100 feet apart nominally on a line between the IC's. The west rail centerline is defined to be the reference track position. (See Figure 2.) Other sets of reference points, including the 100 foot offset line and the 1000 foot pier line, are used by the surveyors. Measurements to and from these references are not directly used in the position vector processing.

The only set of measurements made at interrupter stations is the distance between interrupter blades. All other measurements, such as elevation and gravity, are made at the benchmarks and IC's. All downtrack

SPACE-TIME SYSTEM

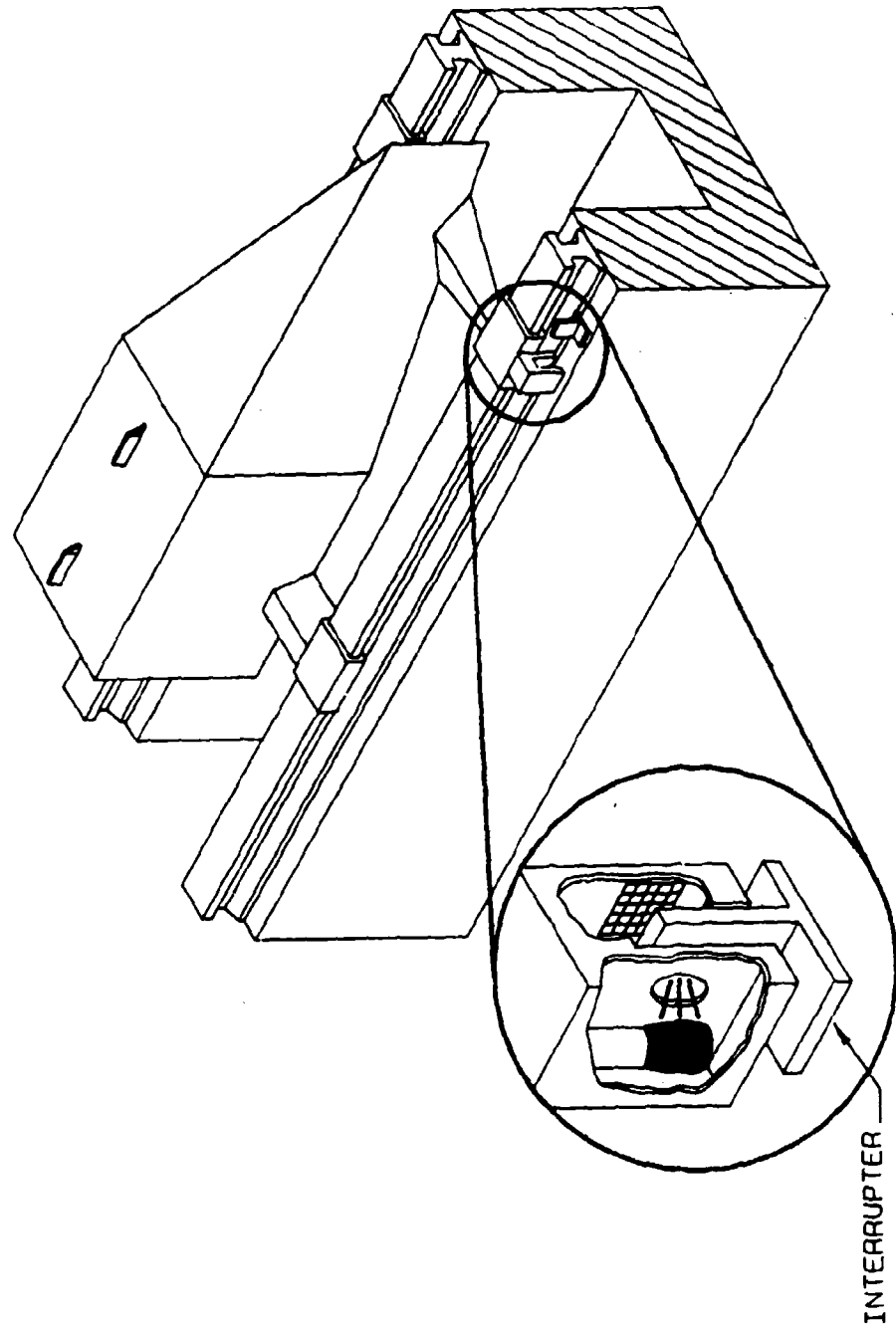
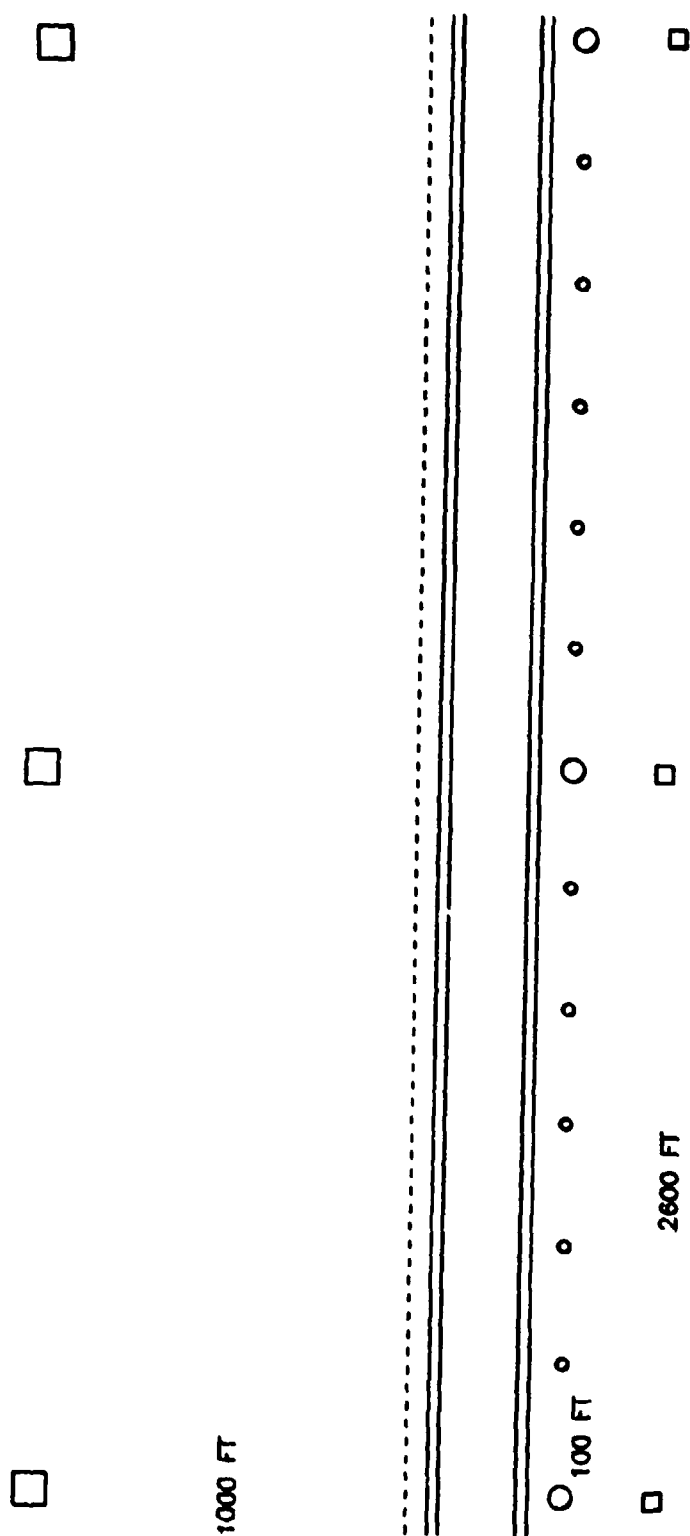


Figure 1. SPACE-TIME SYSTEM



- BENCHMARK
- IC STATION
- 1000 FT PIER
- INTERRUPTER
- 100 FT OFFSET

FIGURE 2. TRACK SURVEY REFERENCES

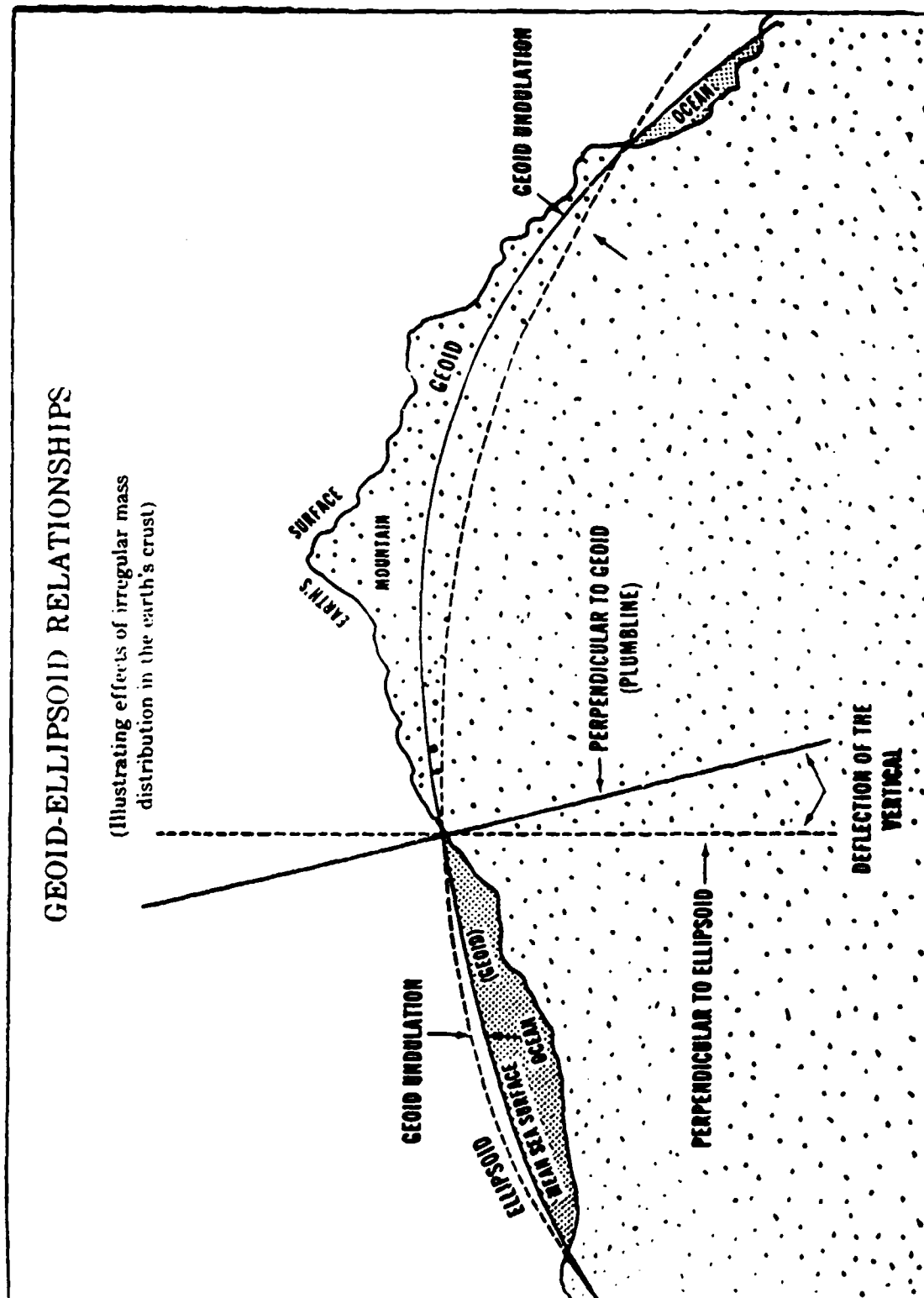


FIGURE 3

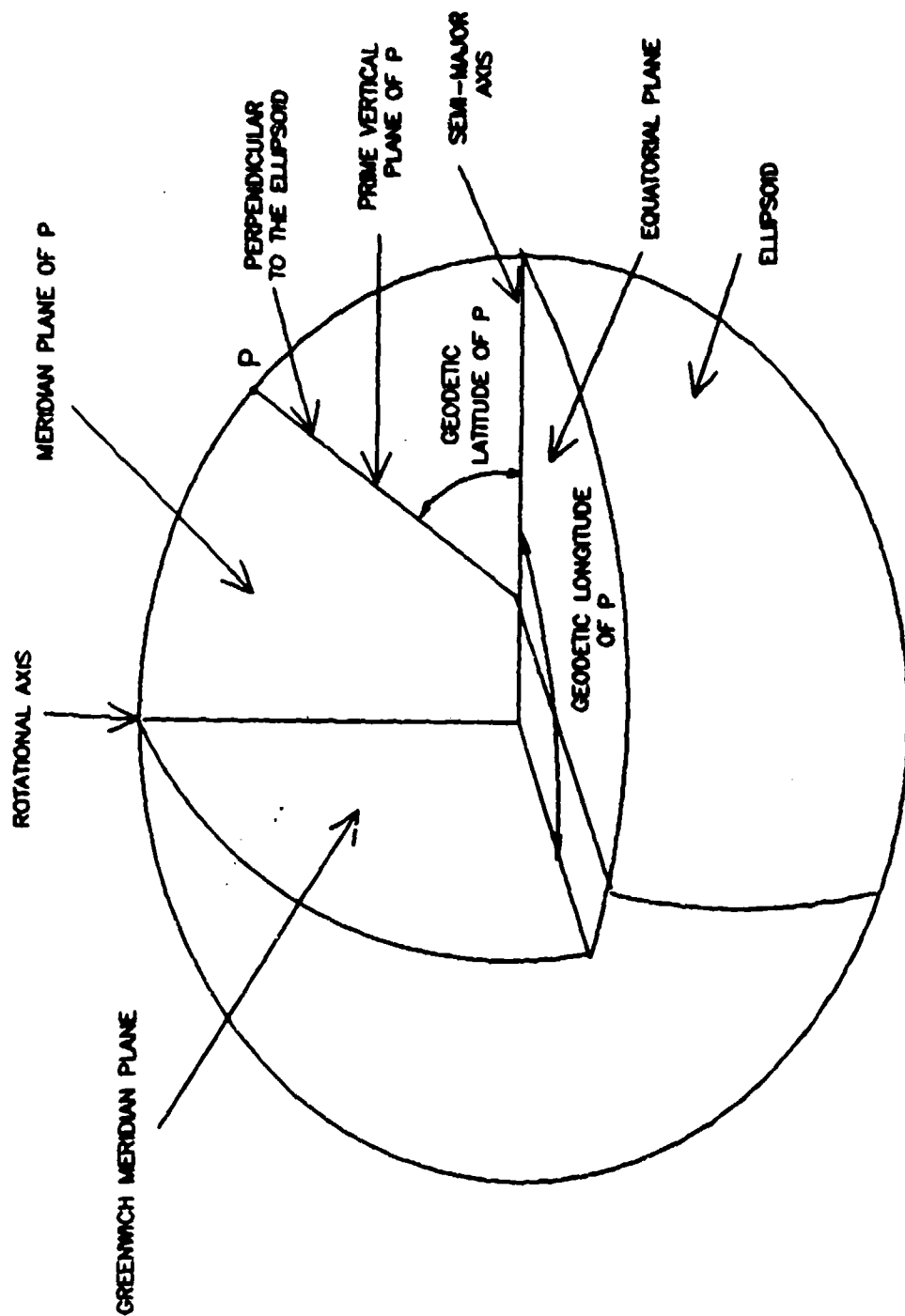


FIGURE 4. THE ELLIPSOID

measurements use STA00 as their south reference point.

3.2 Geodesy.

Because the track is on the surface of the earth, the earth's geometry and geodesy must be understood to correctly use survey measurements for determining the location of the track in LCEF. Before describing the survey measurements and their use in creating the track reference position vector, some general terms need defining. These are the same definitions used by Holdeman, except where noted.

GEOID: A non-analytical surface which is equipotential with respect to the acceleration of gravity. It is referenced to the mean sea level, and it is everywhere normal to the gravity vector. All astronomic survey quantities are referenced to the geoid. See Figure 3.

ELLIPSOID MODEL: A model of the earth which is an approximation to the geoid (See Figure 3.). The 1866 Clarke Ellipsoid is the model used by the Defense Mapping Agency (DMA) in its calculations and reports. Therefore, the Clarke model is used in this report.

ACCELERATION OF GRAVITY: The acceleration of gravity vector is defined as the vector sum of the gravitational acceleration (i.e., mass attraction acceleration) and the centripetal acceleration due to the rotation rate of the earth.

ASTRONOMIC VERTICAL: The normal to the geoid at the point in question. It is directed along the local gravity vector or the plumb bob vertical. (See Figure 3.)

GEODETTIC VERTICAL: The normal to the ellipsoid model at the point in question. (See Figure 3.)

ASTRONOMIC TANGENT PLANE: That plane normal to the astronomic vertical at the point in question.

GEODETTIC TANGENT PLANE: That plane normal to the geodetic vertical at the point in question.

MERIDIAN PLANE: That plane which contains the rotation axis of the earth and the point in question. (See Figure 4.)

PRIME VERTICAL PLANE: That great circle plane which contains the point in question and is normal to the meridian plane. (See Figure 4.)

GEODETTIC LATITUDE: The angle the geodetic vertical makes with the equatorial plane measured in the meridian plane. (See Figure 4.)

GEODETTIC LONGITUDE: The angle between the geodetic vertical

TABLE 1
SURVEY MEASUREMENTS

MEASURE- MENT	DESCRIPTION	ACCURACY	FREQUENCY
DELTAS	distance between south edges of consecutive interrupters	0.0001 ft per 4.3 ft	3/yr. every inter- rupter
BMDIST	distance downtrack of benchmarks	+/- 0.02 ft	
BMGRAV	magnitude of gravity measured along the astronomic vertical	+/- 0.1 mgals*	1/2yrs. every 10th BM
BMELEV	elevation above mean sea level, measured along the astronomic vertical	+/- 1/32 in	1/yr. every BM
ICSTA	distance downtrack of IC	+/- 0.5mm	1/yr. every IC
ICAZBM	distance from BM to azimuth line between consecutive IC's	+/- 0.5mm	1/yr. every 3rd BM
BMTK	distance from BM to west rail	1/32 in	1/yr every BM
ICTK	distance from IC to west rail	1/32 in	1/yr every IC
PV	prime vertical component of deflection of the vertical	+/- 0.25 arcsec	1/2yrs. every IC
MC	meridian component of deflection of the vertical	+/- 0.1 arcsec	1/2yrs. every IC
LAT	geodetic latitude	1 ppm	1/yr. every IC
LONG	geodetic longitude	1 ppm	1/yr. every IC
GEOH	height of the geoid above the ellipsoid	+/- 0.01m	1/2yrs. every IC

* relative to the absolute gravity station at AITL

at Greenwich, England and the geodetic vertical at the point in question measured in a plane parallel to the equatorial plane. (See Figure 4.)

DEFLECTION OF THE VERTICAL: The difference between the astronomic vertical and the geodetic vertical. It is normally broken into two components: one in the meridian plane and one in the prime vertical plane. A positive deflection exists when the astronomic vertical is deflected to the north or west of the geodetic vertical. (See Figure 3.)

ASTRONOMIC AZIMUTH OF A LINE SEGMENT: The angle between the line segment and the meridian plane measured in the astronomic tangent plane and positive clockwise from north. (Holdeman measures from south)

GEODETTIC AZIMUTH OF A LINE SEGMENT: The angle between the line segment and the meridian plane measured in the geodetic tangent plane and positive clockwise from north. (Holdeman measures from south)

Table 1 contains definitions and information about all the survey measurements needed for the proposed survey transformation. The first column contains abbreviations which are the variable names used in the calculations of the following sections. Generally, the measurements needed are elevation, gravity, deflection of the vertical, latitude, longitude, crosstrack offset distance (i.e., distance between the IC line and the west rail), and downtrack distances of IC's, benchmarks and interrupters. The use of these measurements is described in following sections.

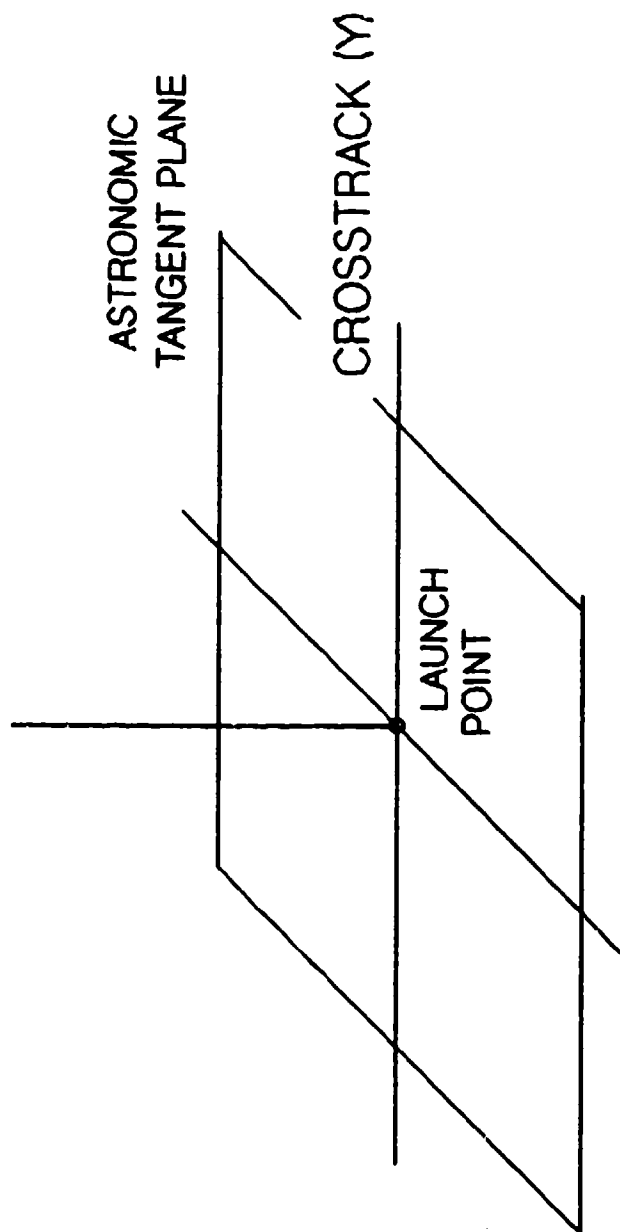
4.0 SURVEY TRANSFORMATION

The survey data must be combined in a manner that results in finding the position of the track relative to the launch point astronomic tangent plane (LCEF). In this reference system, the launch point is the origin. The X axis is along the average astronomic track azimuth, the Y axis is perpendicular to the azimuth, and both are in the astronomic tangent plane. The astronomic vertical is the third axis, Z. See Figure 5. Several steps are involved in transforming the data to this reference system: 1) interpolating all survey data to interrupter positions, 2) transforming the distance measurements to LCEF, and 3) transforming the gravity data to LCEF. The interpolation is described first. In the equations in this paper any variable ending with a 0 refers to the launch point, and any variable ending in I is measured at an interrupter.

4.1 Interpolation.

The first step in the survey transformation is interpolating, using a straight line interpolation scheme, the survey data to each interrupter. Gravity (GRAVI) and elevation (ELEVI) are found using equation 1. Gravity is used as an example.

ASTRONOMIC VERTICAL (Z)



AVERAGE ASTRONOMIC
TRACK AZIMUTH (X)

FIGURE 5. LAUNCH CENTERED EARTH FIXED COORDINATE FRAME.

$$\text{GRAVI} = \text{BMGRAV}(\text{BM}) + (\text{BMGRAV}(\text{BM}+1) - \text{BMGRAV}(\text{BM})) * \frac{(\text{DIST} - \text{BMDIST}(\text{BM}))}{\text{BMDIST}(\text{BM}+1) - \text{BMDIST}(\text{BM})} \quad (1)$$

where GRAVI is the gravity at the interrupter,
 BM is the number of the benchmark immediately preceding the interrupter in question,
 BMGRAV is the gravity at the benchmark,
 DIST is the actual distance downtrack of the interrupter,
 i.e., the sum of the DELTAS measurements,
 DELTAS is the distance between interrupters, and
 BMDIST is the actual distance downtrack of the benchmark.

(Refer to Table 1 for more detail on the variables in all equations.)
 Likewise, deflection of the vertical in the prime vertical and meridian planes (PV, and MC respectively), latitude (LAT), longitude (LONG), and geoid height above the ellipsoid (GEOH) are interpolated between the nearest IC's according to equation 2. PV is used as an example.

$$\text{PVI} = \text{PV}(\text{IC}) + (\text{PV}(\text{IC}+1) - \text{PV}(\text{IC})) * \frac{(\text{DIST} - \text{ICDIST}(\text{IC}))}{(\text{ICDIST}(\text{IC}+1) - \text{ICDIST}(\text{IC}))} \quad (2)$$

where IC is the number of the interrupter control station immediately preceding the interrupter in question, and
 ICDIST is the actual distance downtrack of the IC.

Crosstrack offset is the distance from the IC's to the center of the track's west rail (ICOFFSET), measured perpendicular to the geodetic azimuth. Because the IC's are so far apart, intermediate measurements are made at every third benchmark. The offset at a benchmark (BMOFFSET) is the distance between the west rail centerline and the straight line connecting the two IC's which surround the benchmark. (See Figure 6)

$$\begin{aligned} 1) \quad \text{BMOFFSET} &= \text{ICAZBM} + \text{BMTK} \\ \text{ICOFFSET} &= \text{ICTK} \end{aligned} \quad (3)$$

where ICAZBM is the distance from the benchmark to the line connecting the two nearest IC's
 BMTK is the distance from the west rail centerline to the benchmark.

The offset at an interrupter (OFFSI) is calculated by interpolating between the nearest benchmarks and/or IC for which BMOFFSET or ICOFFSET are available. The equations used for interpolation are similar to Equations (1) and (2) above.

Now that the data is interpolated, the transformation to the launch point astronomic tangent plane can begin.

4.2 Geodetic/Astronomic Transformation.

The transformation between geodetic and astronomic north-west-vertical (NWV) coordinate frames at any point is defined by the two deflection of the vertical angles, PV and MC. Because both of these angles are defined in the geodetic coordinate frame, they cannot be used in consecutive

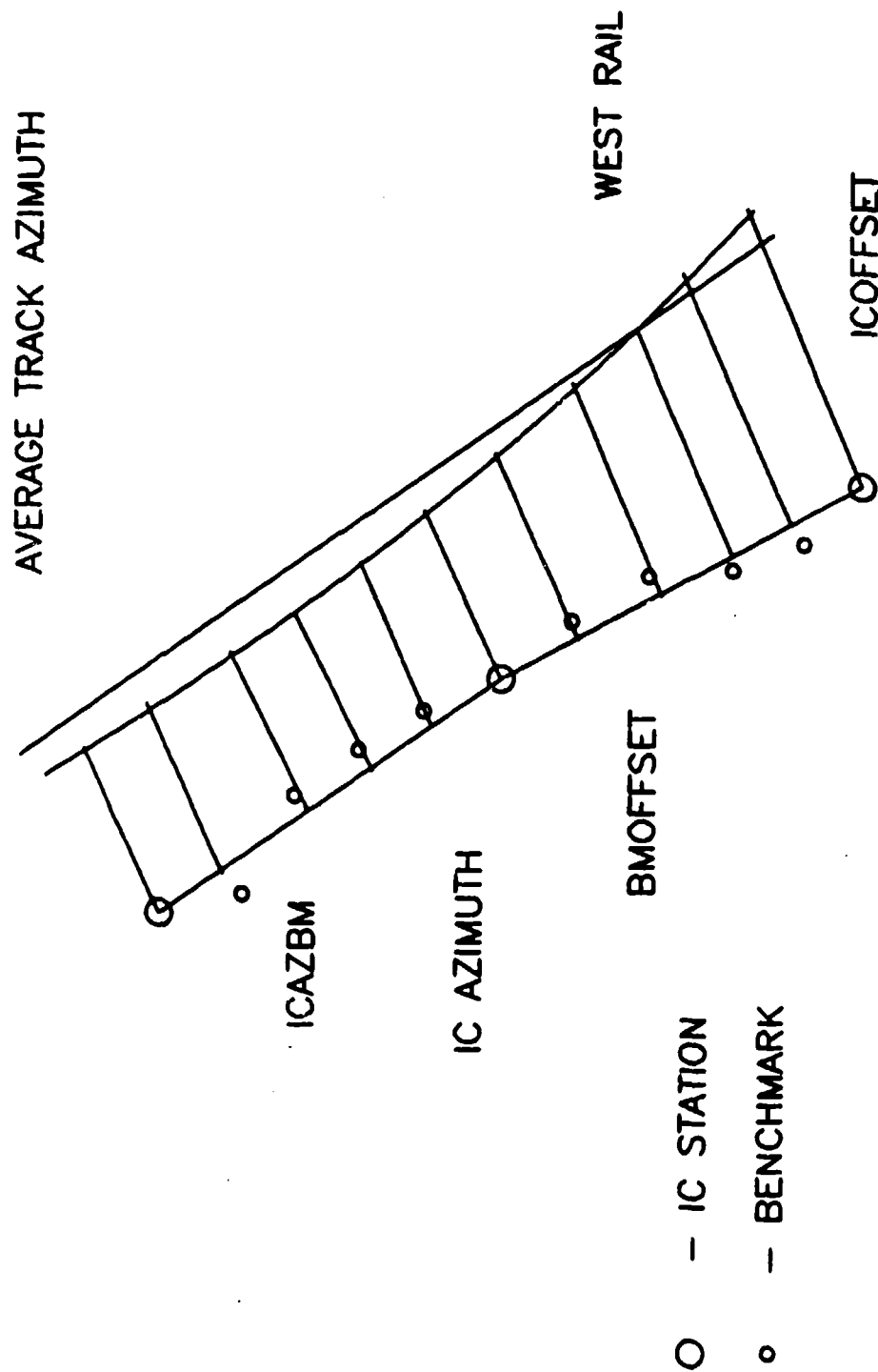


FIGURE 6. CROSSTRACK SURVEY MEASUREMENTS.

transformations, but rather, must be used in a single transformation. The method used for performing this transformation is quaternions. Quaternions are a four parameter set of numbers that describe any right handed coordinate transformation using one number (d) to indicate the magnitude of rotation and three numbers (a, b, and c, which are coefficients of unit vectors i, j, and k, respectively) to form a unit vector about which the rotation is performed. One major advantage of quaternions is they have no singularities. The direction cosine matrix taken from the quaternion is used in calculations to transform from the geodetic to the astronomic coordinate frames and vice versa.

The direction cosine matrix computed from the four elements of the quaternion is:

$$\begin{bmatrix} a^2+b^2-c^2-d^2 & 2(bc+ad) & 2(bd-ac) \\ 2(bc-ad) & a^2-b^2+c^2-d^2 & 2(ab+cd) \\ 2(ac+bd) & 2(cd-ab) & a^2-b^2-c^2+d^2 \end{bmatrix}$$

Where,

$$\begin{aligned} a &= PV / \phi \sin(\phi/2), \\ b &= MC / \phi \sin(\phi/2), \\ c &= TKAZ / \phi \sin(\phi/2), \text{ and} \\ d &= \cos(\phi/2), \end{aligned}$$

$$\text{where } \phi = \sqrt{PV^2 + MC^2 + TKAZ^2}.$$

TKAZ is explained in the next paragraph.

The direction cosine matrix taken from the quaternion with PV (rotation about north), MC (rotation about west), and no rotation about vertical (i.e., TKAZ=0 in the previous equations) as inputs gives the transformation from geodetic NWV to astronomic NWV, hereafter called Matrix A. The inverse of Matrix A, Matrix AI, transforms astronomic to geodetic. Because Matrix A is orthogonal, its inverse is equal to its transpose. The geodetic azimuth of the track is measured in the same frame as PV and MC. See Figure 7. Therefore, using PV, MC, and geodetic track azimuth, TKAZ, as inputs to the quaternion, the direction cosine matrix, hereafter called Matrix B, transforms from the geodetic north-west-vertical frame to the astronomic X-Y-Z frame (LCEF) where Z is along the astronomic vertical, X is along the average astronomic track azimuth, and Y is perpendicular to X in the astronomic tangent plane. Working in the geodetic frame is desirable because the geodetic frame is defined at each point relative to a regular geometric shape, the ellipsoid. (See Figure 4.) The relationship between two geodetic frames is determined by the latitudes and longitudes of the two points.

In summary, Matrix A is the transformation from geodetic NWV to astronomic vertical, Matrix AI is the transformation from astronomic NWV to geodetic NWV, and Matrix B is the transformation from geodetic NWV to LCEF.

4.3 Transformation of Distances.

There are three parts to determining the west rail location at the interrupters in LCEF coordinates. The first is determining the location of the benchmarks and IC's in the earth centered frame. The second is finding the location of the west rail with respect to the benchmarks and IC's in

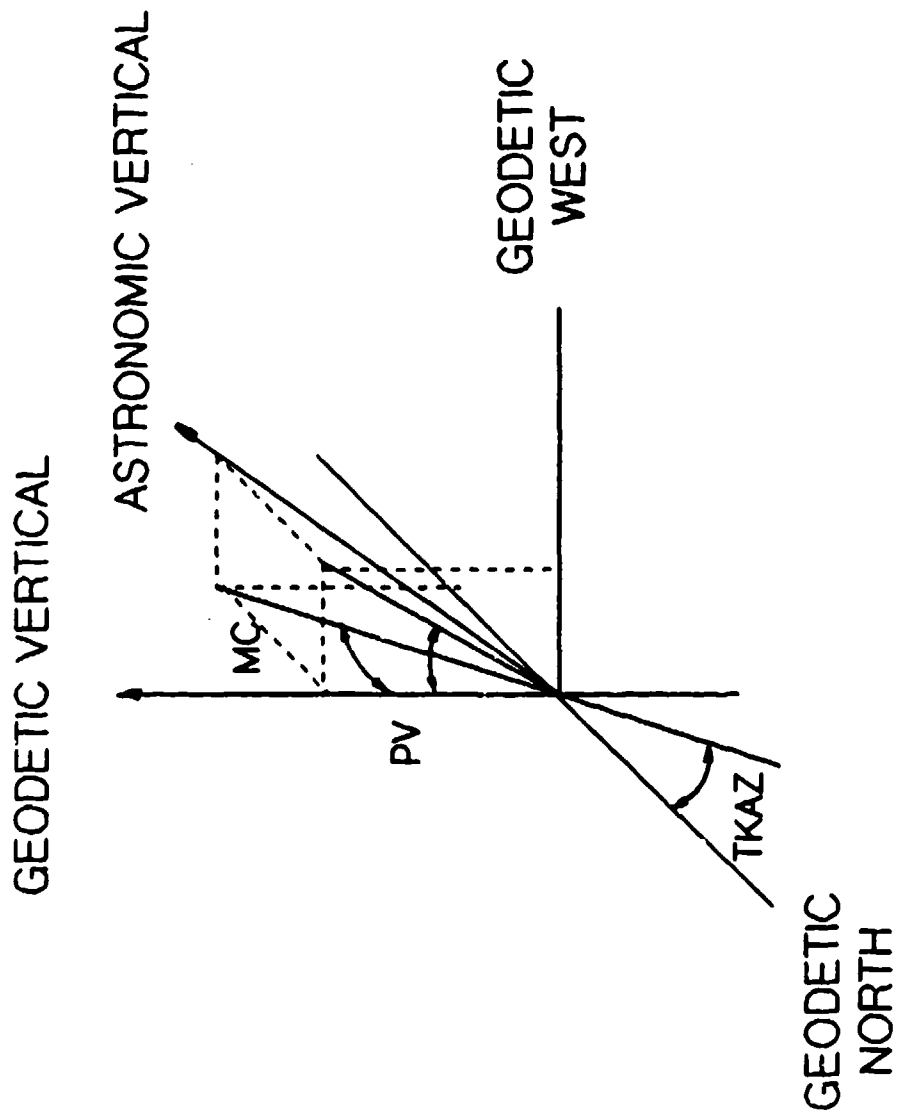


FIGURE 7. ANGLE LOCATIONS FOR GEODETIC TO ASTRONOMIC TRANSFORMATIONS.

the earth centered frame, and the third is combining the two in order to get the location of the west rail (at interrupter distances downtrack) and transforming to LCEF.

4.3.1 Finding the Location of Benchmarks and IC's.

The location of a point on the surface of the earth can be defined with two cartesian coordinates (relative to the earth's center) and the geodetic longitude. In the subsequent equations the subscript e designates a variable referenced to the earth's center, and the subscript eiL, earth center referenced at the interrupter longitude. For example, N_e is directed from the earth's center through the north pole (along the polar axis), and V_{eiL} is perpendicular to N_e (parallel to the equatorial plane) at the longitude of the interrupter in question. See Fig. 8. At any given longitude the cartesian coordinates of a point on the earth's surface can be found using the formulas:

$$Nl_e = \left(\frac{A_e(1-E^2)}{(1-E^2(\sin^2(LATI)))^{1/2}} + H \right) \sin(LATI) \quad (4)$$

$$Vl_{eiL} = \left(\frac{A_e}{(1-E^2(\sin^2(LATI)))^{1/2}} + H \right) \cos(LATI) \quad (5)$$

where A_e and E are the semi-major axis length and eccentricity, respectively, of the Clarke Ellipsoid model. LATI is the geodetic latitude of the point in question. Nl_e is the distance along the polar axis from the equator to the interrupter and Vl_{eiL} is the distance measured parallel to the equator and radially from the polar axis to the interrupter. See Fig. 9. H is the height above the ellipsoid of a point on the earth's surface, measured perpendicularly to the ellipsoid.

The elevation measurement, ELEVI, is the west rail height above the geoid (mean sea level), measured perpendicularly to the geoid. The difference between the geoid and the ellipsoid heights at the interrupter, GEOHI, is also measured along the astronomic vertical and must be added to the elevation measurement to obtain the height of the interrupter above the ellipsoid, ELEVT (equation 6). See Fig. 10. The height above the ellipsoid must be transformed into geodetic NWV coordinates (perpendicular to the ellipsoid) using Matrix AI (equation 7). H is the resulting vertical component, ELEVG3.

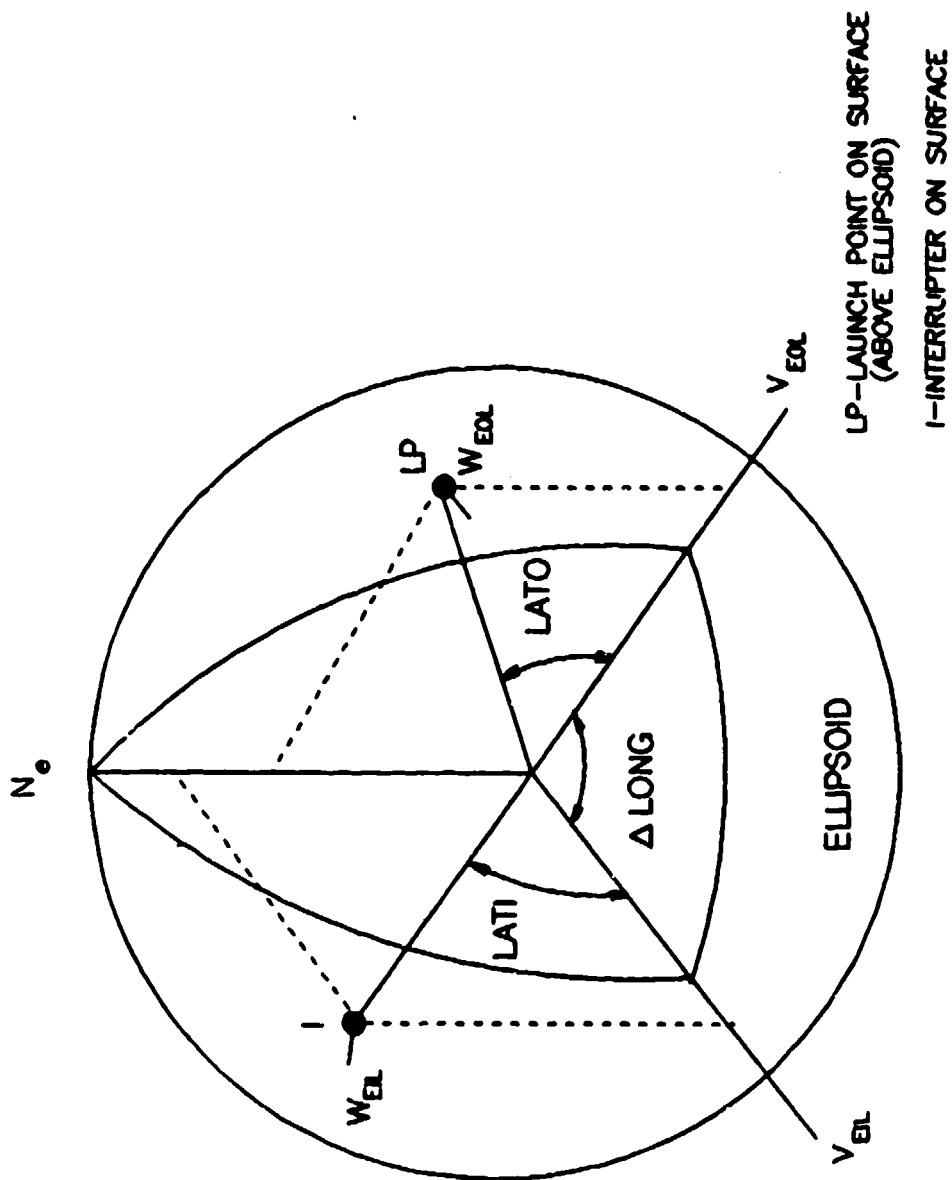


FIGURE 8. EARTH CENTERED COORDINATE SYSTEM

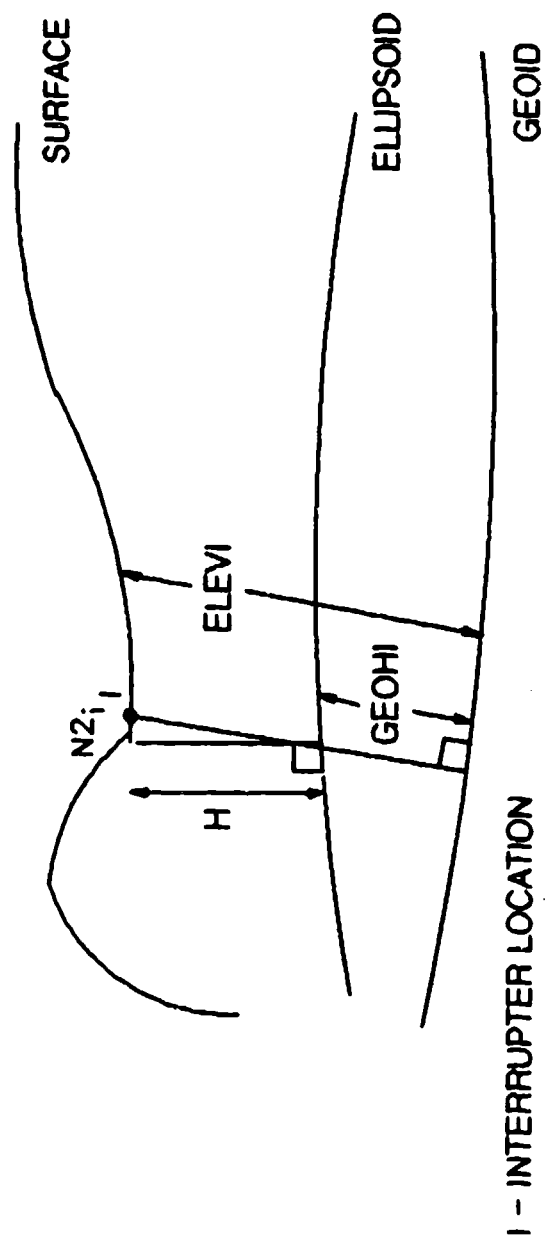


FIGURE 10. ELEVATION SURVEY MEASUREMENTS.

$$\text{ELEV} = \text{ELEV} + \text{GEOHI} \quad (6)$$

$$\begin{bmatrix} \text{ELEV} \\ \text{ELEV} \\ \text{ELEV} \end{bmatrix} = \begin{bmatrix} \text{MATRIX} \\ \text{AI} \end{bmatrix} \begin{bmatrix} 0 \\ 0 \\ \text{ELEV} \end{bmatrix} \quad (7)$$

The north and west components of elevation must be taken into account also. The geodetic north component, ELEV, is rotated by latitude, LATI, to compute N_e and V_{eiL} components (equations 8 and 9). The west component, ELEV, is in the W_{eiL} direction, i.e. geodetic west at the longitude of the point in question.

$$N_e = \text{ELEV} * \cos(\text{LATI}) \quad (8)$$

$$V_{eiL} = -\text{ELEV} * \sin(\text{LATI}) \quad (9)$$

$$W_{eiL} = \text{ELEV} \quad (10)$$

The location of the benchmarks and IC's in an earth centered reference frame are the sum of N_e , V_{eiL} , and W_{eiL} components from equations 4, 5, 8, 9, and 10.

$$N_{e,ELEV}^3 = N_e^1 + N_e^2 \quad (\text{Eq}(4)+\text{Eq}(8)) \quad (11)$$

$$W_{eiL,ELEV}^3 = W_{eiL}^2 \quad (\text{Eq}(10)) \quad (12)$$

$$V_{eiL,ELEV}^3 = V_{eiL}^1 + V_{eiL}^2 \quad (\text{Eq}(5)+\text{Eq}(9)) \quad (13)$$

4.3.2 Finding the relationship of BM's and IC's to West Rail.

The offset measurements, OFFSI, relate the benchmarks and IC's to the west rail, and are made perpendicular to the track azimuth. In order to transform OFFSI into the earth centered reference frame, OFFSI must be rotated by the geodetic track azimuth to calculate its geodetic NWV components at the appropriate interrupter, and then rotated by the latitude to get into the earth centered frame (equations 14, 15, and 16). (See Figure 11.)

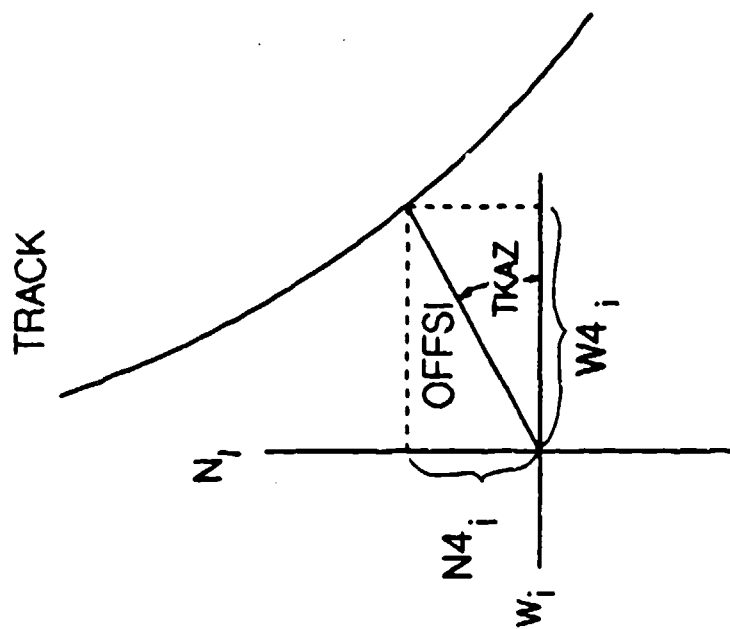
$$N_e^4 = -\text{OFFSI} * \sin(\text{TKAZ}) * \cos(\text{LATI}) \quad (14)$$

$$W_{eiL}^4 = \text{OFFSI} * \cos(\text{TKAZ}) \quad (15)$$

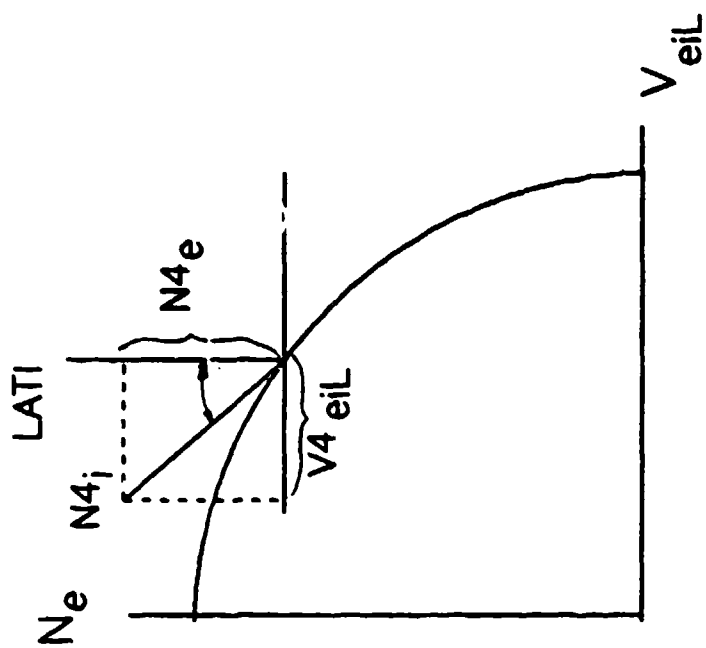
$$V_{eiL}^4 = \text{OFFSI} * \sin(\text{TKAZ}) * \sin(\text{LATI}) \quad (16)$$

4.3.3 Finding the location of the West Rail.

The components of OFFSI, N_e^4 , W_{eiL}^4 , V_{eiL}^4 , equations 14, 15, and 16, are added to the N_e^3 , W_{eiL}^3 , and V_{eiL}^3 components from the elevation calculations, equations 11, 12, and 13, to result in the three components of the true location of the west rail in the earth centered reference frame



(1)



(2)

FIGURE 11. CROSSTRACK ROTATIONS

at the equator at the longitude of the interrupter ($N5_e, W5_{eiL}, V5_{eiL}$).

The rail location in the earth centered frame at the interrupter longitude is then rotated to the launch point longitude using equation 17.

$$\begin{bmatrix} N6_e \\ W6_{eOL} \\ V6_{eOL} \end{bmatrix} = \begin{bmatrix} 1 & 0 & 0 \\ 0 & \cos(\text{LONG}) & -\sin(\text{LONG}) \\ 0 & \sin(\text{LONG}) & \cos(\text{LONG}) \end{bmatrix} \begin{bmatrix} N5_e \\ W5_{eiL} \\ V5_{eiL} \end{bmatrix} \quad (17)$$

where LONG is interrupter longitude minus the launch point longitude. The location of the launch point is subtracted from the location of the interrupter (both in the N_e, W_{eOL}, V_{eOL} coordinate frame) to obtain the distance components between the launch point and the interrupter, ΔN_e , ΔW_{eOL} , and ΔV_{eOL} .

The distance between the launch point and the interrupter in the N_e, W_{eOL}, V_{eOL} frame is then transformed to the launch point astronomic tangent plane frame using equation 18.

$$\begin{bmatrix} X \\ Y \\ Z \end{bmatrix} = \begin{bmatrix} \text{Matrix B} \end{bmatrix} \begin{bmatrix} \cos(\text{LATO}) & 0 & -\sin(\text{LATO}) \\ 0 & 1 & 0 \\ \sin(\text{LATO}) & 0 & \cos(\text{LATO}) \end{bmatrix} \begin{bmatrix} \Delta N_e \\ \Delta W_{eOL} \\ \Delta V_{eOL} \end{bmatrix} \quad (18)$$

X, Y, and Z, are the components of the distance between the launch point and the west rail at an interrupter. Repeating the process for every interrupter determines the shape of the west rail in the astronomic tangent plane of the launch point.

4.4 Gravity.

The gravity components at each interrupter in the launch point astronomic tangent plane are calculated for use in the final position vector calculations. These position vector calculations can be found in a later section. Written as one equation, the transformation of gravity from the astronomic vertical at the interrupter to the astronomic tangent plane frame of the launch point (LCEF) is:

$$\begin{bmatrix} \text{GravX} \\ \text{GravY} \\ \text{GravZ} \end{bmatrix} = \begin{bmatrix} \text{MATRIX B} \end{bmatrix} \begin{bmatrix} \cos(\text{LATO}) & 0 & -\sin(\text{LATO}) \\ 0 & 1 & 0 \\ \sin(\text{LATO}) & 0 & \cos(\text{LATO}) \end{bmatrix} \begin{bmatrix} 1 & 0 & 0 \\ 0 & \cos(\text{LONG}) & -\sin(\text{LONG}) \\ 0 & \sin(\text{LONG}) & \cos(\text{LONG}) \end{bmatrix} \\
 \begin{bmatrix} \cos(\text{LATI}) & 0 & \sin(\text{LATI}) \\ 0 & 1 & 0 \\ -\sin(\text{LATI}) & 0 & \cos(\text{LATI}) \end{bmatrix} \begin{bmatrix} \text{MATRIX AI} \end{bmatrix} \begin{bmatrix} 0 \\ 0 \\ \text{GravI} \end{bmatrix} \quad (19)$$

The first transformation is from astronomic vertical to geodetic NWV coordinates at the interrupter by the inverse direction cosine matrix from the quaternion. The next transformation is from geodetic at the interrupter to the geodetic coordinates of the equator. Next, the geodetic NWV at the equator is rotated through the change in longitude to the longitude of the launch point. The next rotation is from the equator to the latitude of the launch point and the final rotation is from geodetic north-west-vertical at the launch point to LCEF.

5.0 LVDT DATA COLLECTION

At this point in the calculations the reference consists of the location of the west rail (at intervals corresponding to interrupter locations) relative to the launch point in the LCEF reference frame. As mentioned above, the test article is carried downtrack in a sled whose outer body rides on the track. The system under test rides on a pallet that is separated from the sled's outer body by isolators. Therefore, the system senses motion relative to the sled outer body and hence to the west rail. Typically, six linear variable displacement transducers (LVDTs) are used to measure the pallet movement relative to the rigid sled body. These six LVDTs are divided so that two LVDTs measure the displacement in each direction, downtrack, crosstrack, and vertical. The LVDTs are placed so that an average of the two measuring the same direction will approximate the motion of the center of the pallet relative to the sled.

A seventh LVDT is used in tethered tests. Some tests require that the sled be tethered at the launch point for several seconds after the engines fire in order to obtain the desired acceleration profile. While the sled is tethered and the engines are firing, the sled moves a small amount downtrack due to slack in the tethering mechanism. The seventh LVDT, called the trackside LVDT, measures the amount the sled moves downtrack before the tether is released.

The downtrack (including the trackside LVDT if applicable), crosstrack, and vertical LVDT measurements at the interrupters plus the location of the west rail in LCEF gives the location of the pallet containing the test article relative to the launch point. However, the LVDT data can not be added directly to the west rail location (in LCEF) because the LVDT's measure in local rail coordinates (i.e., fixed to the sled) rather than LCEF. The LVDT data must be transformed to the LCEF coordinate frame before it can be included in the reference.

6.0 LVDT TRANSFORMATION

The transformation of the averaged LVDT data taken in rail coordinates to LCEF is almost identical to the transformation of gravity to LCEF. Some

assumptions have to be made in order to begin the transformations. Vertical is assumed to be along the local geodetic vertical, downtrack is assumed to be along the average track geodetic azimuth in the local geodetic tangent plane, and crosstrack is assumed to be mutually perpendicular to vertical and downtrack. Written as one equation, the transformation of LVDT data to LCEF is:

$$\begin{bmatrix} \text{LvdtX} \\ \text{LvdtY} \\ \text{LvdtZ} \end{bmatrix} = \begin{bmatrix} \text{MATRIX B} \end{bmatrix} \begin{bmatrix} \cos(\text{LATO}) & 0 & -\sin(\text{LATO}) \\ 0 & 1 & 0 \\ \sin(\text{LATO}) & 0 & \cos(\text{LATO}) \end{bmatrix} \begin{bmatrix} 1 & 0 & 0 \\ 0 & \cos(\text{LONG}) & -\sin(\text{LONG}) \\ 0 & \sin(\text{LONG}) & \cos(\text{LONG}) \end{bmatrix} \begin{bmatrix} \cos(\text{LATI}) & 0 & \sin(\text{LATI}) \\ 0 & 1 & 0 \\ -\sin(\text{LATI}) & 0 & \cos(\text{LATI}) \end{bmatrix} \begin{bmatrix} \cos(\text{TKAZ}) & -\sin(\text{TKAZ}) & 0 \\ \sin(\text{TKAZ}) & \cos(\text{TKAZ}) & 0 \\ 0 & 0 & 1 \end{bmatrix} \begin{bmatrix} \text{LVDTDT} \\ \text{LVDTCT} \\ \text{LVDTV} \end{bmatrix} \quad (20)$$

where,

LVDTDT is the average of the two downtrack LVDTs, plus the trackside LVDT,

LVDTCT is the average of the two crosstrack LVDTs,

LVDTV is the average of the two vertical LVDTs, and

LVDTX, LVDTY, and LVDTZ, are the X, Y, and Z LVDT values in LCEF.

The first transformation is a rotation from geodetic downtrack, crosstrack, and vertical to geodetic NWV coordinates at the interrupter by the average track azimuth. The next transformation is from geodetic NWV at the interrupter to the geodetic NWV coordinates of the equator. The resulting vector is then rotated from the geodetic NWV at the equator to the longitude of the launch point by the difference in longitude. The next rotations are from the equator to the latitude of the launch point, and, finally, from geodetic NWV at the launch point to astronomic XYZ at the launch point.

LVDT data is referenced to time (as measured by a LVDT clock) rather than location along the track. In order to include the LVDT data in the reference position vector, the location along the track must be correlated with the time the sled passed it.

7.0 TIME CORRELATION

The position vector, up to this point, consists of survey data transformed to LCEF and referenced to interrupter station number, space-time data, i.e., the time the sled passed each interrupter, and LVDT data referenced to time. The data from the test article is also referenced to time. Therefore, it is essential to reference the position vector to time.

The space-time data is the link between time and location. By simply matching the station numbers from the two sets of data, space-time and survey, the time correlated survey data is produced. The LVDT data is then interpolated to the space-time time series, transformed to LCEF, and added to X, Y, and Z from equation (18) to create the position vector which can be compared to the navigated output from a system under test.

The space-time data, LVDT data, and the test article data are time

tagged by separate clocks. Before these three sets of measurements can be correctly combined, the three clocks must be aligned. The alignment process may include applying a scale factor and/or bias to one or more of the clocks.

8.0 GRAVITATIONAL AND CORIOLIS ACCELERATION COMPENSATION

The inertial test article senses the specific force due to gravity and coriolis acceleration. Some test articles compensate for these acceleration forces and output a navigated position, while others do not and output a guided position. In order to compare the reference position vector to the guided position of the test article, position changes sensed by the inertial unit due to gravity and coriolis acceleration must be added to the position vector created in the previous section. The calculation of the position changes due to gravity and coriolis are described next.

8.1 Gravity.

In order to add gravitational acceleration to the position vector, the three components of gravity in LCEF (see para. 4.4) are integrated twice with respect to time to provide position components in X, Y, and Z. Integration is done using trapezoidal integration.

8.2 Coriolis Acceleration.

The common form of the coriolis acceleration equation is:

$$\text{coriolis accel.} = 2W_e \times V \quad (21)$$

where,

W_e = angular rate of the earth, and
 V = velocity of object moving on earth.

The earth rate used in equation (21) is the earth rate of the launch point in LCEF coordinates. The earth rate of the launch point is calculated using the following equation:

$$\begin{bmatrix} W_1 \\ W_2 \\ W_3 \end{bmatrix} = \begin{bmatrix} \text{Matrix B} \end{bmatrix} \begin{bmatrix} \cos(LAT0) & 0 & -\sin(LAT0) \\ 0 & 1 & 0 \\ \sin(LAT0) & 0 & \cos(LAT0) \end{bmatrix} \begin{bmatrix} w \\ 0 \\ 0 \end{bmatrix}$$

where,

$w = 7.29211585 \times 10^{-5}$ rad/s, (15 deg/hr)

W_1, W_2, W_3 , are the components of earth rate at the launch point,
 W_0 , and

Matrix B is as defined in paragraph 4.2.

In order to find the position due to coriolis acceleration, equation (21) is integrated twice with respect to time.

$$\text{coriolis position} = 2W_0 \int_{t_0}^{t_1} (\text{distance travelled}) dt$$

When the input distances travelled are in LCEF, the output coriolis positions will also be in LCEF.

9.0 CONCLUSION

Because the track is no longer surveyed independently of the conventional survey datums, the calculations done to create the reference position vector have been improved to take advantage of the better survey. There are fewer assumptions made in the survey transformation described here than previously used. Therefore, this new method of obtaining a reference position vector is currently being used for all guidance sled test analysis.

REFERENCES

1. Defense Mapping Agency; 'Geodesy For The Layman';DMA TR 80-003, (December 1983)
2. Lenzo, J., 'Test Planning Information, Sled Testing of Guidance Systems and Components', (1987)
3. Holdeman, Richard E., 'The Use of the Holloman Track Reference System in the Quantitative Testing of Inertial Guidance Systems', AFMDC Technical Report MDC-TR-70-7, (Feb 1970)
4. Hosmer, George L., 'Geodesy', John Wiley Sons, Inc., (July 59)
5. White, Jerry E., Bate, Roger R., Mueller, Donald D., 'Fundamentals of Astrodynamics', Dover Publication, Inc., (1971)

**ROBOTICS APPLICATIONS IN THE TESTING
OF INERTIAL SENSORS**

Joy Y. Greig

**Central Inertial Guidance Test Facility
6585th Test Group, Holloman AFB, NM**

**Zdzislaw H. Lewantowicz
Air Force Institute of Technology
Wright-Patterson AFB, OH**

Unclassified; Distribution Unlimited

Abstract

This study investigates the technical and economic feasibility of using robots as low to medium grade testbeds for inertial sensors in lieu of the current generation of unique, expensive, and relatively inflexible gyro and accelerometer test facilities.

A PUMA 560 robot arm is used as the experimental testbed. The design and demonstration of three tests are described which illustrate the alignment, calibration, and resulting performance of the robot as a test device. Actual high precision inertial accelerometers and gyros were used to establish a performance baseline and to evaluate the robot's test capabilities.

The robot was programmed to act as a precision test servomechanism which was calibrated and aligned automatically using the high quality sensors. The robot was effective in providing quick-look results of error coefficient parameters for bias, scale factor, and elastic (g -squared) effects, but as expected could not provide inherently the precision required for very high quality sensor testing.

Testing was easily implementable and varied to suit individual applications, and this illustrated the value and potential for devising new tests which cannot be performed on existing precision test equipment. The problem of lack of precision was investigated using an advanced computer simulation. This simulation shows that there are serious limitations due to unmodeled noise and flexure of the robot arm, which is significant for the high precision required for inertial testing. The need for this precision does not have to be supplied by the robot, however, if sufficiently precise calibration tools (e.g. lasers) are used to establish reference position and attitudes. Economic analyses established that, given precision measurement capability, using a robot arm as a test mechanism is viable, cost effective, and a practical engineering test procedure.

I. Introduction

Specialized test facilities, such as the Central Inertial Guidance Test Facility (CIGTF) at Holloman Air Force Base, New Mexico, are responsible for the testing of high quality inertial rate sensors and accelerometers. Due to the large investment in resources, it is important that all sensors be free from major defects when scheduled for precision testing. Initial sensor checkout tests, for example, should not tie up unique and specialized test equipment which may cost millions of dollars (2).

Although these expensive devices for testing inertial sensors have been very effective, due to their unique design they often lack the flexibility required to implement new test procedures. Moreover, there is little evidence of rapid innovation in designing and building new test fixtures with enhanced capabilities. These problems of cost, inflexibility, and lack of new capabilities impose significant constraints on component testing programs.

A potential approach to addressing these problems comes from the rapidly developing engineering science of robotics, where cost is decreasing due to the exponential rise in the number of units being produced (increasing from 20,000 units in 1976 to 250,000 in 1984), and where the digital capabilities being designed into robots have the potential to provide flexibility in systems tests and data acquisition (16). Finally, robotics is a highly innovative area fueled by vast research funding. It is probable that if the key difficulty of precision can be solved, the use of programmable robots for inertial testing should become a reality.

This paper discusses the feasibility of robotics applications to inertial component testing by addressing three major areas: technical feasibility, economic feasibility, and limitations.

Technical feasibility is discussed in Section II where the design and implementation of three tests using a PUMA 560 robot arm (19;20) are accomplished. These are a vertical-seeking test for robot arm alignment, an accelerometer four-point test for investigating robot precision, and a

gyroscope step-tumble test for demonstrating robot adaptability.

Also in Section II robot performance criteria for supporting inertial sensor testing are developed. Current industrial robots which meet the criteria are identified (18), and four are selected for study and comparison with three non-robotic precision test units.

Section III contains an investigation of economic feasibility where simple life cycle costs for robots are defined and compared with the non-robotic units of Section II (9:1).

Current robotics limitations are discussed in Section IV, and the attempt to solve the precision problem using computer simulations is illustrated by a case study. The robot simulator used is the Integrated Robotic System Simulation Program ROBSIM developed by Martin Marietta Denver for NASA Langley (3).

Section V examines the potentials of robotics for precision sensing, cost reduction, and development and application of new test technologies. Recommendations are made for further research and development of robotics applications to inertial sensor testing.

II. Technical Feasibility

The robot in itself is not a precision test device relative to inertial sensor accuracies. These accuracies were investigated in this study to determine the feasibility of using a robot as a testbed. Three tests on a PUMA 560 robot arm were accomplished to illustrate this and to examine robot performance criteria for sensor/system laboratory testing.

Robot Alignment

As with any other test stand, a robot must be calibrated and aligned. To demonstrate the alignment of the robot arm with local vertical, a vertical-seeking test was designed, using the output of a Systron-Donner 4841F accelerometer and the PUMA 560's operating system to accomplish the calibration. In an actual testing situation a high-precision accelerometer, a triad of accelerometers, a laser, or some other means could be used either to verify the robot's position or to position it (if its own positioning system were limited). In this demonstration, however, a single accelerometer was used to locate local vertical.

The direction of vertical could be determined by simply maximizing a single accelerometer reading and using a numerical algorithm to zero in on vertical. However, most practical applications are faced with limited numerical accuracy in reading an accelerometer. Because of the non-linear nature of accelerometer reading accuracies, it is more accurate to find the horizontal plane.

Locating the horizontal plane defines a vector which lies in a plane 90 degrees from the gravity vector. To locate the vertical, however, determination of a second horizontal vector perpendicular to the first is required. The cross-product of two vectors in the horizontal plane yields the desired location of vertical. (For an expanded discussion of the theory behind finding horizontal, the reader is referred to Reference 10.)

The natural precision geometry of the PUMA 560 manipulator (see Figure 1) supplies the proper configuration to determine vertical. Since horizontal is determined twice, it is desirable to obtain two determinations of vertical about perpendicular axes of rotation and implement this for joints with the largest degrees of rotational freedom. It is also desirable to minimize the actuator command torque required to hold the arm in position as well as the horizontal extension of the arm, as they may lead to errors in determining the orientation of the accelerometer in relation to the PUMA 560 (11). These criteria lead to the natural choice of Joint 5 (wrist bend) in conjunction with a 90 degree rotation in Joint 1 (waist); see Figure 1.

The first horizontal vector is determined with the PUMA 560 in the READY position, where the axis of rotation of Joint 5 is parallel to the World y-axis (the World Coordinate System is the base coordinate system indicated in Figure 1). It is assumed that the input axis of the accelerometer lies in

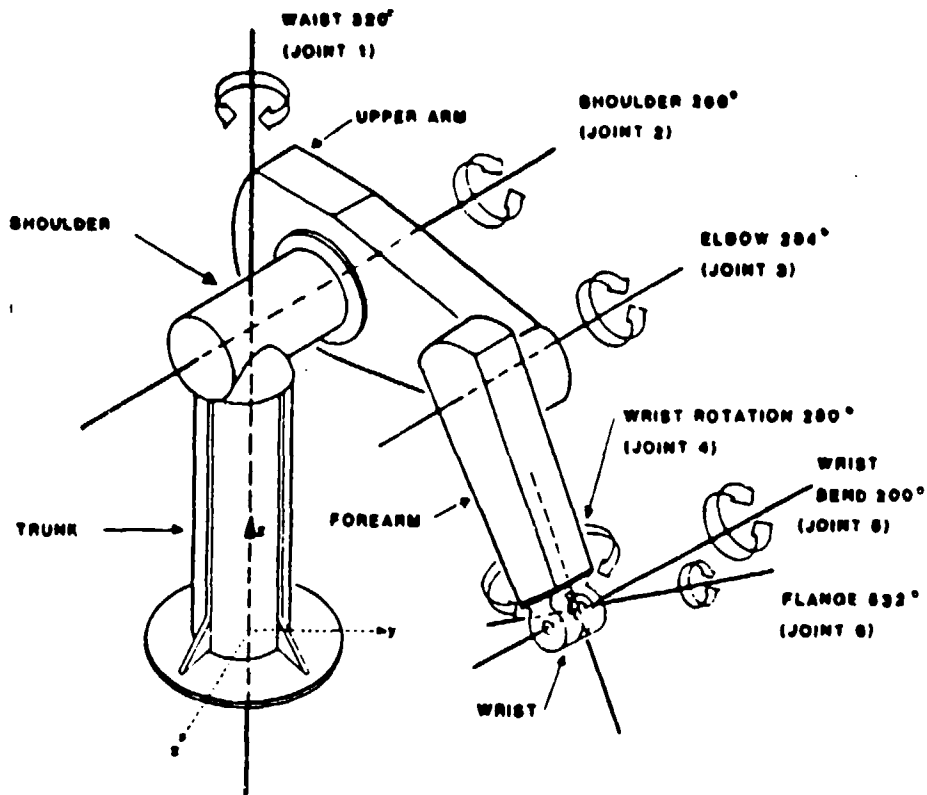


Figure 1. PUMA 560 Robot Arm (Reference 19)

the World x-z plane. This assumption allows the determination of the direction of the input axis of the accelerometer when it has been oriented in the direction of vertical by decomposition of the position of the tool. Decomposition of a point yields the following information:

X Y Z O A T

where X, Y, and Z define the position of the tool in World coordinates and O, A, and T are angles which define the orientation of the tool (Figure 2). The variable A defines the angles between the tool z-axis and the x-y plane.

The tool z-axis is horizontal and lies along the unit vector

$$V_1 = \cos A_1 i + 0j + \sin A_1 k \quad (1)$$

which is defined in the World Coordinate System.

The second horizontal vector is then determined by placing the rotational axis of Joint 5 parallel with the World x-axis. The tool axis is positioned horizontally by rotation about the Joint 5 axis; it is assumed that the accelerometer input axis lies in the World y-z plane. The tool z-axis then lies along the unit vector:

$$V_2 = 0i + \cos A_2 j + \sin A_2 k \quad (2)$$

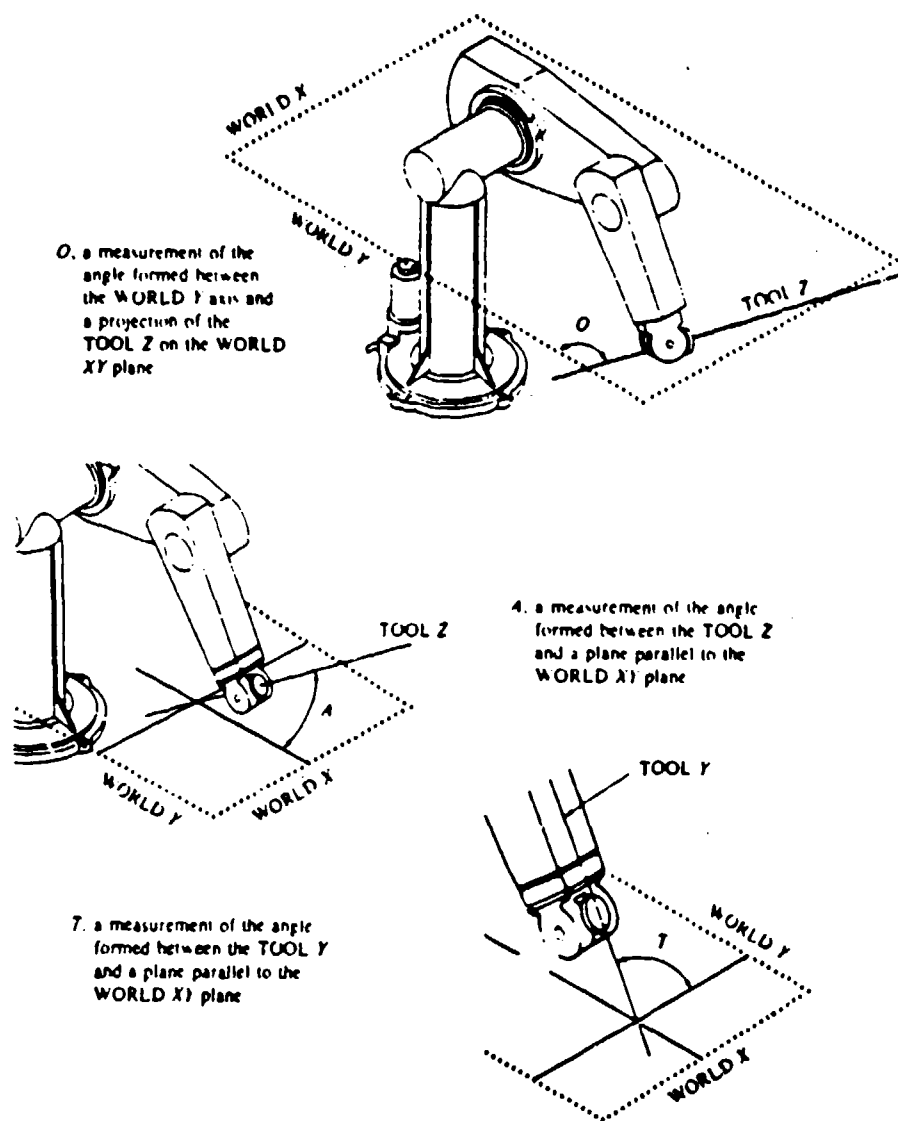


Figure 2. Definition of Euler Angles O, A, and T

which is defined in the World Coordinate System.

The cross product of the vectors $V_1 \times V_2$ (a vector oriented along vertical) can be defined as the determinant of the following matrix:

$$V_3 = \begin{vmatrix} i & j & k \\ \cdots & v_1 & \cdots \\ \cdots & v_2 & \cdots \end{vmatrix} \quad (3)$$

Substituting for Equations (1) and (2) yields:

$$V_3 = \begin{bmatrix} i & j & k \\ \cos A_1 & 0 & \sin A_1 \\ 0 & \cos A_2 & \sin A_2 \end{bmatrix} \quad (4)$$

$$V_3 = -\cos A_2 \sin A_1 i - \cos A_1 \sin A_2 j + \cos A_2 \cos A_1 k \quad (5)$$

This vector contains the information needed to position the tool z-axis along the calculated direction of vertical. An angle θ_1 is defined as the arctangent of the World x and y components of Equation (5):

$$\theta_1 = \tan^{-1} \left[\frac{\cos A_1 \sin A_2}{\cos A_2 \sin A_1} \right] \quad (6)$$

An angle θ_2 is defined as the angle between the world z component of Equation (2.11) and the World x-y plane:

$$\theta_2 = \tan^{-1} \left[\frac{\text{SQRT}[(\cos A_1 \sin A_2)^2 + (\cos A_2 \sin A_1)^2]}{\cos A_2 \cos A_1} \right] \quad (7)$$

Note that the sign of the numerator and denominator is important for uniquely defining an angle. The arctangent function in the VAL II programming language requires the input of the numerator and denominator separately.

The angle θ_1 can be used to define the O angle in the world x-y plane while the θ_2 angle is used to define the A angle. The PUMA 560 is then oriented in this direction.

These algorithms are implemented on the PUMA 560 using the Unimate controller and VAL II programming language. The simulation produces two points V_1 and V_2 . These two points are defined in Table 1.

The cross product of these two vectors is defined as (see Equations (3) and (4)):

$$V_3 = \begin{bmatrix} i & j & k \\ \cos(1.071) & 0 & \sin(1.071) \\ 0 & \cos(.917) & \sin(.917) \end{bmatrix} \quad (8)$$

$$V_3 = -0.0187 i - 0.0160 j + 0.9997 k. \quad (9)$$

The angles θ_1 and θ_2 are then calculated from Equations (6) and (7):

$$\theta_1 = \tan^{-1} \left[\frac{-0.0160}{-0.0187} \right] = 220.55^\circ \quad (10)$$

$$\theta_2 = \tan^{-1} \left[\frac{0.0246}{0.9997} \right] = 1.406^\circ. \quad (11)$$

Table 1 Position and Orientation of Points V1 and V2						
Point	X*	Y	Z	O**	A	T
V1	36.00	149.09	863.81	90.006	1.071	0.000
V2	-149.09	36.03	863.97	-180.000	0.917	-0.011
* X, Y, and Z are in millimeters						
** O, A, and T are in degrees						

The PUMA 560 is oriented according to these two angles.

Since the Systron-Donner 4841F accelerometer was the most accurate instrument available for the study, analysis was limited to that of a qualitative nature. First, visual inspection could ascertain whether the tool was oriented in the direction of vertical. Visual inspection of the orientation of the tool did indicate that the vertical-seeking algorithm found vertical.

Secondly, one would expect the z axis of the World Coordinate System to be roughly aligned with vertical; therefore, the cross product of the two vectors situated in the horizontal plane is a vector that has its major component along the World z axis. Equation (9) clearly shows that this is the case.

The theory and analysis presented here have presumed no robot joint positioning errors. There are, however, small accumulated errors via quantization of robot movement and calculations by the robot arm controller (19). No attempt was made to include these errors in the vertical-seeking algorithm. The algorithm did, however, locate vertical more precisely than could be done by simply placing the arm in the "ready" position, or by using a single accelerometer output determination.

Robot Precision

The degree of testing precision achievable with the PUMA 560 Robot Arm was investigated by performing an accelerometer four-point test using the arm as a testbed and the Systron-Donner 4841F as the test item. The accelerometer output was analyzed by calculating and determining the stability of the accelerometer scale factor, 1-g bias, null bias, and misalignment angle.

The complete performance-model equation for an accelerometer can be found in Reference (10). The +1g (90°) and -1g (270°) positions of the accelerometer are used to determine the 1g bias (M_0) and the two-point scale factor (M_1). The null positions (0° and 180°) yield the accelerometer null bias (N_0) and misalignment error (δ_0) (21:A-3). These characteristics are calculated using the following relationships:

$$M_1 = K_1(1 + K_3) = 1/2 [E(90^\circ) - E(270^\circ)] \text{ (output units/g)} \quad (12)$$

$$M_o = K_o + K_2 = [E(90^\circ) + E(270^\circ)]10^6/2M_1 \text{ (}\mu\text{g)} \quad (13)$$

$$N_o = K_o + K_{pp} = [E(0^\circ) + E(180^\circ)]10^6/2M_1 \text{ (}\mu\text{g)} \quad (14)$$

$$\delta_o = \delta_o + K_{ppp} = [E(0^\circ) - E(180^\circ)](2.06 \times 10^5)/2M_1 \text{ (arcsec).} \quad (15)$$

Experiment Methodology. The Systron-Donner 4841F accelerometer is a conventional single-axis, pendulous, fluid floated, torque rebalance accelerometer, with an analog output in volts direct current (VDC) proportional to the applied acceleration. For the series of four-point tests, the accelerometer was secured to an aluminum mount which was screwed on to the robot tool flange (see Figure 1). The robot arm was aligned parallel to local gravity. The pendulous axis (PA) of the accelerometer was aligned parallel to the Y-axis of the tool flange (see Figure 1) and its input axis (IA) perpendicular to the Y-axis of the tool flange. The robot wrist joint was rotated 90 degrees, followed by a 90 degrees rotation of Joint 5, in order to position the accelerometer IA up and parallel to local vertical. The flange was then rotated in the following pattern (21:A-3):

- a. Initial position at 90 degrees (IA up)
- b. Rotate clockwise (CW) to 270 degrees (IA down)
- c. Rotate counterclockwise (CCW) to 180 degrees (IA horizontal-null)
- d. Rotate CW to 0 degrees (IA horizontal null)
- e. Return to 90 degrees.

The software was designed to rotate the accelerometer to the four positions and allow sufficient time to read the accelerometer output voltage at those positions. This was accomplished by the VAL II operating system DRIVE command to rotate the accelerometer to the four positions by rotating Joint 6 (the flange) the appropriate number of degrees.

Results. The results of the four-point test are summarized in the following table. Although the performance characteristic values are larger than those derived from four-point tests of similar instruments (see Table 2.3 from 21:27-28), the standard deviations and peak-to-peak spread are comparable. The laboratory environment for this research was much less controlled than that of a test facility such as CIGTF; noise sources from the laboratory and perhaps from the robot arm itself, and lack of temperature control contributed to the magnitude of the coefficients. However, the stability of the outputs is an indication of the positioning repeatability of the robot arm.

The goal of the four-point tests was to investigate the degree of testing precision achievable with the PUMA 560 Robot Arm. The data showed that positioning precision can be achieved. This demonstrates that the robot is certainly a viable testbed for performing initial performance checks on a high-accuracy sensor, and perhaps the evaluation tests as well on lower-accuracy instruments. A more controlled test environment and an evaluation of the noise characteristics of the robot arm are necessary to completely determine its potential for evaluation tests of high-accuracy sensors.

Robot Adaptability

Robot adaptability was demonstrated by performing a gyroscope (gyro) step-tumble test. This test demonstrated the maneuverability of a robot arm and the ease of reconfiguring the robot for different tests. For the step-tumble test the robot must be positioned to align the gyro's output axis parallel to the earth's rotational axis pointing north and then pointing south. The output of the gyro in these orientations is used to calculate the gyro drift characteristics. (For a thorough discussion of the gyro error model and drift coefficient determinations, see References 10 and 22.)

Experiment Methodology. The gyro used for the experiment was a Humphrey Model RG51-0106-1, a conventional single-degree-of-freedom (SDOF) torque-rebalanced rate gyroscope. The PUMA 560 Robot Arm was used as the test platform. The gyro was mounted to a metal support base

Table 2 Accelerometer Performance Characteristics from Four-point Tests				
	Scale Factor (volts/g)	1-g Bias (μ g)	Null Bias (μ g)	Misalign (arcsec)
ON ROBOT ARM:				
Mean	1.018805	1207	1720	8154
Standard Deviation (ppm)	29	60	66	9
Peak-to-peak Variation	115	241	255	30
ON VERTICAL TABLE (21:27):				
Mean	0.02493	184.5	148.4	-30.6
Standard Deviation (ppm)	40	45.8	36.4	7.5
Peak-to-peak Variation (ppm) *	471	471	244	58
* Over 39 days. No data available for a single day's testing.				

which was in turn attached to the robot flange. The step-tumble test required the following gyro orientations to separate the drift coefficients for the gyro:

(1) Gyro OA parallel to the earth's spin axis (EA) pointing north, IA pointing west at the start of the rotations (OA \parallel + EA)

(2) OA parallel to EA pointing south, IA pointing west at the start of the rotations (OA \parallel - EA)

To align the gyro with the EA it was first necessary to determine the relationship between the PUMA World Coordinate System (WCS) and the EA. To find the WCS relative to EA it was necessary to know the latitude of the robot and the direction of True North with respect to the robot. This information was readily available for the test site and was used to determine the proper robot joint angles to align the gyro OA with the EA.

Once the OA and IA were properly aligned, the gyro was stepped through 360 degrees of rotation by rotating the flange 360 degrees clockwise (cw) followed by 360 degrees counterclockwise (ccw), pausing at each 45-degree increment. One cw and ccw rotation of the flange for each orientation constituted one set of data for each step-tumble test. Eight sets of data were collected with OA south and eight with OA north (a total of 128 points in each direction).

The software was written for the robot's VAL II operating system which was accessed through a Zenith 100 (Z-100) running communication software to act as a smart terminal. The programs,

written in the VAL II language, positioned the robot arm for each of the required gyro orientations and rotations.

Results. The statistical package BMDP was used to perform the least squares fit of the output voltage to the gyro model. Table 3 summarizes the drift coefficients (and their standard error) of the performance model equation.

Since the duration of the tests was approximately three hours and the gyro's output axis was aligned with the earth's rotational axis, error sources did not include earth rate. All drift coefficients except D_0 were significant. From previous rate-table tests D_F was determined to be 1.5 volts. Except for D_F , there was no test data with which to compare the drift coefficients. However, the coefficients are reasonable, and as with the accelerometer four-point tests indicated the feasibility of using the robot arm for testing inertial sensors.

The main purpose of the gyro test was to demonstrate the robot arm's ease of reconfigurability and its maneuverability and therefore its usefulness as a multi-purpose testbed. This was clearly demonstrated by the gyro step-tumble test.

Robot Performance Criteria

A final important aspect of determining technical feasibility is to answer the questions:

- (1) What are the robot performance criteria for inertial sensor/system testing?
- (2) Which of today's robots meet those criteria?

All the criteria for selecting a robot for industrial applications are fully described in the robotics literature (6:214-301; 12:263-272; 15). In this study we are addressing only the criteria pertinent to inertial sensor/system testing.

Table 3 Performance Model Equation Coefficients		
Drift Coefficient	Calculated Value	Standard Error
D_F	1.49999	0.00188
D_I	0.00249	0.00031
D_s	0.07619	0.00031
D_0	0.00188	0.00295
D_{Is}	0.00117	0.00035
D_{II}	0.00107	0.00035
D_{ss}	0.00107	0.00035
D_{OI}	0.00389	0.00036
D_{Os}	0.00120	0.00036

Load Requirement. Today's inertial sensors weigh five to ten pounds, and inertial measurement units (IMU's) weigh up to twenty five pounds (4). The weight of the sensor/system plus its mount or gripper determined the robot load requirement for this research.

Drive Method and Number of Axes. The class of robots considered was electric motor driven manipulators with six degrees of freedom. Electric motor drives were selected because they are the most accurate over the load requirement range (10:109-111). While six degrees of freedom reduces stiffness with some resultant loss of accuracy, it allows a greater variety of configurations. This makes the robot adaptable to a wider range of test situations and allows for the development of new types of tests not possible on existing test equipment.

Axis Rotation. The static gyro and accelerometer tests demonstrated the need for at least one joint to rotate 360 degrees or more. This capability is most frequently available at the robot wrist (the PUMA 560 flange, for example, was a part of the wrist assembly). Other joint rotations are important also, as in the gyro step-tumble test. Thus wrist pitch, roll, or yaw of 360 degrees or more is required, and maximum rotation of the other three joints should be at least 180 degrees.

Robot Task Programming. Robot tasks in industrial applications are frequently programmed by manual or lead-through teaching methods (12:210-216, 266-271). However, this is not practical for the inertial sensors/systems application. The robot must respond to algorithmic commands, especially in dynamic tests. Off-line programming using either robot programming languages or standard languages provides instructions to move the manipulator, read sensors, send output signals, and many other instructions essential to sensor/system testing (12:216). Off-line programming also permits the development of several programs at once. Therefore off-line programming capability is essential.

Positioning Accuracy. Positioning accuracy is another characteristic to consider in robot selection. Positioning accuracy is defined as "the difference between the position desired and the position actually achieved" (6:76). Repeatability is a statistical term associated with accuracy. It is a measure of the difference between successive movements to the same commanded position (6:76). Since the accuracy depends upon the particular load that the gripper carries, most robot manufacturers provide a numerical value for repeatability rather than accuracy (12:19). The requirement for inertial sensor/system testing is to achieve the greatest positioning accuracy and repeatability possible. For today's robots that means a repeatability of 0.010 inches or less.

Other Criteria. Variable acceleration and/or deceleration capability is an asset, and in fact a requirement for some dynamic testing. The robot mount is a final consideration. Robot manipulators may be mounted to the floor, the wall, or overhead (gantry). In general the authors believe that the floor mount is most desirable. Floor "mounted" robots can be moved from one location to another fairly easily for the situation in which they are being used as a "quick-look" test stand at different test stations. A floor mounted robot is more stable and less susceptible to positioning errors caused by joint and link flexures than a wall mount, and does not require the elaborate installation structure of a gantry model.

Identification of Suitable Robots. A comprehensive listing of prospective robots containing their physical characteristics and estimated base prices was obtained (18) using a commercial computer package called "Robot Search Program" (Robot Analysis Associates, Inc.). This list was reduced to four robots by entering the data into a spreadsheet (Lotus 1-2-3) and using the spreadsheet's capabilities to highlight the manipulators with the maximum performance capabilities (5:435-448) and is summarized in Table 4.

The final choices from the spreadsheet analysis are the first three on the list. The PUMA 560 is included because it was the robot used in this research; it was not selected by the Robot Search Program because of its maximum load of only 5.5 pounds.

The non-robotic tables have the advantage of continuous rotation and accuracies in the arcseconds range. However, the load capabilities are comparable, including the 100-pound load. For example, in addition to the robots listed above, the Cincinnati Milacron T3-776 meets the rotational and accuracy requirements while carrying a load of 150 pounds. The robotic testbeds, however, are more versatile and less expensive and have other potentials which are discussed in Section V.

Table 4
Performance Characteristics and Base
Prices of Robotic and Non-Robotic Testing Units

Name	Mount	Max Rot (Wrist)	Other Rot	Joint	Max Load (lbs)	Accuracy (ins)	At (ips)	Variable Accel/Decel	Base Price
A'matix AID-900	Floor	440	p315	Wrist	66	0.008	30	Y	50000
Yaskawa	F/O/W	360	YR330	Wrist	26	0.008	80	Y	69600
Cinn Mil T3-646	Floor	900	PY238	Wrist	50	0.010	25	N/A	70000
PUMA 560	Floor	532	P200	Wrist	5.5	0.004	20	N	80000
Name	Mount	Max Rot (Wrist)	Other Rot	Joint	Max Load (lbs)	Accuracy (arcsec per axis)	At (ips)	Variable Accel/Decel	Base Price
Vertical Table	F	Contin.			50	< 1		N	150000
2-axis Contraves		Contin.			75	1		N	500000
3-axis Contraves	Floor	Contin.			100	# 3		N	## 3000000
# Difference in accuracy due to different type of bearings, not number of axes									
## Estimated cost of new 3-axis table									

III. Economic Feasibility

Once technical feasibility has been established, the next important question must be answered: "Is the proposal economically feasible?" This section assesses economic feasibility by performing a life cycle costing analysis for both the robotic and non-robotic testing units.

A vertical table, a 2-axis Contraves table, and a 3-axis Contraves table are the non-robotic testing units. Table 4 (of the previous section) shows the performance selection criteria of the four robots, the performance characteristics of the testing tables, and base prices for all units.

Estimated robot prices, even base prices, varied widely. Test table costs were obtained from the Central Inertial Guidance Test Facility (CIGTF), Holloman Air Force Base, New Mexico (4;2).

Life Cycle Costing

Life Span Costs. Life Cycle Costing (LCC) defines "life span" as the time to replacement or major modification (mechanical or electronic). Even though major mechanical modifications may occur only every ten years or so, advances in electronics determine a life span of three to five years for robotic and non-robotic testing units alike (1:20; 2). Therefore, a life span of five years was chosen for the analysis.

Once the life span is determined, three specific costs must be analyzed (9:66-67):

- (1) Research and developments costs
- (2) Investment costs
- (3) Operational costs.

The variation of the costs must be estimated for each year of the unit's life. The costs are totaled for each year and then summed to calculate the LCC via the equation:

$$LCC = \sum_{i=1}^N \frac{R_i}{(1+r)^i} \quad (16)$$

where:

- LCC = Life Cycle Cost
- R_i = Yearly Costs (R & D + Investment + Operational)
- i = Year number
- r = Interest rate (10% assumed).

Lotus 1-2-3 automatically calculated the LCC. Formulas were entered into the spreadsheet cells, which facilitated rapid and efficient economic analysis without writing computer programs. More detailed LCC determination can include calculating cost ranges for each item, assigning probabilities to the estimates, and thus including random variables, which does require some programming. The results can then be compared via a spreadsheet analysis.

Research and Development Costs. Research and development (R & D) costs are defined as "the resources required to develop the new capability to the point where it can be introduced into the operational inventory at some desired level of reliability" (9:66). The economic study is for the development of a prototype robotic test station, and thus the R & D costs are greater than they would be for a previously developed robotic test station. R & D estimates included in the study were:

- Investigation of which "standard" tests can be performed on a robot
- Research to determine which robot best suits the application
- Development of software for tests
- Installation of precision measuring device, such as lasers (or adaptation of lasers presently used in robotics (14))
- Development of new "non-standard" tests using the full robotics capabilities; costs included development of theory, software and testing and comparison with the results of non-robotic units.

Based on the equivalence of one man-year of work plus computer time, the first year's R & D cost was estimated to be \$40,000, 15% of that amount for year 2, 5% for year 3, and 1% for each of years 4 and 5. The continuing R & D costs were for ongoing development of new tests and study of the applicability of new robots on the market.

R & D costs for the vertical and 2-axis tables were 15% of the robot costs for the first year, to account for changes in electronics which could be introduced. However, the new 3-axis table being developed was treated the same as a prototype robot for the first 3 years, using the same R & D percentages.

Investment Costs. Investment costs are one-time outlays required to introduce some capability into the operational inventory (9:66). Investment estimates were adapted from manufacturing applications (1) as follow:

1. Base price. For this study the base price included the robot arm, controller, and teach pendant.
2. Support costs--15% of the base price.
 - Additional disks
 - Interface with existing data acquisition hardware and software
 - Installation, including mounts and safety arrangements
3. "Soft" costs--25% of the base price.
 - Training of personnel in use of hardware and software
 - Training of personnel in use of hardware and software
 - Programming/Systems analysis
 - Integrated data acquisition system documentation

Investment costs were spread over a two-year period, with 100% of the Initial Total Cost in year 2 and an additional 10% for unaccounted-for costs in year 3. Investment cost allocation was the same for robots and testing tables.

Operating Costs. Operating costs, the "recurring outlays required year by year to operate and maintain the capability in service over a period of years," (9:67) included:

- Maintenance
 - (1) Parts replacement
 - (2) General upkeep of arm (periodic oiling of joints, calibration, etc.)
- Periodic personnel training.

For the robots, years 2 and 3 were estimated at 20% of the total investment cost, year 4 was 10% of the total, and year 5 included periodic retraining costs and was estimated at 25% of the total investment cost. More specific figures are available for the testing tables (2). Operating costs for years 2 and 5 included both maintenance and personnel training; years 3 and 4 were maintenance expense only.

The life cycle costs of the robot arms and test tables are presented in Table 5.

Results

From the above analysis it is feasible that a prototype robotic test station, the T3-646 for instance, could replace one table, perhaps the vertical table, with a resultant decrease in LCC of \$17,364. Of course the savings increase substantially if the robot replaces the 2- or 3-axis tables.

Another important advantage and source of savings is the versatility of a robot arm. Over the long term both standard and experimental inertial instrument tests can be performed by simply reprogramming the robot, rather than rebuilding or developing a new test table. In the short term, as was the case for the gyro tests, the robot can be quickly reconfigured at any point in the test with no manual readjustments involved.

IV. Limitations

In this section the technical limitations of robots are discussed in detail as they relate to testing. Practical engineering limits, computer modeling limits, and measurement and instrumentation limits

Table 5 Total Life Cycle Costs	
Device	LCC
Automatix AID-900	\$ 146,279
Cincinnati Milacron T3-646	186,618
Yaskawa V-12	185,811
PUMA 560	206,787
Vertical Table	203,982
2-axis Contraves	522,239
3-axis Contraves	2,818,062

are examined and related to the sensor testbed application.

Practical Engineering Limits

Practical engineering limits include flexure of the links and joints of the robot arm (which will vary from one robot to another), and robot control schemes. A simple test using the PUMA 560 arm and the Robotic Simulation (ROBSIM) program demonstrated these limitations imposed.

The PUMA 560 has six joints. These experiment used only two of these joints, the shoulder and the flange. As the shoulder link rotates from the vertical, it exerts a large moment about the base y-axis due to gravity (see Figure 1). This produces a bend in the robot arm which is measurable by a high accuracy accelerometer mounted on the end of the arm. The flange on the other hand, with a smaller radius of rotation and mass, exerts a much smaller moment about its x-axis. The Systron-Donner 4841F accelerometer was first mounted on the flange, then the flange was rotated from the vertical 90° and back about its x-axis in 10° increments. The experiment was then repeated in the same configuration but with the flange fixed and the shoulder rotated in 10° increments about the base y-axis starting from a vertical position. The results showed larger shoulder rotation alignment errors than flange alignment errors when the position was 30° to 90° from vertical. Next a plot of the actuator torque versus time for the shoulder rotation was generated by the Robotic Simulation ROBSIM (discussed in the "Computer Modeling Limitations" section which follows).

The accelerometer outputs demonstrated the inaccuracies of robot positioning and indicate that the flexibility of the robot arm should be a consideration when precise positioning and orientation is needed. The ROBSIM plot showed that the torque is a function of the robot orientation and that the orientation errors are due in part to mechanical flexure.

Robot control is also limited by control method and unmodelled forces, and by the restrictions of robotic programming languages. The most widely used control method today applies a separate axial control loop for each joint designed with linear-control laws (12:80), often with fixed gain (12:72). The required gain is highly dependent on the moment of inertia at each joint of the robot arm which in turn varies with the arm position and robot payload. A variety of schemes, including adaptive control, have been proposed and implemented (12:51- 81), but research is still being done to represent previously unmodelled forces (13) and implement adaptive control.

Robotic programming languages, too, can be a control limitation in that they often do not include the facilities to implement complex mathematical formulas. One must bypass the robot operating system to implement experimental control techniques and gain greater precision.

Computer Modeling Limits

An important element in the effective use of robots and in designing unique inertial sensor tests for a robot is an accurate and comprehensive computer simulation program. Simulation programs are being developed in several different environments, including universities such as Arizona State University (17) and AFIT (3) as well as private industry. The Robotic Simulation (ROBSIM) program was installed and studied to determine both its advantages and its shortcomings. A brief overview of ROBSIM's capabilities may be found in Reference 10.

Applications. In many cases, computer simulation is directed strictly to industrial applications, including multiple arms, creation of workstations and assembly lines, and so forth. ROBSIM includes the industrial applications, but it also allows for simulation of different types of control schemes and for the creation of data files and plots of the robot forces, torques, etc. for analysis purposes. This makes it attractive for the testbed application.

Mechanical Model. The kinematic (and dynamic) analysis tools implemented in ROBSIM are based on a rigid-link model (8) of serial, open-loop kinematic chains with one-degree-of-freedom joints. (Details and examples may be found in the "Kinematics Analysis" section of Reference 7). Although this is not completely realistic, it does provide help in determining the behavior of the robot and the identification of possible flexure errors, as demonstrated in the flexure test above. The comprehensiveness and accuracy of the simulator's mechanical model of a specific arm is critical in determining the validity of the simulation.

Dynamics Model. An accurate dynamics model is also essential for acceptable simulation. ROBSIM uses homogeneous transformation matrices for calculating transformations between arbitrary sets of coordinates. The difficulty with robotics dynamics models relative to inertial navigation models lies in the differences of notation. There has as yet been little cohesion established between classical methods of inertial navigation and methods of describing the dynamics of robots. A means of melding the two fields is needed. The beginning of that melding is to parallel the dynamics equations and error analysis methods developed for robotics with the classical inertial navigation techniques. A notation to accomplish cohesiveness and followed by a tutorial presentation of introductory robot kinematics using inertial navigation notation is developed and presented in Appendix F, Reference 10.

Measurement and Instrumentation Limits. The tests and performance criteria study of Section II demonstrated the positioning and measurement accuracy limitations of present-day robots. Data acquisition ability is restricted by the fact that robot controllers do not usually include high-accuracy analog-to-digital converters and the rapid sampling ability necessary for sensor testing (although either 12- or 16-bit converters can be installed). Possible solutions to the measurement and instrumentation limits are discussed in Section V.

In this section the robot and robotic simulation limitations which affect the inertial sensor testing application have been addressed. The final section will summarize both the robot's advantages and its shortcomings and will discuss robotic potentials.

V. Conclusions and Recommendations

In an attempt to control robots more precisely and to interface with computers (and computer simulations) other than the robot's particular controller, research is in progress to control robots from computers such as the VAX 11-780 (AFIT, NASA Langley) or interface with such computers for control and data acquisition (for example, Cincinnati Milacron's Robot Offline Programming System, or ROPS).

From the study presented here, robots large and small could begin to be used as checkout testbeds for inertial sensors, possibly in such applications as immediate flightline checkout of sensors or IMU's suspected of being inoperable rather than sending them away to a depot for checkout.

Robots can be multi-purpose testbeds for performing standard tests on inertial sensors, and the potential for devising unique inertial sensor/system tests exists. Robots with variable acceleration/deceleration and a large rotational range suggest dynamic test possibilities that have not yet been explored. Perhaps subjecting the sensor/system to a helical motion, or to a rapid swinging motion of the robot followed by a sudden deceleration would excite sensor/system error terms and thus enhance or replace centrifuge or other testing. Variations of system trajectories could be tracked with lasers and the system errors analyzed by comparison with the laser position data. With extensive computer simulation capabilities such as those of ROBSIM, engineering theory could devise new tests which would be efficiently and safely produced on the simulator, saving both time and money. The simulator-robot combination would encourage engineering creativity, an important commodity in the realm of research and development, where new tests and testing units are needed to keep pace with hardware developments (2).

This research raises further questions. Are robots feasible for system tests? Can the limitations be overcome? What should be done to extend the work presented here?

The solution for robot accuracy constraints may lie not in improving the robot's precision, but rather in providing precision reference measurements for use in sensor output analysis. Laser technology and other instrumentation advances have the potential to accomplish this. For example, providing precision through reference measurement is already in use in noisy, imprecise environments such as the test track at Holloman Air Force Base; and laser technology is currently being used for robot positioning accuracy (14). A cost analysis for laser or other precision measurement technology should be accomplished to extend the economic feasibility study.

The potential for testing precision sensors/systems should be further determined by noise characterization of the robot arm. In addition, the sensors used in this study, or similar sensors, should be tested under more controlled laboratory conditions and compared to test results from non-robotic units.

It is also recommended that test engineers and analysts take a new look at the possibilities for dynamic tests using robotic capabilities and begin devising those tests. The groundwork for a prototype effort has been presented in this study and is recommended for future implementation.

BIBLIOGRAPHY

1. Abundis, M., "Making Robots Count," Robotics Engineering, pp. 17-20, December 1986.
2. Alexander, R., Telephone interview. Central Inertial Guidance Test Facility (CIGTF), Holloman AFB, New Mexico, April 1987.
3. Black, A. J., A Programmer's Assistant for a Special-Purpose Dataflow Language, MS Thesis, AFIT/GCS/ENG/85D-2, School of Engineering, Air Force Institute of Technology, Wright-Patterson AFB OH, December 1985.
4. Bustle, A., Telephone interview. Central Inertial Guidance Test Facility (CIGTF), Holloman Air Force Base, NM, January, 1987.
5. Cobb, D., Douglas Cobb's 1-2-3 Handbook, Bantam Books, New York, 1986.
6. Critchlow, A. J., Introduction to Robotics, Macmillan Publishing Company, New York, 1985.
7. "Evaluation of Automated Decisionmaking Methodologies and Development of an Integrated Robotic System Simulation," NASA Contractor Report 172401, Martin Marietta Aerospace, Denver CO, September 1984.
8. "Evaluation of Automated Decisionmaking Methodologies and Development of an Integrated Robotic System Simulation," NASA Contractor Report 178050, Martin Marietta Aerospace, Denver, CO, March 1986.
9. Fisher, G. H., Cost Considerations in Systems Analysis, American Elsevier Publishing Co., Inc., New York, 1971.
10. Greig, J. Y., Robotics Applications for the Testing of Inertial Sensors, MS Thesis, AFIT/GE/ENG/87J-4, School of Engineering, Air Force Institute of Technology, Wright-Patterson AFB OH, June 1987.
11. Greig, J. Y., D. A. Karnick, D. J. Biezad, and G. B. Lamont, "Implementing and Testing a Robot Simulator," Proceedings of the North Central and Indiana-Illinois Sections of the ASEE, pp. 404-411, Purdue University, West Lafayette, IN, 1986.
12. Koren, Y., Robotics for Engineers, McGraw-Hill Book Company, New York, 1984.

S02B

13. Leahy, M. B. Jr. and G. N. Saridis, "Compensation of Unmodeled PUMA Manipulator Dynamics," Proceedings of the IEEE International Conference on Robotics and Automation, pp. 151-156, Raleigh, NC, March 30-April 3, 1987.
14. Montalbano, G. and R. Schlais, "Laser Guided Precision Positioning With A Gantry Robot," Robotics Engineering, vol. 8, pp. 23-25, February 1986.
15. Nof, S. Y. editor, Handbook of Industrial Robotics, John Wiley & Sons, New York, 1985.
16. O'Toole, T. and M. Cetron, "The Coming Trend of Robots," Press Interview, 1984.
17. Pai, A. L. and J. W. Pan, "A Computer Graphics Simulation System for Robot Manipulator Kinematics," Proceedings of the Phoenix Conference on Computers and Communications, pp. 237-241, March 1985.
18. Simmons, W., Rohr Industries, Inc., Riverside, CA, Feb 1987. Personal correspondence.
19. Unimation, Inc., Unimate Industrial Robot User's Guide to VAL II, Part 1, Version 1.4B, Danbury, CT, May 1985.
20. Unimation, Inc., Unimate Industrial Robots and Cartesian Coordinates, Danbury, CT, 1983.
21. Laboratory Tests of Systron-Donner 4841F Accelerometer Conducted by the Central Inertial Guidance Test Facility (CIGTF), Report No. AD-TR-81-13, Holloman AFB, NM: CIGTF, 6585th Test Group, January 1981.
22. Wrigley, W., W. Hollister, and W. Denhard, Gyroscopic Theory, Design and Instrumentation, The M.I.T. Press, Cambridge, MA, 1969.

CSDL-P-2764

**THE OPTIMUM SOLUTION OF
INSTRUMENT QUANTIZATION EFFECTS**

**by
Thomas Reed**

October 1987

**Presented at
Thirteenth Biennial Guidance Test Symposium
Holloman Air Force Base, New Mexico
October 1987**

The Optimum Solution to Instrument Quantization Effects

By

T. E. Reed

C. S. Draper Laboratory, Inc.

Certain types of precision inertial-grade instruments have outputs that consist of non-coherent pulse trains. In some applications, the pulse granularity or quantization appears to be a major operational constraint.

This paper will describe an optimal method for eliminating this constraint. An optimal method is defined as any method that extracts all of the information contained in the output and converts it, without loss, as a compatible input for a computer or other coherent processor.

The method described essentially eliminates quantization, reduces the effects of pulse "jitter" by the theoretical maximum, and inputs the information as a coherent scalar quantity without phase distortion.

Introduction

There are a variety of precision instruments whose output consists of unsynchronized pulse trains. This includes Ring Laser Gyros, certain types of pulse torque on command accelerometers and analog to digital conversion using voltage controlled oscillators. For a perfect instrument these pulse trains are unique. At the instant a pulse occurs there is no error, there is no storage in the instrument. All of the information is contained in the actual time of occurrence. In almost all cases, this information contained in these pulses, will be inputted to a synchronized, clocked data acquisition device - usually a computer. The question is, what is the best method of extracting all the information out of this pulse train? In most cases, the variable of interest is the frequency of this pulse train, yielding angular rate for an RLG, indicated acceleration for an accelerometer, and voltage for a VCO analog to digital converter. For purposes of this paper we will assume the device is an RLG with each pulse having a weighting of, Q , arc seconds and our interest is angular rate, $\dot{\theta}$, in arc seconds per second (or degree/hour). The acquisition device will have a sampling period of, t_s , seconds.

Methods

The simplest interface would be an accumulator that counts the incoming pulses and then its contents are transferred to the computer at its sampling rate. The computer can then determine the indicated rate, $\dot{\theta}_I$, as follows:

$$\dot{\theta}_I = NQ/t_s$$

where N is the number of pulses accumulated during the last sample interval. The uncertainties of this indicated rate $(U)\dot{\theta}_I$, is:

$$(U)\dot{\theta}_I = Q/(t_s\sqrt{6})$$

This quantization or data granularity can be a major limiting feature in the use of these instruments.

The HSF

The input method recommended will, for all practical purposes, eliminate this quantization or essentially reduce it to a negligible size. It will have no phase distortion, its average value cannot be "contaminated" by higher frequency aliasing, and it's implementation is straight forward.

The high speed filter (HSF) uses an age old technique referred to as triangular filtering or AOA for Average of Average. The only unique quality is that this function will be performed at a high speed at the computer interface.

Now perhaps the best way to explain how this filter interprets and transfers time of pulse occurrence into the computer is by looking at a single pulse. Figure 1a shows a single pulse located at some point in time between two computer sample times. This pulse has no information in its height, only in its time of occurrence. Now if we could split this unit pulse into two pulses and input them at, t_{n-1} and t_n in such a manner that their height (i.e., value) yields the proper time weighting then all the information has been transferred. This can be done by superimposing a unit height triangle centered on the pulse whose sides are, t_s , long and then by reading its height at, t_{n-1} , and t_n (See Figure 1b).

The above method can be done graphically but it is, of course, impossible to do in real time. But if these triangles are synchronized with the computer, with bases $2t_s$ long then the value of this triangle at the time of pulse occurrence places the proper weighting for that sample time (See Figure 1c). The two pulses have now been generated and they are identical to the ones shown in Figure 1b except they are delayed in time by one interval. Also, note that these two pulses are simple scalars and multiple pulses just add so that the same equation holds for finding rate:

$$\dot{\theta}_I = NQ/t_s$$

except now, N is not, in general, an integer. The uncertainty of this rate has theoretically been reduced to zero.

Now to get back to reality. These split pulse values will not have infinite resolution nor is the instrument perfect. These pulses do not occur at exactly the "zero error" time, they will have some "jitter" about that point.

Assume a "jitter" value of, xQ , where, $x < 1$, then the uncertainty of the measured rate becomes:

$$(U)\dot{\theta}_I = \sqrt{2} xQ/t_s$$

for the accumulator method and:

$$(U)\dot{\theta}_I = xQ/(\sqrt{N} t_s)$$

for the HSF method where N is the actual number of pulses occurring during that sample period. This, incidentally, is the smallest uncertainty possible!

Now back to the finite resolution. Assume that this triangle height is read with an, n, bit resolution then the uncertainty due to finite resolution becomes:

$$(U)\dot{\theta}_I = Q/(2^{n-1} \sqrt{6} t_s)$$

or an eight bit resolution reduces the uncertainty by a factor of 128.

Now the uncertainty associated with jitter is independent of resolution so a point of diminishing returns is reached when the resolution uncertainty is less than the jitter uncertainty. This occurs when:

$$Q/(2^{n-1} \sqrt{6} t_s) < xQ/(\sqrt{N} t_s)$$

$$n \geq \log_2 \left[\sqrt{N/6/x} \right] + 1$$

For example, assume an RLG with a one arc second quantization ($Q = 1$) operating at $150^\circ/\text{second}$ ($\dot{\theta} = 3600 \cdot 150$) with a 5% jitter ($x=0.05$). Assume the computer will sample at a ten millisecond interval ($t_s = 0.01$). Then:

$$n \geq \log_2 \left[\sqrt{900/0.05} \right] + 1$$

$$\geq 9.23$$

Set, n, to 10. Then:

$$(U)\dot{\theta}_I = \sqrt{\left[\frac{100}{\sqrt{6}(512)} \right]^2 + \left[\frac{(0.005)(100)}{\sqrt{900}} \right]^2}$$

$$= 0.185 (^\circ/\text{hr})$$

This is in contrast to the uncertainty of the accumulator method which is 39 times larger.

The above uncertainty is at the 10 millisecond period. If this data is filtered internally over a longer period, t, using the same technique, then the uncertainty will reduce as follows:

$$\dot{\theta}_I = \dot{\theta}_{I(10 \text{ millisecond})} \left[0.001/t^{3/2} \right]$$

The resolution directly effects the speed of the filter. The update frequency of the filter, f_{HSF} , becomes

$$f_{HSF} = 2^n/t_s$$

which, for the example, becomes, $F_{HSF} = 409,600$ HZ.

Interface Requirement

It is assumed that the HSF is an appendage to the computer or acquisition equipment and that it outputs the data onto a parallel input. The number of parallel lines, l_p , required is set by the resolution used, 2^n , as well as the maximum number of pulses, N_{max} , per sample interval:

$$l_p \geq n + \log_2 N_{max}$$

($l_p = 23$ for the example given).

Now if this number, l_p , is excessive it can be reduced by eliminating either some least significant bits or some most significant bits. If least significant bits are dropped the lost information must be saved and added to the next sample. This eliminates accumulative error.

Some most significant bits can be dropped if the computer can non-ambiguously replace them. In general, this is possible if the number of bits remaining are greater than: $n + \log(N_{max} - N_{min}) + 1$, where N_{min} is the least amount of pulses during any sample period.

Filter Implementation

The HSF can be implemented in a μ processor if the update frequency is low enough. Figure 2 shows a flow design of a simple recursive algorithm.

If the update frequency is above the capability of a μ processor then a straight forward set of digital circuits can be used. These circuits could be designed to perform the algorithm above.

Another method would use a counter which counts the update frequency and whose value would be added to one register at each input pulse and the counters complement value added to a second register at every input pulse. At every computer request the second register is added to an auxiliary register and outputted, the first register is transferred to the auxiliary and the counter is reset. This method only works if the sample interval is exactly, 2^n , longer than the update period.

Summary

In conclusion, the HSF input method essentially eliminates the effects of quantization and reduces the effect of pulse jitter down to the theoretical limit. While it has a built in time delay, it does not have any phase shift and the transfer has a zero slope at all multiples of the Nyquist frequency yielding no aliasing at dc and very small aliasing at low frequencies. It can be implemented using a simple algorithm or straight forward circuits.

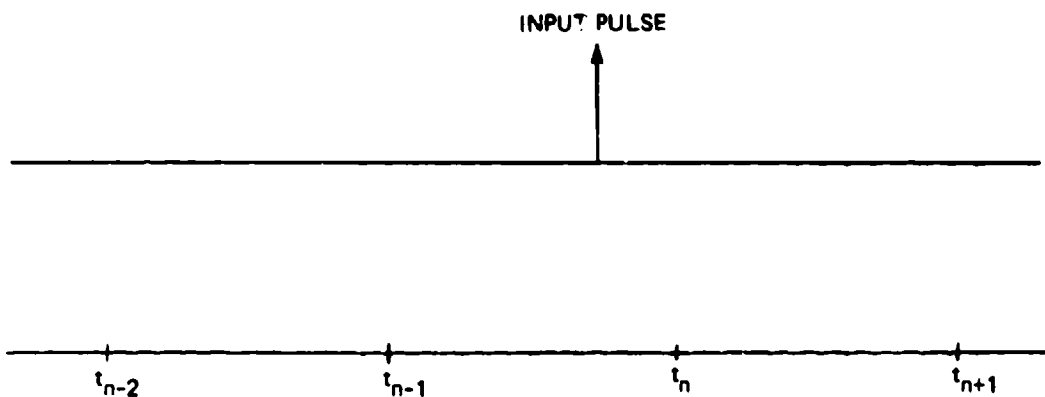


Figure 1a. Random pulse w/computer input samples.

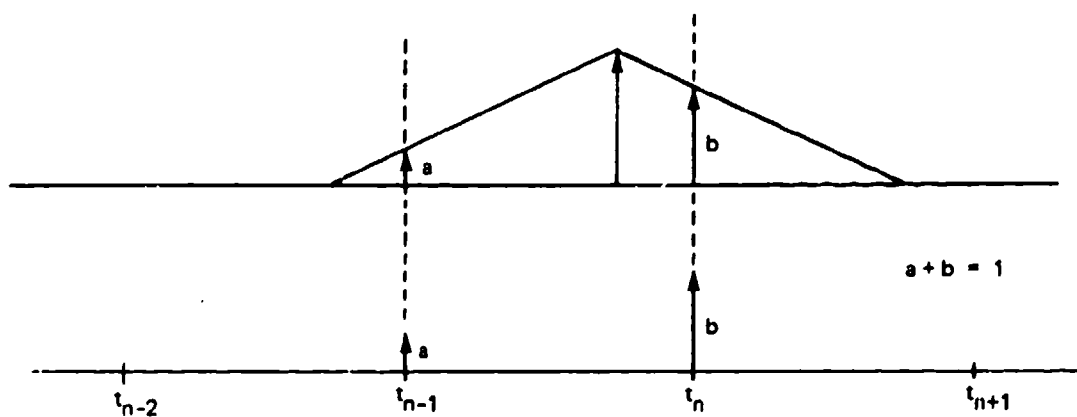


Figure 1b. Ideal computer input.

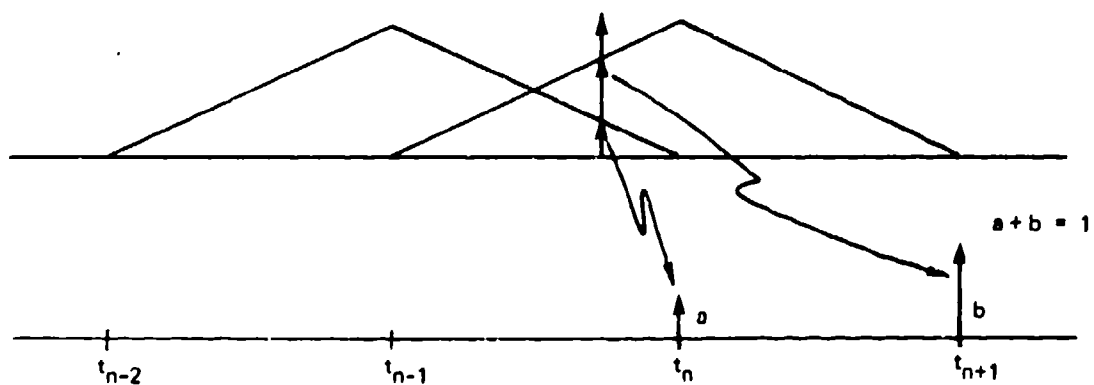
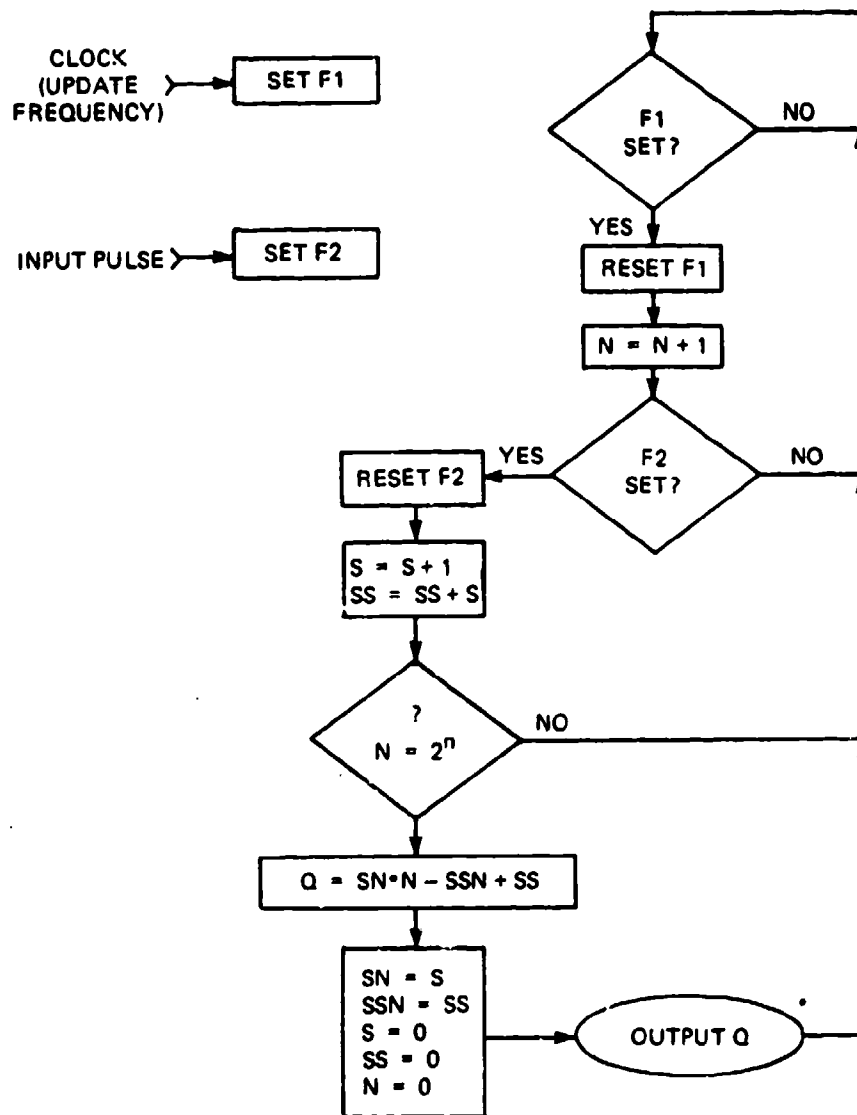


Figure 1c. HSF computer input.



*Note Q is integer whose binary point is $2n$ from the right.

Figure 2. Flow diagram for HSF.

DISTRIBUTION

H. Baker
J. Barker
L. Freier
C. Kochakian
E. Porter
T. Reed (8)
L. Schnee
J. Volp

"Evaluation of a Minature Horizontal Pendulum Tilt Transducer," H. D. Valliant and L. J. Burris, LaCoste and Romberg Gravity Meters, Inc., 6606 N. Lamar, Austin TX; J. Levine, Joint Institute for Laboratory Astrophysics, National Bureau of Standards and University of Colorado, Boulder CO (S03A)

"An Improved Data Reduction Procedure for Accelerometer Centrifuge Data," George H. Neugebauer, 28850 Pebble Beach Dr., Sun City CA (S03B)

"Control Test and Validation for a Large Diameter High Stability Centrifuge," S. Willis, M. Harshman, B. Popovich, M. Guardiani, R. Strane, J. Profeta, Contraves Goerz Corporation, 610 Epsilon Dr., Pittsburg PA (S03C)

EVALUATION OF A MINIATURE HORIZONTAL PENDULUM TILT TRANSDUCER

H. D. Valliant and L.J. Burris
LaCoste and Romberg Gravity Meters, Inc.
6606 N. Lamar
Austin, Texas 78752
(512-458-4205)

J. Levine
Joint Institute for Laboratory Astrophysics
National Bureau of Standards and Univ. of Colorado
Boulder, Colorado 80309
(303-492-7785)

ABSTRACT

EVALUATION OF A MINIATURE HORIZONTAL PENDULUM TILT TRANSDUCER

H. D. Valliant and L.J. Burris
LaCoste and Romberg Gravity Meters, Inc.
6606 N. Lamar
Austin, Texas 78752
(512-458-4205)

J. Levine
Joint Institute for Laboratory Astrophysics
National Bureau of Standards and Univ. of Colorado
Boulder, Colorado 80309
(303-492-7785)

This work was supported in part by a grant from AFGL.

A miniature horizontal pendulum tilt transducer, designed by Instech, Austin, Texas in 1978 was first used by AFCRL (now AFGL) to directly measure the angular tilt of test gyros. After this project was abandoned, the 6585 Test Group acquired the transducers and are currently having them repackaged into a free-standing format. In the meantime an additional eight pairs of transducers have been extensively employed as borehole tiltmeters by the University of Colorado. This technology has recently been acquired by LaCoste and Romberg Gravity Meters, Inc., Austin, Texas.

The transducers have a natural resonance period of one second. Built-in shock protection makes the instrument extremely rugged. Barometric effects are virtually eliminated through careful design. Temperature effects are compensated so that the instrument's temperature coefficient is no worse than $0.5 \mu\text{rad/K}$. This measured sensitivity to temperature is an upper bound and may include a significant contribution due to the thermoelastic tilt of the test boreholes. Long term drift has been measured to be less than $0.5 \mu\text{rad/a}$, and drifts as small as $0.1 \mu\text{rad/a}$ have been observed. The package size for an orthogonal pair of transducers is approximately 12 cm (4.75 in.) in diameter by 6.5 cm (2.5 in.) in height and the weight is approximately 1.9 kg (4.25 lbs). The performance of such sensitive devices cannot be tested directly and must be inferred from the results of long term usage. Several years of monitoring crustal tilts in boreholes provides a massive data set from which to draw. Unfortunately the precision of the transducer itself cannot be separated from the effects of coupling the transducer to the earth's crust. However the characteristics of the transducers are at least no worse than the combined results of the transducer and its mounting. The analysis of three years of nearly continuous observations with two adjacent identical systems suggests the following:

<u>Frequency/Period band</u>	<u>Remarks</u>
> Few minutes	-170 dB (relative to $1 \text{ rad}^2/\text{Hz}$) (ie a tilt of 3 nrad is detectable with a signal to noise ratio of unity). Close to transducers' natural resonance.
Several hours	Some residual temperature effects indicate that ambient temperature stability to a few mK may be needed. Coherence of nearby instruments is poor. Not recommended for this frequency regime.
Several cycles per day	Main application. Tidal amplitudes observed with precision of ± 1 nrad. Good nearby coherence.
> One day	Borehole instrument degrades rapidly with increasing period. Possible temperature and pressure effects. Poor nearby coherence possibly caused by very local tilts.
> One year	Best data in Southern California shows secular drift of less than $0.5 \text{ } \mu\text{rad/a}$. Larger drift rates observed in other regions are probably due to real secular crustal tilting.

INTRODUCTION

Inclinometers have been around in one form or another for many years. Many diverse techniques have been used, including water-tube tiltmeters, measuring lake-levels on opposite shores, measuring water levels at opposite ends of artificial basins, long (and short) vertical pendulums and simple spirit levels. One class of tiltmeter, based on the principle of the horizontal pendulum, was invented around 1830 by Hengler. Figure 1, illustrates its principle. A mass is located at one end of a rigid beam. The beam is pivoted at the opposite end and is supported by a fine wire attached to a rigid support nearly vertically above the pivot. If the wire attachment and pivot are in an exact vertical line the mass receives no restoring force and can assume any azimuth. The mass-beam assembly therefore has an infinite period and consequently is infinitely sensitive to horizontal accelerations acting at right angles to the beam. That is to say, a very small horizontal

acceleration would cause the beam to move through an angle limited only by a physical constraint such as a mechanical stop. A tilt of the vertical axis perpendicular to the plane containing the beam and suspension wire has the same effect as a horizontal acceleration. If the axis is tilted forward (toward the mass) in the plane of the beam and wire, gravity will provide some restoring force to center the beam in the plane of the tilt. One simple way to visualize the system behavior is as an equivalent vertical pendulum whose length is determined by the period of the horizontal pendulum. The sensitivity (i.e. the displacement of the pendulum mass for a given horizontal force) increases with increasing period. Melchior (1983) reviews the history of horizontal pendulums and summarizes their theory in considerable detail.

In 1978, one of the authors (LJB) under the business name INSTECH, developed a miniature horizontal pendulum for measuring precise tilts. Four of these were originally procured by AFCRL to measure the angular tilt of gyros undergoing test. This program was abandoned and the instruments were ultimately transferred to the 6585 Test Group. The Test Group is presently having them repackaged into a free-standing format for monitoring the tilt of precise test beds for inertial applications. In the meantime the University of Colorado has made extensive use of the device for monitoring tidal and secular crustal tilts in boreholes. As a result of this effort the instrument was refined over the years until a nrad sensitivity with a long term drift of better than $0.5 \mu\text{rad/a}$ had been achieved. As a result of the close relationship between Instech and LaCoste and Romberg Gravity Meters, Inc. many of the design features used in the manufacture of gravity meters were incorporated into the design of the tilt meters. In 1986, LaCoste and Romberg Gravity Meters, Inc., of Austin, Texas acquired the design from Instech and now includes tiltmeters in its standard product line.

DESIGN PHILOSOPHY

The Tilt Transducer.

Fig 2 illustrates the design, which was especially constructed to avoid torsional vibration modes and to provide exceptional temperature stability. The instrument is tuned to a one second period which provides a $1.22 \mu\text{m}$ displacement for a $5 \mu\text{rad}$ tilt. This is equivalent in response to a 0.24 m vertical pendulum. Such low sensitivity assures that the instrument has good stability but does require very high electronic amplification to achieve sensitivities in the order of several nrad. The electronic readout uses a capacitive position indicator (CPI) transducer. Two capacitor plates are located on either side of the beam whose displacement is measured as a differential change in capacitance. Air dampers, forming an integral part of the CPI plates, overdamp the system. In this configuration torsional vibration modes would increase the electronic noise and it was for this reason that the mechanical system was designed to avoid these unwanted vibrations. The electronics for the CPI system were designed by and procured from Jerry Larson of Maryland Instrumentation. These were modified somewhat by the

University of Colorado (Levine, 1985) to obtain the nrad precision required for geophysical measurements.

One important feature of the mechanical design is the small springlets incorporated into each of the suspension wires to provide protection from shock and vibration thereby increasing the ruggedness of the sensors. Another feature is the pantograph arrangement of the suspension which allows expansion due to temperature changes to translate the entire structure vertically without changing the angle of inclination θ . As Melchoir (1983, Eqn 8.18) shows, the sensitivity of a horizontal pendulum depends only on the angle of inclination and this arrangement greatly reduces the sensitivity of the sensor to changes in temperature. A small second-order sensitivity to temperature remains. It results from a differential elongation of the springlets which results in small rotations of the beam in a vertical plane with a concomitant variation in sensitivity. Migration of the bending points of the suspension wires with temperature could have a similar effect. Also, because the CPI measures linear rather than angular displacement, changes in the length of the beam result in changes in sensitivity. The small springlets again come to the rescue absorbing most of the expansion of the beam without affecting the length of the lever arm. Calculations show that the temperature coefficient of this effect is 4.6 ppm/K. With a dynamic range of $\pm 25 \mu\text{rad}$ the maximum error is $\pm 0.1 \text{ nrad/K}$. Extensive testing has shown no detectable change in period over a 10 K change in temperature. We are therefore confident in the claim that the calibration is uniform to better than 1% over this temperature range. Also periodic recalibrations have shown that after an initial rapid drift lasting approximately one month, the calibration is stable to better than 1% over long time intervals. Automatic nulling of the beam could eliminate all of these effects. Although an electrostatic feedback system developed for gravity meters (Valliant et al., 1986) is available we have not thought it necessary to apply this technology to the horizontal pendulum as yet.

The Mounting Platform

The coupling of the transducer to the body whose tilt is to be measured is possibly even more critical than the transducer itself. Any differential expansion of the mounting platform due to temperature gradients or distortion due to barometric pressure causes directly measurable noise tilts. Fig 3 illustrates the mounting platform that supports the two orthogonal tilt transducers. The mounting base is machined from a single piece of stainless steel. The design provides a heavy mass for physical stability and extreme mechanical rigidity. The thick cross-section of the base (A) encourages heat-flow thereby minimizing differential expansion due to thermal gradients. A sub-platform (B), connected to the base with a small central pedestal (C) minimizes tilt errors due to distortion of the base caused by barometric pressure changes. It is estimated that a 2 PSI pressure differential will deflect the center of the base by 2.1 nm which is equivalent to a tilt of approximately $0.05 \mu\text{rad}$. This tilt is not transferred to the sub-platform due to symmetry. The single support column for the sub-platform also eliminates erroneous tilts due to thermal

gradients that would occur if it were supported on separate legs. Finally, the adjustable invar legs and the base of the sub-pedestal are mounted in a common plane (D) further reducing temperature induced tilting. The complete assembly is sealed with a stainless steel cover and filled with dry nitrogen. The results of tests in boreholes indicate that temperature induced tilts are less than 30 nrad/K.

For geophysical applications, the tiltmeters are installed in boreholes to isolate them from surface tilts produced by rainfall or by thermo-elastic effects. The boreholes are usually 30 m deep, although other depths have also been tried. The good temperature stability at this depth minimizes the importance of the residual thermal sensitivity of the sensors. To improve the coupling to the earth, the tiltmeters are mounted in a 1.8 m sonde (Harrison et al., 1982) to provide a longer baseline in contact with the crust. Fig 4 details the sonde and tiltmeter attachment. A 15 cm hole is drilled and lined with a steel casing cemented in place. The bottom section of the casing is stainless steel. The sonde is lowered down the bore-hole where it rests on a central ball support at the bottom and is pressed against the side of the casing with leaf springs.

LABORATORY TESTS

Calibration and Linearity:

The instrument sensitivity is calibrated by observing its response to a 48.5 μ rad incremental tilt at various points in its dynamic range. Table 1 shows the results of such a calibration. The sensitivity is extremely uniform over the entire range and non-linearity amounts to no more than 0.3% of the scale factor. This technique is used rather than directly observing the output at various tilts because a sufficiently precise reference tilt table is unavailable.

TABLE 1
CALIBRATION MEASUREMENTS

TILT (μ rad)	RESPONSE (Volts/48.5 μ rad)
24.1	1.790
15.8	1.796
6.7	1.790
-0.8	1.795
-8.1	1.797
-14.2	1.795
-22.1	1.805
MEAN	1.795
STANDARD DEVIATION	0.005

Measurement of Resonant Period

The resonant period can be measured in two ways. Firstly it can be measured by finding the time for several oscillations when the dampers are removed. Secondly it can be inferred from the observed sensitivity. When first manufactured the design specification of 1 ± 0.1 sec was verified by direct timing. Nearly ten years later unit No. 003 was rechecked by the second method and found to still have a period of 0.9992 sec. Fig 4 shows the observed sensitivity for ± 0.75 deg tilts, in the plane of the pendulum (angle i), superimposed on the theoretical relative sensitivity curve. As the nominal tilt angle is unknown the two observations, exactly 1.5 deg apart, are slid horizontally until they coincide with the theoretical curve. The mid-point of the two observations approximates the sensitivity at the nominal tilt from which the period of the equivalent pendulum is calculated. This method is used, rather than attempting to measure the sensitivity directly, because it permits measuring much larger angles consistent with the precision of the available test table.

Step Function Response and Damping Ratio

The response of the pendulum to a series of 5 μ rad step tilts is shown in Fig 6. The time taken for the signal to reach a percentage (say 63%) of its final value can be scaled from the record and the damping ratio calculated from the theoretical response of an overdamped second-order system to a unit step function. The damping ratio for the case illustrated was 5.5 times critical.

PERFORMANCE INFERRED FROM BOREHOLE OBSERVATIONS

These sensors have been used at several sites in Colorado, Wyoming and California. Most of the measurements were made in 30 m boreholes, although boreholes ranging from about 8 m to about 70 m have been tried.

The smallest secular tilts have been recorded in Southern California at Pinon Flat Observatory. The total secular tilt during about 15 months of operation is about 0.6 micro-radian, but there are several periods during the record when much smaller tilts were observed.

The diurnal and semi-diurnal earth-tides, whose total amplitude is about 200 nrad, can be determined with a signal-to-noise ratio of about 45 db, when using a record about 30 days long. A signal-to-noise ratio of 45 db corresponds to a measurement sensitivity of 1.1 nrad. This signal-to-noise ratio is somewhat better than we have seen elsewhere; the noisiest station has a signal-to-noise ratio of about 30 db for the same observation period.

At shorter periods, ranging from a few hours to a few minutes, two nearby instruments show poor correlation. It is not clear why this is so, but small-scale irregularities in the borehole and its immediate

surroundings are probably important. We have not conducted extensive analyses of the tilts in this period range. The lack of coherence suggests that the data may represent sensor noise or very local tilts.

We have also conducted several experiments using the sensors as horizontal seismographs to record teleseisms. Our studies have been only qualitative, however, since the signals are close to the resonant frequency of the sensor and significant variations in the amplitude and phase response of the instrument across the seismic band have been observed.

In each case, the observed noise or error signal is the combination of the transducer, sonde, and actual tectonic signals. Therefore these observations represent an upper bound to the performance limitations of the transducer alone.

SUMMARY

An inclinometer (Fig 7), suitable for general metrology including geophysical measurements has been available since 1978. Unfortunately details of the device have not been published before and it therefore has not been widely deployed. Measurements in boreholes for geophysical applications indicate that a precision and sensitivity of the order of nanoradians has been achieved. When using the device for general metrological observations in laboratories, great care must be taken to assure the integrity of the interface between the inclinometer and the test object and to provide a controlled environment, or else its performance can be seriously degraded. In the free-standing laboratory mode, performance is often limited to the stability of the test surface or pier to which the instrument is attached. Differential expansion between the stainless steel instrument case and a granite or concrete test surface can cause serious noise tilts. In some cases the material of the instrument case can be chosen to match the test base.

REFERENCES

Harrison, J.C., J. Levine, C.M. Meertens. Design of a deep borehole tiltmeter. Proc. 9th Intl Symp on Earth Tides, Stuttgart, Germany, 1982.

Levine, J., A study of secular and tidal tilt in Wyoming, final report June 1981-Dec 1984. Air Force Geophysics Command, USAF, Hanscom Air Force Base, Mass., 1985.

Melchior, Paul. The tides of the planet earth. Pergamon Press, 2nd ed., 1983.

Valliant, H.D., C. Gagnon and J.F. Halpenny. An inherently linear electrostatic feedback method for gravity meters, JGR, 91, pp 10463-10469, 1986.

CAPTIONS

Fig 1. Principle of the horizontal pendulum and its relationship to an equivalent vertical pendulum. $AB = OB/\sin(i)$ is the length of the equivalent simple pendulum, where OB is the length of the horizontal pendulum.

Fig 2. Design principles of the LaCoste and Romberg (Instech) horizontal pendulum tilt transducer.

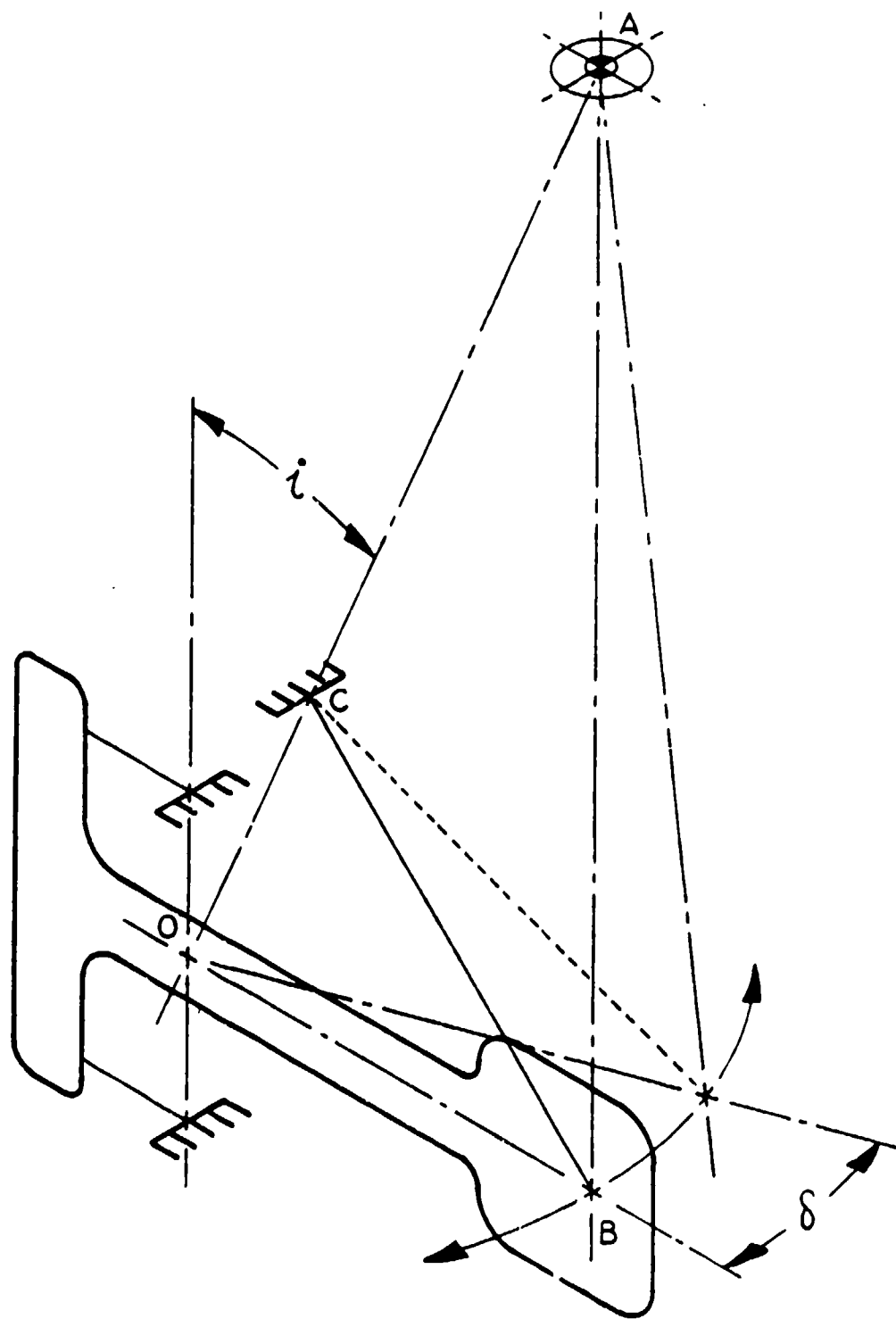
Fig 3. Construction of the tilt transducer mounting platform. (A) Stainless steel base; (B) sub-platform eliminates errors due to distortion of the base caused by barometric pressure variations; (C) central pedestal supporting the sub-platform; (D) common plane for mounting of legs and pedestal.

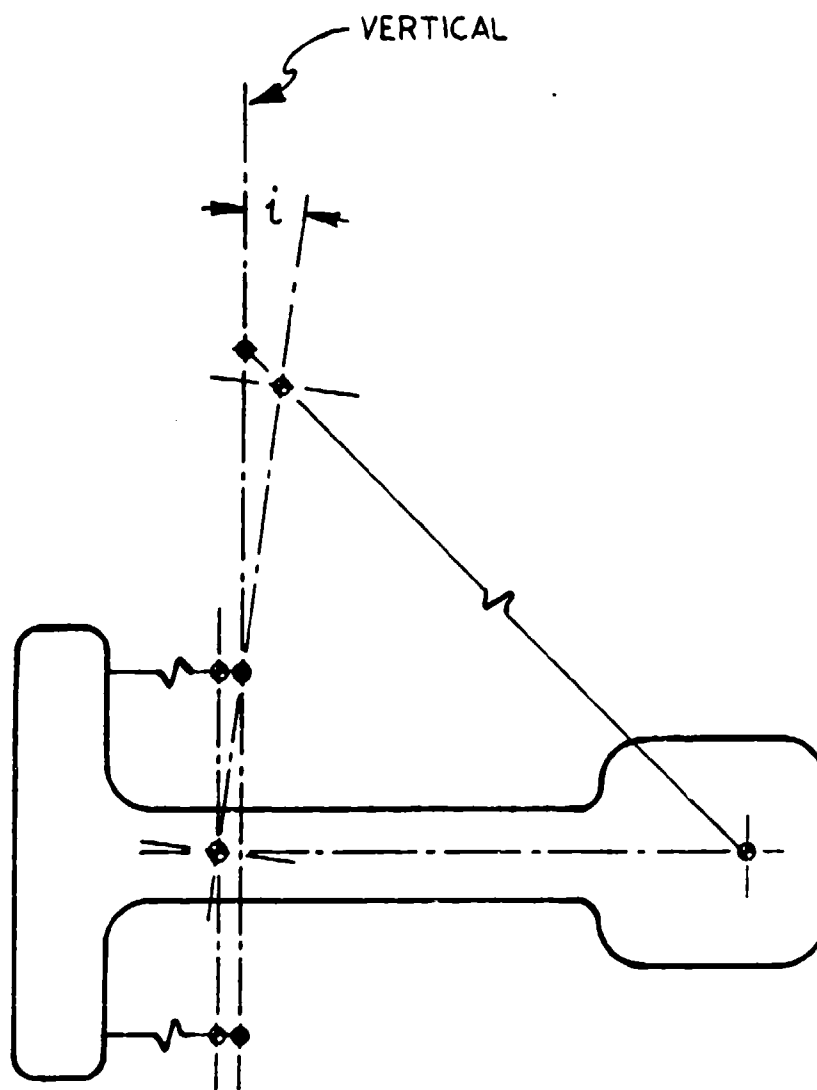
Fig 4. Construction of the sonde for borehole observations after Harrison et al (1982). The inset at the upper right details the mounting of the transducer in the sonde.

Fig 5. Determination of the natural period of a horizontal pendulum (Serial No. 003). Circles represent sensitivities relative to a one second pendulum. Points with error bars represent observed sensitivity for ± 7.5 deg displacements. The inferred period is calculated from the sensitivity at the mid-point of the two observed displacements.

Fig 6. The response of the horizontal pendulum (Serial No. 003) to a series of approximately $5 \mu\text{rad}$ step-function tilts.

Fig 7. Photograph of the completed tiltmeter as configured for test applications not involving boreholes.

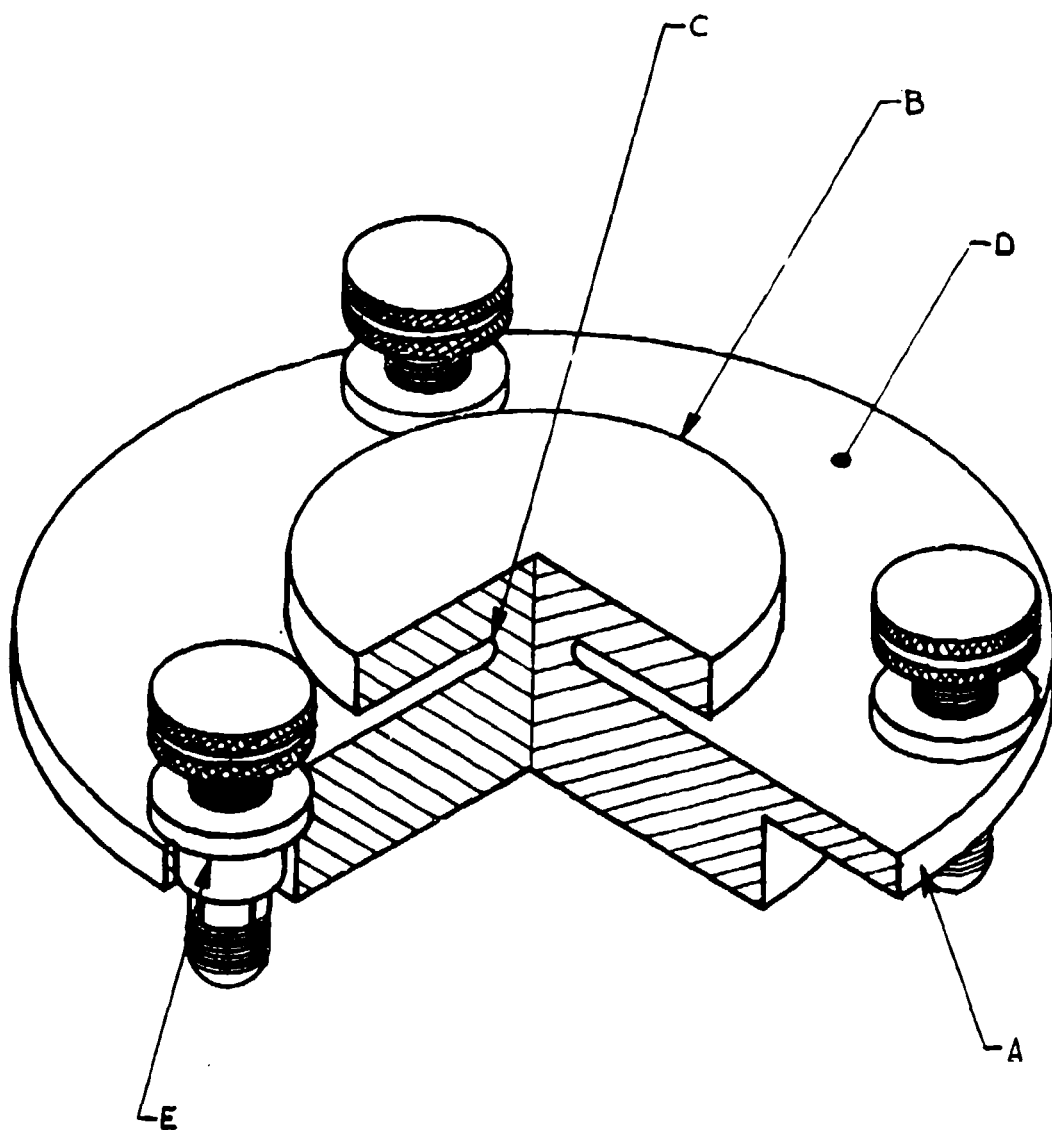


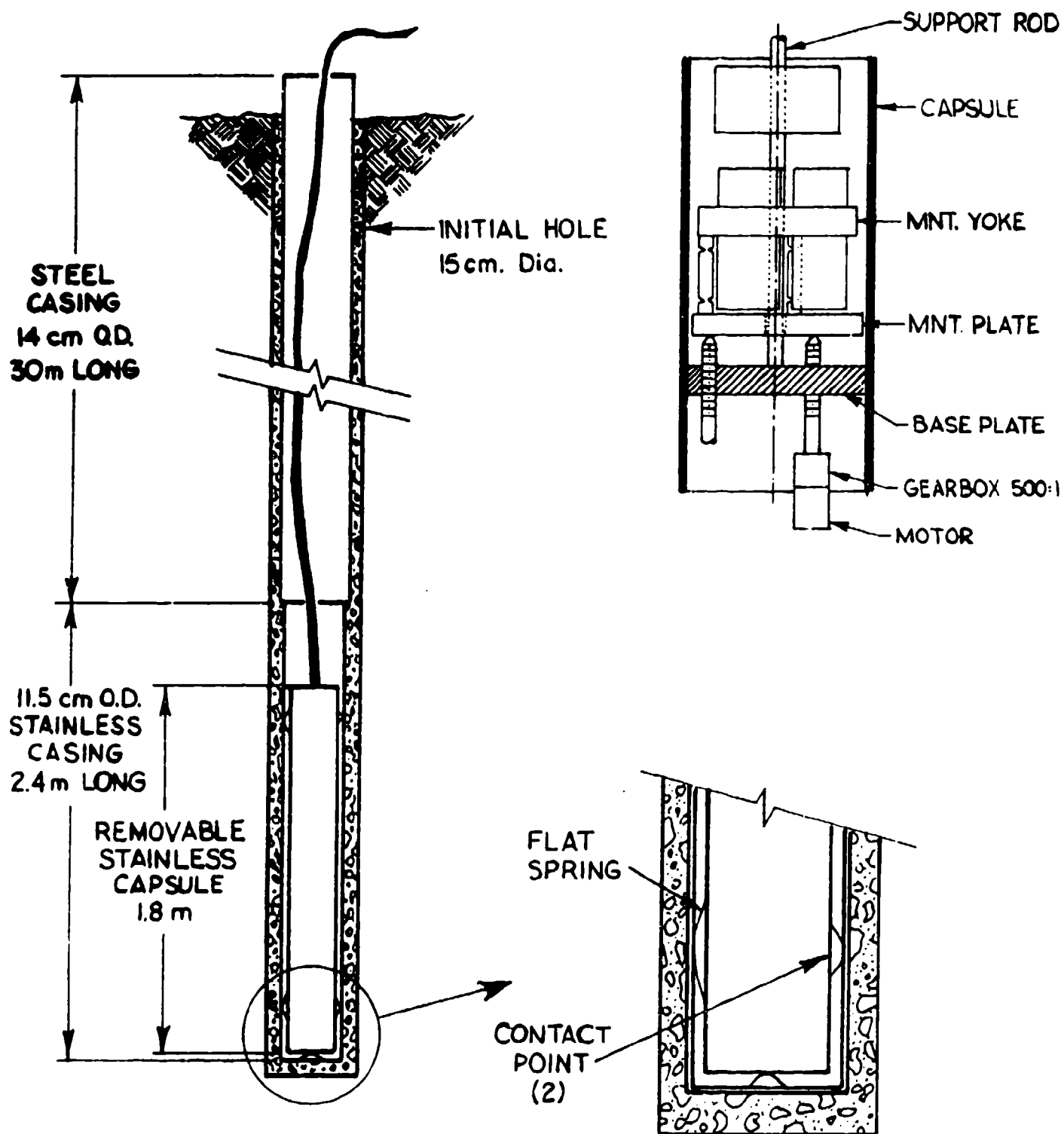


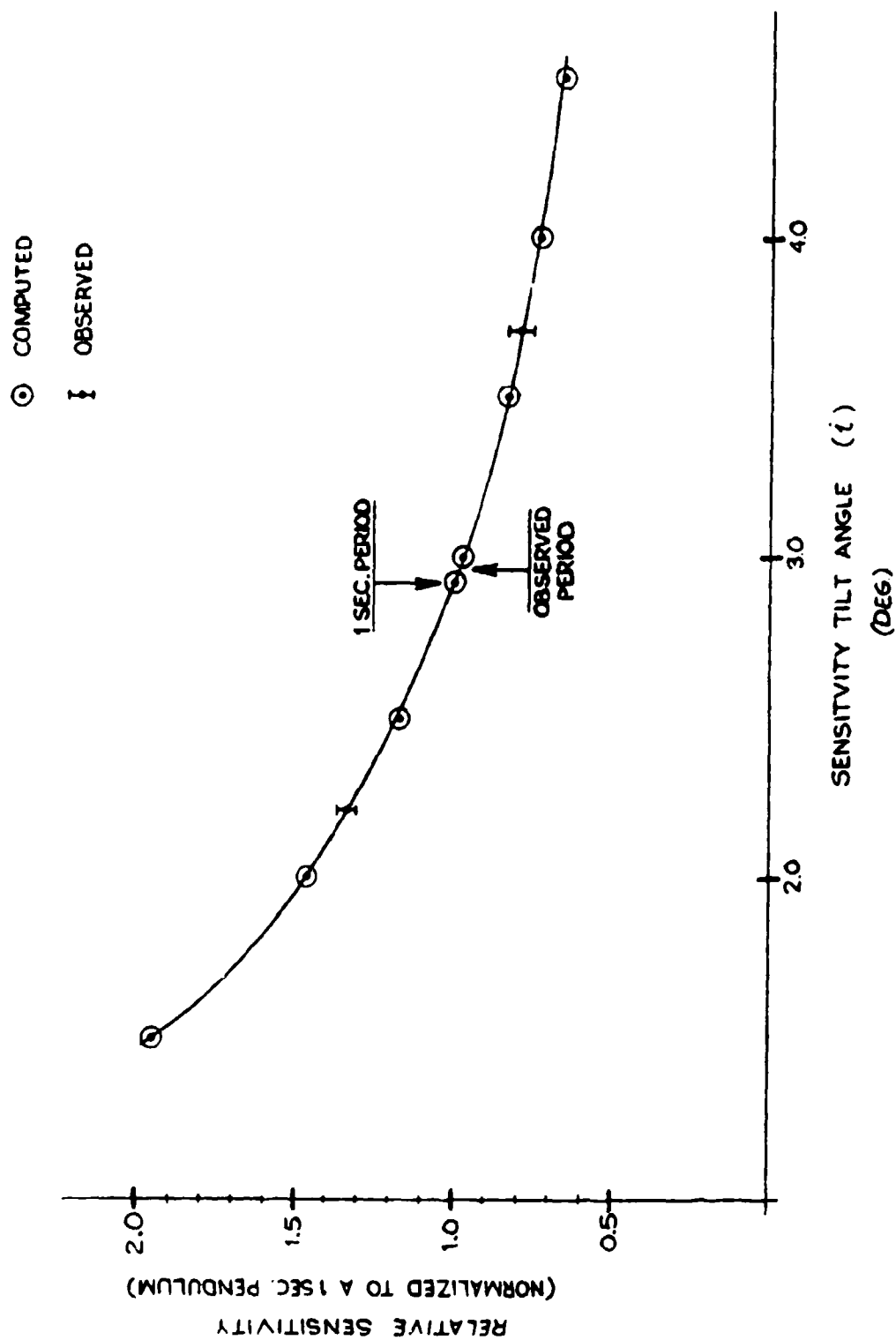
- ◆ HINGE POINT
- ATTACHMENT POINT

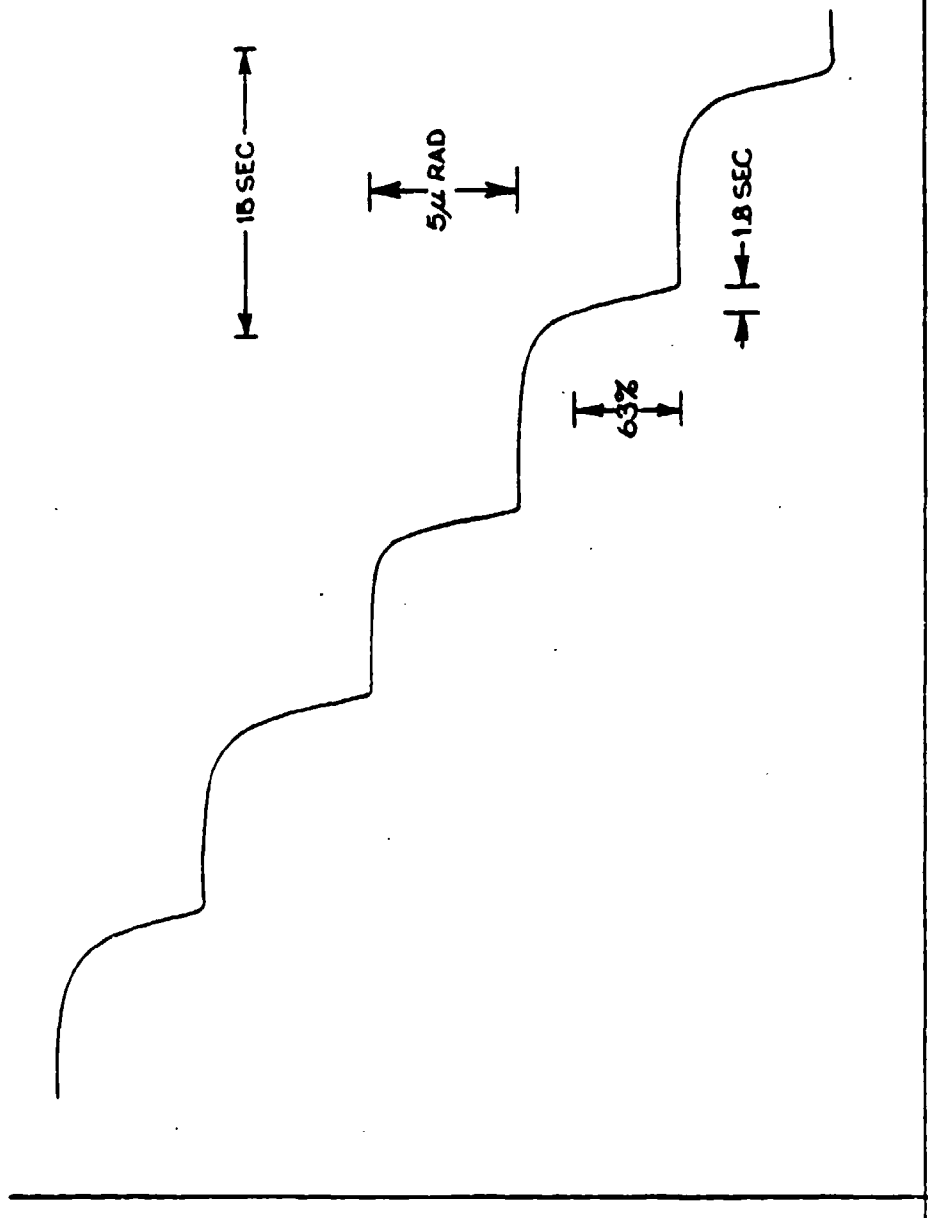
$$\text{SENSITIVITY} = \delta = \frac{d}{i}$$

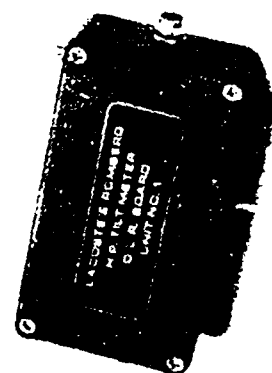
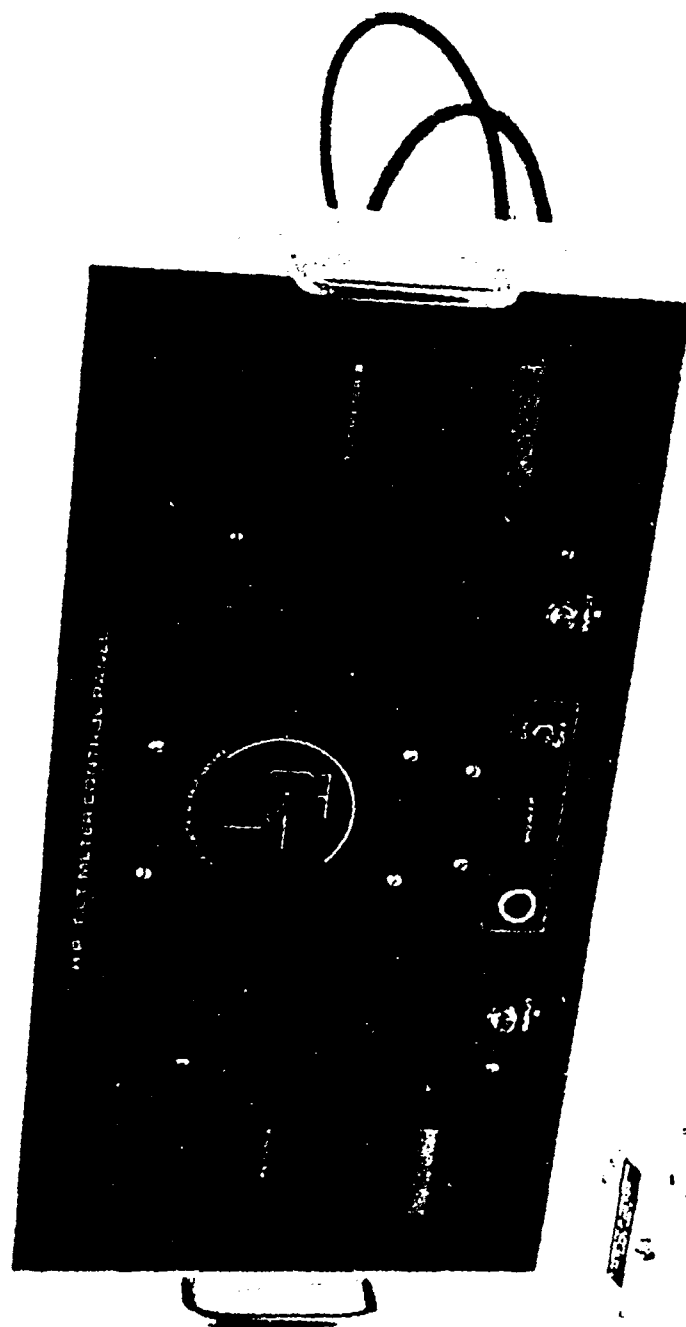
δ = ANGLE OF ROTATION OF PENDULUM
 d = ANGLE OF TILT TO BE MEASURED (\perp PLANE OF DRAWING)
 i = ANGLE OF INCLINATION











AN
IMPROVED DATA REDUCTION PROCEDURE
FOR
ACCELEROMETER CENTRIFUGE DATA

by
George H. Neugebauer
Consultant
1987

AN IMPROVED DATA REDUCTION PROCEDURE

FOR

ACCELEROMETER CENTRIFUGE DATA

ABSTRACT

A simple iterative procedure is presented for obtaining the nonlinear performance coefficients of an accelerometer which virtually eliminates the effects of radius measurement errors and the misalignments of the input axis with the radius through the effective center of mass of the seismic element. It is necessary that the vertical component of the misalignment angle be held within narrow limits but this is easily done.

The effects of input acceleration range in the presence of noise in the input/output data on the recovery of the nonlinear coefficients is also investigated.

INTRODUCTION

Most companies and government agencies that centrifuge test precision accelerometers use the author's type of data reduction equations as illustrated by Eq.(3) in references (1) and (2). The unique feature of that type of equation over what had been previously used is that it covers the full range of input acceleration in one equation by using separate biases and linear factors for the two mounting positions: input axis (IA) pointing inward and then outward along the radial arm of the centrifuge. By using the full range of input acceleration, the nonlinear coefficients are more accurately determined.

The principal source of error in any data reduction procedure is the uncertainty in the measurement of the radius to the effective center of mass (ECM) of the seismic element. The misalignment of the IA with the radius is only a secondary source of error providing the vertical component of the misalignment is small, say less than 0.01 radians. This vertical component is easily controlled since it is only necessary that the static output of the accelerometer when mounted in position on the centrifuge arm be in the range $K_0 \pm 0.01K_1$, where K_0 and K_1 are the bias and the scale factor in output units and output units/g, respectively as determined from precision dividing head data.

Noise in the input/output data must also be controlled or its effects minimized by taking multiple readings at each acceleration level. Computer simulations show, as would be expected, that the nonlinear coefficients obtained from centrifuge data are the sums of the coefficients that would be obtained if there were no noise and the corresponding coefficients for the noise distribution alone.

A few years ago, it occurred to me that the deviation of the linear factor from unity when expressed in nondimensional units such as in g/g were measures of the combined effects of radius measurement and misalignment errors. Thus, an iterative data reduction procedure based on the deviations from unity would essentially eliminate the effect of those errors and thus yield

better estimates of the nonlinear coefficients. Obviously, neither the proposed data reduction procedure nor any other procedure can be proven by using actual centrifuge data. However, computer simulated data with known coefficients to which has been added the effects of radius measurement and misalignment errors can be checked to see how well that procedure recovers the nonlinear coefficients.

THEORY

It is here assumed that the type of model equation appropriate for the particular accelerometer under test over the specified range of input acceleration has been previously determined either analytically or experimentally. In either case, the adequacy of the model equation should be checked by a study of the residuals for evidence of systematic errors that indicate the chosen model equation requires modification. Also, each coefficient should be checked to see if it is significantly different than zero at some specified confidence level.

A note of caution: even though a model equation may fit the centrifuge data quite well over the tested input range, it is not wise to extrapolate its use beyond that range.

As a specific example, assume the following model equation is appropriate for the accelerometer under test:

$$A_{oj} = \frac{D_{oj}}{K_1} = K_0 + a_1 + K_2 a_1^2 + K_{oq} |a_1| a_1 + K_3 a_1^3 \quad (1)$$

where: A_{oj} = accelerometer output - g

D_{oj} = accelerometer output - output units

K_1 = scale factor - output units/ g

a_1 = input acceleration - g

K_0 = bias - g

K_2 = second degree coefficient - g/g^2

K_{oq} = odd quadratic coefficient - g/g^2

K_3 = third degree coefficient - g/g^3

g = local acceleration of gravity

The odd quadratic coefficient K_{oq} may be due to thermal effects or it may be only an artifact of the data reduction process if there is a large algebraic difference in the radius measurement errors in the two mounting positions. The iterative procedure presented in this paper will essentially remove the effects of radius measurement errors regardless of magnitude (within reason) or signs, including the artifact effect. However, it will not remove the effects of the vertical components of the misalignment angles but these are easily controlled to within 0.01 radians which is quite acceptable.

In general the accelerometer input axis is not precisely aligned with the

radius through the effective center of mass (ECM) of the seismic element and different in the two mounting positions. This is not surprising when one considers all the tolerances on the manufactured parts, the assembly tolerances, the tolerances of the mounting fixture, and the tolerances on the mounting surfaces of the centrifuge arm. These same tolerances affect the ability to precisely measure the radius to the ECM of the seismic element. The measured radii in the two mounting positions will, in general, be in error by different amounts. The iterative procedure does not require accurate measures of the radii, however, it does require, as would any other procedure, that changes in radii be monitored as closely as possible either directly or indirectly and the estimated input accelerations be adjusted for those changes.

Let the true radius to the ECM be $R' = (1 + \delta)R$, where R is the best estimate of the radius and δR is the measurement error. Let θ be the acute angle between the IA and the radius through the ECM. Let ϕ be the projection of the angle θ on a vertical plane containing IA, the angle being positive when the vector IA has an upward component and negative when it has a downward component. The angle ϕ should be controlled within narrow limits, say ± 0.01 radians. As previously noted, the angle ϕ is easily controlled. With misalignment and radial measurement errors, the actual output of the accelerometer is:

$$A_{cj} = K_0 + a'_p + a'_n + K_2[(a'_p)^2 + (a'_n)^2] + K_{Oq}[(a'_p)^2 - (a'_n)^2] + K_3[(a'_p)^3 + (a'_n)^3] + \mathcal{E}_p + \mathcal{E}_n \quad (2)$$

where terms with subscript 'p' apply only when the input acceleration is positive and terms with subscript 'n' apply only when the input acceleration is negative. The true input accelerations are:

$$a'_p = \sin \phi_p + a_p(1 + \delta_p) \cos \theta_p \quad (3)$$

$$a'_n = \sin \phi_n + a_n(1 + \delta_n) \cos \theta_n$$

where a_p and a_n are the best estimates of the input accelerations based on the measured radii plus Corioli's acceleration. The terms \mathcal{E}_p and \mathcal{E}_n are the inevitable noise components.

Equation (2) gives the true output of the accelerometer but there is no a priori knowledge of the true input accelerations a'_p and a'_n , only the estimated values a_p and a_n are known. Therefore, Eq. (2) cannot be used to determine the coefficients. Instead the following approximate data reduction equation will be used:

$$A_{cj} = K_{Op} + K_{On} + (1 + c_p)a_p + (1 + c_n)a_n + K_2[a_p^2 - a_n^2] + K_{Oq}[a_p^2 - a_n^2] + K_3[a_p^3 + a_n^3] \quad (4)$$

If a_p and a_n were the true inputs, then c_p and c_n would each be zero and $K_{Op} = K_{On} = K_0$. In general, this will not happen so $c_p a_p$ and $c_n a_n$ are first approximations of the errors in the estimated inputs. Before going further, Eq. (4) is rearranged for better computational accuracy.

$$A_{cj} - a_i = K_3 a_i^3 + K_{oq} |a_i| a_i + K_2 a_i^2 + c_n a_n + c_p a_p + K_{on} + K_{op} \quad (5)$$

where a_i is either a_p or a_n as appropriate. The seven coefficients of Eq.(5) are determined by the method of least squares which results in matrix Eq.(6) where N_p and N_n are the number of data sets (A_{op}, a_p) and (A_{on}, a_n) , respectively.

As noted above, $c_p a_p$ and $c_n a_n$ are first approximations of the errors in the estimated inputs. Closer approximations of the input accelerations would then be:

$$\begin{aligned} a'_p &= (1 + c_p) a_p \\ a'_n &= (1 + c_n) a_n \end{aligned} \quad (7)$$

Equations (7) are not quite in the correct form since they do not properly include the effects of the gravity components $\sin \theta_p$ and $\sin \theta_n$. However, if θ_p and θ_n are kept small, as is easily done, they will have only a very minor effect. The terms K_{op} and K_{on} will, of course, include the effects of the gravity components.

With the improved approximations of Eqs. (7), the elements of Eq. (6) are revised by the following formulas:

$$\begin{aligned} \sum (a'_p)^k &= (1 + c_p)^k \sum a_p^k, \quad k=1,2,\dots,6 \\ \sum (a'_n)^k &= (1 + c_n)^k \sum a_n^k, \quad k=1,2,\dots,6 \\ \sum (A_{op} - a'_p)(a'_p)^k &= (1 + c_p)^k [\sum (A_{op} - a_p) a_p^k - c_p \sum a_p^{k+1}], \quad k=0,1,2,3 \\ \sum (A_{on} - a'_n)(a'_n)^k &= (1 + c_n)^k [\sum (A_{on} - a_n) a_n^k - c_n \sum a_n^{k+1}], \quad k=0,1,2,3 \end{aligned} \quad (8)$$

In the illustrative model equation, Eq. (1), the powers k are all integers but that is not a requirement of the iterative procedure. Thus, Eqs.(8) are applicable for any value of k whether integral, fractional, or decimal. With the revised elements substituted in Eq. (6), again solve for the coefficients. The new values of c_n and c_p may be used to further revise Eq.(6). The iterative procedure converges rapidly so that usually only one or two revisions are sufficient.

ILLUSTRATIONS

The iterative procedure will be illustrated by several examples in which the nonlinear coefficients are many orders of magnitude smaller than unity and presumably difficult to determine. All examples are assumed to have Eq. (1) as the model equation.

EXAMPLE 1. The true performance coefficients of an accelerometer are $K_o = 0.02$, $K_{oq} = -3 \times 10^{-6} \text{ g/g}^2$, $K_2 = 2 \times 10^{-6} \text{ g/g}^2$, and $K_3 = 1 \times 10^{-7} \text{ g/g}^3$. The misalignment angles are $\theta_p = 0.10 \text{ rad}$, $\theta_p = 0.01 \text{ rad}$, $\theta_n = 0.09 \text{ rad}$, and $\theta_n = -0.01 \text{ rad}$. The relative

$\sum a_i^6$	$\sum(a_p^5 - a_n^5)$	$\sum a_i^5$	$\sum a_r^4$	$\sum a_p^4$	$\sum a_n^3$	$\sum a_p^3$	κ_i	$\sum(\Lambda_{oi} - a_i)a_i^2$
$\sum(a_p^5 - a_n^5)$	$\sum a_i^4$	$(a_p^4 - a_n^4)$	$-\sum a_n^3$	$\sum a_p^3$	$-\sum a_n^2$	$\sum a_p^2$	κ_{cqi}	$\sum(\Lambda_{oi} - a_i) a_i a_i$
$\sum a_i^5$	$\sum(a_p^4 - a_n^4)$	$\sum a_i^4$	$\sum a_n^3$	$\sum a_p^3$	$\sum a_n^2$	$\sum a_p^2$	κ_z	$\sum(\Lambda_{oi} - a_i)a_i^2$
$\sum a_n^4$	$-\sum a_n^3$	$\sum a_n^3$	$\sum a_n^2$	0	$\sum a_r$	0	c_r	$\sum(\Lambda_{on} - a_n)a_n$
$\sum a_p^4$	$\sum a_p^3$	$\sum a_p^3$	0	$\sum a_p^2$	0	$\sum a_p$	c_p	$\sum(\Lambda_{op} - a_p)a_p$
$\sum a_n^3$	$-\sum a_n^2$	$\sum a_n^2$	$\sum a_n$	0	N_{ri}	0	κ_{cn}	$\sum(\Lambda_{on} - a_n)$
$\sum a_p^3$	$\sum a_p^2$	$\sum a_p^2$	0	$\sum a_p$	0	N_{pi}	κ_{cp}	$\sum(\Lambda_{op} - a_p)$

(6)

radius measurement errors are $\delta_p = -0.008 \text{ in/in}$ and $\delta_n = -0.005 \text{ in/in}$ [see Eq.(3)]. The best estimates of the input accelerations (including Coriolis's) are $a_p = 5, 10, 15, 20, 30, 40, 60, 80, 100, 80, 60, 40, 30, 20, 15, 10$, and $5g$. For convenience with no real loss of generality, let $a_n = -a_p$. The true input accelerations are obtained from Eqs.(3) which are then substituted in Eq.(2) to get the true accelerometer outputs A_{oj} . These outputs and the estimated inputs are substituted in Eq.(6). The solution is:

$$\begin{array}{ll} K_3 = 9.673,982,2(-8) & c_n = -9.030,563,0(-3) \\ K_{oq} = -2.939,262,3(-6) & c_p = -1.295,245,4(-2) \\ K_2 = 1.881,096,2(-6) & K_{cn} = 9.971,089,6(-3) \\ & K_{op} = 2.997,075,6(-2) \end{array}$$

Though only eight significant figures are given in the above table, all calculations were carried out to thirteen significant figures. The elements of Eq.(6) are revised by means of Eq.(8) and again solved for the coefficients.

$$\begin{array}{ll} K_3 = 1.000,033,3(-7) & c_n = 3.485,569,4(-6) \\ K_{oq} = -2.997,546,5(-6) & c_p = -3.452,994,6(-6) \\ K_2 = 1.999,903,4(-6) & K_{cn} = 1.000,039,8(-2) \\ & K_{op} = 2.999,962,1(-2) \end{array}$$

With but one revision of the elements of Eq.(6), the nonlinear coefficients have been recovered with great accuracy. A further revision of Eq.(6) using the above values of c_n and c_p give the following results.

$$\begin{array}{ll} K_3 = 1.000,000,3(-7) & c_n = -2.086,564(-8) \\ K_{oq} = -2.997,004,3(-6) & c_p = -2.515,517(-8) \\ K_2 = 1.999,998,9(-6) & K_{cn} = 1.000,016,9(-2) \\ & K_{cp} = 2.999,083,1(-2) \end{array} \quad (9)$$

The second iteration has caused no significant changes in the results. Note that K_{on} and K_{op} are almost exactly equal to the bias plus the component of gravity due to the angles θ_j , as they should be.

It will now be shown that most of the remaining errors in the results of Ex.1 are due to the vertical components of the misalignment angles.

EXAMPLE 2. All parameters will remain the same as in Ex.1 except that $\theta_n = 0$. Again using Eqs.(2) and (3) to determine A_{oj} and substituting the results in Eq.(6) along with the estimated input accelerations, it is found that:

$$\begin{array}{ll}
K_3 = 9.073,982,1(-8) & c_n = -9.030,463,9(-3) \\
K_{cq} = -2.942,196,7(-6) & c_p = -1.295,243,5(-2) \\
K_2 = 1.881,107,8(-6) & K_{cn} = 1.997,092,2(-2) \\
& K_{op} = 1.997,092,2(-2)
\end{array}$$

Revising the elements of Eq.(5) by use of Eqs.(8), we find:

$$\begin{array}{ll}
K_3 = 1.000,033,2(-7) & c_n = 3.485,641,8(-6) \\
K_{cq} = -3.000,545,9(-6) & c_p = -3.453,061,2(-6) \\
K_2 = 1.999,904,7(-6) & K_{cn} = 2.000,023,1(-2) \\
& K_{op} = 2.000,023,1(-2)
\end{array}$$

A second revision yields:

$$\begin{array}{ll}
K_3 = 1.000,000,1(-7) & c_n = -2.088,484(-8) \\
K_{cq} = -3.000,003,2(-6) & c_p = -2.517,764(-8) \\
K_2 = 2.000,000,1(-6) & K_{cn} = 2.000,000,2(-2) \\
& K_{cp} = 1.999,999,9(-2)
\end{array} \tag{10}$$

Comparing Eqs.(9) of Ex.1 with Eqs.(10) of Ex.2, it is seen that the error in K_{cq} in Ex.1 is due to the vertical component of the misalignment angle.

The errors in the other nonlinear coefficients are negligible. If the vertical components had been of the same sign instead of opposite sign, it would have been K_2 that would have been affected. With coefficients of the magnitude chosen here, it appears that the arbitrarily set limit of $\pm 0.0^\circ$ rad. for the vertical component of the misalignment could be safely relaxed, but since it is so easily controlled, why add this error to the others which cannot be controlled.

The next example will show the effect of reducing the input acceleration range.

EXAMPLE 3. All parameters are the same as in Ex.1 except that the input range has been cut by a factor of five. Let $a_p = -a_n = 2, 4, 6, 8, 10, 12, 14, 16, 18, 20, 18, 16, 14, 12, 10, 8, 6, 4$, and $2g$.

The output of the accelerometer is obtained from Eqs.(3) and (2), as before. With these values of a_i and A_{oj} substituted in Eq.(6), it is found that:

$$\begin{array}{ll}
K_3 = 9.673,998,6(-8) & c_n = -9.027,296,9(-3) \\
K_{cq} = -2.939,267,6(-6) & c_p = -1.295,557,2(-2) \\
K_2 = 1.949,384,0(-6) & K_{cn} = 1.992,796,9(-2) \\
& K_{cp} = 2.999,946,3(-2)
\end{array}$$

After three revisions of Eq.(6), the results are:

$$\begin{array}{ll} K_3 = 1.000,050,8(-7) & c_r = -7.140,64(-9) \\ K_{cq} = -2.997,170,6(-6) & c_p = -5.594,10(-9) \\ K_2 = 2,000,009,0(-6) & K_{cn} = 1.000,017,2(-2) \\ & K_{op} = 2.999,983,0(-2) \end{array}$$

Comparing the above results with those of Ex.1, it is evident that the errors with the reduced input range is only slightly higher but it required more iterations to reach that level of accuracy.

EFFECTS OF NOISE

The question of what effect noise in the input/output data has on the recovery of the nonlinear coefficients has been raised many times but never satisfactorily answered. Computer simulations will be used to throw some light on this thorny subject. In addition, a method is suggested for estimating the noise at any particular centrifuge facility and the effect of that noise on the recovery of the nonlinear coefficients.

EXAMPLE 4. We will use the same parameters and acceleration range as in Ex.1 but with noise added to the accelerometer output as given in Eq.(2). A standard deviation of $100\mu g$ was chosen as being fairly typical though possibly on the high side. This noise level is three orders of magnitude greater than the cubic coefficient and almost two orders of magnitude greater than the other two nonlinear coefficients.

To generate noise, the random number table in "Handbook of Mathematical Functions" by Abramowitz and Stegun, Bureau of Standards AMS 55 was used to obtain the cumulative probability from which the noise was gotten in terms of the assumed standard deviation. The noise vs acceleration is listed in Tables I and II. Three readings were taken at each acceleration level and the means of the three readings, given in the last column, were used in Eq.(2) to obtain A_{oj} . Using the means instead of each individual reading saves work and will not significantly affect the results. Note that the actual standard deviation in Tables I and II are very close to the desired $100\mu g$. The outputs A_{oj} and the estimated inputs a_i are substituted in Eq.(6) which is then solved for the coefficients.

$$\begin{array}{ll} K_3 = 9.600,940,4(-8) & c_r = -9.032,592,2(-3) \\ K_{cq} = -2.857,259,9(-6) & c_p = -1.295,378,9(-2) \\ K_2 = 1.873,333,6(-6) & K_{cn} = 1.000,609,9(-3) \\ & K_{op} = 2.997,413,9(-2) \end{array}$$

After two scale corrections, the results are:

$$\begin{array}{ll} K_3 = 9.925,206,0(-8) & c_r = -2.038,817(-8) \\ K_{cq} = -2.914,191,5(-6) & c_p = -2.464,151(-8) \\ K_2 = 1.991,719,2(-6) & K_{cn} = 1.000,609,9(-2) \\ & K_{op} = 3.000,267,0(-2) \end{array}$$

Thus for the $\pm 100g$ range, the nonlinear coefficients have been recovered

TABLE I

a_p	Ran. #	$\zeta_p \mu g$	Ran. #	$\zeta_p \mu g$	Ran. #	$\zeta_p \mu g$	$x_p \mu g (\text{ave.})$
5	.28105	-57.94	.36833	-33.63	.46248	-9.42	-33.66
10	.59231	23.35	.65732	40.52	.42054	-20.05	14.61
15	.87437	114.74	.15263	-102.53	.63174	33.65	15.29
20	.24046	-55.21	.35695	-36.67	.34049	-41.42	-44.33
30	.62035	30.64	.81925	91.26	.42840	-18.05	34.62
40	.04814	-166.32	.53582	10.99	.53205	8.04	-49.10
60	.45028	-12.50	.78714	79.66	.68257	47.49	38.22
80	.82758	94.47	.61435	29.07	.71902	57.99	60.51
100	.01301	-222.61	.03483	-181.42	.04851	-165.95	-189.99
80	.71886	57.95	.71494	56.79	.81683	90.34	68.36
60	.85170	104.38	.25986	-64.38	.94868	163.23	67.74
40	.01173	-226.62	.43644	-16.00	.14385	-106.32	-116.31
30	.94505	159.88	.10369	-126.08	.71182	55.87	29.89
20	.55343	13.43	.57315	18.44	.65914	41.02	24.30
15	.94506	159.88	.95401	168.51	.21459	-79.07	83.11
10	.86490	110.26	.46005	-10.03	.48711	-3.23	32.33
5	.08848	-135.03	.79436	82.17	.38856	-28.31	-27.06

$$\begin{aligned}\bar{\zeta}_p &= 0.501 \mu g \\ \sigma_p &= 97.14 \mu g \\ N_p &= 51\end{aligned}$$

$$\begin{aligned}\bar{x} &= 0.502 \mu g \\ \sigma_x &= 71.29 \mu g \\ N_x &= 17\end{aligned}$$

TABLE II

a_n	Ran. #	$\sum_n \mu g$	Ran. #	$\sum_n \mu g$	Ran. #	$\sum_n \mu g$	$x_n \mu g$ (ave.)
-5	.40666	-23.62	.20431	-82.64	.82295	92.65	-4.54
-10	.40588	-23.82	.69540	51.13	.94182	157.03	61.45
-15	.78237	78.02	.52876	7.22	.50982	2.46	29.23
-20	.98247	210.79	.95841	173.26	.49932	-0.17	127.96
-30	.80048	84.34	.37256	-32.51	.92543	144.27	65.37
-40	.43328	-16.81	.00243	-281.73	.26430	-63.02	-120.52
-60	.90087	128.66	.01169	-226.75	.42308	-19.40	-39.16
-80	.86556	110.57	.47673	-5.84	.32900	-44.27	20.15
-100	.67474	45.31	.25590	-65.61	.23245	-73.08	-31.13
-80	.59973	25.27	.20317	-83.04	.97977	204.86	49.03
-60	.87379	114.46	.02303	-199.51	.87377	114.45	9.80
-40	.37729	-31.26	.03320	-183.58	.07361	-144.45	-119.76
-30	.50276	2.69	.41020	-22.71	.32097	-46.50	-22.17
-20	.71455	56.68	.54137	10.39	.00862	-238.17	-57.03
-15	.73368	62.40	.53316	8.32	.52728	6.84	25.85
-10	.86418	109.94	.71029	55.43	.69977	47.63	71.00
-5	.08667	-136.16	.67017	44.04	.39483	-26.68	-39.60
$\bar{\sum}_n = 1.525 \mu g$ $\sigma_n = 110.23 \mu g$ $N_n = 51$							$\bar{X} = 1.525 \mu g$ $\sigma_x = 66.41 \mu g$ $N_x = 17$

with only fair accuracy which is not too unexpected when one considers that the standard deviation of the noise is more than an order of magnitude greater than any of the nonlinear coefficients. With more data, the accuracy would be improved. Since noise is a random element, another set of data would give somewhat different results.

EXAMPLE 5. The parameters will be the same as in Ex.4 except that the acceleration inputs are reduced by a factor of four so that the input range is only $\pm 25g$. The noise from Tables I and II are applied to the reduced acceleration inputs. With this new data solve Eq.(6) for the coefficients.

$$\begin{array}{ll} K_3 = 5.056,817,0(-8) & c_n = -9.035,246,8(-3) \\ K_{oq} = -1.647,167,6(-3) & c_p = -1.296,096,7(-2) \\ K_2 = 1.823,734,2(-6) & K_{cn} = 1.000,600,0(-2) \\ & K_{cp} = 3.000,421,1(-2) \end{array}$$

After two scale corrections, the results are:

$$\begin{array}{ll} K_3 = 5.268,774,3(-8) & c_n = 3.915,68(-9) \\ K_{cq} = -1.692,008,7(-6) & c_p = 2.763,92(-9) \\ K_2 = 1.869,478,0(-6) & K_{cn} = 1.000,655,5(-2) \\ & K_{cp} = 3.000,413,4(-2) \end{array}$$

It is obvious that further iterations will not significantly change the results. The noise in the data has made it impossible to accurately recover the coefficients when the input range is only $\pm 25g$. However the results are of the correct order of magnitude and may be acceptable in some applications where it is enough to know that the absolute value of a coefficient is less than a specified limit.

Note that the error in K_3 is very nearly equal to 4^3 times the error in Ex.4 and the errors in K_{oq} and K_2 are very nearly equal to 4^2 times the corresponding values in Ex.4, which is what they should be theoretically.

EXAMPLE 6. The parameters are the same as in Ex.5 except that the means of six noise readings will be used in Eq.(2) at each acceleration level. The additional sets of three noise readings are given in Tables III and IV which were obtained in the manner as were Tables I and II. The average of all six readings are given in the last columns of Tables III and IV which were used in Eq.(2) to get the outputs A_{oj} . With these data sets, the solution of Eq.(6) gives:

$$\begin{array}{ll} K_3 = 1.210,428,0(-7) & c_n = -9.016,502,5(-2) \\ K_{cq} = -4.058,222,6(-6) & c_p = -1.294,478,2(-2) \\ K_2 = 1.886,731,7(-6) & K_{cn} = 1.002,456,0(-2) \\ & K_{cp} = 2.998,250,9(-2) \end{array}$$

TABLE III

a_p	Ran. #	$\zeta_p \mu g$	Ran. #	$\zeta_p \mu g$	Ran. #	$\zeta_p \mu g$	$x_p \mu g$ (ave.)
1.25	.59526	24.11	.92315	142.67	.67719	45.71	18.58
2.50	.26240	-63.60	.26162	-63.84	.83339	96.77	2.19
3.75	.84892	103.19	.44722	-13.27	.90630	131.83	44.60
5.00	.83086	95.76	.43211	-17.10	.33435	-42.80	-16.19
7.50	.42436	-19.08	.92823	146.28	.58295	20.95	42.00
10.0	.40238	-24.72	.65783	40.66	.52515	6.31	-20.84
15.0	.44643	-13.47	.24899	-67.77	.14988	-103.70	-11.72
20.0	.13956	-108.24	.69210	50.18	.71863	57.88	30.23
25.0	.81982	91.47	.69255	50.31	.53869	9.72	-69.75
20.0	.26636	-62.39	.77578	75.80	.40823	-23.21	32.55
15.0	.40577	-23.85	.59640	24.41	.03037	-187.55	2.71
10.0	.83287	96.56	.20551	-82.21	.99937	322.73	-1.98
7.50	.98899	229.03	.69117	49.92	.95053	165.01	88.94
5.00	.14538	-105.65	.81874	91.06	.52769	6.95	10.88
3.75	.83903	99.06	.19839	-84.74	.41330	-21.91	40.29
2.50	.38351	-27.02	.09337	-132.03	.81699	90.40	4.73
1.25	.97391	194.17	.31151	-49.16	.13213	-111.64	-7.97

$$\begin{aligned}\bar{\zeta}_p &= 21.76 \mu g \\ \sigma_p &= 98.92 \mu g \\ N_p &= 51\end{aligned}$$

$$\begin{aligned}\bar{x} &= 11.13 \mu g \\ \sigma_x &= 34.84 \mu g \\ N_x &= 17\end{aligned}$$

TABLE IV

a_n	Ran. #	$\zeta_n \mu g$	Ran. #	$\zeta_n \mu g$	Ran. #	$\zeta_n \mu g$	$x_n \mu g (\text{ave.})$
-1.25	.55532	13.91	.44876	-12.88	.48790	-3.04	-2.60
-2.50	.18801	-88.53	.85319	105.03	.64892	38.24	39.85
-3.75	.21093	-80.32	.86693	111.21	.39601	-26.73	15.37
-5.00	.17106	-95.00	.48479	-3.81	.56877	17.33	50.40
-7.50	.30177	-51.93	.78314	78.29	.09976	-128.30	15.69
-10.0	.60908	27.69	.47185	-7.06	.11602	-119.52	-76.74
-15.0	.25820	-64.89	.47814	-5.48	.96346	179.25	-1.44
-20.0	.93882	154.51	.98854	227.51	.56140	15.45	76.32
-25.0	.64982	38.49	.63799	35.31	.40794	-23.29	-7.15
-20.0	.47967	-5.10	.97013	188.28	.76580	72.51	67.21
-15.0	.84108	99.89	.81425	89.37	.83043	97.59	52.71
-10.0	.96198	177.43	.08075	-140.01	.79065	80.87	-40.17
-7.50	.49192	-2.03	.61946	30.41	.25513	-65.85	-17.33
-5.00	.60834	27.50	.04811	-166.35	.13948	-110.27	-70.04
-3.75	.93793	153.77	.05763	-157.51	.02645	-193.58	-19.96
-2.50	.55342	13.43	.73260	62.07	.22247	-76.39	35.35
-1.25	.66518	42.06	.54909	12.34	.26999	-61.29	-20.95

$$\bar{\zeta}_n = 9.82 \mu g$$

$$\sigma_n = 97.3 \mu g$$

$$N_n = 51$$

$$x = 5.68 \mu g$$

$$x = 44.8 \mu g$$

$$N_x = 17$$

Comparing the above results with those of Ex.5, it is seen that doubling the number of data sets has roughly halved the errors in the non linear coefficients. However, the errors are still very much greater than those in Ex.4 where the acceleration was $\pm 100g$.

A STUDY OF NOISE COEFFICIENTS

The coefficients obtained from centrifuge data are the sums of the coefficients if there were no noise in the data and the corresponding coefficients for the noise distribution alone. This statement appears to be self-evident, nevertheless its truth will be demonstrated for the skeptics. The noise distribution will be fitted to the following equation which is analogous to Eq. (5) except that the input accelerations are the scale corrected ones rather than the estimated inputs.

$$j = k_3(a'_i)^3 + k_{oq} a'_i a'_i + k_2(a'_i)^2 + k_{1n} a'_n + k_{1p} a'_p + k_{on} + k_{op} \quad (11)$$

The matrix equation for the determination of the noise coefficients by the method of least squares is:

$$[A'] \begin{bmatrix} k_3 \\ k_{oq} \\ k_2 \\ k_{1n} \\ k_{1p} \\ k_{on} \\ k_{op} \end{bmatrix} = \begin{bmatrix} \sum_j (a'_i)^3 \\ \sum_j |a'_i| a'_i \\ \sum_j (a'_i)^2 \\ \sum_j a'_n \\ \sum_j a'_p \\ \sum_j \\ \sum_j \end{bmatrix} \quad (12)$$

where $[A']$ is the scale corrected square matrix of Eq.(6).

EXAMPLE 7. Taking the noise from Tables I and II and the scale corrected input accelerations from Ex.4, determine the noise coefficients using Eq.(12).

$$k_3 = -7.472,697,0(-10)$$

$$k_{oq} = 8.263,095,9(-8) \quad (13)$$

$$k_2 = -8.256,972,0(-9)$$

When these noise coefficients are subtracted from the corresponding coefficients in Ex.4, it is found that

$$K_3 - k_3 = 9.999,993,0(-8)$$

$$K_{oq} - k_{oq} = -2.996,822,5(-6)$$

$$K_2 - k_2 = 1.999,976,2(-6)$$

The noise corrected coefficients are closely equal to those in Ex.1 where the residual errors are primarily due to the vertical component of the misalignment angles and secondarily to accumulated round-off errors.

EXAMPLE 8. Taking the noise from Tables I and II but dividing the input accelerations by four as in Ex.5 and using the scale corrected inputs from Ex.5, determine the nonlinear noise coefficients. Solving Eq.(12) with this data, we find:

$$k_3 = -4.616,106,2(-8)$$

$$k_{cq} = 1.258,866,8(-6)$$

$$k_2 = -1.271,418,1(-7)$$

When these coefficients are subtracted from the corresponding coefficients in Ex.5, the results are:

$$K_3 - k_3 = 9.885,106,2(-8)$$

$$K_{cq} - k_{cq} = -2.950,867,1(-6) \quad (14)$$

$$K_2 - k_2 = 1.996,620,9(-6)$$

These are fair approximations to the true nonlinear performance coefficients but not as good as in Ex.7 where the input range was $\pm 100g$. Examples 5 and 8 show how important it is to control noise, particularly at the lower input ranges. The ratio of k_3 in Eqs.(14) to k_3 in Eqs. (13) is approximately 64 and the ratios k_{cq} and k_2 in Eqs.(14) to those in Eqs.(13) are approximately 16 as expected.

EVALUATING THE NONLINEAR COEFFICIENTS

When an equation is fitted to centrifuge data by the method of least squares, numerical values will be obtained for each coefficient whether the equation is appropriate or not. To help determine if the model equation is a viable one, the residuals should be plotted to see if there is any evidence of systematic errors that additional or different nonlinear terms are required. It must be kept in mind that with too few data points even purely random errors may appear to be systematic.

If there are no systematic errors, then one must ask if each coefficient is significantly different from zero at some specified confidence level, say 90%. The Student t statistic is generally used for this determination.

Nonlinear coefficients may appear as artifacts of the data reduction procedure from misalignment and radius measurement errors. The iterative data reduction procedure outlined in this paper essentially eliminates all effects due to misalignments or radius measurement errors providing the vertical components of the misalignment angles are kept small, say no more than 0.01 radians.

As was seen in the previous section, noise in the data can have a very profound effect on the recovery of the performance coefficients. The following steps are suggested as a means of estimating the effects of noise in any particular facility for a given accelerometer.

(a) A rough estimate of the noise standard deviation may be obtained by recording the variation in output over each of a number of revolutions at a "steady" input acceleration. The noise would properly include the effect of variation in the "steady" input. This should be done at a number of inputs over the full acceleration range for the accelerometer under test.

(b) Construct several sets of tables similar to Tables I and II using the estimated standard deviation from Step (a). Because of the random nature of noise, at least six sets of tables should be constructed.

(c) Using an equation for noise appropriate for the data reduction equation for the accelerometer under test as Eq.(11) was appropriate for the data reduction equation, Eq.(5), determine the noise coefficients for each set of tables constructed in Step(b).

(d) From a study of the noise coefficients found in Step (c), estimate the standard deviation of each noise coefficient.

(e) Determine if the standard deviation of each noise coefficient is compatible with the requirements of the particular application. Do not overlook the linear noise coefficients since they directly affect the iterative procedure.

(e) If the noise coefficients obtained in Step (d) are unsatisfactory, then one or more of the following corrective actions must be taken.

(1) Reduce the noise by improving the instrumentation and/or the centrifuge controls.

(2) Design more rigid mounting fixtures.

(3) Redesign the accelerometer.

(4) Increase the input acceleration range, if possible. A 50% increase in range will reduce the effect of noise on a cubic coefficient by a factor of 3.375 and on a quadratic coefficient by a factor of 2.25.

SUMMARY

It has been shown how an iterative data reduction procedure can effectively eliminate the effects of input axis misalignments and radial measurement errors. A method is suggested on how to estimate the effects of noise at a centrifuge facility on the recovery of the nonlinear coefficients.

REFERENCES

- (1) Neugebauer, George H., Precision Centrifuge Testing of an Accelerometer, The Aerospace Corp., Report No. TR-0172(S2970-10) -1, Sept. 15, 1971.
- (2) Neugebauer, George H., Precision Centrifuge Testing of an Accelerometer, Sixth Biennial Guidance Test Symposium, Holloman AFB, October 1972.

CONTROL TEST AND VALIDATION FOR A LARGE DIAMETER HIGH STABILITY CENTRIFUGE

S. Willis, BSEE; M. Harshman, BSEE, IEEE; B. Popovich, BSEE;
M. Guardiani, BSEE; R. Strane, BSEE; and J. Profeta, BSEE, IEEE
Contraves Goerz Corporation

Abstract

A large (120-inch radius) precision centrifuge test bed is currently being designed and built. The control system design for the centrifuge is based on the results of a design study completed⁽¹⁾. The control system along with a precision drive system controls the main axis to within 5 ppm g-stability. Utilizing a high speed computer system, the control system uses state estimation and digital control techniques. The precision drive system employs AC torque ring motors.

Introduction

This paper summarizes the design of a control system for a large diameter high stability centrifuge. The actuator drive system design is also summarized. The centrifuge test and validation considerations are presented. The design of the control system and drive system are derived from a design study completed by a team of engineers from Contraves Goerz Corporation. The Centrifuge illustrated in Figure 1 has a 120-inch radius to the intersection of the two-axis platform axes. The operational range of the centrifuge main axis is from 0.5 g to 50 g. All axes of the centrifuge are designed for continuous rotation.

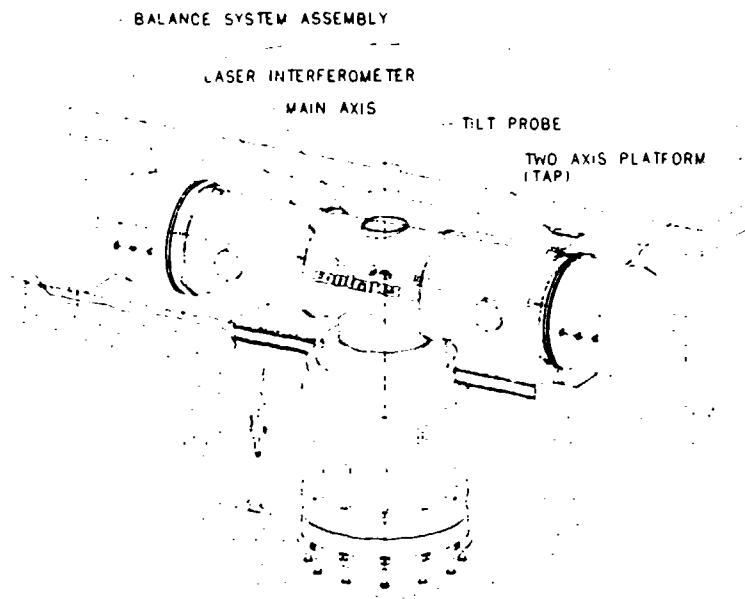


Fig. 1 Model 445 centrifuge.

The design goals of the control system are:

1. Control the main axis rate stability to within 0.4 ppm.
2. Position track the two axis platform with the main axis of the centrifuge to within 1 arc second.

Control System Model

The control system model has three main components: the single axis controllers; the state estimators for each axis; and the three-axis coupling model. The overall model is shown in Figure 2. The input to the axis controllers are the error signals generated from the axis commands and the state estimates ($\hat{\theta}_c, \hat{\theta}$). The axis command consists of a position command (θ_c) and a rate command ($\dot{\theta}_c$) for each individual axis. The output of the controllers are torque commands (τ_c) that feed the plant and the torque decoupling matrix. The plant supplies the position outputs (θ), used to drive the error signals in the state estimators. The decoupling matrix converts the torque commands into three decoupled acceleration estimates ($\ddot{\theta}$).

The acceleration estimates are the driving input to the state estimators. The three-axis coupling model generates feedforward torque commands (τ_{ff}) that are added to the controller torque commands.

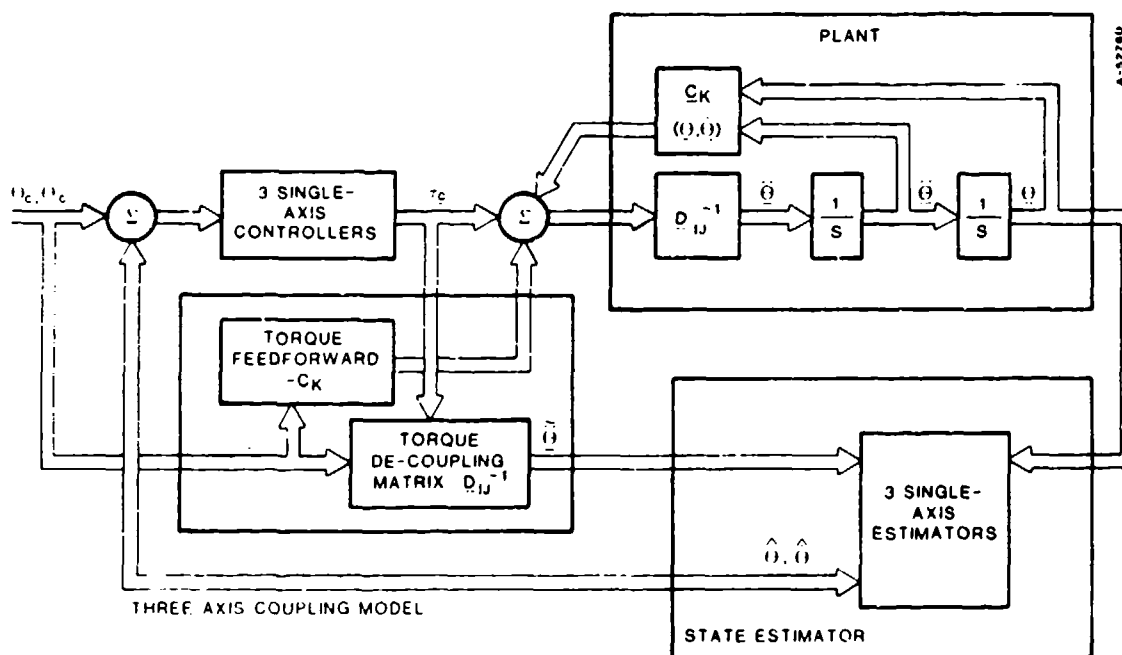


Fig. 2 Multi-axis control system.

Three-Axis Coupling Model

To enhance the performance of the control system, a three-axis coupling model is included. The three-axis coupling model is a computer model of the reaction torques based on Euler's equations. The coupling model is given in Equation 1.

$$\underline{\tau} = \underline{D}_{ij}^{-1} (\theta, \dot{\theta}) * \ddot{\theta} + \underline{C}_k (\theta, \dot{\theta}) \quad (1)$$

The torques (\underline{C}_k) are large gyroscopic torques, produced when all three axes are rotating simultaneously. The three-axis coupling model counteracts the torque effects by generating torque feedforward signals ($-\underline{C}_k$). The torque decoupling matrix (\underline{D}_{ij}^{-1}) decouples the acceleration estimates from the torque commands. The decoupling of the accelerations enables the axis controllers to be designed on an individual basis.

Single-Axis Controllers

Digital control design techniques are used in the design of the single-axis controllers. Each controller consists of a position compensator and rate compensator. Both compensators are digital filter equivalents of stopped integrators. An error signal, calculated from the command and state estimate, is input to each compensator. Illustrated in Figure 3, is a block diagram of a single axis controller. The position compensation (K_1, A, B) is calculated

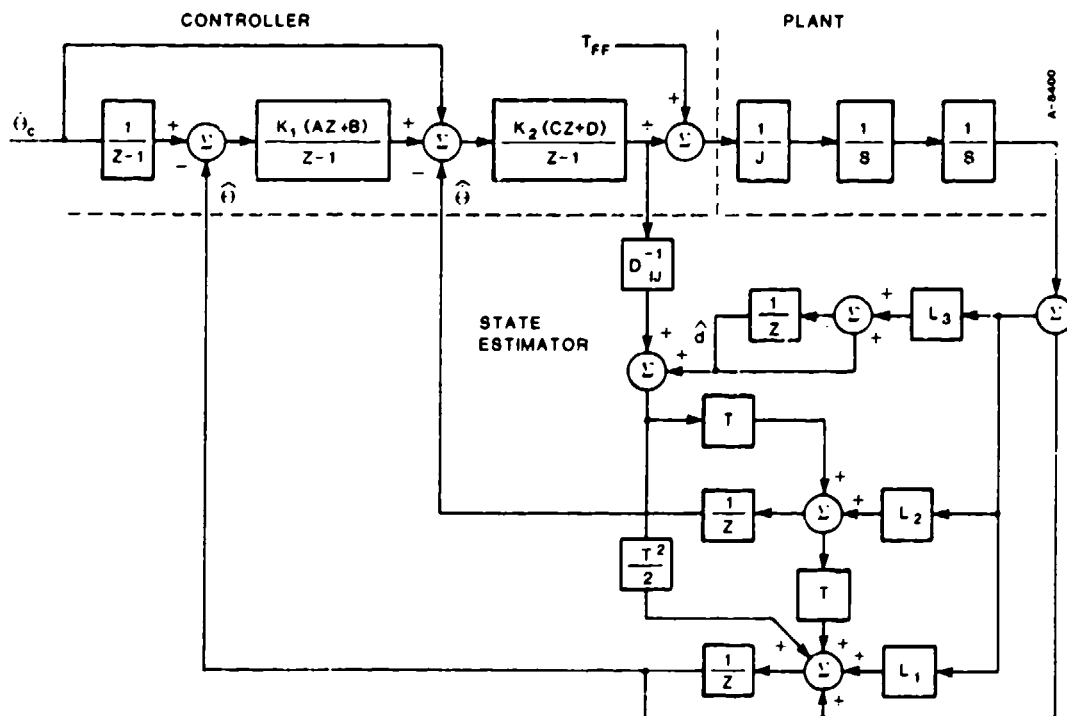


Figure 3. Single axis controller and state estimator

by using classical design techniques, to compute the gain and compensation. Tustin's approximation⁽²⁾ is then used to compute the appropriate parameters in the z-plane. The sample time (T) was chosen sufficiently small (1 millisecond) so as to alleviate any problems with the controller or estimator operating at slow sample rates. Root locus design techniques are used to compute the rate compensation (K2,C,D). The rate feedforward torque (τ_{ff}) is summed in after the rate compensator. Table 1 summarizes the values used for the gains and compensation variables.

Table 1 Gain and compensation values

Axis Loop	Bandwidth		Gain		Compensation			
	Pos(Hz)	Rate(Hz)	K1	K2	A	B	C	D
1	2	60	39.5	15.3	0.319	-0.318	1	-0.911
2	2	30	39.5	15.3	0.319	-0.318	1	-0.893
3	2	8	39.5	2442.2	0.319	-0.318	1	-0.948

State Estimators

The feedback for each axis is generated by a Luenberger Observer with an appended tracking system. The tracking system consists of a single integrator driven by the observer error. This will estimate any first order disturbance corrupting the plant after the power amplifier. The appended observer/tracking system will be referred to as an estimator. Equation 2 is the observer and equation 3 describes the disturbance estimator. A and M are the system matrices, B is the input vector, and C and N are the output vectors.

Each state estimator is a prediction estimator with a position, rate, and disturbance state. The state estimator model is given by equation 4. It is easily seen that equation 4 has the form of equation 5. In equation 5 \underline{X} is the state vector, \underline{F} is the estimator dynamics matrix, \underline{G} is the input matrix, \underline{U} is the input vector, and \underline{L} is the estimator gain vector. Figure 3 includes a block diagram of the state estimator. The inputs to the state estimator are the position measurement (θ_p) and the acceleration estimate ($\ddot{\theta}$) from the three-axis coupling model. The estimator gains (\underline{L}) can be selected by either pole placement or by sub-optimal stochastic techniques. If pole placement is used, Ackermann's formula² will provide a solution. If a sub-optimal solution is desired, \underline{L} can be found as the solution to the Riccati Equation which is the solution to the infinite optimal control problem.

$$\hat{\underline{X}}(k+1) = \underline{A} * \hat{\underline{X}}(k) + \underline{b} * u(k) + \underline{b} * \hat{d}(k) + \underline{L} * (\theta_m)(k) - C * \hat{\underline{X}}(k) \quad (2)$$

$$P(k+1) = M * P(k) + D * (\theta_m(k) - C * \hat{\underline{X}}(k)) \quad d(k) = N * P(k) \quad (3)$$

$$\begin{bmatrix} \hat{\underline{X}}(k+1) \\ P(k+1) \end{bmatrix} = \begin{bmatrix} \underline{A} & \underline{B} * \underline{N} \\ 0 & \underline{M} \end{bmatrix} \begin{bmatrix} \hat{\underline{X}}(k) \\ P(k) \end{bmatrix} + \begin{bmatrix} \underline{B} \\ 0 \end{bmatrix} u + \begin{bmatrix} \underline{L} \\ \underline{D} \end{bmatrix} (\theta_m(k) - C * \hat{\underline{X}}(k)) \quad (4)$$

$$\hat{\underline{X}}(k+1) = \underline{F} * \hat{\underline{X}}(k) + \underline{G} * U(k) + \underline{L} * (\hat{X}_1(k) - \theta_m(k)) \quad (5)$$

Control System Description

The control system performs all the functions associated with the control of the centrifuge. Some of these functions include:

- Position and Rate Calculations and Profiles
- State Estimation
- Gyroscopic Motion Calculations
- Torque Commands
- User Input/Output
- Mechanical and Electrical interlocks

The control system consists of three Single Board Computers (SBC's) and three Encoder Input/Output Processor boards (EIOP's). These boards are housed in a Multibus* card cage chassis. The control console houses all the power supplies, control electronics, and power control switches.

Single Board Computers

Hardware. The Single Board Computers are INTEL iSBC386/21** boards. Each board is a Multibus I processor board that contains an 80386-16 CPU, 80387-16 math coprocessor board, and one megabyte of dynamic RAM (Figure 4). The 80386-16 CPU is a high performance microprocessor that operates at 16-megahertz and conforms with the

* Multibus is a registered trademark of Intel Corporation.

** iSBC386/21 is a trademark of Intel Corporation.

ANSI/IEEE-754-1985 for Binary Floating-Point Arithmetic Standard. Other features of this board are as follows:

- 64 kilobyte cache static RAM
- One RS-232 serial communication channel
- Two programmable timers
- Hardware interrupt controller for a total of 16 interrupts
- One iSBX*** (System Bus Extension Interface) connector
- Two EPROM sites (up to 512 kilobytes)

Software. Each Single Board Computer will have specific task(s) that it is to perform. The Supervisor Processor (SP) board will perform the following tasks:

- Position and Rate profiles and commands - The SP will calculate all position and rate information from user input. The command will be converted into radians and radians/second and command to the Control Processor board (CTP) at one kilohertz rate.
- Communication - The SP will control the flow of information to and from the user, EIOP's, and CTP on Multibus.
- Interlocks - The SP will read and process all interlock information. Some of the interlocks that will be monitored:
 - System status
 - Excessive rate on axes
 - Access doors
 - Communication flags
 - Tilt/Radius probes
 - Power amplifiers

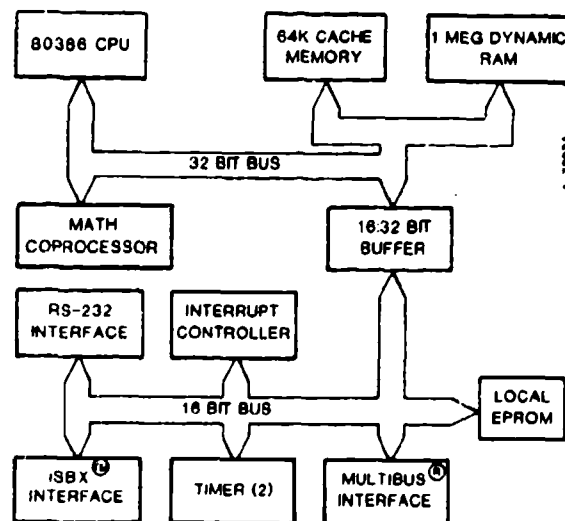


Fig. 4 386/21 block diagram

***iSBX is a trademark of Intel Corporation.

- User Input/Output - The SP will control all terminal and IEEE-488 communication with the user or user computer.
- Tilt/Radius Probes - The SP will process all information from the tilt/radius probes for output.

The control processor (CTP) performs the following tasks:

- Compensation - The CTP performs the position and rate compensation of the control loops for all axes.
- State estimation - The CTP performs the state estimation of all axes.

The coupling processor (COP) performs the following tasks:

- Coupling matrix - The COP calculates the three-axis coupling matrix.
- Torque feedforward - The COP computes the feedforward torques that are added to the torque commands of the axis controllers.

Encoder Input/Output Processor

The Encoder Input/Output Processors (EIOP's) are responsible for encoding the position transducer feedback signals and for performing all I/O required to control the centrifuge. To achieve the required accuracy specifications, it is necessary for the EIOP's to compensate the encoded position feedback for the repeatable errors of the position transducers and to compensate the torque commands for deterministic torque disturbances. The EIOP's perform these tasks using a pair of loosely coupled microprocessors and dedicated hardware and software.

Position Transducers. Each axis of the centrifuge uses a single speed resolver and a multispeed Inductosyn* to sense position. The resolver is used to determine in which cycle of the Inductosyn the axis is positioned. The resolver is only encoded once after power-up. After the resolver has been encoded, the Inductosyn becomes the position transducer.

Inductosyns and resolvers both operate on the same principle. Both transducers are driven with a sine reference signal and return two sinusoidal feedback signals. The feedback signals' amplitudes are proportional to the sine and cosine of the axis position within the current cycle.

$$\begin{aligned}\text{Ref} &= A * \sin(\omega t) \\ \text{Sin} &= A * K * \sin(\omega t + \theta) * \sin(\phi) \\ \text{Cos} &= A * K * \sin(\omega t + \theta) * \cos(\phi)\end{aligned}$$

*Inductosyn is a trademark of Farrand Industries, Inc.

where

- ω = reference frequency
- A = reference amplitude
- K = transducer transformation ratio
- θ = transducer phase shift
- ϕ = axis position within transducer cycle

The EIOP's encode the position transducers by sampling the amplitude of the sine and cosine feedback and then taking the arctangent.

EIOP Analog Hardware. Shown in Figure 5 is a block diagram of the EIOP's analog hardware. The major features of the analog circuitry are:

- feedback amplitude sampling section
- Inductosyn are resolver excitation
- multiplexed Digital to Analog Converter
- and a multiplexed Analog to Digital Converter

The feedback amplitude measurement section includes a circuit that measures the amplitudes of the feedback signals. The section also incorporates circuitry to reduce the effects of noise in the feedback.

The Inductosyn and resolver excitation is generated by low pass filtering the output of a digital timer to produce a low distortion sine wave. The excitation signals each have independent processor controlled amplitude and phase. By adjusting the amplitude of the excitation, the EIOP can cause the maximum amplitude of the position feedback to be full scale on the analog to digital converter (ADC). This allows maximum measurement resolution. The EIOP can also adjust the phase of the excitation. The phase adjustment allows the EIOP to compensate for the phase shift of the position transducers and low pass filters. This is necessary to bring the feedback into phase with the excitation so that the amplitude measurement circuitry may properly sample the amplitude of the feedback.

The EIOP is able to monitor various analog signals. These signals include: the power supply voltages, sine and cosine feedback amplitudes, proximity probe feedback, and the output of the digital to analog converter (DAC). The ability to monitor the power supply voltages and the DAC output allow the EIOP to detect an incipient failure and shut down the centrifuge before the problem becomes catastrophic.

A single multiplexed DAC allows the EIOP to output numerous analog signals. These signals include: Inductosyn and resolver drive amplitudes, ADC offset control, ADC test signals, and the axis torque command output.

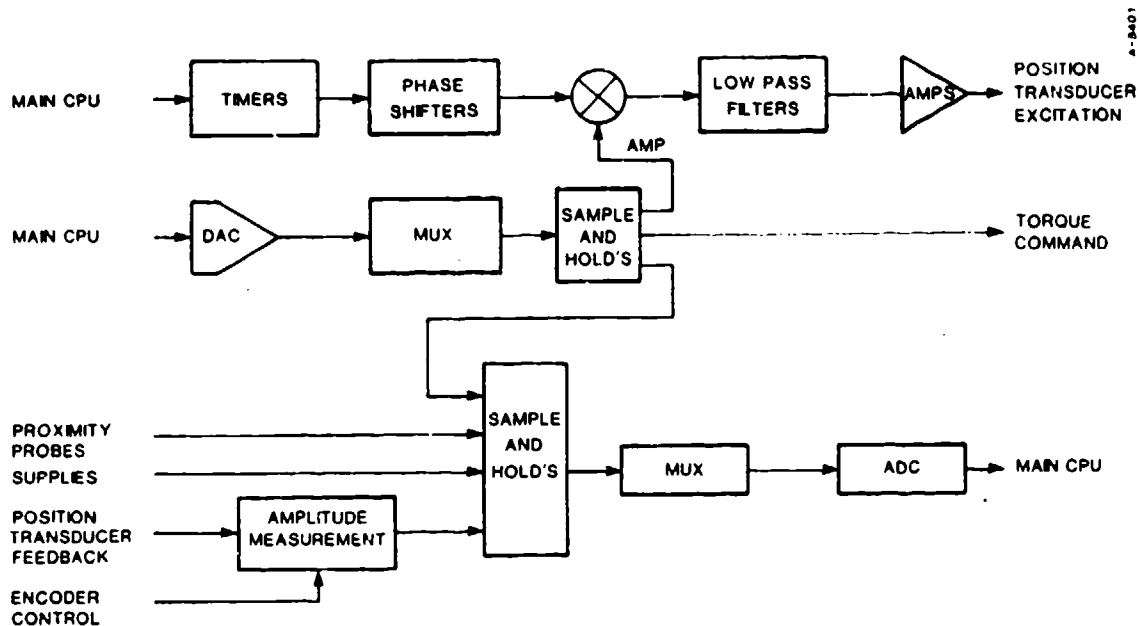


Fig. 5 EIOP analog block diagram

EIOP Digital Hardware. Shown in Figure 6 is a block diagram of the EIOP digital hardware. The major features of the digital hardware include:

- dual microprocessors
- dual-port-memory interfaces
- a watchdog timer
- and an iSBX interface

The microprocessors in the EIOP consist of a pair of Intel 80188 High Integration CPU's each running at 10 MHz. The Main CPU has access to all I/O provided by the EIOP. While the Auxiliary CPU has no I/O and simply provides the EIOP with additional numerical processing capability.

The EIOP's microprocessors communicate with each other through a dual-port-memory (DPM). Communication is simply a matter of depositing commands and data in predefined memory locations within the DPM. The Main CPU also communicates with the Single Board Computers (SBC's) through a second DPM, depositing commands and data in predesignated memory locations.

The Main CPU controls all analog and digital I/O required by the EIOP. This I/O includes: the DAC and ADC, iSBX bus, optically isolated digital sense lines, digital status indicators, relay contacts for power amplifier control, and feedback amplitude sampling control.

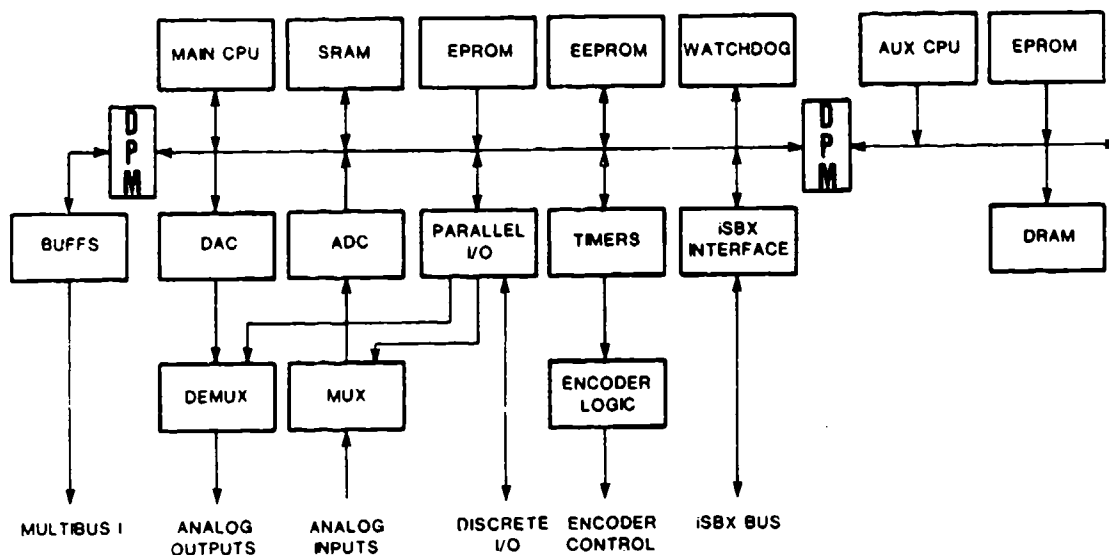


Fig. 6 EIOP digital block diagram

The EIOP also incorporates a watchdog timer to monitor the status of the Main CPU. If the Main CPU should fail, it will no longer trigger the watchdog, and the watchdog will time out. The time out will cause the relay contacts controlling the power amplifier for that axis to open, shutting down that axis. The Auxiliary CPU is also protected. The Auxiliary CPU must communicate with the Main CPU on a regular time base. If the Auxiliary CPU fails to communicate properly, the Main CPU will shut down the power amplifier.

EIOP Software. Shown in Figure 7 are the software flow diagrams for the Main and Auxiliary CPU's. This software covers:

- self tests
- position encoding
- position error correction
- torque error correction
- event pulse calculation
- and system safety check

Self tests are performed by each microprocessor immediately after power up. The self tests are done to ensure the operational status of the EIOP. The self tests cover the memory, ADC, DAC, digital timers, and the encoder control logic.

The process of encoding the sine and cosine feedback from the position transducers is a relatively straight forward though time consuming process. The process involves four steps:

1. Correct the sine and cosine feedback for offsets and gain errors.
2. Take the arctangent of the sine and cosine.
3. Correlate the arctangent output to an estimate of the current position of the axis.
4. Correct the position feedback word for repeatable errors.

The uncompensated position feedback is corrected by using the uncompensated position to look up two compensation terms; a coarse term and a fine term. The coarse term represents the errors which repeat on a multiple of once per revolution. The fine term represents the errors which repeat on a multiple of once per Inductosyn cycle. The two compensation terms are added to the uncompensated position feedback to form the compensated position feedback.

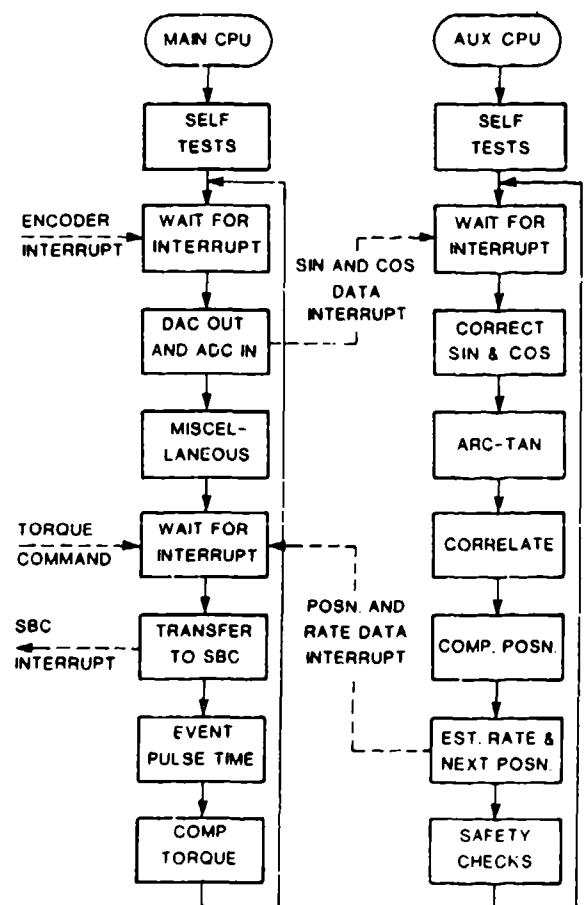


Fig. 7 EIOP software flowcharts

The torque command to the power amplifier is corrected in a manner similar to the position feedback. The compensated position feedback is used to index and interpolate a lookup table to find the torque error correction term. This term is then added to the torque command to be output on the next position encoding cycle.

The Main CPU also provides event pulses for the testing of guidance packages and system accuracy. These pulses indicate the occurrence of a once per revolution or once per Inductosyn cycle event. The pulses are generated by computing the time to the occurrence of the event from the next feedback sample interrupt and loading this value into a digital timer. The timer is triggered by hardware at the next feedback sample interrupt and automatically generates a pulse at the precalculated time. Since the digital timer operates from the CPU clock, the EIOP can generate event pulses with a 100 ns resolution.

To protect system integrity, certain safety checks are made during the normal operation of the EIOP. These checks include an over-rate check, a loss of feedback check, DAC/ADC loopback test, and the communication handshake.

Computer Development System

The development system consists of a Intel System 310AP computer. This computer is a multi-user, multi-tasking system which will provide:

- A Software development station for the computer control system
- RS-232 ports for terminals
- Interfacing to the computer control system
- Interfacing to a printer
- Magnetic storage media for software storage

For the development of software for the computer control system, the System 310AP has C-386, PL/M-386, and ASM-386 to compile/assemble programs. Utilities are supplied to link, map, and debug programs for the computer control system.

Actuator Drive System

The Actuator Drive System consists of AC torque motors and power amplifiers. Together they provide the high torques necessary to overcome the large gyroscopic reaction torques when operating under simultaneous rates.

A typical AC drive console is shown in Figure 8. The console contains six power amplifier/power supply sets.

The computer model of the reaction torques based on Euler's equations was used to determine the torque motor requirements. These requirements are summarized in Table 2.

Table 2 Torque motor requirements

<u>Parameter</u>	<u>Main axis</u>	<u>Outer platform</u>	<u>Inner platform</u>
Max. operating Speed (rad/sec)	12.7	12.7	12.7
Peak torque at max speed (ft-lb)	4700	2700	1750
Continuous torque at max. speed (ft-lbs RMS)	2400	1700	1150

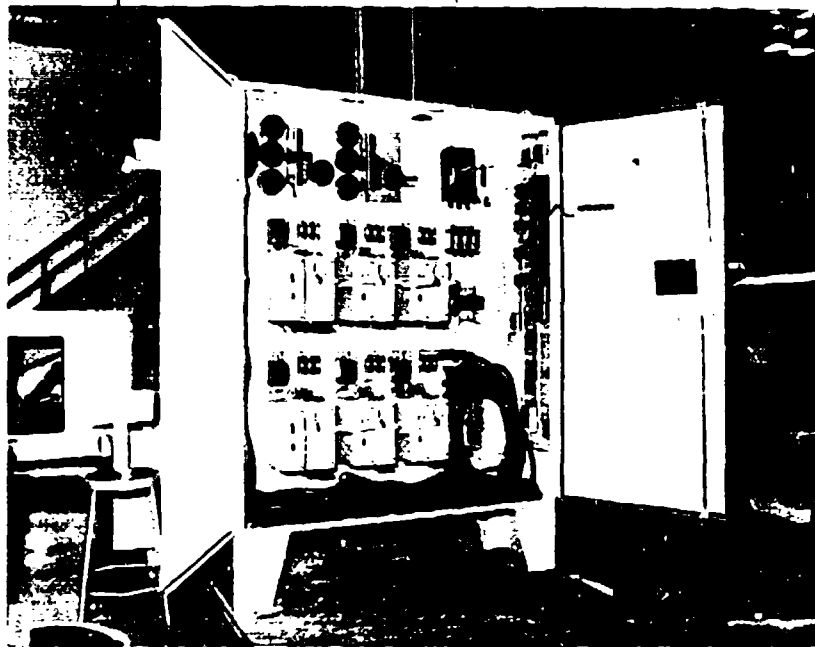


Fig. 8 Typical AC drive console

AC brushless torque motors were selected for the main axis and the two-axis platform. These torque motors offer the advantage of a much higher torque-to-inertia ratio than a DC motor.

The main axis torque motor consists of five individual, three-phase, wye-connected circuits. The outer platform motor consists of four circuits and the inner platform motor consists of two circuits. Each circuit is driven by a separate power amplifier. The multiple circuit configuration makes it possible to achieve the high torques and speeds simultaneously.

Figure 9 shows a block diagram of the power amplifier and torque motor. The power amplifier sinusoidally excites the motor windings to orient the electromagnetic field. This requires absolute knowledge of the motor shaft position which is provided by a commutation resolver. The amplitude of the electromagnetic field is modulated in proportion to the torque command. The angle of the field is maintained perpendicular to the permanent field of the magnets (rotor). This keeps the torque sensitivity at its peak regardless of shaft position, and minimizes the torque ripple due to commutation errors.

Each power amplifier is capable of providing a continuous RMS current of 50 amperes and a peak current of 140 amperes. Current is produced by pulse-width modulating the 325 VDC bus voltage at a frequency of 4 kHz.

The 4 kHz switching of the power amplifier tends to generate electromagnetic interference (EMI) which could potentially contaminate the control system electronics. Therefore, EMI-filtering consisting of a four-winding balun and L-C filters is incorporated at the output of the power amplifiers.

The balun provides ground isolation, and the mutual inductance between windings causes stray ground currents from the motor to flow back through the fourth winding of the balun instead of into the mechanical structure where the Inductosyn could be affected.

The L-C filters provide a second-order roll-off which is effective in attenuating the harmonics of the 4 kHz switching frequency.

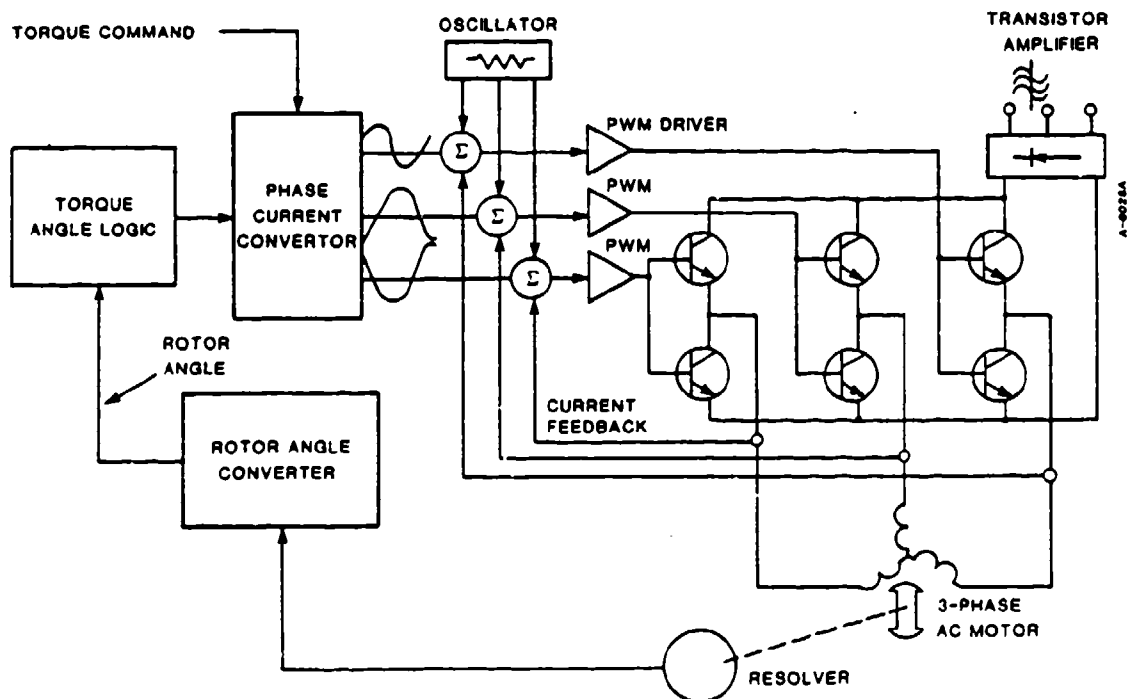


Fig. 9 Brushless AC servo drive block diagram

Centrifuge Test And Calibration

This section identifies the most common centrifuge error terms and the proposed methods of measurement and calibration. It should be noted that no attempt is made in addressing the post-processing of UUT data or UUT compensation based on the measurement of centrifuge parameters.

There are three major areas which introduce errors into the acceleration imparted to the UUT. These areas are grouped as follows:

1. Radius measurement
2. Centrifuge/boom Tilt
3. Rate Measurement

Radius Measurement

The measurement of centrifuge radius in this discussion is confined to dynamic measurements. The measurement system uses a laser interferometer and is illustrated in Figure 1. The laser interferometer is an optical device which is mounted directly to the centrifuge arm. Optical access is available so that radius growth can be measured at the UUT with the output available on a continuous basis.

The laser system is sensitive to changes in temperature and pressure. To reduce the effect of these error sources, an environmental tube is placed between the laser head and the retroreflector as shown in Figure 1. The g-stability errors associated with the radius measurement system for various environmental conditions are given in Table 3.

Table 3 G-stability errors

<u>Condition</u>	<u>G-stability errors</u>
1 degree F 0.1 in Hg	1.7 ppm
0.1 degree F 0.1 in Hg	1.1 ppm
0.1 degree F 0.01 in Hg	0.26 ppm

It should be noted that no attempt is made to identify specific error sources contributing to radius growth. The intent is to measure the composite error in radius uncertainty caused by all factors (e.g., thermal, g-loading, etc.).

For purposes of this discussion, the radius measurement includes such error sources main axis wobble, thermal effects, and boom stretch due to g-loading. Rate uncertainty is composed of several error sources which are component related (e.g., motor cogging torque, sensor errors, etc.) which are addressed in the "EIOP Software" section.

Centrifuge Tilt

Tilting of the main centrifuge axis and boom causes the acceleration input to the UUT to vary sinusoidally with each revolution. This error is typically eliminated by averaging the accelerometer output over an integer number of revolutions of the boom.

The centrifuge has proximity probes mounted to the stationary enclosures to measure boom sag or main axis tilt dynamically. These probes are illustrated in Figure 1. The major advantages to this arrangement include the fact that no slip rings are required and the probes are not subjected to forced convection heat transfer currents. However, the probe outputs are valid for a short time while the boom swings by requiring fast sample and hold circuits. In the past, this arrangement was used for radius measurements. This concept was rejected as a radius measurement technique since the proximity probes cannot measure the stretch of the boom at the UUT, but must measure the surrounding structure. This philosophy resulted in utilization of the proximity probes for tilt measurement only.

The proximity probes can measure with a precision of 0.05×10^{-6} radians. To obtain the precision the two probes must be separated by 40 inches. The distance increases the required range of the probes but is within the capability of commercially available units. This measured angle is the average angle between the two points.

The capacitance probe system has the advantage of being simple, rugged, and easy to use on a daily basis. The initial setup is critical since the setup is performed while the boom is stationary and the probes are placed within 0.010 inch of the centrifuge. Shielding from aerodynamic disturbances is required; however, the shielding is not critical since the two probes will see similar wind speeds.

Rate Measurement

The average centrifuge rate can be determined by measuring the time required for the centrifuge to rotate through a known angle. This is typically done by measuring the time required for an integer number of revolutions. The time is measured with a counter which has a precision time source as its input. The counter is triggered by an event marker which occurs once per centrifuge revolution. The accuracy of this measurement is limited by the accuracy of the time source and the position repeatability of the event marker. A time source accurate to within 1 microsecond will produce a rate uncertainty of 1 ppm when measuring a time of one second. A 1 arc second variation in the event marker location yields a rate

uncertainty of 0.8 ppm over one revolution. A simpler solution implemented on the centrifuge for determining axis rate is to monitor the rate state of the state estimator. The rate estimate is explained in more detail in the "State Estimators" section.

Conclusions

The centrifuge control system design plays an integral part in the overall design of the large diameter high stability centrifuge. The rate stability design goal represents a significant advancement in the state of the art of centrifuge design. Some of the key elements in the design are the position measurement and compensation and the precision torque actuation. The elaborate controllers and estimators are limited in performance by the transducers and actuators to which they interface.

Acknowledgments

This work was completed for the U.S. Air Force (Contract F08635-84-C-0276), Central Inertial Guidance Test Facility, Holloman Air Force Base, Project Manager, R. Alexander.

References

- (1) L.A. DeMore, et al, "Design study for a high stability large centrifuge test bed", paper no. 2100, presented at AIAA Guidance, Navigation, and Control Conference, 1986.
- (2) Franklin, G.F. and Powell, D., "Digital Control of Dynamic Systems", Addison Wesley, Reading, Massachusetts, 1960.

"The Global Positioning System as an Aid to the Testing of Inertial Navigation Units," C. P. Bruner, A. Matthews, R. E. Morgan, Litton Guidance & Control Systems, 5500 Canoga Avenue, Woodland Hills CA (S04A)

"A Cause of Divergence in the Kalman Gain Equation," James B. Gose, Physical Science Laboratory, P.O. Box 30002-NMSU, Las Cruces NM (S04B)

"Rate and Dynamic Tests on the Canadian Strapdown Gyroscope (CSG-2)," M. Vinnins, L. D. Gallop, F. Paquet, Defence Research Establishment Ottawa, Department of National Defence, Ottawa, Canada (S04C)

"The German Honeywell Ring Laser Gyro (Status Report on Development and Test Results)," Dr. B. Bolzmann, Honeywell Regelsysteme GmbH, Unternehmensbereich Sondertechnik, Honeywellstr, D-6457 Maintal 1 (S04D)

UNCLASSIFIED

The Global Positioning System as an Aid to the Testing
of Inertial Navigation Units

C. P. Bruner

A. Matthews

R. E. Morgan

Litton Guidance & Control Systems
5500 Canoga Avenue,
Woodland Hills, California 91367.

Paper for presentation at the 13th Biennial Guidance Test
Symposium at the Central Inertial Guidance Test
Facility, Holloman A.F.B., New Mexico October 1987.

UNCLASSIFIED

S04A

This paper was published separately. The Public Release Approval was not received in time to include the paper in this volume.

A CAUSE OF DIVERGENCE IN THE KALMAN GAIN EQUATION

James B. Gose
New Mexico State University

Abstract: this paper describes a source of divergence in Kalman filters which is inherent in the formulation of the gain equation. The paper presents a solution to the problem, and describes the characteristics of the solution.

BACKGROUND

In its original form, the Kalman filter is mathematically described by six equations:

$$X_1 = A_1 X_{1-1} + e_x \quad \text{Eq. 1}$$

$$X_{1/1} = X_{1/1-1} + K_1 r_1 \quad \text{Eq. 2}$$

$$\text{wherein } r_1 = y_1 - H_1 X_{1/1-1} \quad \text{Eq. 3}$$

$$K_1 = P_{1/1-1} H_1^t (R_1 + H_1 P_{1/1-1} H_1^t)^{-1} \quad \text{Eq. 4}$$

$$\text{wherein } P_{1/1-1} = A_1 P_{1-1/1-1} A_1^t \quad \text{Eq. 5}$$

$$P_{1/1}^{-1} = A_1 P_{1-1/1-1}^{-1} A_1^t + H_1^t R^{-1} H_1 \quad \text{Eq. 6}$$

These equations have achieved widespread use since they provide a unique tool for the discrete integration of differential equations in combination with the employment of external measurements in an optimal way. This widespread use has revealed a problem of application - the so-called divergence problem - about which much is being written in the literature. This problem is one wherein the Kalman update (Eq. 1) tends to dominate the solution such that very large residuals in the measurement (Eq. 2) are encountered. Typically, the more time points input to the Kalman filter, the larger the residuals that are seen.

A number of explanations have been put forth to explain this phenomenon. These explanations have been well categorized by Guard(1976) as:

"- The first category of problem is caused by computational errors. When this occurs, the covariance matrix can become non-positive definite and the computational algorithm becomes unconditionally unstable. In classical control system terminology, the filter gain matrix K_1 provides a positive instead of negative feedback based on the measurement residuals r_1 .

- The second category of problems with the covariance matrix occurs when the system to be estimated is improperly modeled, because of invalid measurement

error or state error statistics, incorrect mathematical model for the state dynamics, or because of non-linear phenomena aggravated by poor estimation of initial conditions. If, for any of these causes, $P_{i/i}$ becomes much too small, the gain matrix K_i will also be too small.

When this occurs, the correction term $K_i r_i$ will have negligible effect on the state estimate, which will diverge from its optimum value. The divergence in itself causes an increase in errors attributable to the linearization process, which tends to accelerate the divergence once it starts."

As might be expected, these rather sweeping generalities have arisen from a very large number of corrective algorithms tailored to each application. The success of the algorithms appears to be strongly related to the degree of rigour with which the state dynamics can be formulated and to the paucity of variables in the state dynamics model.

EXAMINATION OF THE GAIN EQUATION WEIGHT MATRICES

Different Covariance Estimates:

A problem would appear to lie in the use of $P_{i/i-1}$ (as defined in Eq. 6) in Eq. 5. If we examine the two error terms R_i and $P_{i-1/i-1}$ in turn, we will begin to understand the source of a problem. R_i is the covariance of y_i , a variable with Gaussian variability. The covariance of such a variable is a constant, i.e. for a sufficient number of measurements the covariance can be exactly known. $P_{i/i}$ on the other hand, is the covariance of an estimate of the state variables at the i^{th} instant of time. Such a variable will have Gaussian variability. This covariance, however, will not be a constant. For a sufficient number of measures, the covariance will become zero, i.e. the estimate will be exact.

This is a classic example of the covariance of a measurement in the former case and the covariance of the mean in the latter case.

It is important to recognize that the use of a covariance of measurements together with a covariance of an estimate of a mean in a weighted average, will inevitably result in the elimination of the measurement. It will simply be weighted out of the solution as we shall see.

Least Squares Formulation:

Before proceeding to a more quantitative examination of the problem, it is beneficial to present the Kalman filter equations in the format of a weighted least squares estimate (which, in fact, they are). This provides more insight into the nature of both the problem, and an avenue for an improved algorithm.

In the least squares estimation process, Mikhail (1976) tells us that we may consider the solution problem as one of combining two measurements; one an indirect measurement and the other a direct measurement.

The indirect measurement is described by the equation

$$y_i = H_i x_i + e_y \quad \text{Eq. 1}$$

The direct measurement described by the equation

$$\underline{x}_i = x_i + e_x \quad \text{Eq. 11}$$

The simultaneous least squares estimate of \underline{x} is found from:

$$\underline{x}_1 = (H_1^t W_y H_1 + W_x)^{-1} (H_1^t W_y y_1 + W_x \underline{x}_1) \quad \text{Eq. iii}$$

in which W_y and W_x are weight matrices for the indirect and direct measurements respectively, each being the inverse of its respective covariance matrix.

For this situation, the covariance matrix for the estimate may be expressed as:

$$P_x = (H_1^t R^{-1} H_1 + P_u^{-1})^{-1} \quad \text{Eq. iv}$$

where R and P_u are the covariances matrices of the indirect and direct measurements.

Transforming Eq. iii into a recursive format (about the update estimate \underline{x}_1) and substituting Eq. 5, we have:

$$\underline{x}_1 = \underline{x}_1 + (H_1^t R^{-1} H_1 + P_{1/1-1}^{-1})^{-1} H_1^t R^{-1} (y_1 - H_1 \underline{x}_1) \quad \text{Eq. v}$$

in which $\underline{x}_1 = \underline{x}_{1-1} + C_1 \underline{x}_{1-1}$, (C_1 is the dynamics state coefficient matrix used for the direct measurement) may be expressed as Eq. 1 by the simple algebraic manipulation:

$$\underline{x}_1 = (I + C) \underline{x}_{1-1} = A \underline{x}_{1-1}$$

Eq. v has been shown to be identical to Eq. 2 (see attached).

Decomposition of the Mixed Covariances Equation:

We now are ready to attempt a more concise examination of the problem posed by the mixing of the two types of covariance matrices in the Kalman filter. Proceeding to the decomposition of the covariance equation shown in Eq. iv above:

$$P_{1/1}^{-1} = A_1 P_u^{-1} A_1^t + H_1^t R^{-1} H_1$$

and substituting $P_{1-1/1-1}$ for P_u

$$P_{1/1}^{-1} = A_1 P_{1-1/1-1}^{-1} A_1^t + H_1^t R^{-1} H_1 \quad \text{Eq. 6}$$

Expand this by substituting successive values of $P_{i-k/i-k}$ and simplifying our notation. Since A and R are both constants in any given application; we may write:

$$P_{n/n}^{-1} = A^{n-1} P_{0/0}^{-1} (A^t)^{n-1} + \sum_{k=0}^{n-1} A^k H_k^t R^{-1} H_k (A^t)^k \quad \text{Eq. vi}$$

Examining this equation near some limiting conditions: - As the time between samples becomes small then A approaches I . Also note that $P_{0/0} = g$ a constant.

$$P_{n/n}^{-1} = g^{-1} + \sum_{i=1}^n H_i^t R^{-1} H_i$$

$$\text{or } P_{n/n} = gR(R + g \sum_{i=1}^n H_i^t H_i)^{-1} \quad \text{Eq. vi.a}$$

since $\sum_{i=1}^n H_i^t H_i = n$ times a constant, Eq. vi.a tells us that as n approaches infinity, $P_{n/n}$ approaches 0 and $P_{n/n}^{-1}$ approaches infinity.

From the foregoing, we correctly conclude that the Kalman filter equations weight the measurements by some constant, while weighting the update by a value which approaches infinity. Clearly this will result in the divergence problem so widely seen in the Kalman filter.

A SUGGESTED ALTERNATIVE ALGORITHM

How do we remedy the problem now that we can see its origin?

- 1) Use a revised Kalman update covariance relationship, and
- 2) recognize that the inaccuracy in the update is at least as large as the measurement error plus any extrapolation (update) error.

Following these two lines of thinking, one may readily rewrite Eq. 6 as follows:

$$P_{i/i}^{-1} = A_i(g^{-1} + H_{i-1}^t R^{-1} H_{i-1})^{-1} A_i^t + H_i^t R^{-1} H_i \quad \text{Eq. 6.a}$$

wherein both error contributions are covariances of observations and $P_{i/i}$ is a covariance of the estimate of the mean.

It will also follow that Eq. 5 will become:

$$P_{i/i-1} = A_i(g^{-1} + H_{i-1}^t R^{-1} H_{i-1}) A_i^t \quad \text{Eq. 5.a}$$

Figures 1 and 2 show the behavior of Eq's. 6 and 6.a, respectively, near the limits discussed above.

Figure 1 depicts, for the mixed covariances of Eq. vi., the relative contribution of the Kalman update and the measurement data to the final estimate, versus the number of points which have been estimated since the initialization of the Kalman filter. Note that in Figure 1, the combined estimate approaches the Kalman update quite rapidly. The measurement contribution to the final answer being only 9% at the tenth point, and 2% at the twentieth point.

Figure 2 depicts the error using Eq. vi.a. This equation, of course, is not a function of the number of points since the initialization of the filter. It uses the trace of the covariance matrices to show the behaviour of the total covariance against the Kalman update covariance and the measurement covariance.

Note that total covariance approaches a constant as the measurement covariance becomes large (contributes less to the total covariance). Also note that the total covariance does not grow inordinately as the measurement covariance becomes small (contribution to the estimate becomes large). In summary, neither error will cause the other to be weighted out of the solution.

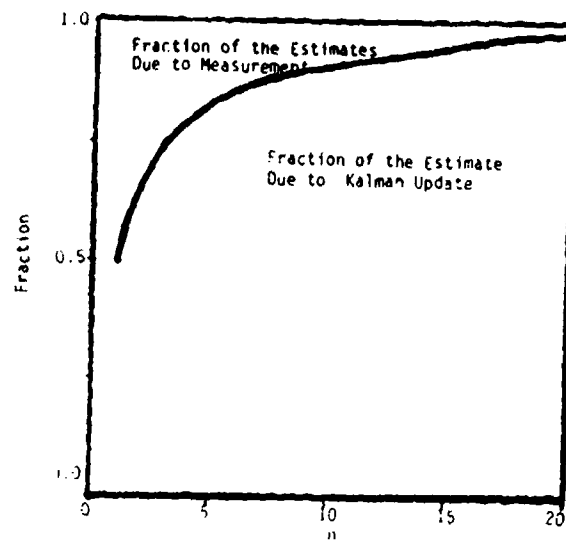


Figure 1

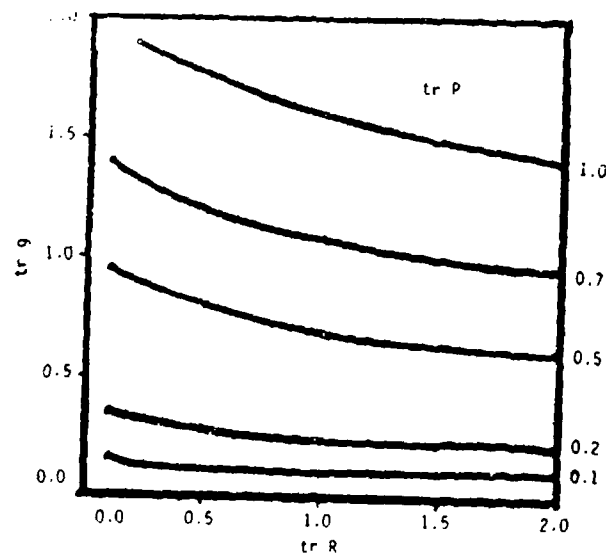


Figure 2

REFERENCES

Guard, Keith; Estimation of Variances in a Kalman Filter, Doctorial Dissertation; 1972; University of Delaware.

Mikhail, Edward M. and Ackerman, F.; Observations and Least Squares; 1976; IEP-A Dun-Donnelley Publisher, NY.

Gose, James B.; "Data Systems Manual - Least Squares"; 1981; WSMR, NM 88002.

ATTACHMENT

PROOF THAT THE KALMAN WEIGHT COEFFICIENT K_1 IS THE SAME AS THE CORRESPONDING LEAST SQUARES COEFFICIENT from Gose (1981).

The recursive form of the least squares development shows a coefficient term of

$$[H_1^t R_1^{-1} H_1 + P_{1/i-1}^{-1}]^{-1} H_1^t R_1^{-1}$$

The corresponding coefficient from the Kalman filter formulation is:

$$K_1 = P_{1/i-1} H_1^t [R_1 + H_1 P_{1/i-1} H_1^t]^{-1}$$

These two may be shown to be equal as follows (dropping the index for convenience).

The relationship,

$$[H^t R^{-1} H + P^{-1}]^{-1} H^t R^{-1} = P H^t [R + H P H^t]^{-1}$$

may be shown to be an identity by front multiplying both sides by

$$(H^t R^{-1} H + P^{-1}),$$

then by back-multiplying both sides by

$$(R + H P H^t)$$

to obtain

$$I H^t R^{-1} (R + H P H^t) = (H^t R^{-1} H + P^{-1}) P H^t I,$$

which simplifies to

$$H^t R^{-1} R + H^t R^{-1} H P H^t = H^t R^{-1} H P H^t + P^{-1} P H^t$$

which becomes the identity

$$H^t + H^t R^{-1} H P H^t = H^t R^{-1} H P H^t + H^t.$$

QED.

Rate and Dynamic Tests on the
Canadian Strapdown Gyroscope
(CSG-2)

M. Vinnins
L.D. Gallop
F. Paquet

Defence Research Establishment Ottawa
(DREO)
Department of National Defence
Ottawa, Canada

RATE AND DYNAMIC TESTS ON THE CANADIAN STRAPDOWN
GYROSCOPE (CSG-2)

1.0 BACKGROUND

In 1979, DREO became involved in the development of a unique strapdown gyroscope which now, 7 years later, is reaching fruition and showing good potential for numerous DND applications.

This development is the Litton (Canada) two-degree-of-freedom (TDF), tuned rotor gyroscope known as the CSG-2 (Canadian Strapdown Gyroscope, Mod 2).

1.1 Development Background

The CSG-2 gyro design was developed by Litton Systems (Canada) Limited (LSL) as an engineering exercise and was subsequently proposed to the Canadian Government for a technological grant. With the assistance of funding from the Canadian Department of National Defence the development program commenced in 1982 and was concluded in July of 1983 with the delivery of two instruments.

The CSG-2 gyroscope has several unique features, the most significant of which are the 'machine-from-solid' flexure mechanization and the use of sophisticated laser welding techniques during the assembly process. The overall design promises high instrument performance at low cost due to the ease of manufacturing techniques employed.

2.0 DESIGN AIMS

The CSG-2 was developed around a requirement for a Canadian bore-hole survey tool. The overall aim was to meet the requirements of that application while rendering a design which would be directly useable, or easily modified, for high rate aircraft applications or low rate aerospace applications. Miniaturization was not considered to be a major criteria for the design. A typical tuned rotor gyroscope mechanization is shown in figure 1.

In order to meet the performance and adaptability requirements there were several design aims;

- to design magnetic circuits for high rate applications
- to develop rotor construction methods for improved stability over gyros of similar design.
- to design suspension for high stability and
- to implement low cost components and improved assembly methods.

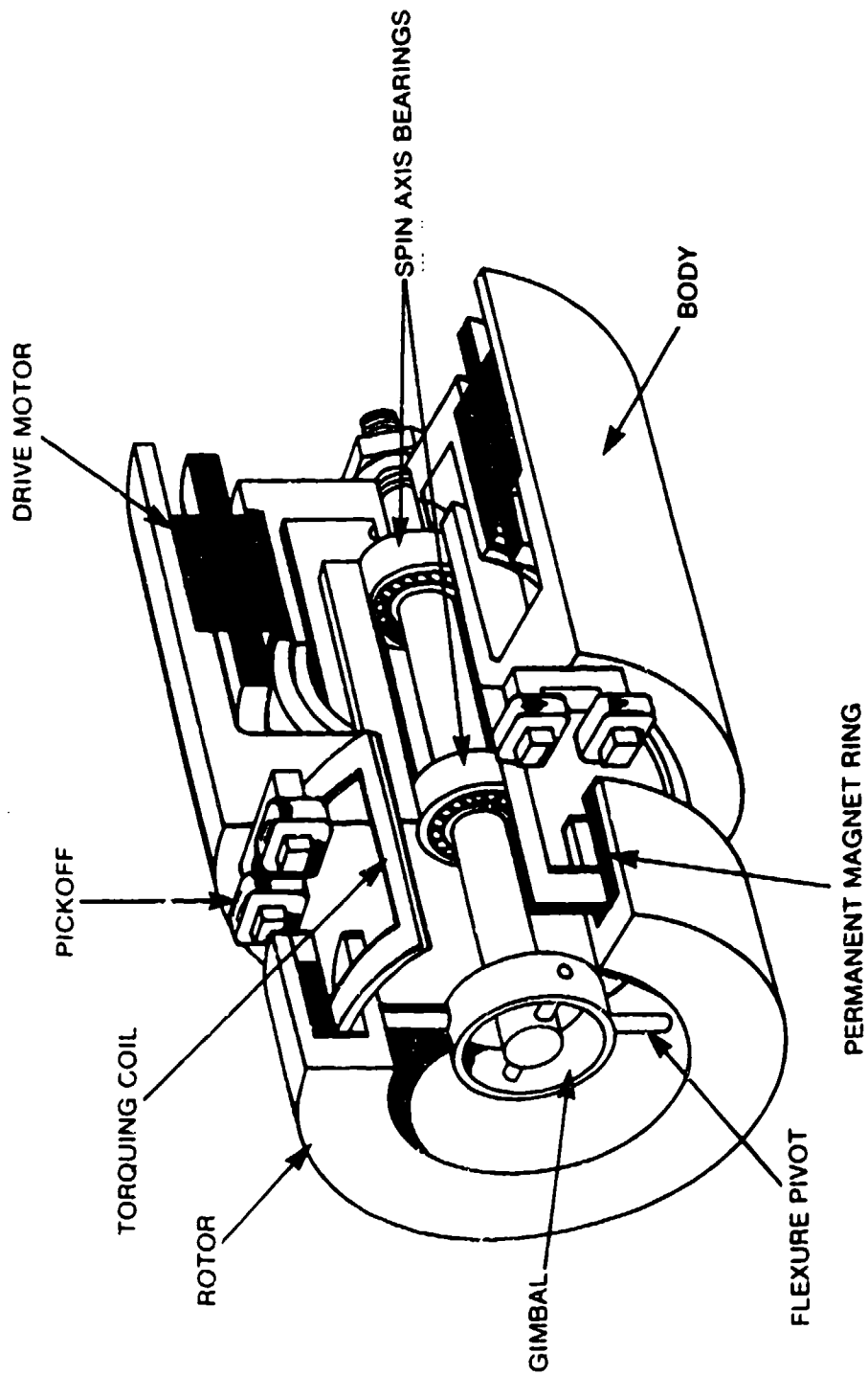


Figure 1. Typical Tuned Rotor Gyroscope Mechanization

2.1 Unique Aspects of the Design

As the intent was to utilize the thermal properties and resulting improved bearing life of hydrogen fill gas, the use of low cost Samarium Cobalt magnets was initially ruled out. This was due to the hydrogen absorption and embrittlement phenomenon. Platinum Cobalt magnets were used for their known long term stability. The development of processes to eliminate Samarium Cobalt embrittlement was initiated at the time of this decision and is ongoing. In fact, the most recent CSG-2's employ Samarium Cobalt magnets plated with nickel alloy.

2.2 Rotor Construction

For high mass stability and reduced thermal drifts it was decided that a close tolerance, all-welded construction should be the design aim. The design consisted of two suspension shaft rings welded together (single gimble), the suspension assembly welded onto the rotor, and magnets welded into the rotor. Laser welding was successfully developed for the whole rotor assembly.

Considerations had been applied in selection of materials for component to component weldability. While welding of Platinum Cobalt to the rotor material was found to be quite feasible, the reduction in field strength in the heat affected zone was seen to be undesirable. Spot welding reduced this affect, but did not offer sufficient joint strength, so a fine epoxy adhesive joint was used in the initial gyros. This problem has since been rectified through the design of a special fixture which permits uniform laser welding of the rotor.

2.3 Suspension Design

The design is based on "machine from solid" cantilevered flexures. It consists of double rings, inner and outer, which are initially aligned using precision slots machined into the base of the rings. The flexures are machined in line in each axis using Electro Discharge Machining (EDM). To produce an opposite angle double flexure in two positions in each axis, the rings are simply rotated thru 180°. They are keyed in position using the same precision slots to provide good coplanarity of both axes, then laser welded together. See figure 2.

At that stage there are already two semicircular slots machined in each ring by EDM which, after assembly of the suspension are joined by a "separation" EDM operation. This "frees up" the suspension into a hub, single gimbal, and an outer ring, which is now welded to the rotor. This technique yields a single gimbal suspension with "built in" flexures and welded construction without unstable epoxy adhesives.

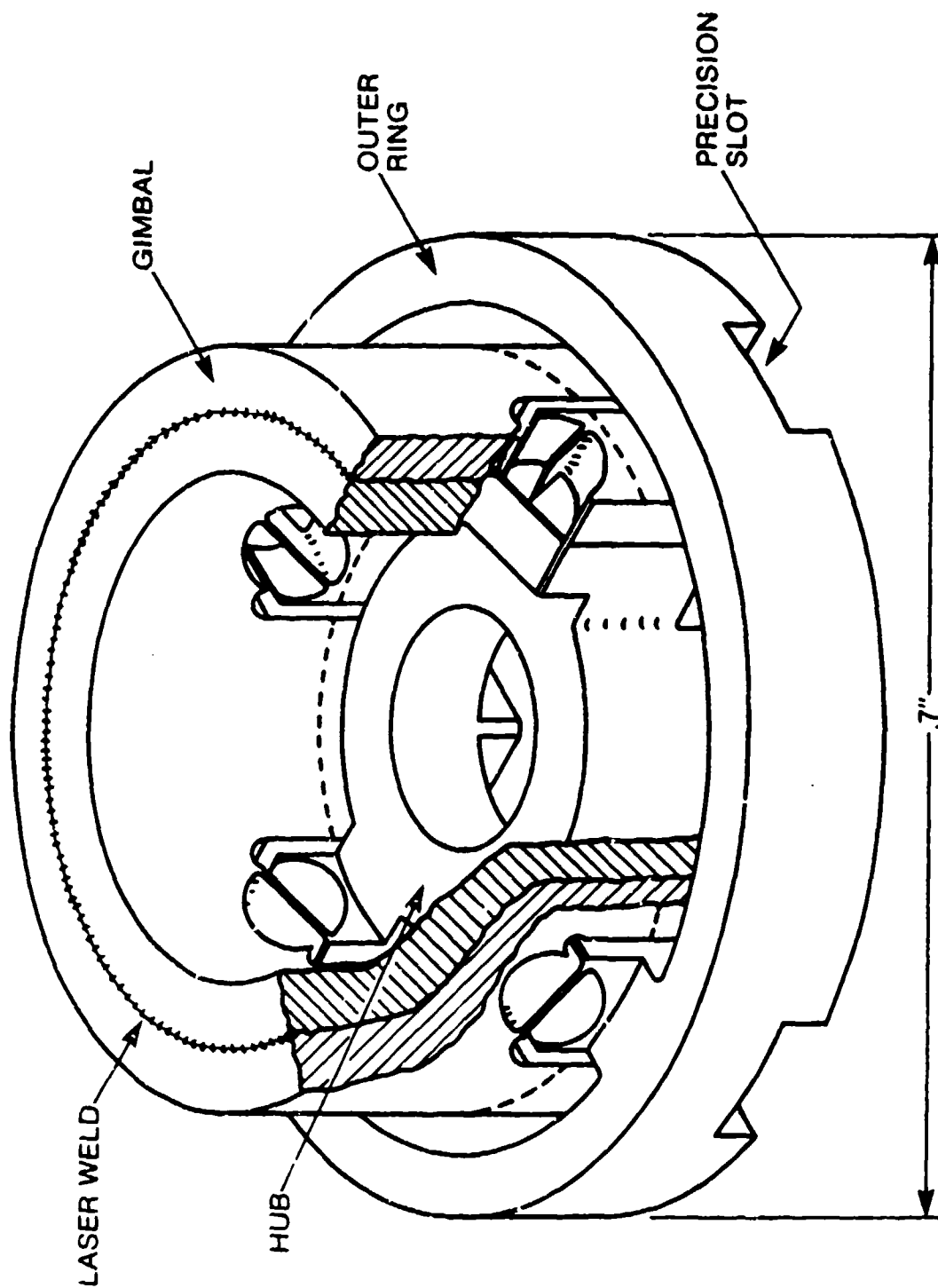


Figure 2. CSG-2 Flexure Mechanization

2.4 Low Cost Approach

The approach taken was to aim for low cost design where possible, with low cost redesign in mind for higher accuracy applications. The real cost saving achieved is in the assembly and balance of the CSG-2:

Assembly - The whole gyro assembly is broken down into sub-assemblies for ease and cost effectiveness of manufacture. Interchangeability for differing applications is thereby designed in.

Balance - The rotor and suspension have no adjustment screws for mass unbalance and pendulosity; another source of performance instability is thus eliminated. Balance is achieved by material removal. The long term intent is for volume production balance to be performed on an automatic laser machining station.

2.5 CSG-2 Design Goals

The initial specifications to which the CSG2 gyro was designed, in general, fall within the limits of a medium accuracy inertial grade instrument as shown in table 1. The initial design called for a large torquer scale factor to demonstrate the high rate performance capabilities of the instrument.

A gyroscope was delivered to the Defence Research Establishment Ottawa (DREO) in September 1983 for evaluation in the DREO Inertial Navigation Laboratory. A photograph of the CSG-2 gyro is shown in figure 3.

3.0 GYROSCOPE TESTING AND EVALUATION

3.1 DREO Inertial Navigation Laboratory

The DREO Inertial Navigation Laboratory was designed to be a highly versatile and flexible test facility for inertial components and systems. The core of the facility is a Contraves-Goerz 2-axis motion simulator (Model 57CD) capable of azimuth rates from 0- 1000 deg/sec. System support equipment includes variable frequency wheel and signal generator supplies controlled by a highly stable frequency source. Data acquisition is accomplished automatically through an LS-11 micro-processor connected to all test equipment by way of an IEEE-488 bus. Data reduction is performed on other site computers providing analysis and plotting capabilities. A photograph of the laboratory is shown in figure 4.

<u>PARAMETER</u>	<u>DESIGN GOAL</u>	<u>MEASURED VALUE</u>	<u>TYPICAL INERTIAL GRADE GYRO SPEC'NS</u>	<u>COMMENTS</u>
Random Drift (°/Hr)	<0.005	0.0025	<0.005	
Non-G Sensitive Drift (°/Hr)	<3.0	5.0 (3.0 possible)	<4.0	System com- pensated
Non-G Drift Repeatability (°/Hr)	<0.01	0.0065	<0.007	Turn on, to turn on
Non-G Drift Temp. Sensitivity (°/Hr/°F)	<0.01	0.005	<0.014	
G-Sensitive Drift (rss) (°/Hr/G)	<10.0	4.18	<0.5	System comp, with G-level information
G-Sensitive Drift Repeatability (°/Hr/G)	<0.02	0.0073	<0.02	Turn on, to turn on
G-Sensitive Drift Temp. Sensitivity (°/Hr/G/°F)	<0.05	0.019	<0.04	
Wheel Speed (Hz) (Resonant Freq.)	100 Hz \pm 5 Hz (4 pole motor driven by 400 Hz)	115 Hz (mean of 4 gyros)	--	
Torquer Scale	>1400	1504 (mean of 4 gyros)	--	
Factor (°/Hr/mA)		Predict 1730 at 100 Hz		
Torquer Resistance	<50 Ohms	56 Ohms	--	
Torquer Axis Alignments	<19.39 mrad	6.9 mrad Max.	--	
Motor Power, Start	<8 Watts	7.25 Watts	--	
Run	<3 Watts	1.56 Watts	--	
Wheel Run-Up Time	<30 sec.	8 sec.	--	
Operating Temp.	155°F	155°F	--	

Table 1 CSG-2 Design Specifications



Figure 3. The CSG-2 Gyroscope

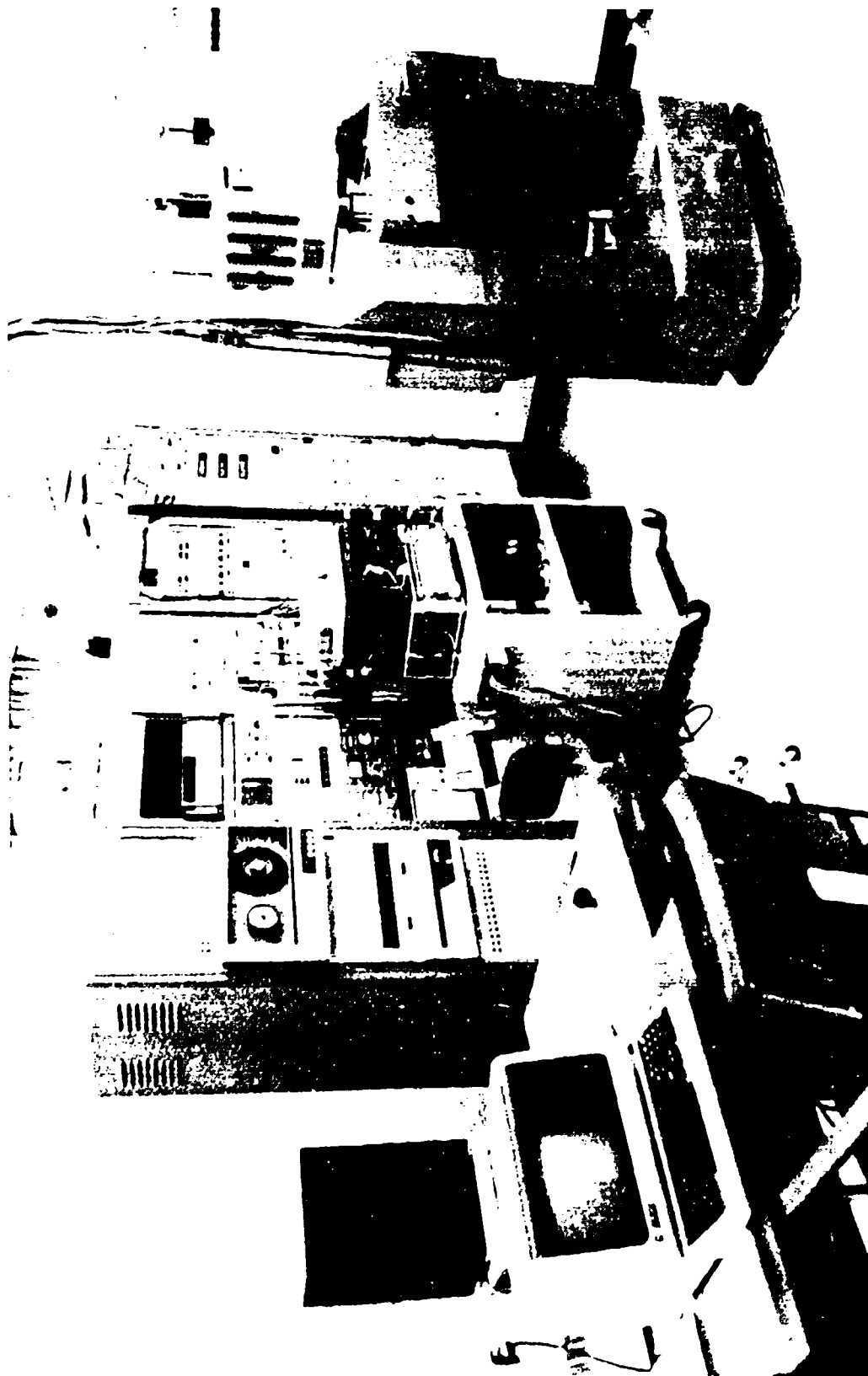


Figure 4. The DREO Inertial Navigation Laboratory

3.2 Test Fixturing for CSG2

In order to perform laboratory tests on the two-degree-of-freedom CGS-2 gyroscope, a fixture with very precise adjustment and alignment capabilities is required. In addition, temperature control, stability and uniform heat distribution are critical. A very precise three-element mechanical fixture was designed for this purpose.

The fixture consists of an aluminum temperature-controlled gyroscope fixture, a rotation element and a two-axis tip and tilt positioner. A photo of the figure is shown in fixture 5. The fixture provides positioning capability about each of 3 axes with an accuracy of 3 arc seconds. The fixture also provides very uniform temperature control since the entire gyroscope is enclosed, heaters and temperature sensors are uniformly distributed and the entire assembly is covered with 1/2 inch of polyethylene foam and isolated from its base by 1/4 inch quartz washers. Temperature tests have consistently shown a temperature gradient of no more than 0.6°C over the length of the fixture with temperature stability at the belly band of the instrument of $\pm 0.05^\circ\text{C}$.

Figure 6 shows the CSG-2 mounted in its alignment fixture on top of the motion table.

3.3 Preliminary Tests

Upon delivery of the CSG-2 gyroscope, instrument integrity tests were performed. These tests included gyro time constant, figure of merit, tuned speed, pickoff offset angles, motor start and run power and runup time.

These tests were followed by static tests for the determination of drift coefficients (bias drift, g-sensitive drift, g^2 -sensitive drift and cross axis coupling terms) as well as drift stability, torque generator sensitivity and temperature effects.

The results of these tests are shown in Table 2.

Of particular interest is the random drift or drift stability of the instrument. This type of performance is indicative of an inertial grade gyro useable in medium accuracy applications.

Figures 7 and 8 show plots of random drift for the x and y axes respectively over a 25 hour period. Both axes are horizontal with x north and y west.

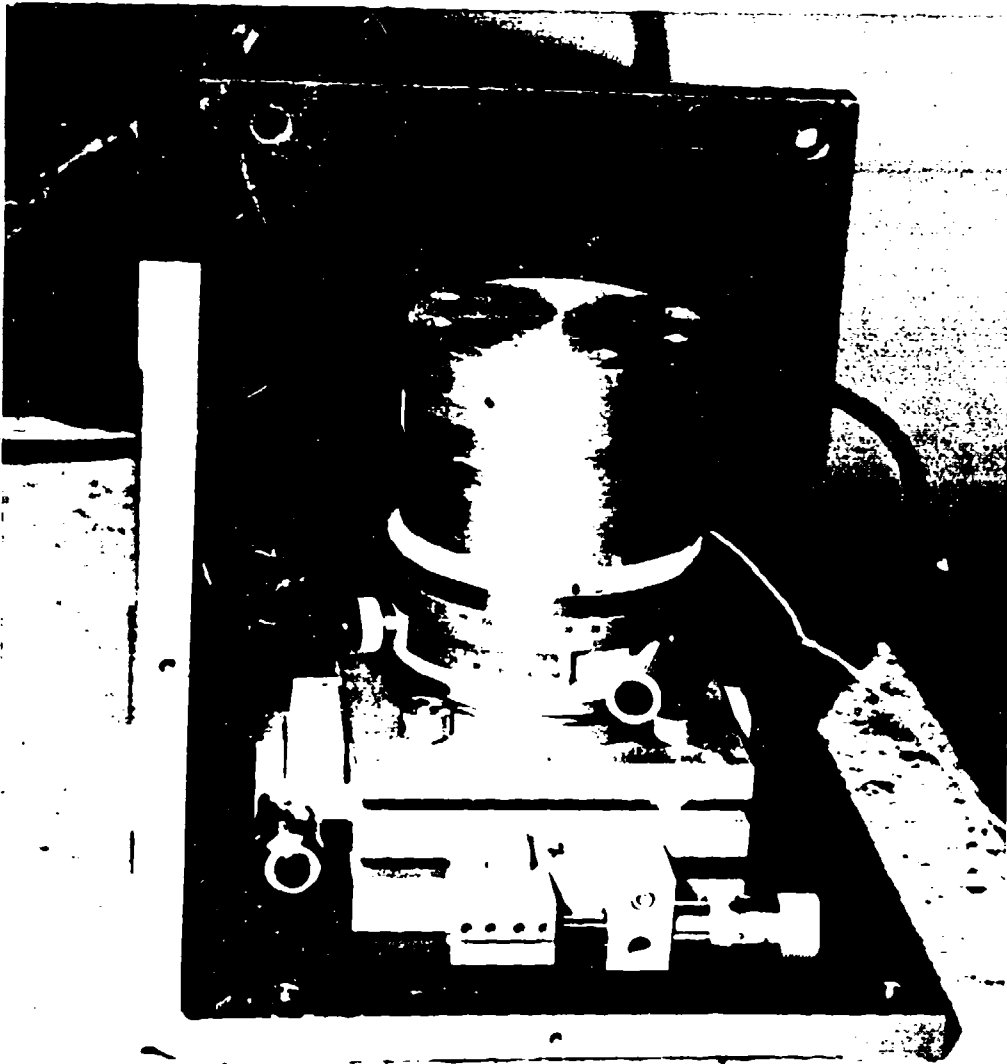


Figure 5. CSG-2 Alignment Fixture



Figure 6. The CSG-2 Mounted on the Motion Table

PARAMETER

Torquer scale factor K_x K_y	1642 Deg/Hr/Ma 1671 Deg/Hr/Ma
Torquer axis misalignment	-850 Arc sec. -1373 Arc Sec.
Motor start power at 12 VRMS	8.0 Watts
Motor run power at 7.5 VRMS	2.0 Watts
Run-up Time RUT	8.2 Sec
Pickoff scale factor K_{POX} K_{POY}	0.716 VRMS/Mrad 0.720 VRMS/Mrad
Pickoff Offset $X_{OX}(x)$ $X_{OX}(y)$	-3.2 Arc Sec. -4.7 Arc Sec.
Figure of Merit F_m	240
Tuned Frequency F_r Mechanical	105.5 Hz
Electrical	422
Time Constant	108 Sec.
Random Drift SRA Vertical	0.0057°/Hr (1) 0.0041°/Hr ()
Non g-sens drift BD_x (bias) BD_y	-1.429 Deg/Hr +5.136 Deg/Hr
g-sens drift MU_x MU_y Q_x Q_y	+3.351 Deg/Hr/g +3.357 Deg/Hr/g -1.635 Deg/Hr/g +1.551 Deg/Hr/g
g ² -sens drift $D(x)_{xx}$ $D(y)_{yy}$	+0.016 Deg/Hr/g ² +0.022 Deg/Hr/g ²
TEMPERATURE	69°C . }

Table 2 CSG-2 (S/N 003) Test Results Feb 87

Using DREO RL-2 Loop

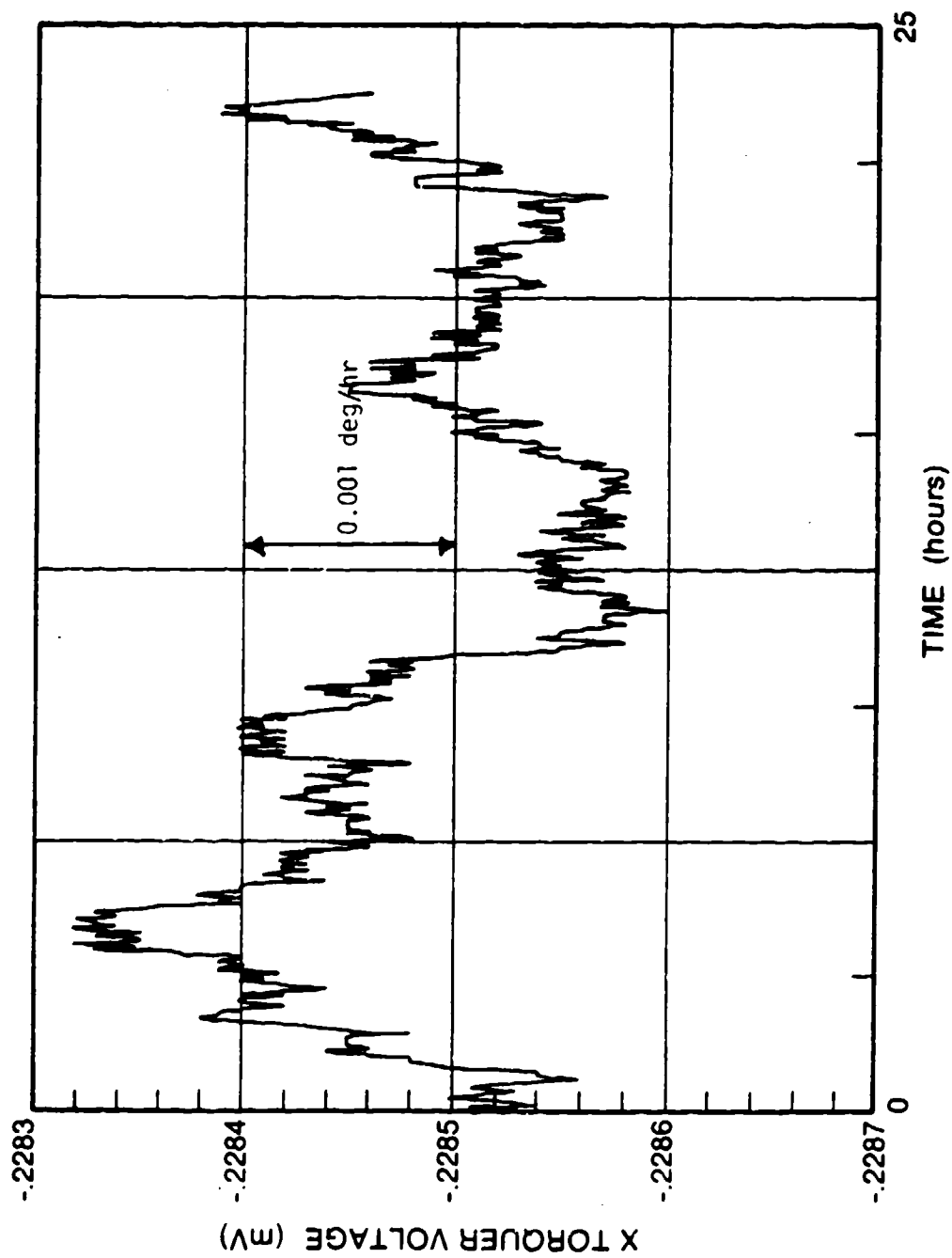


Figure 7. Random Drift, X axis

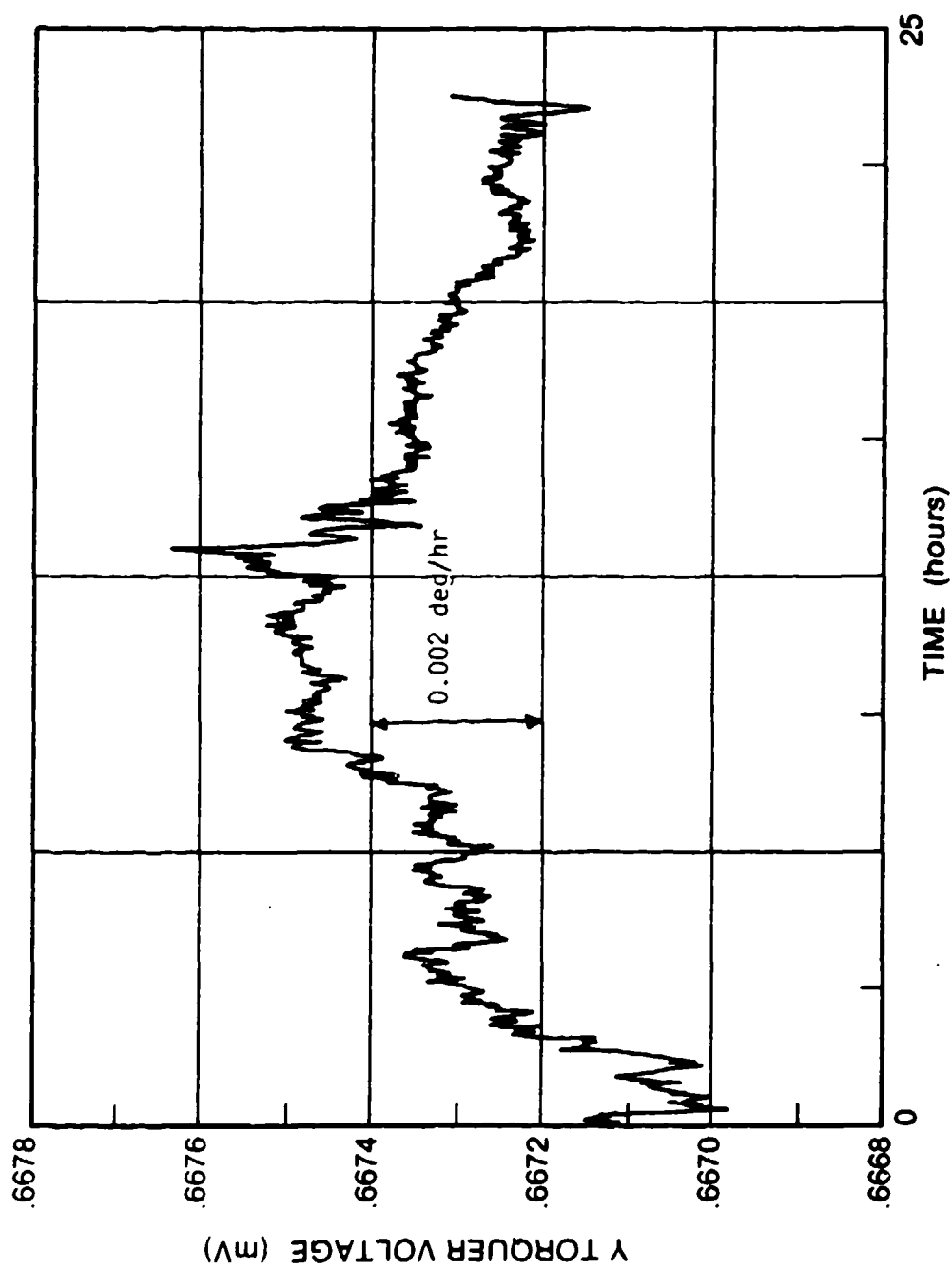


Figure 8. Random Drift Y-axis

Temperature sensitivity of the gyro is less than 0.02 deg/hr/°C in both non-sensitive and g-sensitive drift components.

Drift repeatability for both non-g and g-sensitive drifts was less than 0.01 (deg/hr/g).

The effect of temperature on the drift coefficients of the instrument was determined from multi-position tests performed at various gyroscope temperatures; 50°C, 69°C (normal operating temperature) and 80°C. Some results are shown in Table 3.

The effect of limited temperature changes on the drift coefficients of the gyro seems to be very small and is within the measurement error of the test system.

	50°C	69°C	80°C
$BD_x(\text{deg/hr})$	-1.446	-1.429	-1.539
$BD_y(\text{deg/hr})$	5.335	5.136	4.983
$D(X)_x(\text{deg/hr/g})$	2.863	3.351	3.704
$D(X)_y(\text{deg/hr/g})$	-1.623	-1.635	-1.650
$D(Y)_y(\text{deg/hr/g})$	2.861	3.357	3.689
$D(Y)_x(\text{deg/hr/g})$	1.528	1.551	1.546
$D(X)_{xx}(\text{deg/hr/g}^2)$	0.008	0.016	0.011
$D(Y)_{yy}(\text{deg/hr/g}^2)$	0.002	.0022	-0.028

TABLE 3

TEMPERATURE SENSITIVITY OF DRIFT COEFFICIENTS

4.0 STRAPDOWN RATE TESTS

At this point we have shown that, indeed, we have a gyroscope. But if it is to be usable in strapdown applications, one has to characterize instrument performance under rates and dynamic conditions.

As a first step, let's look at typical performance requirements for a S/D gyro in medium accuracy applications, shown in Table 1.

4.1 ANALOG REBALANCE LOOP SPECIFICATIONS

The static tests described above were performed using a very low-current analog rebalance loop obtained from Litton. Litton Canada does not perform any rate tests on their production gyroscopes and, as a result, have never had a need for a rebalance loop supplying more than a few millamperes of torquer current.

Rate testing of a strapdown gyroscope requires a rebalance loop capable of supplying a wide current range. In the case of the CSG-2, it was decided that a rate range of ± 1.0 rad/sec was desirable and that the rebalance loop must also be capable of sensing and controlling the random drift of the instrument (0.01 deg/hr).

An analog rebalance loop was designed at DREO to the specifications shown in Table 4.

A detailed description of the loop can be found in DREO Tech Note TN 86-10. The design is registered as a DND invention under file number 1416-86-001 (D Pat A), dated 17 January 1986.

4.2 Loop Design

The DREO rebalance loop, designated RL-2, consists of two direct-axis, analog torque-to-balance (ATBL) loops. For constant rate tests, no cross-axis loops (to compensate for acceleration) are necessary.

The direct-axis loops compensate for constant angular input rates. When an input rate is applied to the case of the gyroscope, the pickoffs sense the resulting change in attitude between the case axis and the rotor axis. The pickoff output signals are fed to the analog rebalance loop which then generates a precision current which is fed to the case-fixed torquer coil of the gyroscope as a direct rebalance current.

CONDITIONS: RL-2 SCALING RESISTOR = 50
GAIN = 16 ma/V RMS

RATE RANGE:	± 1 rad/sec
LINEARITY:	BETTER THAN ± 3 PPM
STABILITY:	$\pm .0002$ m rad in 60 MIN (less after warm-up) (± 0.00001 deg/hr)
RANDOM NOISE:	.00005 mrad RMS
P.O. OFFSET ADJUSTMENT:	± 48 ARC SEC
GAIN ADJUST:	0 to 300%
INTEGRATOR CUT-OFF:	3.3 Hz
MUTATION FILTER CUT-OFF:	170 Hz
MUTATION FILTER PHASE DELAY:	-54° at 60 Hz, -88° at 90 Hz -180° 178 Hz

Table 4 DREO RL-2 Specifications

This provides the restoring torque to maintain the gyro at it's null position. The rebalance currents to the torquers are also sampled as a measure of input rate and this provides the readout mechanization. The sampling instruments in the DREO laboratory are high-precision digital voltmeters which sample the voltage across an oil-filled precision sampling resistor in each arm of the rebalance loop. These meters are tied directly into a computer-controlled data collection system.

4.3 Rate Test Procedures

The data of most significance to us is the stability and linearity of the gyro scale factor. In addition, we would like to examine the effects of torquer current (i.e. rate) changes on the scale factor including transients and temperature effects.

4.4 Scale Factor Stability

The stability of the torquer scale factor is determined through rotating the gyro about each of its input axes, in turn, at a constant rate for several hours while measuring the torquer current. The peak to peak variation in the current determines the scale factor stability. Figure 9 shows scale factor deviation for the y-axis at a rate of 20 deg/sec over a period of approximately 12 hours. The scale factor stability is better than 60 ppm.

4.5 Scale Factor Linearity

Linearity of the scale factor over the entire rate range of the gyroscope is very important, particularly in higher grade inertial applications. Due to the nature of a strapdown gyroscope, the instrument is forced to undergo large current changes in the torquer coils due to changes in input rates about each axis. The effects of torquer heating due to current changes can be significant resulting in changes in torquer scale factor and, thus, scale factor linearity over the dynamic range of the gyroscope. Scale factor linearity is determined by rotating the instrument at successive constant rates over the entire dynamic operating range of the gyroscope. In the case of the CSG-2, this is ± 1 rad/sec. The scale factor at each rate is determined and deviation from nominal (static) scale factor is plotted. Figure 10 is a plot of scale factor deviation from linearity for the y-axis. Scale factor deviation is approximately 1800 ppm over the rate range of the instrument. This deviation is due almost exclusively to torquer heating effects. This can be shown through scale factor deviation tests performed at various controlled gyro temperatures. As can be seen in Figure 11, scale factor varies by 500 ppm/ $^{\circ}\text{C}$ change in torquer temperature. This agrees with calculations done on the platinum cobalt magnet material and the changes in magnetic field strength due to temperature. Figure 12 shows that although scale factor linearity is affected by temperature, scale factor stability is not. Scale factor stability at 50, 69 and 80°C is plotted.

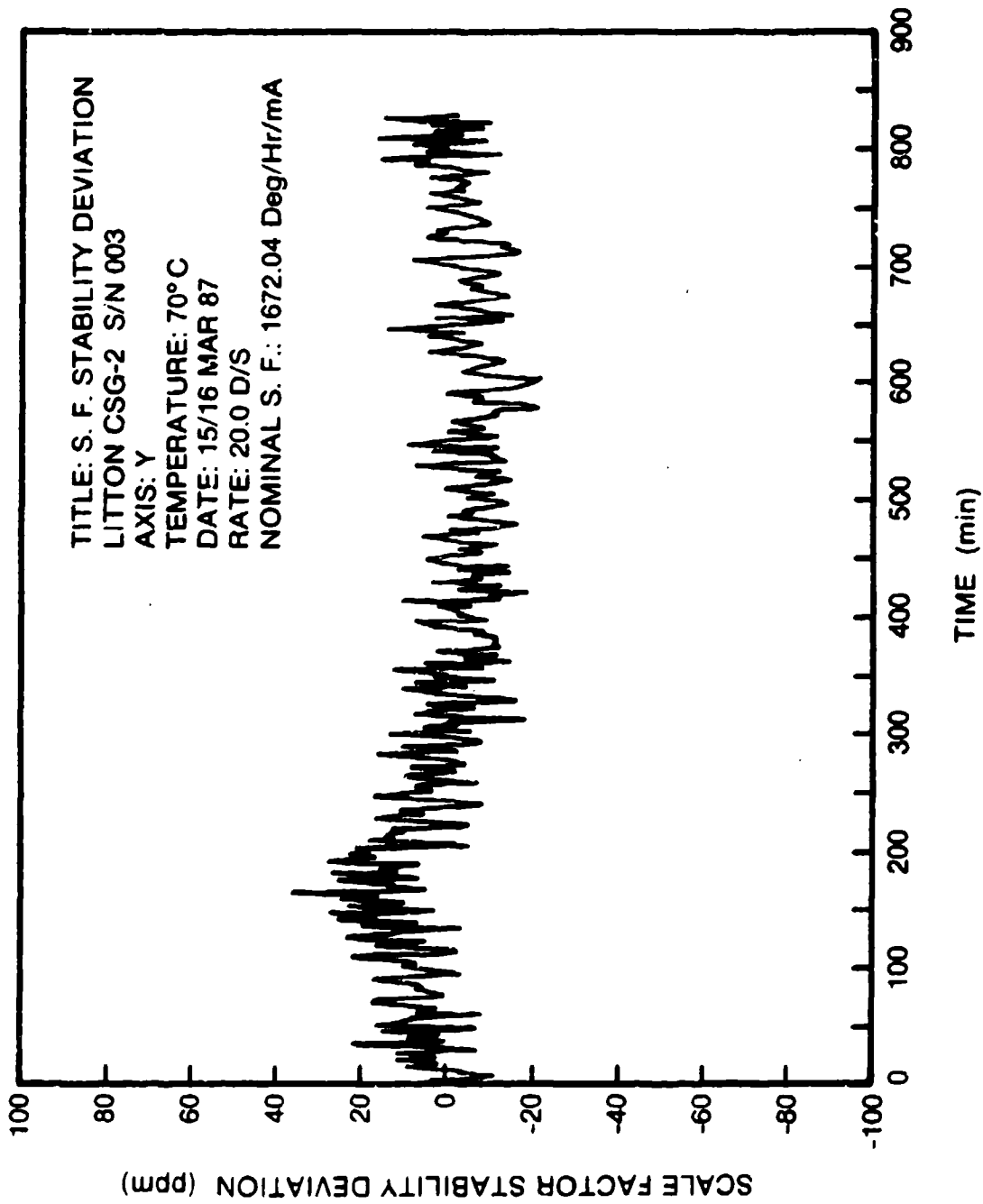


Figure 9. Scale Factor Stability Deviation

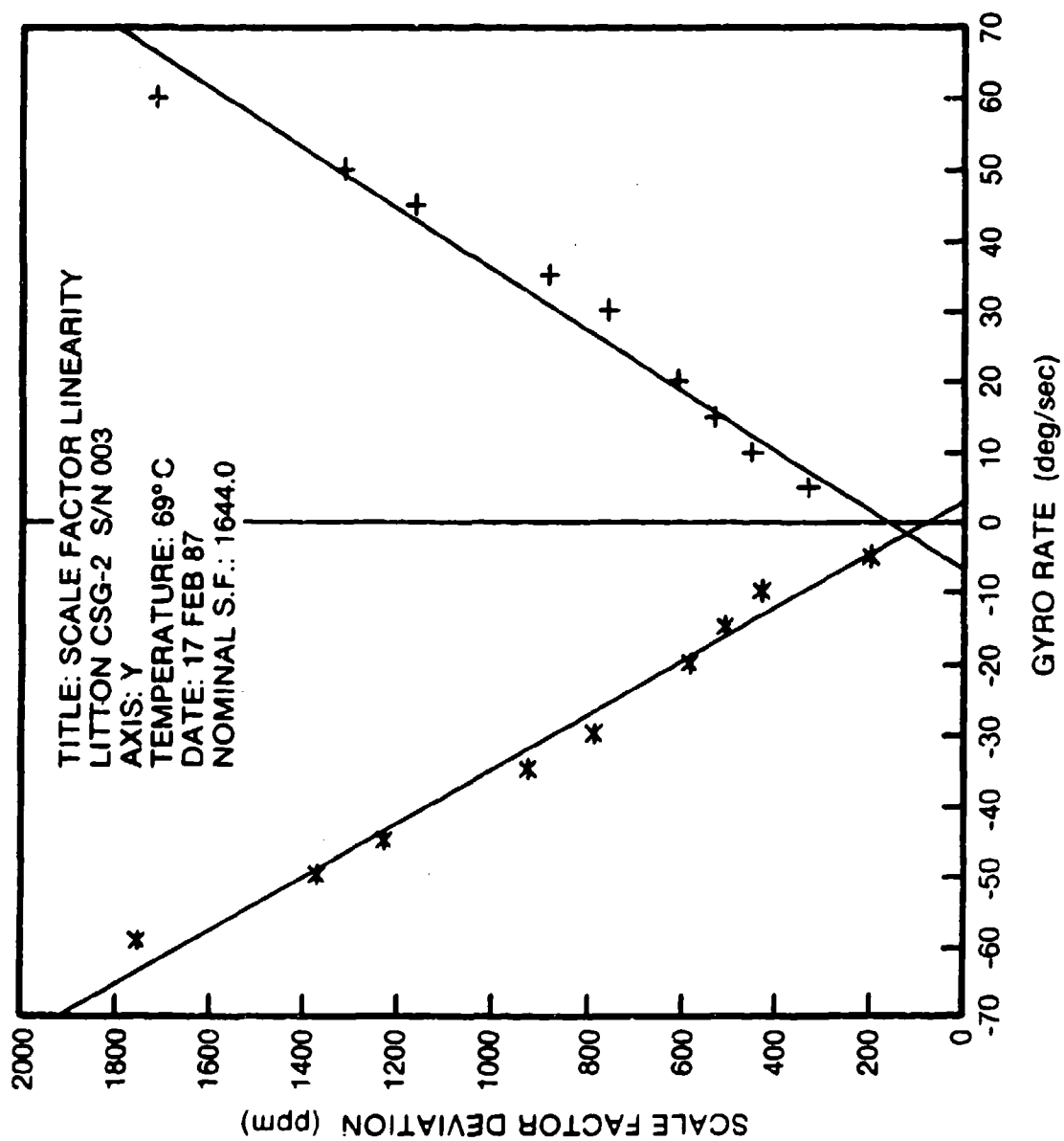


Figure 10 Scale Factor Deviation

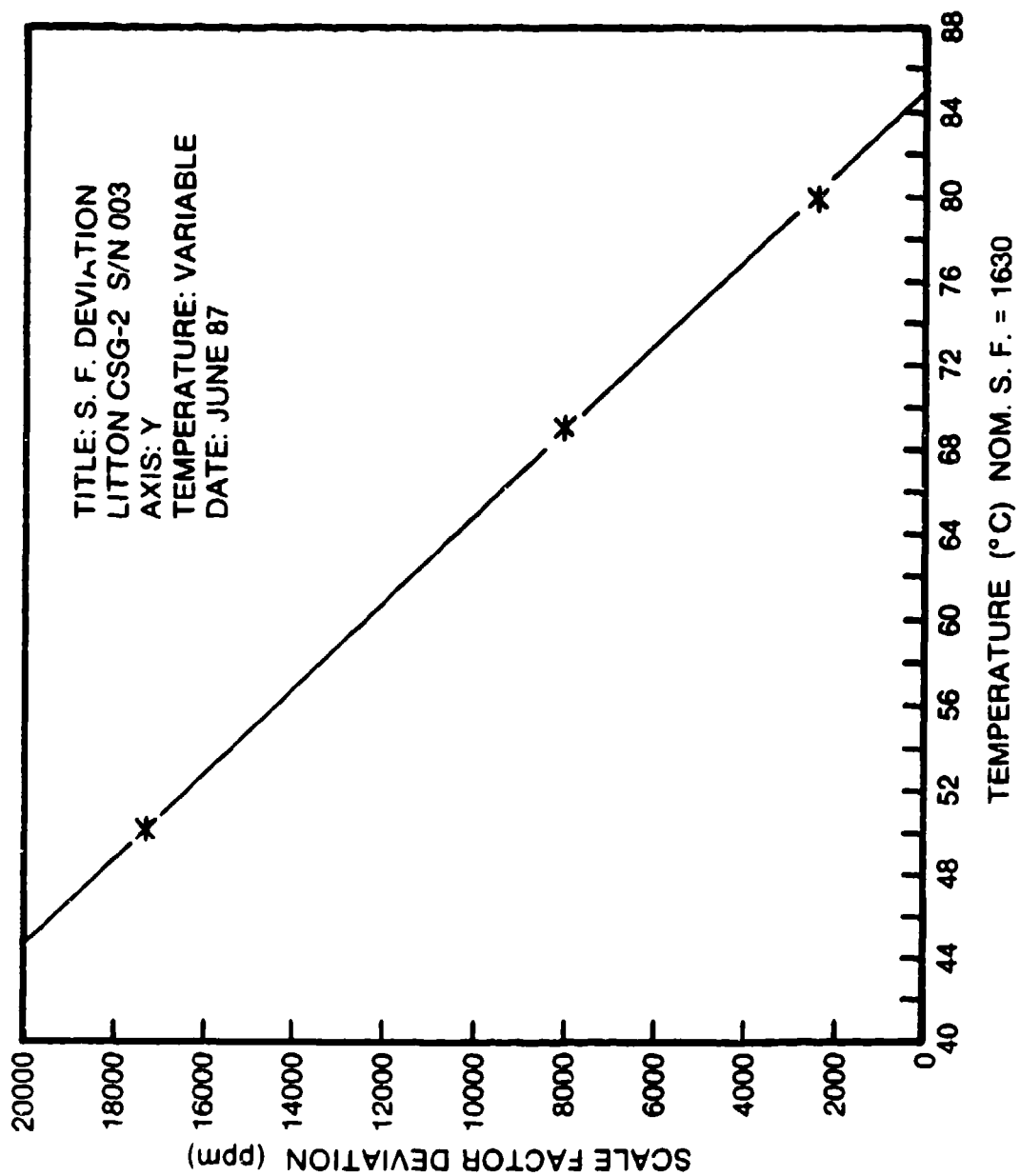


Figure 11. Scale Factor Deviation Versus Temperature

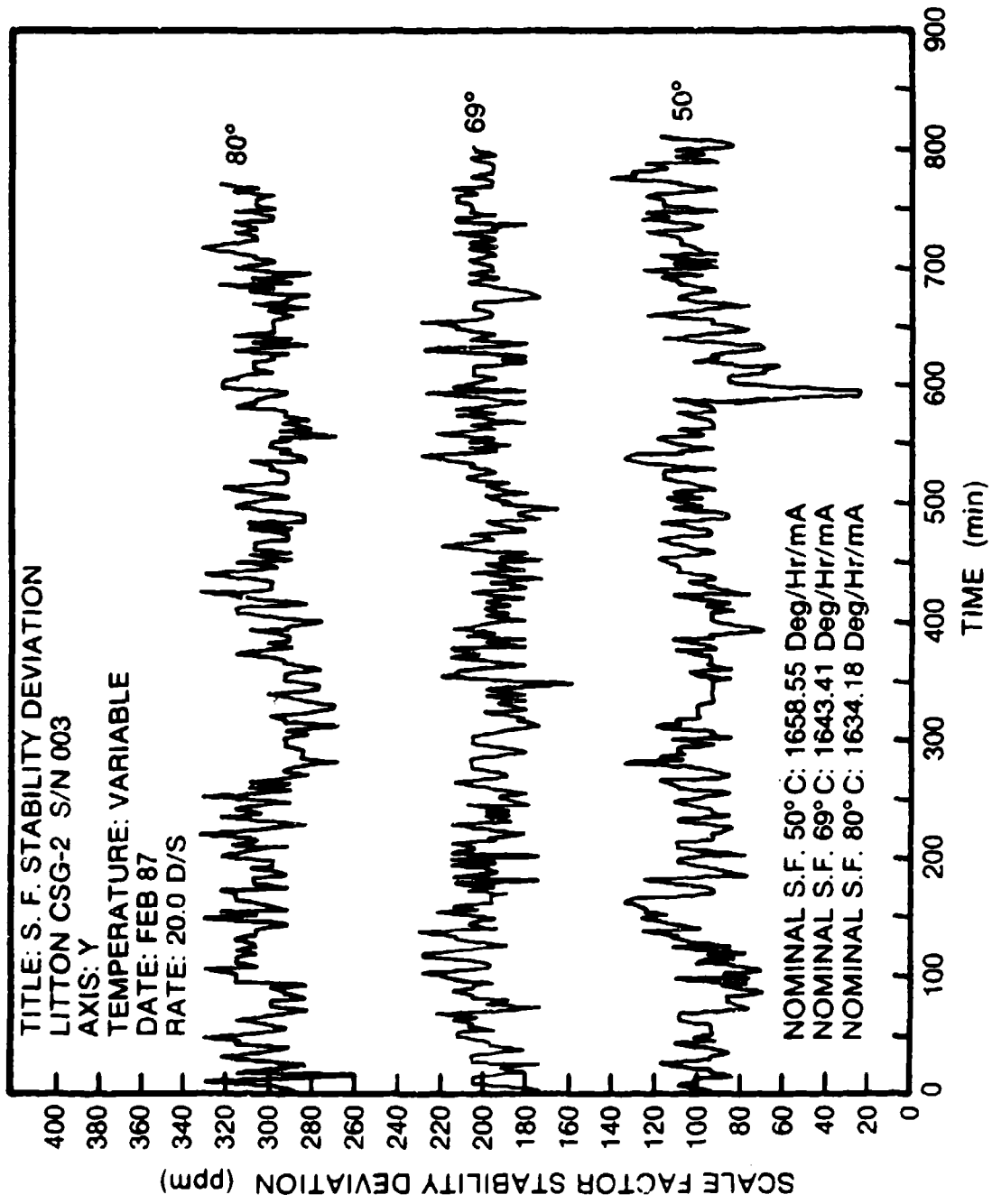


Figure 12. Scale Factor Stability Versus Temperature

Scale factor linearity at low rates is also significant. Figure 13 shows scale factor deviation from 0 to 5 deg/sec. Note the large deviation ('+' symbols) due to earth rate and drift errors. The '*' plot is a 'corrected' scale factor deviation wherein the gyro drift terms have been removed to improve linearity. The correction is a simple one and would ordinarily be performed in compensation software in an operational system.

4.6 Rate Changes

The effect of changes in input rate has already been shown to produce changes in torquer scale factor of a predictable and repeatable nature. Another important area is the transient analysis of these changes.

In order to characterize the effects, the gyro was 'stepped' from one rate to another and back again at regular intervals. The effects on scale factor and transients were studied.

Figure 14 shows successive steps between 25 deg/sec and 45 deg/sec. Note the transient in the scale factor of approximately 100 ppm over an interval of several minutes, settling to a stability of 60 ppm. An expanded view of a single step is shown in Figure 15. Note, also, the absolute change in scale factor between the two rates which is in agreement with Figure 11. Further analysis of dynamic effects are underway including transient effects and angular oscillatory tests.

5.0 POTENTIAL SYSTEM APPLICATIONS

After assessing the existing and future commercial and military market places for inertial technology, significant opportunities for a Canadian system based on the CSG-2 have been identified in the following areas:

- AHRS Attitude and Heading Reference System
- MINS Marine Integrated Navigation System
- HINS Helicopter Integrated Navigation System
- Land Vehicles
- Satellites
- Drones and RPV's
- Synthetic Aperture Radar (SAR)

5.1 Attitude and Heading Reference System (AHRS)

LSL Canada is presently under the sponsorship and direction of Defence Research Establishment Ottawa (DREO) to incorporate CSG-2 gyroscopes into a strapdown AHRS system. The system being used for this demonstration contract is the LTN73, a development system.

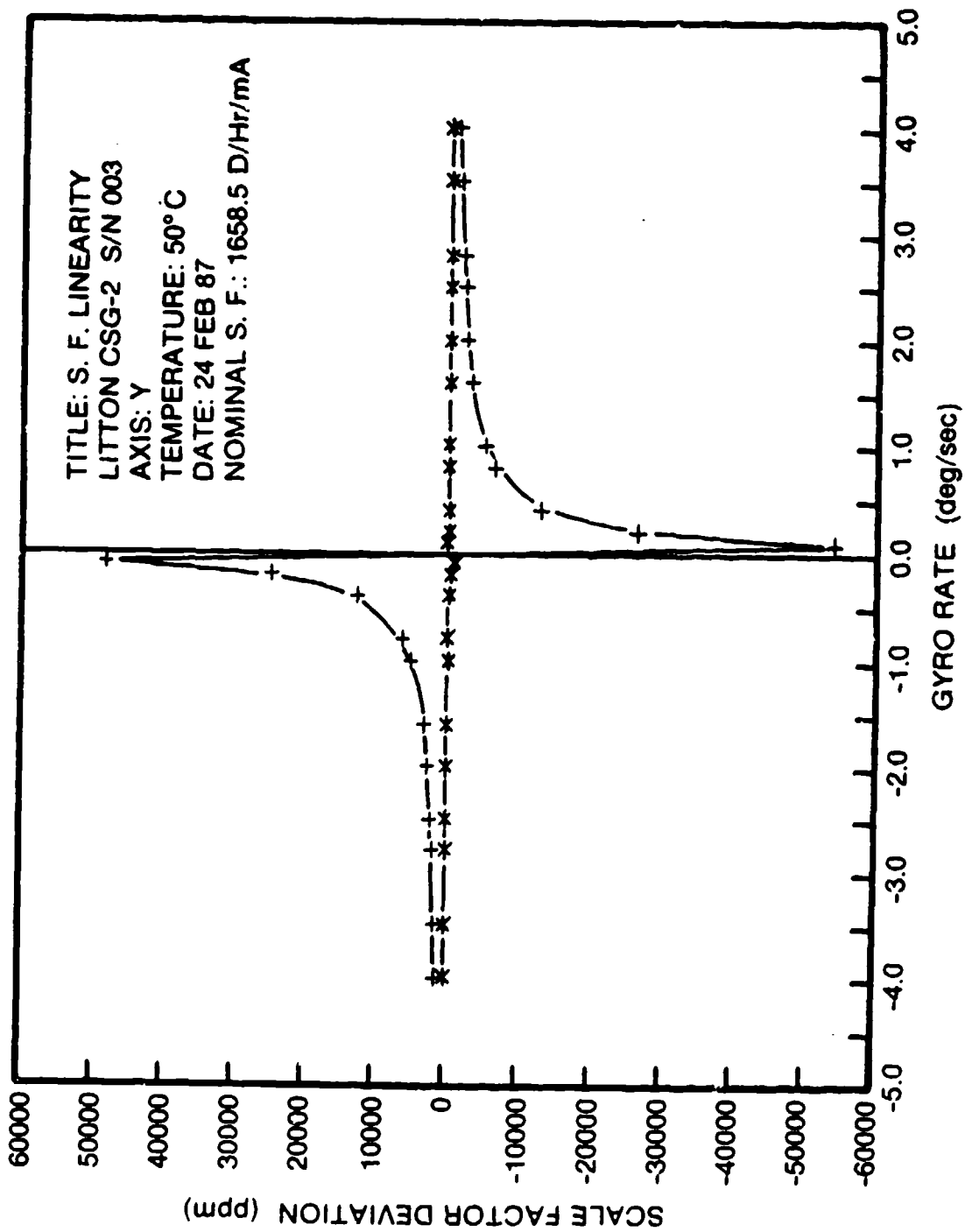


Figure 13. Scale Factor Linearity at Low Rates

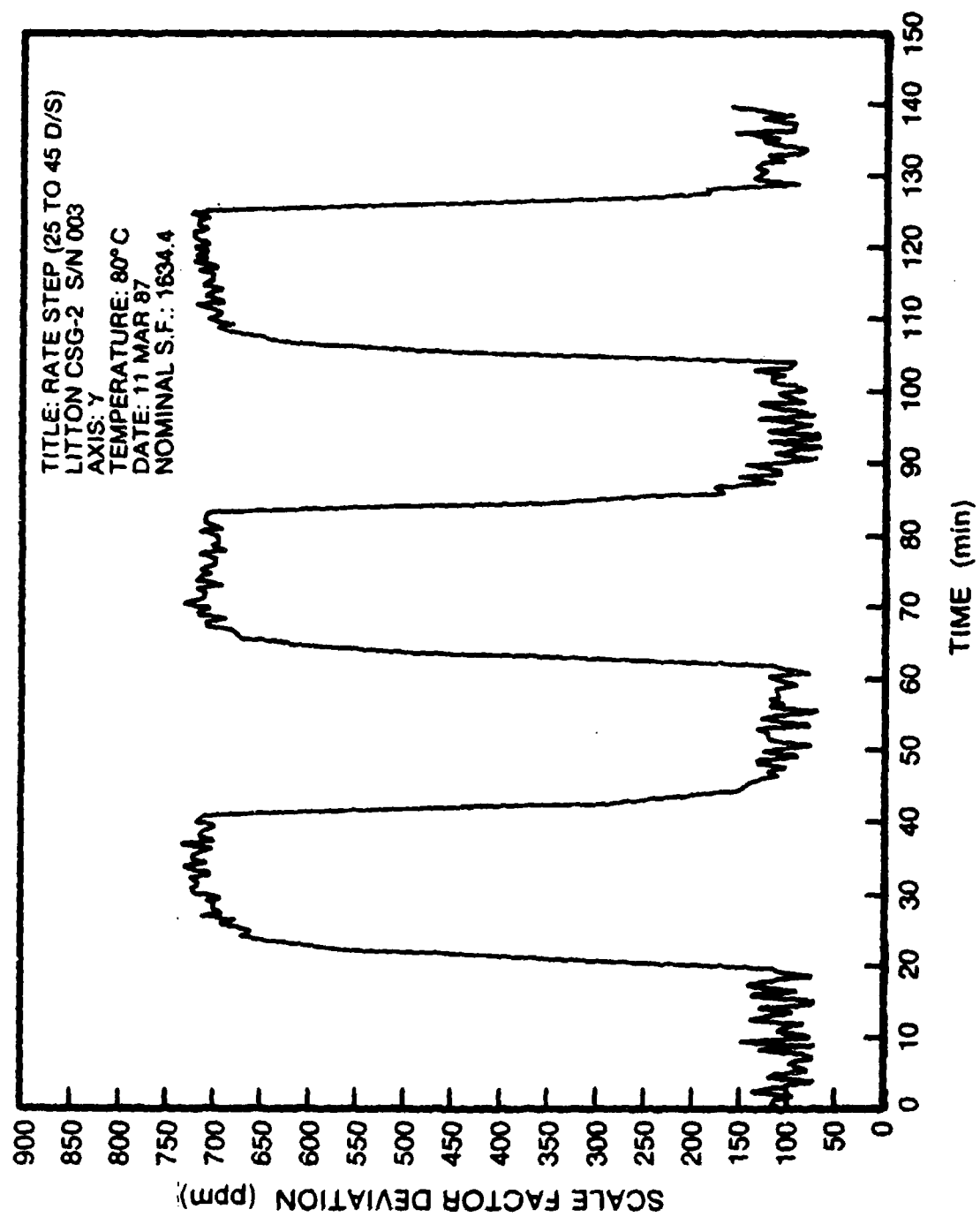


Figure 14 Rate Changes, 25-45 deg/sec

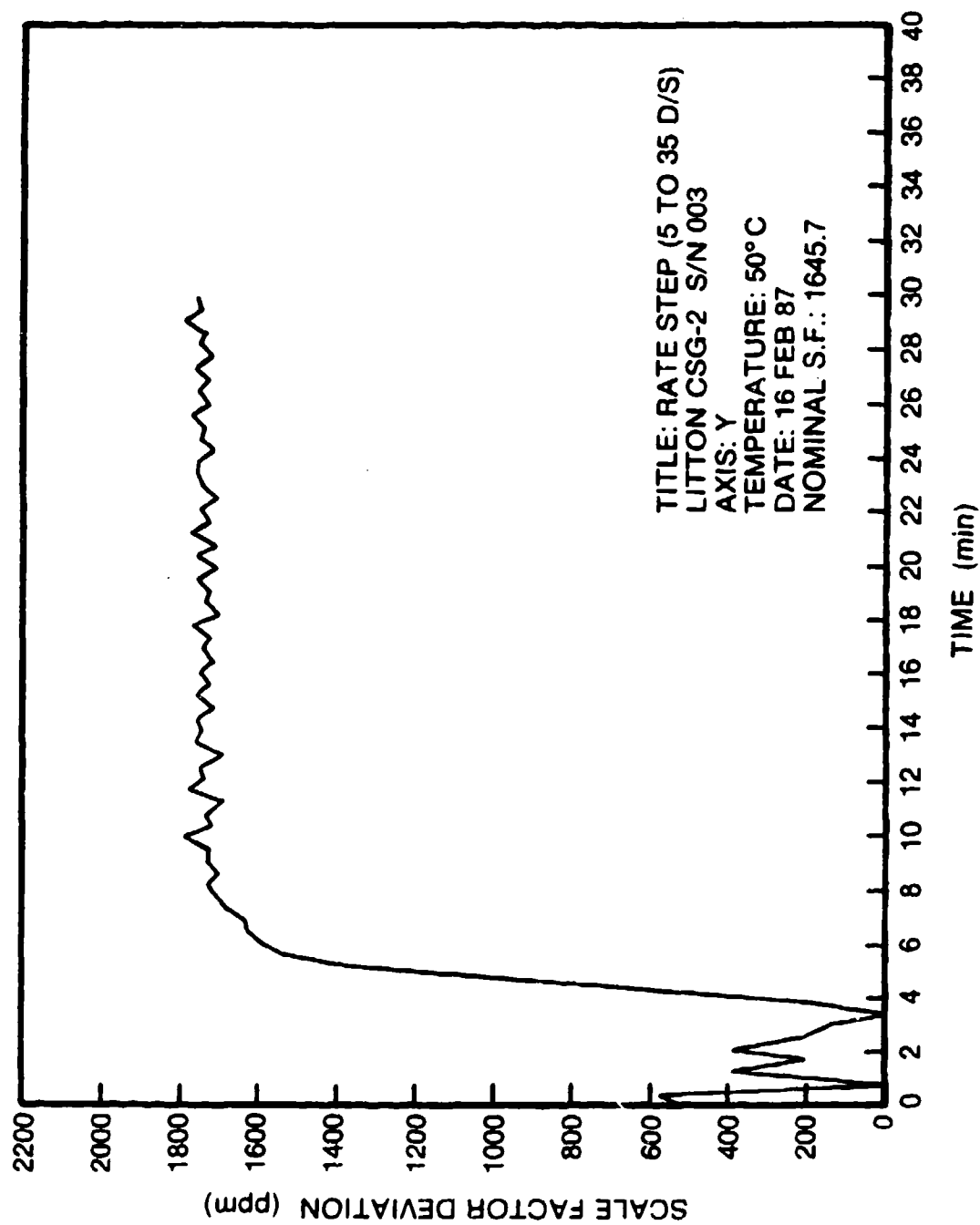


Figure 15 Single rate Step, 5-35 deg/sec

5.2 Marine Integrated Navigation System (MINS)

In a Marine application, the performance and reliability of a CSG-2 system could be exploited in conjunction with Kalman filtering techniques to establish an accurate position fix for vessels of varying sizes. In addition, the navigation and attitude information would facilitate the system's integration with a fire control system. A system of this nature could be retrofitted to existing ships, or submarines or incorporated into new vessels.

5.3 Helicopter Integrated Navigation System (HINS)

Within the world marketplace, Canada operates in excess of 2,000 helicopters, the second largest fleet in the world. Of the Canadian total, the department of National Defence (DND) operates just under 200 vehicles, about 10%. The military role, coupled with the continued advances in technology and the general degradation of logistics support as equipment and components grow older, demand that the Canadian Forces initiate midlife or system update projects. Consequently, a very large market avails itself to the manufacturer for a lightweight, cost effective HINS. It is believed that a system based upon the CSG-2 could address both the commercial and military markets.

5.4 Land Navigation

A land navigation system acts as a self-contained gyrocompass performing initial alignment to determine inertially derived vehicle attitude and heading and, when coupled with vehicle velocity information, carries out the navigational computations.

Many existing land navigation systems are bulky, expensive and imprecise. With the potential advantages of a system based upon the CSG-2, it is believed that a compact, inexpensive system, with operating features superior to those currently available can be developed.

5.5 Satellites

The Canadian Government is presently interested in the Canadian Attitude Sensing System (CASS) developed by Spar with a highly accurate attitude fix, enabling the determination of the attitude of a spacecraft and the position of its associated sensors. A CSG-2 based system could be employed to process the data from the sensor and, in future applications, as an attitude control system responsible for the attitude of the spacecraft.

5.6 Remotely Piloted Vehicles (RPV) and Drone Programs

The marketplace for Drones and RPVs has opened tremendously over the past several years offering application to both the civil and military marketplace. Potential civil applications include border patrol, coastal traffic detection, disaster control, surveying, realtime

meteorological data, fire fighting, riot control, damage assessment, corporate security and various emergency contingencies. A variety of military applications also exist such as surveillance and reconnaissance, target acquisition and laser designation. At present Defence Research Establishment Valcartier (UREV) is interested in the development of this area using the CSG-2 gyroscope.

6.0 CONCLUSIONS

The CSG-2 gyroscope is a unique, Canadian-developed strapdown inertial instrument which shows potential for use in a wide variety of applications at a low predicted cost. Instrument performance is highly repeatable and reduction of thermal effects can be achieved either through changes in the torquer coil magnet material or through software compensation in system applications. Random drift and scale factor stability are very good and show promise for long term, stable instrument performance.

REFERENCES

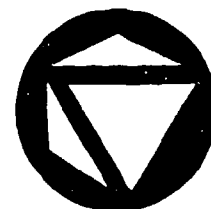
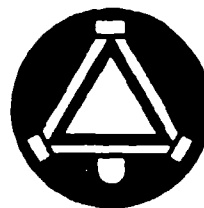
'Test Evaluation of the Litton (Canada) Canadian Strapdown Gyroscope (CSG-2", M. Vinnins, L.D. Gallop, F. Paquet; DREO Report #914, Sept. 1986

'The DREO Inertial Navigation Laboratory: Development and Test Capabilities'; M. Vinnins, DREO Report #895, June 1984

'The Canadian Strapdown Gyroscope (CSG-2); a Low Cost, Inertial Grade Tuned Rotor Gyro"; M. Vinnins, B. Pearson, J. Sinkiewicz; Proceedings Symposium Gyro Technology 1985, Stuttgart; Sept. 1985

Honeywell

SONDERTECHNIK



THE GERMAN HONEYWELL RING LASER GYRO

(Status Report on Development and Test Results)

Dr. B. Bolzmann

Honeywell Regelsysteme GmbH
Unternehmensbereich Sondertechnik
Honeywellstr.

D-6457 Maintal 1

October 1987

Rev.

S04D

In 1980 the German Government, realizing that RLG technology was very important for future inertial guidance and control applications decided to establish an RLG technology base in Germany. The German Ministry of Defence (MOD) then issued a request for proposal to German industry for an RLG development program.

Against strong competition Honeywell Germany won the development program and was awarded the contract in March 1981 (see Fig. 1). The customer was the BWB, the Federal Office for Military Technology and Procurement of the MOD. The contract asked for the development of four modular built RLGs.

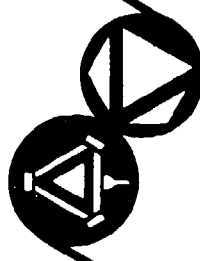
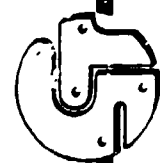
A modular RLG consists of two separate modules, a resonator block module and a laser gain tube module. Each module can be independently pretested and after that mounted together in a rigid structure to form an RLG. The advantage of such a design is the increase of manufacturing yield which at the time of the contract award would have reduced the manufacturing cost considerably.

Since the major goal of the contract was the development of the RLG technology the specification data were fairly marginal (see Fig. 2) and had only to be proven at room temperature. The delivery date which was called out was May 1984, three years and 3 months after receipt of order.

Honeywell Germany was able to get Carl Zeiss in Oberkochen (West-Germany) as a subcontractor for all the RLG glass parts including mirrors. Zeiss is a well known optical company that has been in the optical business for over 100 years. In fact it was Zeiss that in 1935 invented the dielectric coating technology which today is used for the manufacturing of all RLG mirrors. It was also Zeiss that supplied the lens for the camera with which Mr. Armstrong took the first pictures on the surface of the moon during the famous Apollo 11 mission.

Honeywell

GERMANY



GERMAN RLG DEVELOPMENT CONTRACT

CONTRACT AWARD : 3/18/81

CUSTOMER : BWB (Federal Office for Military Technology and Procurement)

TARGET :
- Development of basic RLG technology
- Delivery of four modular RLG engineering models
of low accuracy ($1^{\circ}/h$)

DELIVERY DATE : First RLG: May 1984

SUBCONTRACTOR : CARL ZEISS SPECIAL OPTICS (Oberkochen)

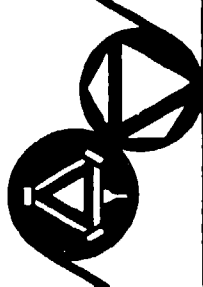
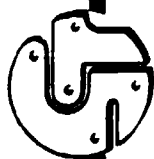
SUPPORT :
-- DFVLR (Deutsche Forschungs- und Versuchsanstalt
für Luft- und Raumfahrt)

-- HONEYWELL INC. (Minneapolis) under coverage
of a TAA of the U.S. Department of State

Fig. 1

Honeywell

GERMANY



SPECIFICATION FOR A MODULAR RIG

DRIFF (DAY-TO-DAY)	:	$< 1^{\circ}/h$
RANDOM WALK	:	$< 0.05^{\circ}/\sqrt{h}$
LOCK-IN-THRESHOLD	:	$< 1^{\circ}/s$
RANGE	:	$\pm / \dots 350^{\circ}/s$
SCALE FACTOR	:	$< 3,5 \text{ sec/Pulse}$
ENVIRONMENTAL	:	Room Temperature

We received support from the DFVLR (Deutsche Forschungs- und Versuchsanstalt für Luft- und Raumfahrt) (German Aerospace Research and Test Establishment) which is known because of its engagement in the Space Lab missions. The DFVLR did some earlier research on modular RLGs, to establish the specification for the development contract. During the course of that research they also developed measuring equipment for mirror reflectivity and scattering which was significantly used for the evaluation of the first laser mirrors. We also received support from Honeywell Military Avionics Division in Minneapolis, MN. When Honeywell Germany received the technology contract the U.S.-Honeywell division was already in RLG series production.

With the approval of the U.S. Department of State a Technology Transfer Agreement (TAA) was set up between these two Honeywell facilities which covered the following assistance: (see Fig. 3)

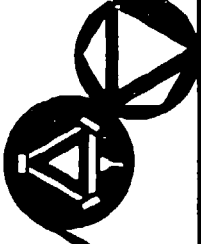
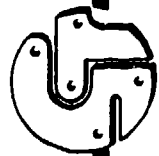
- Assistance in evaluation and selection of German suppliers of ring laser gyro components.
- Support in the design block diagram formulation and candidate geometries.
- Assistance in the definition of evaluation programs at the Honeywell, Germany facility to evaluate breadboard gyros fabricated during the course of the program.

The following restrictions were called out (see Fig. 4):

- No design or manufacturing data on any RLGs currently in development or production in the U.S will be provided.
- No production process or RLG component technology, critical or not, will be provided
- No mirror or mirror related technology will be provided.
- Only lock-in avoidance techniques developed outside the U.S will be used.
- Only non-U.S. subcontractors and/or technology will be used for mirrors, laser gain tubes, glass block material and machining technology.

Honeywell

GERMANY



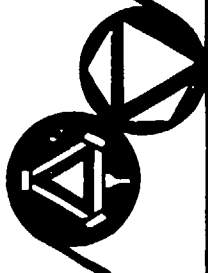
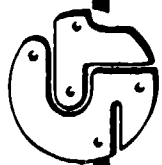
RLG TECHNICAL ASSISTANCE AGREEMENT

ASSISTANCE:

- Assistance in evaluation and selection of German suppliers of ring laser gyro components
- Support in the design block diagram formulation and candidate geometries
- Assistance in the definition of evaluation programs at HONEYWELL Germany facility to evaluate breadboard gyros fabricated during the course of the program

Honeywell

GERMANY



RLG TECHNICAL ASSISTANCE AGREEMENT

RESTRICTIONS:

- No design or manufacturing data on any RLG currently in development or production in the United States will be provided
- No production process or RLG component technology, critical or not, will be provided
- No mirror or mirror related technology will be provided
- Only lock-in avoidance techniques developed outside the U.S. will be used
- Only non-U.S. subcontractors and/or technology will be used for mirrors, laser gain tubes, glass block material and machining technology

S04D

Fig. 4

Despite this TAA having more "No's" than "Go's" it was of great help because it got us started in the proper direction. We developed and installed a new cleanroom lab with vacuum equipment and began hands-on experience with RLG related technologies (see Fig. 5).

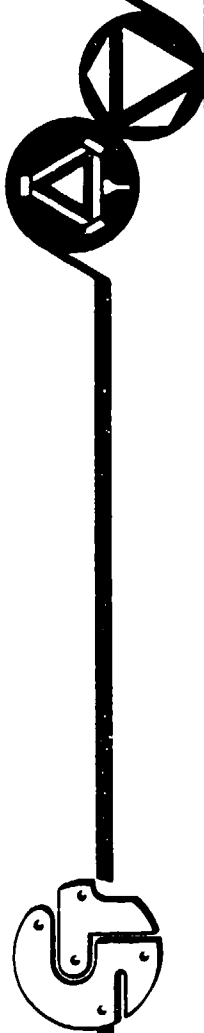
At same time that the RLG was being designed we developed the mirror specification in order to get Zeiss started on the mirror coatings and the block manufacturing. Also at that time we had discussions with Schott in Mainz, a Zeiss subsidiary, (which is only 50 miles away from the Honeywell Germany factory) in order to understand the special properties of the low expansion ZERODUR material which is used for resonator block and mirrors.

Within two years Honeywell Germany demonstrated the first modular RLG to its customer (see Fig. 6), the BWB of the German MOD. The device looked like an RLG and performed like one.

However, it had an unexpectedly high scale factor non-linearity which could not be explained by geometrical deformations of the resonator block. During the following months extensive testing proved that micro movements of the Laser gain tube in the resonator block, such as take place during thermal expansion caused by one or two degrees difference in room temperature, resulted in large differences in output pulse rate. Since there appeared to be no practical way to make the mounting structure for the Laser gain tube sufficiently rigid, (see Fig. 5), a decision was made between the customer und Honeywell, Germany in Summer 1983, to switch the development goal from a modular to an integrated RLG with the gas discharge in the resonator block. This also helped the production cost situation, because a modular RLG is about 20% more expensive than the integrated version.

Honeywell

GERMANY

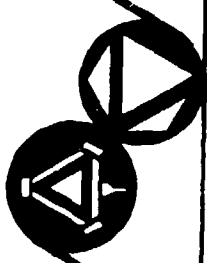
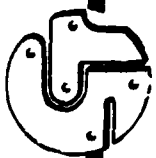


DEVELOPED RLG TECHNOLOGIES

- Extreme cleaning of laser components
- Solder connections between electrodes and ZERODUR
- Activation of electrode surfaces
- Optical contact between ZERODUR and ZERODUR
- Gain mechanisms in small Lasers
- Pump and fill procedures for small Lasers (gas pressure/mixture)
- Evaluation procedures for small Lasers
- Processing of Super Invar for dither springs
- Piezo drives for path length control transducers and dither motors
- Test procedures for RLG's
- Minimizing of scale factor non-linearities
- Computation of mode aperture sizes
- Analysis of geometrical tolerances in RLG's
- Mechano-optical dither compensation
- Design of highly stable drive electronics

Honeywell

GERMANY



RESULT OF THE MODULAR RIG STUDY

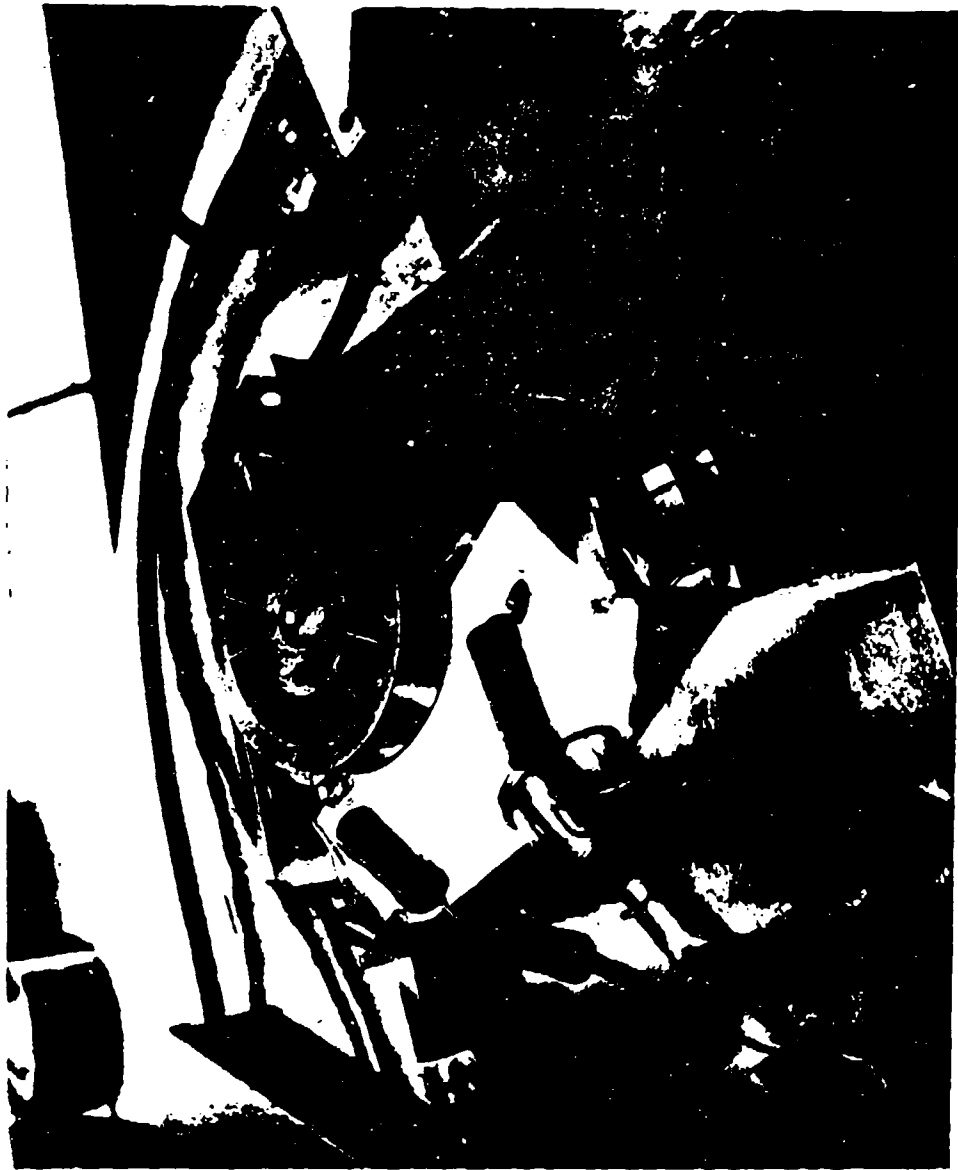


Fig. 6

It took another two years of development. Despite leaving the gas discharge in one leg of the ring resonator (see Fig. 7) in order to keep as many charged particles of the gas discharge as possible away from the mirrors first tests proved that new gas discharge resistant mirrors had to be developed.

In fall 1985 we delivered four RLG's to the IABG, an MOD funded German test facility near Munich, for testing.

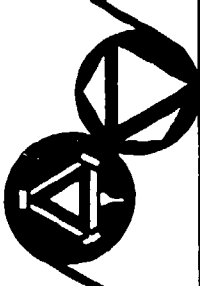
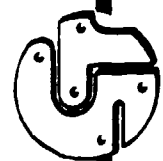
The test results are stated in Fig. 8 (The S/N 005 RLG was added to the contract later for Honeywell internal testing). It is obvious that the S/N 004 RLG is considerably worse in performance than the average. The explanation are 12 temperature sensors which are mounted to the laser block for special gradient measurements. The dampening of the dither motion caused by the connecting wires is responsible for the performance degradation.

A closer look at the other data shows that despite the mirror losses notvarying to much a large variation in scale factor non-linearity can be observed. That means that besides a special positioning procedure for the mirrors other means have to be considered to optimize the lasing triangle. Honeywell Germany, received a follow-on contract in May 1985 (see Fig. 9) for the development of a medium accuracy RLG (0,01 Deg./h).

The award of this contract led Honeywell Germany and Zeiss to make some major investments in the RLG development area. New and bigger laboratories were built, using the recent experience to custom tailor the new development facilities. Honeywell installed inertial measurement laboratory containing a two - axes rate table and a temperature chamber permitting thorough evaluation of the development RLGs.

Honeywell

GERMANY



INTEGRATED RIG GD 4001

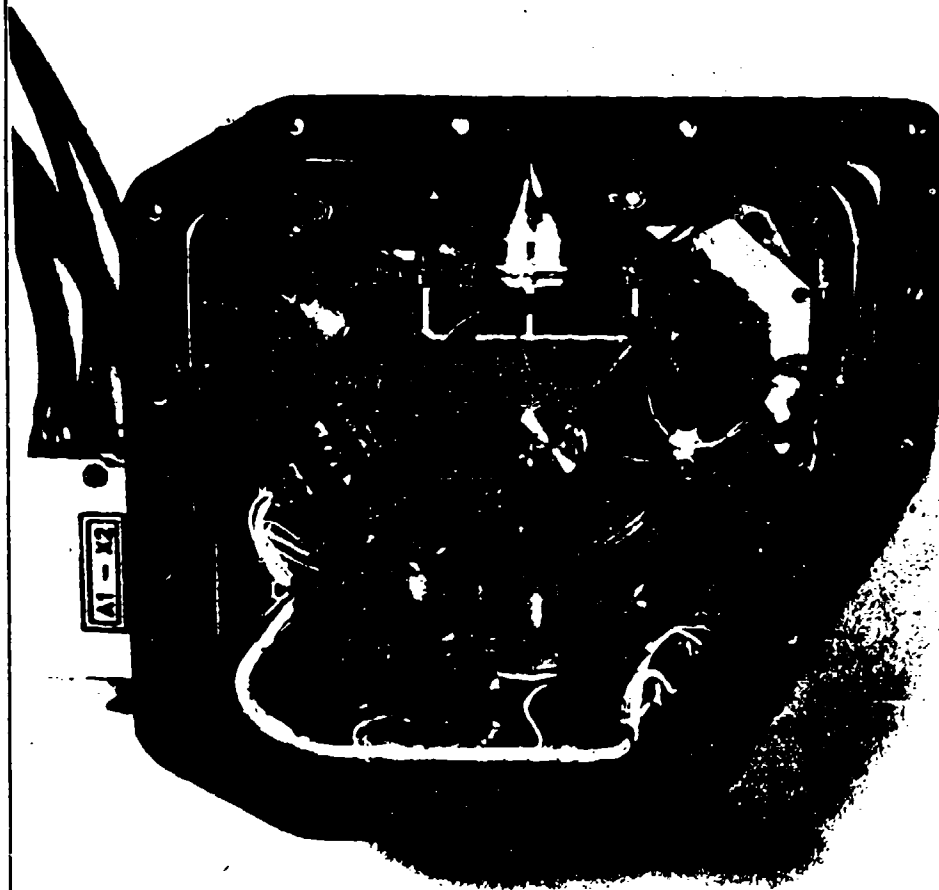
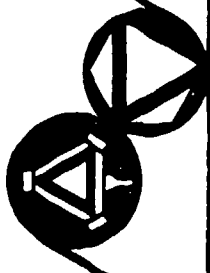
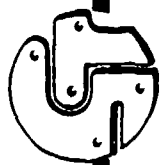


Fig. 7

Honeywell

GERMANY



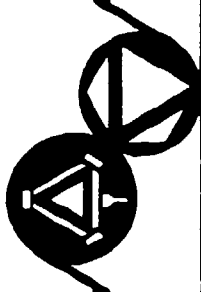
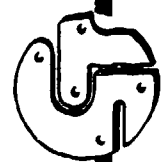
TEST RESULTS OF RLG DEVELOPMENT STUDY

	S/N 001	S/N 002	S/N 003	S/N 004	S/N 005
Lock-In	0.32 °/s	0.37 °/s	3 °/s	6.25 °/s	3.3 °/s
Scale factor non-linearity	217 ppm	14 ppm	208 ppm	1230 ppm	290 ppm
Drift (Day to Day)	0.4 °/s	0.156 °/s	0.47 °/s	1.63 °/s	0.63 °/s
Random Walk	$0.020 \cdot \sqrt{h}$	$0.027 \cdot \sqrt{h}$	$0.034 \cdot \sqrt{h}$	$0.220 \cdot \sqrt{h}$	$0.019 \cdot \sqrt{h}$
Mirror losses	600-650 ppm	500-550 ppm	650-700 ppm	800-850 ppm	690-760 ppm
Scattering	90-150 ppm	90-150 ppm	200-290 ppm	180-230 ppm	110-160 ppm

Fig. 8

Honeywell

GERMANY



GERMAN DEVELOPMENT CONTRACT (PHASE II)

CONTRACT AWARD	:	May 1985
CUSTOMER	:	BWB (Federal Office for Military Technology and Procurement)
TARGET	:	-- Development of RLG with navigation accuracy -- Delivery of four flight worthy RLG's
DELIVERY DATE	:	March 1989
SUBCONTRACTOR	:	C. Zeiss Special Optics (W.--Germany)
SUPPORT	:	-- DFVLR (Germany) -- No US--support

C. Zeiss (Germany) developed procedures to improve the mirrors and to build resonator blocks with the now required higher accuracy. After some iterations Honeywell Germany demonstrated the first German RLG with navigation accuracy to the customer in March, 1987 (see Fig. 10).

In addition to the specification from the customer Honeywell had applied its own requirements to the new RLG: For compatibility reason it was necessary that the new German Honeywell RLG (GD 4003) became a form, fit and function RLG to the RLG GG 1342 from Honeywell, Minneapolis. For this reason we also had to use an isosceles triangle shape. As clearly visible in Fig. 10 it was decided to keep the gas discharge in the base of the triangle. The major improvement is a second movable mirror which helps to stabilize the lasing triangle in position where it sees the least possible lock-in.

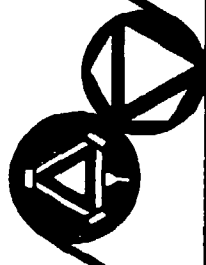
First inertial testing under room temperature proved that Honeywell, Germany has reached its first milestone (Fig. 11) on the way to RLGs with navigation accuracy. The next milestones are the evaluation of the RLG under environmental conditions and delivery of four gyros to the IABG near Munich for official testing by the customer.

At the same time we are beginning a production engineering phase since delivery of the first production German RLG is scheduled for mid 1991. This will be in time for the use of the German RLG in the H423 LINS (US-standard navigator) which has been selected to upgrade the German F-4F fleet and will be manufactured under U.S. license by Honeywell Germany.

Honeywell



GERMANY



RLG GD 4003 (NAVIGATION ACCURACY)

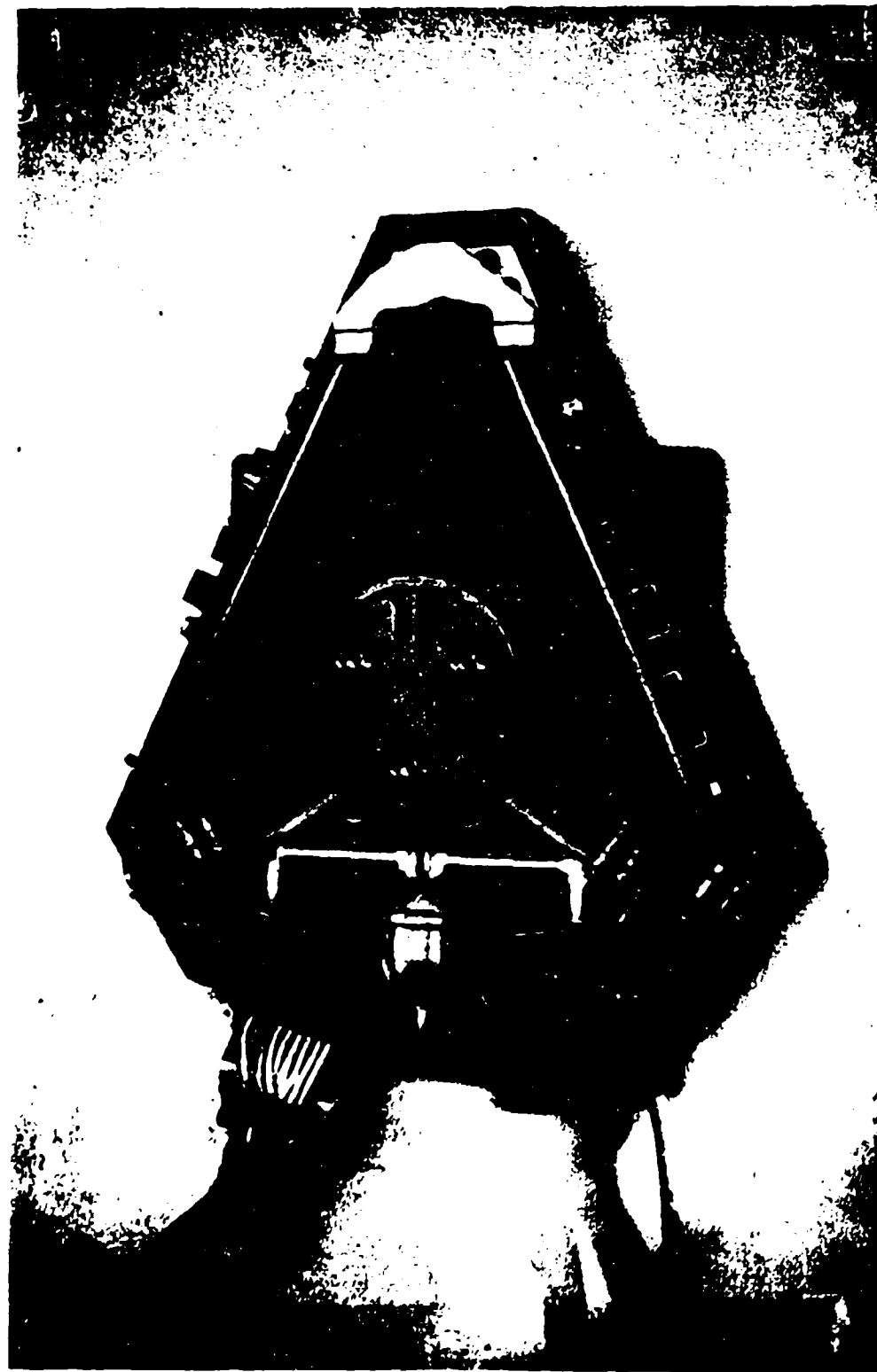
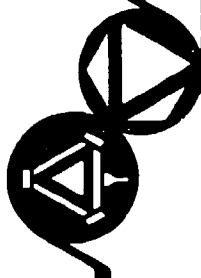
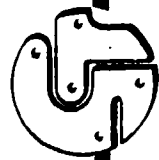


fig. 10

Honeywell

GERMANY



PRELIMINARY TEST RESULTS OF GD 4003 (HAYZ-RLG)

DRIPT (DAY TO DAY)	:	0.03 %/h
RANDOM WALK	:	0.006 %/ \sqrt{h}
LOCK-IN	:	< 0.1 %/s
SCALE FACTOR	:	15 ppm
NON-LINEARITY	:	

Due to time constraints, the following papers were not presented at the symposium.

"Application of Knowledge Based Systems to the Maintenance of Inertial System Electronics," Kenneth B. Cohen, Directorate of Inertial Engineering, Aerospace Guidance and Metrology Center, Newark Air Force Station, OH

(SO4D1)

"Convective Heat Transfer and its Effect on Inertial Measurement Units," John J. Meehan, Rockwell International, Autonetics Strategic Systems Division, Electronics Operations, 3370 Miraloma Avenue, P.O. Box 4192, Anaheim CA

(SO4D2)

"Reference Position Vector," Nancy McClanahan, 6585th Test Group, Central Inertial Guidance Test Facility, Holloman Air Force Base NM

(SO4D3)

**APPLICATION OF KNOWLEDGE BASED SYSTEMS TO THE
MAINTENANCE OF INERTIAL SYSTEM ELECTRONICS**

1 June 1987

**Kenneth B. Cohen
Electronics Engineer**

**Directorate of Inertial Engineering
Aerospace Guidance and Metrology Center
Newark Air Force Station, Ohio**

S04D1

INTRODUCTION

Knowledge based systems are computer programs that 'capture the knowledge' required in order to perform a task. One of the primary advantages of automating a process is that the knowledge possessed is not lost when that individual leaves the organization. Also, these systems are very useful in training new employees and bringing them to the level of the system. This report will examine the process of 'capturing the knowledge' required in fault isolation of electronic modules.

Three knowledge system shells (all available on personal computers) were evaluated and compared using a benchmark circuit. This is by no means an exhaustive list of the packages available. This report will also examine some of the problems of integrating a computer based system into the present work environment.

It was concluded that knowledge based systems might have application to the problem of electronic fault isolation, but the packages examined for this report contain one major drawback. The process of knowledge engineering (that is extracting the knowledge from the expert) is extremely labor intensive. The software used contains no provision for circuit analysis and functional testing. This means that the development of a knowledge based system must be undertaken for each individual module, with little recycling of the information.

BACKGROUND

The FB-111 aircraft uses an inertial navigation system called the N-16H. This unit requires over 40 different electronic modules in order to function. The system and its modules are repaired at the Aerospace Guidance and Metrology Center (AGMC) at Newark Air Force Station Ohio.

The N-16H unit is repaired according to a three tiered system. The N-16H unit itself is a line replaceable unit (LRU). If a failure occurs with the LRU, it is removed from the aircraft and replaced with a good unit. The unit that was removed, is then returned to the intermediate shop (I-shop).

The I-shop isolates the faulty modules and inertial components. These modules and components are shop replaceable units (SRU). The faulty SRU is removed and replaced with a good SRU from another LRU. When the unit requires overhaul beyond the ability for the I-shop to repair, the entire N-16H unit is returned to the depot (AGMC) for repair.

At the depot, faulty modules and inertial components are removed, repaired, and returned to the N-16H unit, which is then returned to the field.

The electronic modules of INS are costly to repair, but more costly to replace. The isolation of faulty components requires highly trained personnel.

THE PROBLEM

If the process of electronic module repair is to be automated, it is proper to look at the current method of repair. When a module is received in module repair, the first step is to perform a functional test. The functional test consists of simulating the electronic stimulus received by the module in the inertial navigation system. If the module passes functional testing, it is then returned to the INS level as a good module.

Sometimes, the functional test is sufficient to isolate the failed component. More often, the technician or engineer must further probe the module while it is on the test station in order to isolate the faulty component. If this is not sufficient, the technician or engineer may then remove power from the module, and take static resistance measurements. Additionally, he may stimulate only a portion of the circuit and get a characteristic reading which can be compared to a good module's characteristic.

Once the faulty component has been isolated, it is replaced and tested again. This process is repeated until the module passes functional testing.

There are two types of errors that can occur during fault isolation. In a type I error, good parts are replaced, and the cycle must be repeated. This results in a waste of components because removed components are rarely reused. In a type II error, nothing is replaced even though a faulty component exists. This results in wasted effort because the faults are usually discovered after the unit is installed in a higher assembly. The unit failing in higher assemblies is more costly to repair than if the fault is caught at the lowest possible assembly.

There are several shortcomings to this system of repair. First of all, the functional test should ideally isolate to the component level. However, many of the functional tests do not. Second, there is not always feedback to the test technician/engineer that his choice of components to change was correct. One technician/engineer may test the module one day, and another may test it the next. Third, sometimes the test equipment is not precise enough to give correct readings. Fourth, it is possible

that the test is not all inclusive, and may not show the failure that occurred in the field.

Another problem presents itself in the repair of electronic modules. The technician must have a knowledge of electronic components and circuit analysis. Given that a circuit does not perform as it should, the technician must be able to locate likely faults to test. Otherwise, the search for faulty components is without direction and time consuming. This process (called shotgunning) leads to type I errors, i.e. replacing components which are not faulty. A knowledge based system could be developed which would have the required information about the modules and eliminate the process of shotgunning.

KNOWLEDGE BASED SYSTEMS

Knowledge based systems are computer programs which use knowledge to solve problems. The programs reason (inference) over the knowledge available to come up with the best solution. These systems are also commonly called expert systems.

Knowledge based systems are beginning to be used in business and industry to aid in routine decision making. Knowledge based systems also assist in training personnel to increase their proficiency, allowing highly trained personnel more time to devote to problems requiring their expertise.

SHELLS

Three knowledge based system shells were evaluated for this paper. They are:

- a. M.1 by Teknowledge
- b. GEMS (General Electric Maintenance System)
- c. EXSYS by Exsys Inc.

Each software package has features useful in this sort of project.

M.1 is a language for fast prototyping. This program runs under MS-DOS on microcomputers. It requires at least 512 kilobytes of memory in order to run. This language is a rule-based, backward chaining inference engine. A text editor capable of outputting an ASCII file (such as Enable or PCWrite) is necessary to use this package. The knowledge base is a self contained text file which is easily readable.

Rules in M.1 are in the form of if then. Interfacing to external programs may be written in C or assembly languages. M.1 version 2.1 will allow up to 2500 rules and facts and has the

SO4D1

ability to segment the knowledge base into several files of up to 2500 rules each. M.1 will perform arithmetic functions, and will deal with uncertain knowledge. Information can be typed in, or can be entered by way of user-defined menus. Executable versions can be created to protect source code programs. AFLC has committed to using M.1 for in-house prototyping. Appendix 1 contains a sample consultation and the knowledge base for the benchmark using M.1.

GEMS is the General Electric Maintenance System. Developed by General Electric for the Air Force Flight Dynamics Laboratory, GEMS is optimized for fault isolation. This program runs under MS-DOS on microcomputers. It requires at least 512 kilobytes of memory in order to run.

There are two different types of files created for GEMS. Truth table files contain possible types of failures that can occur. This type of file also contains the inferencing. Normal Boolean logic is used to represent the inferencing. GEMS uses truth tables to isolate the failure condition. Truth tables are created using an internal editor. Fact files contain questions and explanation information. The fact files provide some provision for friendly interfacing. A text editor is necessary to create ASCII fact files. Because the program uses numerous files, it is slowed down by the disk access time.

GEMS contains the ability to display visual information from a video disk. This feature could be used to display schematics, part locations, or test sequences. GE is developing a pixel graphic system that would serve some of these purposes less expensively. GEMS also had provision to try the highest failure mode first, so it learns what is the most promising path. Appendix 2 contains a sample fact file for the benchmark system.

EXSYS was obtained as a demonstration package. This program runs under MS-DOS on microcomputers. It requires at least 320 kilobytes of memory in order to run. It is a backward chaining inference engine that also allows forward chaining. The key feature of EXSYS is that it is very easy to generate rules. No external editor is required, and it is not necessary to remember any syntax. The rules are developed mostly using menus. It is also possible to make an executable copy of your knowledge base using EXSYS. Rules are if then else type. EXSYS will support a knowledge system of 5000 rules on a PC. The EXSYS benchmark program is included as appendix 3.

KNOWLEDGE ACQUISITION

The process of knowledge acquisition desired for each system is the same. The knowledge is possessed by the 'expert' and acquired by the 'knowledge engineer'. For this report, one person served as both 'expert' and 'knowledge engineer'.

The 'Expert' may be the person who operates the system better than his fellow workers, it may be an engineer who possesses particular knowledge about the operation of the modules, it may be the reference material (schematics, etc.), or most ideally, it is a combination of these. The expert is the person who performs the task much better than average. He is probably the person who others go to with problems. The problem to be solved should be one that he can work easily.

The 'Knowledge Engineer' acquires the knowledge from the 'expert'. This may be done by a combination of research and interviews as appropriate. There should be a continual interaction between the expert and the knowledge engineer as the expert tests the knowledge base to determine if it has drawn the right conclusions.

EVALUATION

A benchmark was developed in order to evaluate each of the knowledge based systems shells used. The benchmark is a small section of the thermoelectric amplifier module. The section tests for an overvoltage condition of the 60 volt power supply. The schematic diagram for this circuit is shown in figure 1.

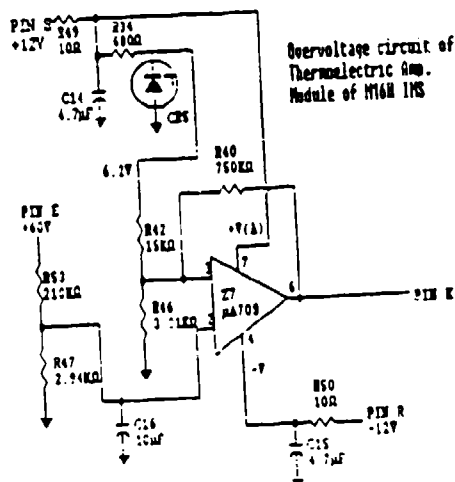


FIGURE 1

This benchmark was chosen because it is a simple circuit that is easily understood by the knowledge engineer. No interview process with the expert was required. This circuit is tested with an automatic tester in the module repair area. The automatic tester simply isolates the fault to this section, and it is left to the technician to isolate to the component.

A comparison of the three expert system shells is contained in figure 2.

COMPARISON OF SHELLS ON BENCHMARK

M.1	GEMS
Type of file - ASCII	Type of files - fact files -
Number of files - 1	ASCII
Size of files - ~4kBytes	tables -
Other metrics - 7 choices	compiled
10 rules	Number of files - 8 tables
8 questions	21 fact files
8 metafacts	Total Size of files - ~10 kBytes
(control statements)	
 EXSYS	
Type of file - not ASCII but readable from EXSYS editor	
Number of files - 2	
Size of File - ~3 kBytes	
Other metrics - 7 choices	
11 rules	
9 qualifiers	
(parameters to check)	

FIGURE 2

Each of the systems ran too quickly to try to gauge the comparative time of running. The systems ask for the next response almost immediately after each question is answered. Only GEMS is different in this respect. GEMS must call between a number of files stored on the disk. It is almost instantaneous until it requires another file. Then you are limited to the disk access time. This problem could be solved using a virtual memory disk emulation.

The development time for each system is also difficult to compare. The knowledge engineer had training in M.I prior to beginning the project, but had to learn GEMS and EXSYS on his own. GEMS was the easiest to visualize as a problem for fault isolation, as GEMS was designed for this sort of problem. It took more time to convert the problem into one for M.I type reasoning, but the problem was solved with EXSYS by directly using the knowledge base created for M.I.

The development system of EXSYS is the easiest to work with. EXSYS has its own editor which assists you in developing the system. It ensures that the knowledge base will be syntactically correct. M.I does not have its own editor, so it is necessary that you learn the very simple syntax. Any text editor can be used for development, and the knowledge base is written in ASCII. The syntax is very understandable to the expert, so he can directly read the information. GEMS has a slightly more complicated syntax, but seems best suited to the solution of this type of problem.

CONCERNS

Human factors - One of the concerns of the knowledge system developer is that the system will be used. Will the computer diagnostician be accepted by the human technician? One way to solve the problem of human acceptance is to make the computer diagnostician as transparent as possible. The mature knowledge base would be integrated into the existing automatic test station. If hosted on a personal computer, the computer and its knowledge base program would act as a 'knowledge server'. The existing test program would query the knowledge base at appropriate times. An interface can be written for M.I to allow it to act in this manner. The development engineers at General Electric have said that a similar interface is planned for GEMS. It is unknown whether EXSYS has or will have the capacity to act automatically.

Software completeness - Another concern in beginning to develop a knowledge system is the validation and verification of the system. For the computer diagnostician, it is necessary that the software be complete. All possible faults should be accounted for. For a project such as module repair diagnostician, all possible faults are not known. The faults may be in any component, combination of components, wiring, or test equipment. Therefore the engineer would have to be familiar with the coding and operation of the knowledge base. He could then add to the system when gaps were found. As the system matured, the engineer would have to make fewer and fewer corrections.

LESSONS LEARNED

The primary problem encountered in developing the benchmark knowledge systems, and subsequently in developing a complete module repair advisor is the problem of knowledge acquisition. The module repair advisor requires an expertise about the circuits which is virtually nonexistent in any one person. The N-16H system is over 20 years old, and the knowledge about the functioning of the circuits must be obtained using exhaustive circuit analysis. None of the packages used in this study have any mechanism for creating a knowledge base given a circuit. The knowledge must be explicitly encoded by the knowledge engineer.

Another problem encountered is that the tests are not all inclusive in fault isolation. Therefore, it was necessary to develop static tests using ohmmeters and signal tracers. Signal tracers input an electrical signal across a component and develop a characteristic curve for a given component. If the curve deviates from the expected curve, the component is considered faulty and is replaced.

SUMMARY

The process of developing a knowledge based system would be very labor intensive. Many of the new weapon systems now being fielded are designed in such a manner that this sort of add-on diagnostic program would be unnecessary. A new systems may already contain fault isolation capability in its test system. The cost of the current method must be compared to the cost of implementation and the cost savings of a knowledge based system. The high turnover rate of experienced test technicians makes a knowledge based system such as this feasible. The N-16H system will probably be fielded long enough to make this feasible, as it is a large workload.

go

What step did the failure occur in?

1 of 100

Is the voltage at -V equal to -12 +/- 0.2 volts?

why

M.1 is trying to determine whether the following rule is applicable in this consultation:

```
kb-23:
  if minusv = fail and
    pinr = pass
  then fault = c15-or-r50.
```

The following entries are also under consideration:

```
kb-2      (a rule)
kb-1      (an initialdata)
```

Is the voltage at -V equal to -12 +/- 0.2 volts?

options

Your response must be chosen from the following:
pass, fail.

Is the voltage at -V equal to -12 +/- 0.2 volts?

fail of 100

Does pin R measure between -11.8 and -12.2 volts?

options

Your response must be chosen from the following:
pass, fail.

Does pin R measure between -11.8 and -12.2 volts?

pass of 100

The fault appears to be in either R50 or C15.
Remove the module from the test adapter.
Using an ohmmeter, check R50. It should measure
between 9.5 and 10.5 kohms. Check C15 using
the signal tracer and the capacitance bridge.
log off

```

initialdata = [step,consultation_over].

if fault = X and
    message(X) = Y and
    display(Y)
then consultation_over.

/* questions    &    legalvals    */

question(step) = '
What step did the failure occur in?
'

legalvals(step) = integer(1,23).

question(pine) = '
Is the voltage at pin E equal to 60 +/- 1.2 volts?
'

legalvals(pine) = [pass,fail].

question(va) = '
Is the voltage at +V(A) equal to 12 +/- 0.2 volts?
'

legalvals(va) = [pass,fail].

question(minusv) = '
Is the voltage at -V equal to -12 +/- 0.2 volts?
'

legalvals(minusv) = [pass,fail].

question(cr5-cathode) = '
Is the voltage of the cathode of CR-5 between 6.15 and 6.25 volts?
'

legalvals(cr5-cathode) = [pass,fail].

question(z7pin3) = '
Is pin 3 of Z7 between .95 and 1.15 volts?
'

legalvals(z7pin3) = [pass,fail].

question(z7pin2) = '
With the adjustable power supply set to 60 +/- 1.2 v,
is the voltage at pin 2 of Z7 between .81 and .86 v?
'

```

```

legalvals(z7pin2) = [pass,fail].

question(pins) = ['
Does pin S measure between 11.8 and 12.2 volts?
'].

legalvals(pins) = [pass,fail].

question(pinr) = ['
Does pin R measure between -11.8 and -12.2 volts?
'].

legalvals(pinr) = [pass,fail].

if step = 1 or
    step = 4 or
    step = 5 or
    step = 6 or
    step = 7 or
    step = 8
then block = i-det-2.

if step = 5 or
    step = 6 or
    step = 1
then z7pin6 = fail.

/*    fault    */

if minusv = fail and
    pinr = pass
then fault = cl5-or-r50.

if va = fail and
    pins = pass
then fault = cl4-or-r49.

if block = i-det-2 and
    z7pin2 = pass and
    z7pin3 = pass and
    z7pin6 = fail and
    va = pass and
    minusv = pass
then fault = z7.

if block = i-det-2 and
    z7pin2 = fail and
    pine = pass
then fault = r42-or-r46.

```

```
if block = i-det-2 and  
  z7pin3 = fail and  
  cr5-cathode = pass  
then fault = r47-or-r53.
```

```
if cr5-cathode = fail and  
  va = pass  
then fault = six-pt2-supply.
```

```
if pins = fail or  
  pine = fail or  
  pinr = fail  
then fault = station.
```

```
message(z7) = [  
The fault appears to be in the area of Z7.  
Remove the unit from the test console.  
Using an ohmmeter, check the resistance of  
R40. It should be between 675 and 825 k ohms.  
If the resistor is bad, replace it, otherwise  
replace Z7. If the problem still persists,  
call the module engineer.  
].
```

```
message(r42-or-r46) = [  
The fault appears to be in the area of R42 or  
R46. Remove the unit from the test adapter.  
Using an ohmmeter, measure the resistance of R42.  
It should be between 14.7 and 15.3 kohms.  
The resistance of R46 should be between 2.9 and  
3.1 kohms. If these both check out, and no  
visible problem exists, contact the module engineer.  
].
```

```
message(r47-or-r53) = [  
The fault appears to be in the area of R47 or  
R53. Remove the unit from the test adapter.  
Using an ohmmeter, measure the resistance of R47.  
It should be between 2.91 and 2.97 kohms.  
The resistance of R53 should be between 207 and  
213 kohms. If these both check out, and no  
visible problem exists, contact the module engineer.  
].
```

```
message(six-pt2-supply) = [  
The fault appears to be in the 6.2 volt supply.  
Measure R34. It should  
be between 648 and 712 kohms. Check CR5 with the signal  
tracer. It should show a diode pattern. If these all check
```

out and no visible problem can be found, contact the module engineer.

'].

message(station) = ['

The fault appears to be in the test station.

Contact Test Equipment!!!!!!

'].

message(c14-or-r49) = ['

The fault appears to be in either R49 or C14.

Remove the module from the test adapter.

Using an ohmmeter, check R49. I should measure

between 9.5 and 10.5 kohms. Check C14 using

the signal tracer and the capacitance bridge.

C15 or R50

'].

FILE:0107

LONG-NAME

Z7 PIN 6 will not switch

EXP

IF PIN 6 OF Z7 will not switch.
THEN Z7 IS FAULTY.

TEST

SUBSTEP

Set the Kepco power supply to 78 V.

SUBSTEP

Is pin 6 of Z7 between -9.5 and -12 VDC.

yes --- PASS <F1>

no --- FAIL <F2>

FILE:0137

LONG-NAME

pin R ~-12V

EXP

Is -12V available to the module.

TEST

SUBSTEP

Using the VOLTMETER, measure pin R.
This should measure between -11.8 and
-12.2 Volts.

yes --- PASS <F1>

no --- FAIL <F2>

Subject:
Benchmark for the module repair consultant

Author:
Ken Cohen AGMC/SNM Newark AFS OH

Starting text:
This program is the benchmark for the N16h module repair advisor. It
uses the Thermoelectric Amplifier module (SQA) from the N16h system.

Uses all applicable rules in data derivations.

RULES:

RULE NUMBER: 1

IF:

The step that fails is 1 or 4 or 5 or 6 or 7 or 8

THEN:

The block is i-det-2

RULE NUMBER: 2

IF:

The step that fails is 1 or 5 or 6

THEN:

Z7 Pin 6 is fail

RULE NUMBER: 3

IF:

The voltage of -V is not $-12 \pm .2$ Volts
and The voltage of Pin R is -12 ± 0.2 Volts

THEN:

C15 or R50 - Probability=1

RULE NUMBER: 4

IF:

The voltage at V(a) is not 12 ± 0.2 Volts
and The voltage at pin S is 12 ± 0.2 Volts

THEN:

C14 or R49 - Probability=1

RULE NUMBER: 5

IF:

The block is i-det-2
and Z7 Pin 2 is .81 to .86 Volts with the adjustable power supply set to 60
+/- 1.2 volts
and The voltage of Z7 pin 3 is .95 to 1.15 volts
and Z7 Pin 6 is fail
and The voltage at V(a) is 12 +/- 0.2 Volts
and The voltage of -V is -12 +/- .2 Volts

THEN:

Z7 - Probability=1

RULE NUMBER: 6

IF:

The block is i-det-2
and Z7 Pin 2 is not .81 to .86 volts with the adjustable power supply set
to 60 +/- 1.2 volts
and The voltage at pin E is 60 +/- 1.2 volts

THEN:

r42 OR r46 - Probability=1

RULE NUMBER: 7

IF:

The block is i-det-2
and The voltage of Z7 pin 3 is not .95 to 1.15 volts
and The voltage of CR5 cathode is 6.15 to 6.25 volts

THEN:

R47 or R53 - Probability=1

RULE NUMBER: 8

IF:

The voltage of CR5 cathode is not 6.15 to 6.25 volts
and The voltage at V(a) is 12 +/- 0.2 Volts

THEN:

6.2 Volt supply - Probability=1

RULE NUMBER: 9

IF:

The voltage of Pin R is not -12 +/- 0.2 Volts

THEN:

test equipment - Probability=1

RULE NUMBER: 10

IF:

The Voltage at pin S is 12 +/- 0.2 Volts

THEN:

test equipment - Probability=1

RULE NUMBER: 11

IF:

The voltage at pin E is not 60 +/- 1.2 volts

THEN:

test equipment - Probability=1

**CONVECTIVE HEAT TRANSFER AND ITS EFFECT ON
INERTIAL MEASUREMENT UNITS**

Prepared for
The Thirteenth Biennial Guidance Test Symposium
October 6-8, 1987
Central Inertial Guidance Test Facility
Hoffman Air Force Base
New Mexico 88330

by
John J. Mehan



Rockwell International

Autonetics Strategic Systems Division
Electronics Operations
Rockwell International Corporation
3370 Miraloma Avenue
P. O. Box 4192
Anaheim, California 92803-4192

Abstract

The objective of this paper is to discuss the effects of convective heat transfer on the performance of inertial systems. This paper discusses the types of errors caused, their effects on calibration accuracy at both the system and instrument levels, and the total effects on flight accuracy of the system. The report draws on empirical information from the MX guidance system program at both the instrument and system level.

Convective heat transfer is seldom considered, difficult to analyze, and, in most cases, easily eliminated.

Introduction

Convection is the transfer of heat by a moving fluid, either gas or liquid. Natural convection occurs when the fluid motion is self induced due to density changes in a gravitational or acceleration field (i.e., g sensitivity that allows convection to raise havoc in a precision inertial guidance system).

The purpose of this paper is to show how convection can be a significant hidden error source in a guidance system and to make suggestions for its elimination. It is beyond the scope of the paper to either model or to analyze convection. In fact, it is strongly recommended that the time and money necessary to adequately model convection are better spent designing it out. Convection is seldom seriously considered during system design. Today's guidance systems are pushing the state-of-the-art in inertial measurements, yet convection still remains a problem and is relatively simple to design out of the system. A lengthy bibliography on the subject is included at the end of the paper.

Effects of Convection

The major effect of convection is modification of the thermal pattern within an inertial platform as a function of acceleration. Figure 1 indicates the non-linear character of convective heat flow as a function of both gap size and temperature gradient.

Component Thermal Sensitivities

Most precision instruments and electronic components have a temperature sensitivity. The sensitivity is generally known and represents the major concern in thermal management during system design. However, the instruments and components will generally have a greater sensitivity to thermal gradients than to overall temperature. One method of reducing an instrument's sensitivity to temperature is by symmetrical design, but this does not reduce the sensitivity to asymmetrical temperature gradients.

An active temperature controller, at best, controls the temperature of a sensor. In the case of a distributed sensor or multiple sensors it controls some composite temperature of these sensors. A single temperature controller

does not reduce thermal gradients, in fact, given asymmetries in the heater(s), they can translate an environmental change in temperature into a thermal gradient change.

In general, asymmetrical temperature gradients cannot be eliminated and need not be, as long as they are stable. The first criteria for maintaining stable gradients is to maintain constant power inputs; the second is to maintain constant thermal paths. This latter condition is impossible if the g vector is changing and convection is present.

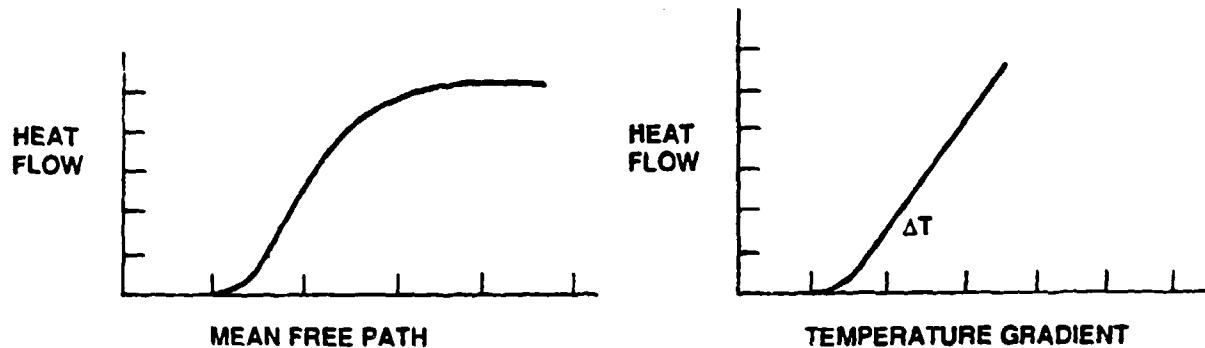


Figure 1. Heat flow due to natural convection as a function of mean free path and temperature gradients (ΔT)

Platform Stability

Mechanical stability in the micro-radian level is critical in an advanced ICBM guidance system platform. Mechanical stability is related to thermal stability by the thermal expansion of the platform material. A temperature gradient can introduce an angular error between two faces of the platform. For example, take a perfect beryllium cube and introduce a 1°F gradient linearly from one face to the opposite. This will yield non-orthogonalities of micro-radians between the side faces and the reference. A cube of aluminum or magnesium would have twice this error.

If the beryllium cube is heated and placed in a convection environment, the top will be hotter than the bottom and the side faces (i.e. normals horizontal) will 'droop' (See Figure 2). If accelerometers were placed on these faces with their sensitive axes outward they would appear to have a negative sensitivity to cross-axis acceleration squared. This will result in a CEP error in a 6000 nm flight of up to 360 feet per $^{\circ}\text{F}$ of convection induced gradient.

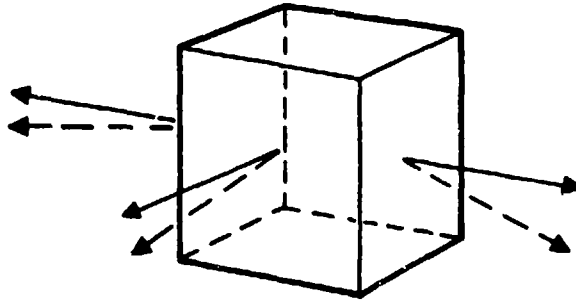


Figure 2. Cube distortion due to thermal gradient

Effects on System Calibration

If the system can be accurately calibrated prior to flight, then the flight becomes anticlimatic. In other words, the major problem in fielding an accurate ICBM guidance system occurs during pre-flight calibration. This, in turn, requires accurate measurements and an accurate model. While convection effects are highly non-linear and complex, they are systematic. They are systematic in relation to both the magnitude and direction of both the g vector and its derivatives. So if these effects are systematic, why not model them and thereby nullify their effects? There are at least four reasons this is not a viable option:

1. The model is far too complex to be adequately defined by analysis.
2. An empirical model cannot distinguish convection effects from other more classical parameters (vis. gyro compliance vs unbalance sensitivity to thermal gradients).
3. Testing in a $1 \bar{g}$ environment can only change the direction of \bar{g} but not its magnitude.
4. Convection effects have finite "set-up times" that are short compared to calibration periods, but long in relation to flight dynamics. In other words, during calibration the system "sees" the total effect of one g convection but this cannot be adequately extrapolated into the multi- g environment of flight.

The compensation for convection effects is unusually complicated, software intensive, and almost impossible to verify. It is also possible that mechanization of the software used to calibrate and align the system may have to factor in the effects of convection.

Performance in Flight

The most interesting thing about the flight is the insight the environment provides with respect to type of convection that exist in the IMU. The flight environment provides acceleration under which free convection is amplified, and zero acceleration where forced convection can be determined from the comparison of the thermal data observed on the ground in a one g environment. The flight environment is probably the best laboratory experiment there is. It provides valuable data for evaluating gimbal and flimbal type of IMU's. The following data is an observation of three thermal signals on the ground, during flight and in a zero acceleration field. Notice the distinct characteristics in these three conditions. The flight data (see Figure 3) provides the final data for the thermal engineers to assess the IMU's performance with respect to trimming up the thermal design.

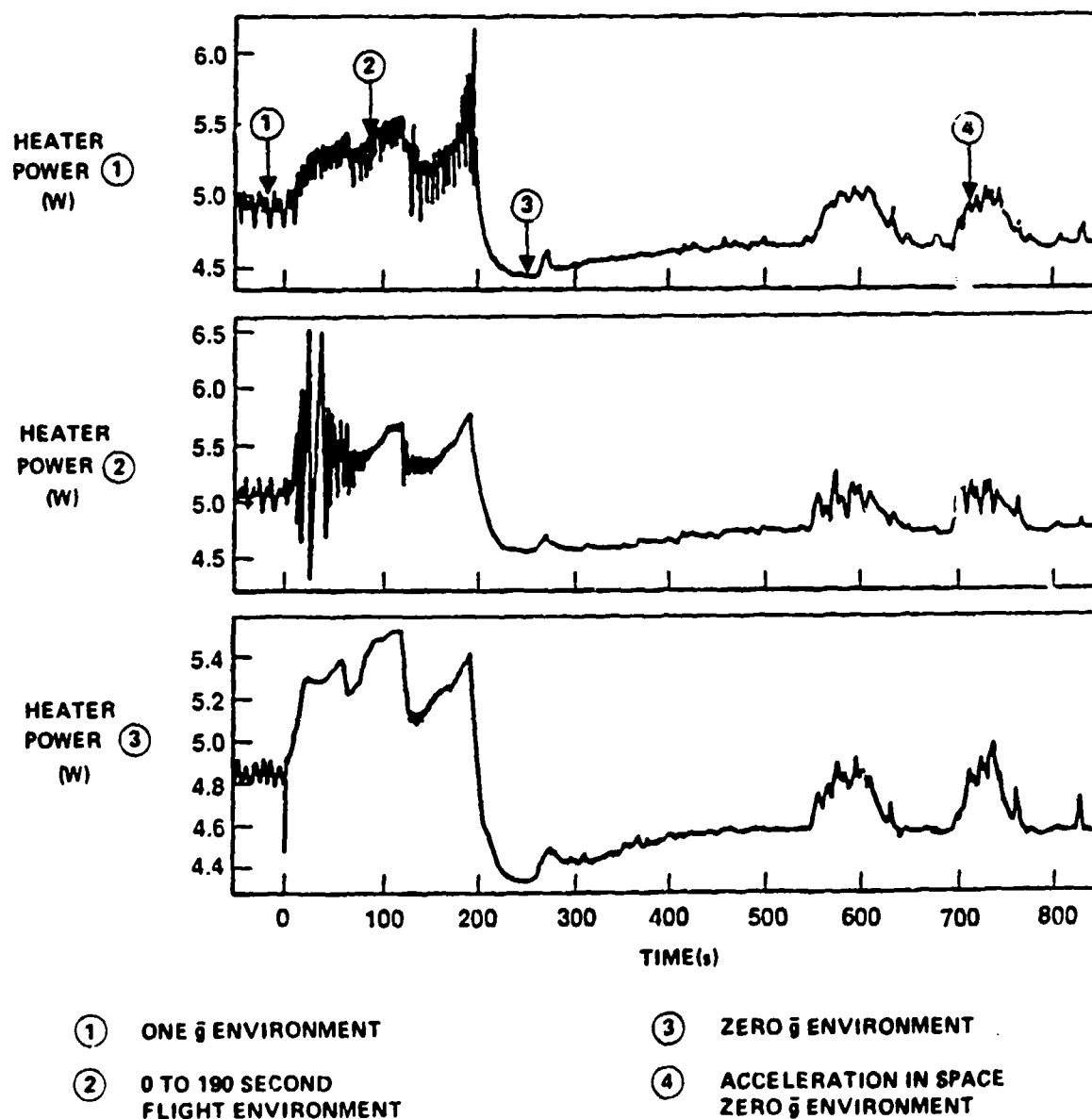


Figure 3. Flight Data

A review of the thermal signals (see Figure 4) which represents three different heaters of the same design reveals that the difference in power from point ① on the ground to point ③ in space is about 0.5 watts. This 0.5 watts represents the contribution mostly from convection. A further review of point ① with point ④ the acceleration in space reveals that the same harmonics appear as those that appear on the ground. These are a few of many of the different characteristics that can be observed in this unique laboratory.

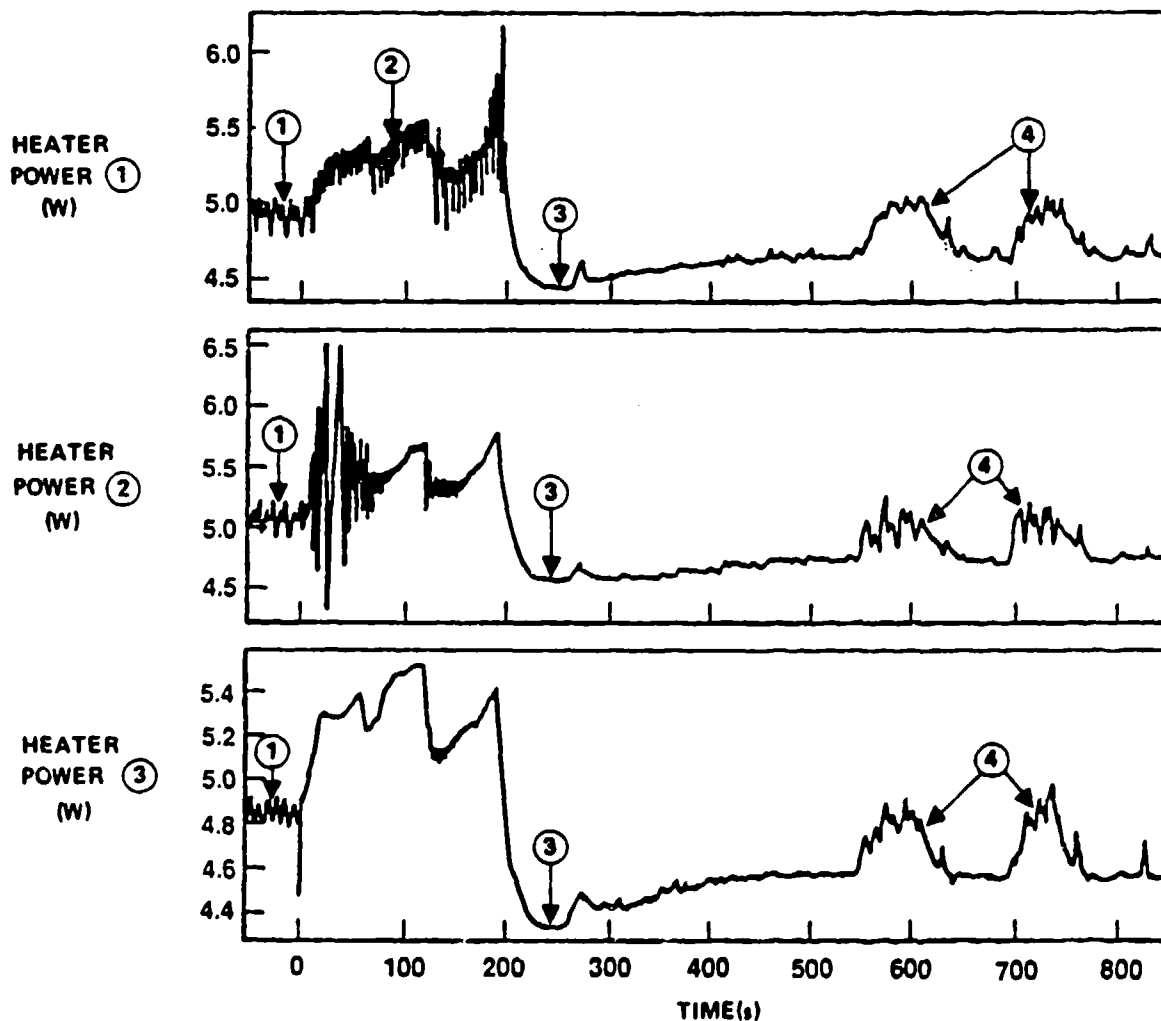


Figure 4. Thermal Flight Data

Quantifying Convection Effects

As stated earlier, it is difficult to determine the magnitude of system errors due to convection. There are two methods that have some validity in obtaining at least a semi-quantitative result. Both methods require the testing of the final configuration, one by reducing convection and the other by increasing it. In both cases, it is assumed that the system goes through a full calibration before and after the modifications and then the results of these calibrations are compared (i.e. parameter values, residuals, etc...).

Decreasing convection in a test system can be done by minimizing the free paths of all fluids. This can be done by filling in the voids with some light thermal insulator. This will increase thermal losses by conduction which must be taken into account when comparing results.

Increasing the convection effects can be accomplished by changing the fluid. In the case of gas, the substitution of helium will dramatically increase convection effects (approximately times six), assuming the normal gas is air or nitrogen. For liquids, a less viscous fluid with an increased thermal capacitance (freon?) can dramatically increase convection effects.

The problem with both of these methods is that they can only be utilized during the latter stages of development (i.e. after the system is built) and requires the dedication of what might be a valuable operating asset.

Recommendations

The solution to the problem of convection lies not in analysis or compensation, but through elimination.

It is very important to take the steps necessary to minimize convection effects during the early design phase of the system. As the design progresses, the requirement to quantitatively verify the need for redesign increases dramatically. Convection effects inherently are difficult to quantify. It is very possible that the total cost of eliminating convection may increase an order of magnitude as the design becomes more rigid. However, the greater danger is that if convection is not eliminated, then the system will go into production with significant but unknown errors.

In the case of gas convection, a perfect vacuum will introduce other thermal interface resistance problems. Therefore a near perfect vacuum that suppresses convection without introducing other thermal problems should be the objective. Convection effects do not reduce directly with gas evacuation as the mean free path of the molecules increases with decreased pressure. This method is not recommended.

When the fluids that support convection are forced to flow across the surfaces, then convection is reduced primarily because the temperature gradients are reduced. Therefore, forced fluid flow can be an effective means of reducing convection effects. Care should be taken to assure that this fluid flow does not change with position or acceleration.

When a liquid is the convection medium, then the use of a higher viscosity fluid or one with a lower heat capacity will reduce the convection effect, but will also usually interfere with the primary function of the liquid (i.e. damping, lubrication, etc.).

Bibliography

1. Holman, J. P., "Heat Transfer", 3rd edition, McGraw-Hill Book Co. New York, 1960
2. McAdams, W. H., "Heat Transmission", 3rd Ed., McGraw-Hill Book Co., New York, 1954
3. Jakob, M., "Heat Transfer", Vol 1. John Wiley & Sons Inc., New York, 1949
4. Dropkin, D., Somerscales, E.: "Heat Transfer By Natural Convection in Liquids Confined By Two Parallel Planes Which Are Inclined At Various Angles With Respect To the Horizontal", J. Heat Transfer, Vol. 87, Pg. 71, 1965
5. Gebhart, B., "Heat Transfer", 2nd Ed., Chapter 8, McGraw-Hill Book Co., New York, 1970
6. Mollendorf, J. C., Gebhart, B., "An Experimental Study of Vigorous Transient Natural Convection", ASME Paper 70-HT-2, May 1970
7. Newell, M.E., Schmidt, F. W., "Heat Transfer By Laminar Natural Convection Within Rectangular Enclosures", J. Heat Transfer, Vol. 92
8. Liepmann, H. W., Rushko, A., "Elements Of Gasdynamics", John Wiley & Sons, Inc., New York, 1957
9. Knudsen, J. D., Katz, D. L., "Fluid Dynamics And Heat Transfer", McGraw-Hill Book Co., New York, 1958

SUPPLEMENTARY

INFORMATION

AD-A185782



DEPARTMENT OF THE AIR FORCE
HEADQUARTERS 6585TH TEST GROUP (AFSC)
HOLLOMAN AIR FORCE BASE, NEW MEXICO 88330-5000

REPLY TO

ATTN OF:

GD

1 February 1988

SUBJECT:

Proceedings - Thirteenth Biennial Guidance Test Symposium
Volume I (AD-TR-87-08)

TO:

WHOM IT MAY CONCERN

Please make the following annotation in this publication:

Page S01B:

Remove the "WARNING" and "DESTRUCTION NOTICE" from
the cover page of this paper entitled, "Simultaneous
Estimation and Detection of Bias Shifts for
Navigation Systems."

This paper was approved for public release. The above
labels were inadvertently left on the document.

Grady S. Nicholson
GRADY S. NICHOLSON
Symposium Manager